Università degli Studi di Genova

Department of Chemistry and Industrial Chemistry

Istituto Italiano di Tecnologia

PhD in

Chemical and Materials Sciences and Technologies

Curriculum: Nanochemistry

Composite porous materials for the removal of organic substances from water

PhD Student (XXXII cycle)

Campagnolo Laura

Matr. No. 4313314

Supervisors

Dr. Athanassia Athanassiou, IIT

Dr. Despina Fragouli, IIT

Prof. Maurizio Ferretti, UniGe

Abstract

The growing demand for clean water clashes with inadequate water availability. Human activities strongly affect the quality of water bodies, inducing their progressive chemical pollution. The sustainable management of water has become a crucial aspect to ensure both the quantity and the quality of water resources needed to support the demand. The limitations of conventional wastewater treatments in addressing the complete removal of contaminants from the effluents require the implementation of legislative measures to reduce the use of certain substances, together with a technological improvement of the treatment plants in order to ensure the quality of water. The improvement of conventional treatments is achieved through the optimization of existing processes or their combination with new advanced treatment technologies. Recently, great efforts have been made towards the development of highly effective, robust and cost-effective composite materials to reduce the entering of aqueous contaminants in water bodies. The progress in nanotechnology offers promising solutions to address the water management challenges, thanks to the use of new advanced engineered nanomaterials in wastewater treatment.

This thesis investigates the use of different techniques for the preparation of porous composite materials aimed at the removal of organic substances from water by means of adsorption processes or photocatalytic degradation. The micro- or nanosized active component is incorporated in a polymer-based matrix which ensures the formation of a solid composite that can be easily handled without requiring further expensive and time-consuming processes for its recovering from the treated water. The first proposed composite material is based on the valorization of agricultural waste for the preparation of a highly porous adsorbent through its combination with a biopolymer. Although their abundance and particular chemical composition make them promising low-cost adsorbents, the difficulties caused by their recovery after the water treatment may limit their manageability and applicability. The incorporation of an agro-waste powder in a solid porous system can overcome this limitation, without significantly compromising its adsorption capacity. Furthermore, using agro-waste as a low-cost active filler reduces the

costs associated with water treatments and the volume of waste derived from food processing.

The following porous composite materials include a photoactive nanomaterial inside the polymer-based matrix, for which the removal of organic compounds occurs by the heterogeneous photocatalytic process. This destructive process is indicated for the abatement of recalcitrant organic pollutants, since it may induce their complete mineralization. The incorporation of the active filler is investigated by using two different approaches, specifically (i) an innovative in-situ fabrication procedure to form the nanomaterials directly inside the polymeric matrix, and (ii) the combination of the pre-synthetized nanomaterials to the polymer-based solution to obtain the porous composite. Different strategies to improve the photocatalytic performance of the porous composite materials are presented, studying the effect of the formation of heterostructures between the *in-situ* grown metal oxide and the noble metals on the photocatalytic degradation of organic contaminants. The proposed *in-situ* fabrication procedure ensures the formation of a metal oxide-based composite, characterized by a high surface area, flexibility and light weight for heterogeneous photocatalytic applications in water treatment, without the need of post-treatment steps for the removal of the photocatalysts from the treated water which may restrict their wide applicability as well as causing secondary pollution. The preliminary results of the incorporation of pre-formed metal oxide nanomaterials in a porous polymeric matrix are then presented, discussing possible future research.

Table of Contents

List of abbreviation and symbols

•OH	hydroxyl radical
$SO_4^{-\bullet}$	sulfate radical
$\bullet O_2^-$	superoxide radical
$\Delta m_s\%$	water uptake capacity
$\Delta m\%$	weight loss
AC	activated carbon
AFM	atomic force microscopy
AOP(s)	advanced oxidation process(es)
BET	Brunauer-Emmett-Teller
BJH	Barrett-Joyner-Halenda
BPA	bisphenol A
CA	cellulose acetate
CA	citric acid
CB	conduction band
$(NH_4)_2Ce(NO_3)_6$	ammonium cerium(IV) nitrate
$Ce(NO_3)_3{\cdot}6H_2O$	cerium (III) nitrate hexahydrate
CeO_2	cerium oxide
C_i	initial concentration
CO	carbon monoxide
CO_2	carbon dioxide
CYS	L-cysteine
DDT	dichlorodiphenyltrichloroethane
DE%	photocatalytic degradation efficiency
DEHP	di(2-ethylhexyl) phthalate
Dhkl	crystallite size
DMF	N,N- Dimethylformamide
D_p	average pore diameter
DSC	differential scanning calorimetry
EDS	energy-dispersive X-ray spectroscopy
Eg	energy band gap
EQS(s)	environmental quality standard(s)
ER	Eley-Rideal
EtOH	ethanol
EU	European Union
FO	forward osmosis
FTIR-ATR	Fourier transform infrared attenuated total reflectance

FWHM	full-width-half-maximum
$Ga(NO_3)_3 \cdot xH_2O$	gallium(III) nitrate hydrate
$Gd(NO_3)_3 \cdot 6H_2O$	gadolinium(III) nitrate hexahydrate
HAADF-STEM	high angle annular dark-field scanning transmission electron microscopy
$HAuCl_4 \cdot 3H_2O$	chloroauric acid trihydrate
HCH	hexachlorocyclohexane
HCl	chloridric acid
$HgCl_2$	mercury chloride
HNO_3	nitric acid
$HO_2\bullet$	hydroperoxyl radical
HRSEM	high resolution scanning electron microscopy
IUPAC	international union of pure and applied chemistry
K	absorption coefficient
k_1	first order rate constant
K_F	Freundlich constant
K_L	Langmuir constant
KM	Kubelka-Munk
KOH	potassium hydroxide
LH	Langmuir-Hinshelwood
LiBr	litium bromide
LO	longitudinal optical
LSPR(s)	localized surface plasmon resonance(s)
MB	methylene blue
MCPA	2-methyl-4-chlorophenoxyacetic acid
MF	microfiltration
MIP	mercury intrusion porosimetry
M_w	weight average molecular weight
n	refractive index
Na_2CO_3	sodium carbonate
NaOH	sodium hydroxide
NCs	nanocrystal(s)
n_{eff}	effective modal refractive index
NF	nanofiltration
$NOBF_4$	nitrosyl tetrafluoroborate
NPs	nanoparticle(s)
Oam	oleylamine
ODA	octadecylamine
ODE	1-octadecene
OP	orange peel
PAH(s)	polycyclic aromatic hydrocarbon(s)
pBDE(s)	polybrominated diphenyl ether(s)
P_c	critical pressure

PEMFC	proton exchange membrane fuel cell
PMMA	poly(methyl methacrylate)
PS(s)	priority substance(s)
PTFE	polytetrafluoroethylene
PVA	poly(vinyl alcohol)
PVC	polyvynil chloride
PVDF-HFP	poly(vinylidene fluoride-co-hexafluoropropylene)
PVP	polyvynilpyrrolidone
Q_e	equilibrium adsorption capacity
$Q_{e(calc)}$	calculated equilibrium adsorption capacity
$Q_{e(exp)}$	experimental equilibrium adsorption capacity
Q_{max}	maximum adsorption capacity
$Q_{max(theor)}$	maximum theoretical adsorption capacity
Q_t	adsorption capacity
R^2	correlation coefficient
RBSP(s)	river-basin specific pollutant(s)
R_L	separation factor
RO	reverse osmosis
ROS(s)	reactive oxygen species
S	scattering coefficient
SAED	selected area electron diffraction
S_{BET}	Brunauer-Emmett-Teller speciic surface area
SCBD	supersonic cluster beam deposition
$scCO_2$	supercritical carbon dioxide
SEM	scanning electron microscopy
SF	silk fibroin
SFOP	silk fibroin-orange peel powder
T_c	critical temperature
TEM	transmission electron microscopy
TGA	thermogravimetric analysis
TiO_2	titanium dioxide
TO	transverse optical
TOC	total organic carbon
UF	ultrafiltration
uPBT	ubiquitous, persistent, bioaccumulative and toxic
UV-C	short-wavelenght ultraviolet
VB	valence band
V_d	real specific total pore volume
V_p	total pore volume
WFD	Water Framework Directive
XPS	X-ray photoelectron spectroscopy
XRD	X-ray diffraction

$(Zn(CH_3CO_2)_2 \cdot 2H_2O$	zinc acetate dihydrate
ZnO	zinc oxide
Λ	Bragg grating period
λ_B	Bragg wavelength
λ_{max}	wavelength of maximum absorbance

Chapter 1.

Introduction

1.1. Global water demand

Global water consumption has become six times higher than one-hundred years ago and continues to increase regularly at a rate of about 1% per year[1]. The continuous rise of water usage is related to the combination of different aspects, such as population growth, which is estimated to rise by a factor of 1.3 in the next thirty years, and economic development[2]. Although, currently, the agricultural water demand prevails, the industrial and domestic needs for water are going to increase much faster than the agricultural one in the next decades[1,2]. However, the prediction of how the demand of water in each sector will change at global scale is difficult due to the interconnection of social, economic and, more important, environmental aspects.

Almost all of the accessible water on Earth is saline, while, to date, only 3.5% is freshwater. The availability of freshwater is diminishing, as climate change, population growth, urbanization and water scarcity have all been contributing factors to the limitation of the resources in the last two centuries[3]. Nonetheless, the increase of global water demand, and the ratio between demand and availability will constantly become higher.

About 80% of European freshwater, used for drinking and other practices, derives from rivers and groundwater, which are extremely exposed to water pollution. Europe possesses abundant freshwater resources compared to other parts of the world; however, despite this, water demand exceeds the available supply in one third of the European territory. This aspect is mostly influenced by climatic change and chemical pollution. Actually, the rapid industrialization and population growth are stressing the water supply and its quality, due to improper water management. Water stress can cause the

deterioration of freshwater resources in terms of available quantity and quality, causing health problems and negative effects on living organisms and ecosystems.

In Europe, the quality of water is mainly affected by the activities in the agricultural and industrial sectors. In the agricultural sector, the intensive use of inorganic fertilizers and active compounds in crops, and of antibiotics in the livestock, has resulted in the diffused water pollution from nitrates and other components of pesticides, as well as from antibiotics. Concerning the industrial effluents, they may contain adverse pollutants, such as heavy metal ions, dyes, oily substances etc. which can enter water supplies due to inadequate wastewater treatment[4]. Therefore, an effective water protection plan is required to preserve the quality and availability of water and to guarantee safe and readily available drinking water.

1.2. Chemical pollution in European freshwater resources

The chemical pollution of the water bodies is one of the major concerns for European Union (EU), eliciting the promulgation of a strong legislation to improve water quality. The aim of EU water policy is to protect the natural resources and the human health. Since 2000, the focus of the Water Framework Directive (WFD) is to ensure that the human use of water resources is compatible with the safety and preservation of the environment, by analyzing the multiple relationships between the pollution sources and their impact on water quality. As reported by WFD, by the continuous monitoring studies in the period from 2010 to 2015, 74% of the European groundwater is "in good chemical status", a classification assigned when the concentration of priority hazardous substances (PSs) is not exceeding the environmental quality standards (EQSs) defined in the Directive 2008/105/EC. However, this condition is achieved only by 38% of surface water. The EQSs are concentration limits of the pollutant substances present in water, defined to protect the environment and the human health from direct toxicity, and for each type of PSs, the annual average concentration monitored in the surface water bodies should not exceed its limit. In addition to the PSs, EU Member States are required to identify also wide priority

substances, namely river-basin specific pollutants (RBSPs), which concentration is regulated by national or regional rules.

Chemical pollution causes adverse effects on organisms and the risk assessment is evaluated by comparing the health response of an organism when it is exposed to increasing concentrations of a pollutant. An aspect to be considered when using these effect-based methods to monitor the quality of water is that they are specific for a targeted chemical, while the presence of unknown substances or transformation products is not evaluated. Furthermore, chemical pollutants are frequently present as mixtures in the aquatic environment. When the organisms are exposed to chemical mixtures, adverse combined effects may be observed, even if the concentration of the singular substances is below the EQS. For this reason, the effect-based methods have to include additional pollutant mixtures considerations to assess the water quality with respect to chemical pollution [5,6].

The monitoring of the listed priority substances by the EU States Member is important in order to plan the appropriate water treatment considering the chemical substances that are exceeding the EQS, and to evaluate the progress on pollution control. Since it can be extremely difficult to clean the water bodies once harmful chemicals enter the environment, or to stop their migration towards other areas, it is important to improve wastewater treatments and, in the near future, to reconsider the substances used in the agricultural sectors.

1.2.1. Common classes of water pollutants

Table 1.1. List of pollutants which most frequently exceed EQSs in EU surface water bodies. Data updated on February 2018.

Pollutant	Pollution source	No EU Member States / water bodies exceeding EQSs	PS/RBSP
Metals			
Mercury	atmospheric /industrial	22 / 45739	PS([a])
Cadmium	industrial	19 / 991	PS
Nickel	industrial	18 / 600	PS
Lead	industrial	17 / 413	PS
Copper	industrial	16 / 808	RBSP
Chromium	industrial	10 / 110	RBSP
PAHs			
Benzo[g,h,i]perylene + Indeno[1,2,3-cd]-pyrene	atmospheric	13 / 3080	PS([a])
Fluoranthene	atmospheric	13 / 1324	PS
Benzo[a]pyrene	atmospheric	11 / 1627	PS([a])
Benzo[b]fluoranthene + benzo[k]fluoranthene	atmospheric	10 / 460	PS([a])
Anthracene	atmospheric	9 / 102	PS
Phenanthrene	atmospheric	4 / 68	RBSP
Plasticizers			
di(2-ethylhexyl) phthalate (DEHP)	Industrial/domestic	11 / 1014	PS
Pesticides			
Hexachlorocyclohexane (HCH)	agricultural	10 / 104	PS([a])
Isoproturon	agricultural	7 / 198	PS
2-methyl-4-chlorophenoxyacetic acid (MCPA)	agricultural	6 / 159	RBSP
Terbuthylazine	agricultural	6 / 51	RBSP
Malathion	agricultural	4 / 13	RBSP
Parathion	agricultural	4 / 7	RBSP
Flame-retardants			
Polybrominated diphenyl ethers (pBDE)s	domestic	7 / 23320	PS([a])

([a]) Substance is classified as uPBT

The WFD defined the list of PSs that have a significant risk for the aquatic environment. In the first proposed list in 2001, 33 substances, or group of substances, have been considered to be of major concern for EU waters. In this group, 11 substances have been classified as priority hazardous substances due to their toxicity, persistency and bioaccumulation and, for this reason, they have been subjected to a scheduled cessation or gradual decrease of their discharges, emission and losses in 2020.

In 2013, the Directive 2013/39/EC includes other PSs to this list, for a total of 45 substances. Small groups of these contaminants of emerging concern, such as mercury and its compounds, polybrominated dipheniylethers and certain polycyclic aromatic hydrocarbons (PAHs), are classified as ubiquitous, persistent, bioaccumulative and toxic (uPBT). The concentration of uPBT substances in surface waters often exceeds the EQSs, resulting in the failure to achieve the good chemical status for most of the monitored water bodies. In Table 1.1 are listed the pollutants that most often are found above the allowed concentration in the surface water bodies. The pollutants are grouped in different chemical classes, including the most influent source that causes their presence in the water bodies, and will be discussed separately below.

1.2.1.1. Metals

As shown in Table 1.1, metals, such as cadmium (Cd), nickel (Ni), lead (Pb), copper (Cu), chromium (Cr) and cyanide ion, have been detected exceeding the EQSs in the surface water bodies of different EU Member States. Such metals are natural substances which have been widely used in the industrial sector. The natural emissions that can contribute to their presence in the environment, such as volcanic eruptions, wildfires and rock erosions, occur at a slow rate compared to the anthropogenic activities. With the exception of naturally metalliferous areas, the metal pollution in surface water is therefore mainly caused by metallurgical industry discharge, fuel combustion, vehicle emissions and agricultural practices [7,8]. Due to the natural presence of metal in the environment, the assessment of the concentration above which the metal may have hazardous effects

on the ecosystems is difficult to be defined. To do this evaluation, it should be considered the metal bioavailability in both water and sediment phase and the effect of mixtures with other pollutants[9]. Although some metal are essential for living beings, higher exposed concentration or mixture effects, can in fact cause adverse and toxic effects to humans and aquatic ecosystems [9,10].

However, the most common pollutant in European surface waters is mercury (Hg) (Table 1.1). It is classified as uPBT and its presence in the environment is the result of natural and anthropogenic activities. The atmospheric emissions of Hg are mainly due to coal burning and industrial processes, as cement production[11]. It is globally distributed and, through atmospheric deposition, it can easily enter the aquatic systems, where inorganic Hg can be converted in the extremely toxic methylmercury[12]. In this form, Hg can be biomagnified and bioaccumulated through the food chain, reaching humans[11,12]. A continuous exposure to Hg causes adverse effects on the nervous, immune and digestive systems, while its combined exposure with other pollutants can cause synergistic effects that can further worsen or cause additional health problems[13].

1.2.1.2. PAHs

Another class of hazardous substances which, for many EU water bodies, was the reason for not being classified in "good chemical status" is the one of the PAHs. They are a large group of organic compounds characterized by two or more fused aromatic rings, which are formed from the incomplete combustion of organic material such as coal, petrol and wood[14]. Sources of PAHs are both natural, as crude oil and wildfires, and anthropogenic, most from the production and processing of metals, vehicle exhaust and domestic heating emissions. Upon releasing in the atmosphere, PHAs are adsorbed on small particles[15] and they can enter the surface waters via atmospheric deposition or from municipal and industrial effluents. Many PAHs are classified highly carcinogenic, mutagenic and teratogenic and therefore are considered a serious threat to the human health[15].

1.2.1.3. Plasticizers

Considering the chemical pollution derived from the domestic sector, the concentration of DEHP exceeds the EQS in 11 EU State Members (Table 1.1). DEHP was a widely used plasticizer in the manufacturing of polyvinyl chloride (PVC) and in other daily use products, such as plastic bags and as additive in paints, cosmetics and toys[16]. Due to its proved harmful effect as endocrine disruptor with toxic effect on reproductive system, its use in consumer products[16], together with other phthalates, has been restricted in the EU market (Regulation 2018/2005/EU amending the REACH Annex XVII). However, DEPH is widespread in the environment, because of its persistence in sediments and soils. Nonetheless, its concentration is above the EQS only in a relatively low number of water bodies, thanks to its successful removal by conventional wastewater treatment processes[17].

1.2.1.4. Pesticides

Pesticides are a group of active substances widely used in the modern agricultural practices to enhance the agricultural productivity and yield and to improve pest control. In Europe, the use of pesticides is regulated by the framework Regulation 1107/2009/EC, in which only the authorized active substances can be used in plant protection products. Although their use is regulated, the concentration of pesticides in surface water bodies may exceed the permitted thresholds, due to their transfer from the treated soil to the water[18]. Actually, the chemical status of the surface water bodies is affected by the presence of pesticides in several EU Member States (Table 1.1). For this reason, there is an increasing concern about the effect on the aquatic ecosystems and on the human health caused by the introduction of active substances in the environment and by their combination as mixtures [19].

The insecticide HCH, also known as lindane, belongs to the organochlorine pesticide group, together with dichlorodiphenyltrichloroethane (DDT), aldrin and heptachlor. It has been used as broad-spectrum insecticide, acting through contact;

however, it can easily volatilized from soil and, due to its sufficiently long atmospheric lifetime and its relatively high solubility, it has been detected in all environment compartments[20]. Due to the high persistency and toxicity of this compound, as well as of the other organochlorine pesticides, many of these previously widely used, insecticides have now been banned (Regulation 850/2004/EC). Other insecticides identified to exceed the EQSs only in few EU Member States, are malathion and parathion, both organophosphorus compounds. Concerning the herbicides, isoproturon is mainly used in the cultivation of cereals and it can be found in water bodies draining from soil. It has been listed as PS because of its toxicity towards aquatic ecosystems[21]. Two other herbicides used to control weeds in cereal and other crops, MCPA and terbuthylazine, also exceed the EQS values, as shown in Table 1.1.

1.2.1.5. Flame-retardants

Among the listed priority substances, the pBDEs are organobromine compounds used as flame retardant which concentration is found to exceed the EQSs in few European Member States (Table 1.1). Flame retardants are incorporated to different materials as additive mainly via physical interactions, in order to stop or reduce the growth of the fire. However, they may diffuse out from the treated material, causing important adverse effects on the human health and environment. In fact, pBDEs are considered toxic and potentially harmful to human beings since they are classified as neurotoxicants and endocrine disruptors[22]. The main sources of flame retardants entering the environment are domestic and industrial wastewater treatment plants effluents, releasing from treated materials and atmospheric deposition[23].

1.2.1.6. Emerging pollutants

Emerging pollutants are a class of chemicals that have received increasing attention over the last twenty years. They are not necessarily new chemicals and they are usually present in low concentration in the environment. Recently, thanks to the

innovation in analytical technologies and instrumentations, it has been possible to detect concentrations of several chemicals in the order of ng/L or μg/L[24]. Despite their low concentration, the emerging pollutants may have a significant hazardous impact on the aquatic organisms. This class includes all the pollutants which are not subjected to any monitoring programs and, due to their toxicity and potential health effect, they can be candidates for future EU regulations. Some examples of emerging substances are industrial dyes, surfactants, organophosphorus flame-retardants, pharmaceuticals and personal care products, biocides, polar pesticides and chemicals with proven or suspected endocrine disruptor effect[25]. Although the prevalence of pharmaceuticals classified as emerging pollutants derives from industrial and domestic sectors, the misuse of active compounds in agriculture is increasing also the discharge of antibiotics and hormones mainly used to treat diseases and to promote growth in livestock and fishes[26].

1.3. Wastewater treatments

Wastewater must be treated in order to be disposed in the ambient without causing harm to natural environment and to human health. Conventional wastewater treatments consist of a combination of physical, chemical and biological processes to remove solid, organic matter and nutrients, as nitrogen and phosphorous, from waste effluents. To be effective, the treatment approach changes considering the incoming water, due to the different sources of water contamination[27]. In particular, most industrial processes produce large volumes of polluted water, in which the specific composition of the industrial effluents is strictly related to the manufacturing procedure. The industrial effluents are therefore composed of specific organic compounds, heavy metals and salts or any mixtures of the above, presenting often extreme conditions of pH or high turbidity. In these cases, it is important to pre-treat the primary industrial effluents before they reach the wastewater treatment plants, in order to ensure an effective purification[28].

In general, the decontamination process starts with a physical and mechanical pre-treatment of the wastewater, to eliminate larger debris, followed by the primary treatment, which involves the partial elimination of solid and organic matter by physical and chemical methods, such as precipitation and coagulation (Figure 1.1).

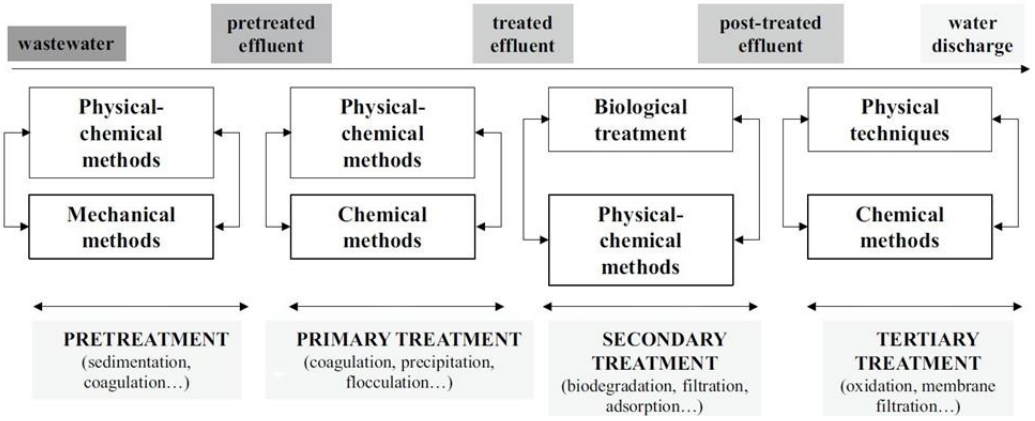

Figure 1.1. Schematic diagram of the main processes in a conventional wastewater treatment, adapted from reference[4].

The treated effluent is subjected to the secondary treatment, in which the dissolved and suspended organic solid matters are set down by means of a chemical and biological treatment. In this phase, the bio-degradable organic matter is removed using aerobic biological treatments, which include the use of micro-organisms or activated sludge, usually in combination with filters in case of high concentration of organics. The effluent is further treated with a tertiary treatment before being discharged into the environment. The tertiary treatment involves physical techniques and chemical methods to improve the quality of the water. Nutrients, dissolved solid, resistant organics and heavy metals are removed by means of advanced wastewater treatments, such as oxidation processes and use of specific membranes or adsorbents [4]. Conventional wastewater treatments are however ineffective in the removal of numerous chemical compounds, which have been recently introduced in the domestic, industrial and agricultural sectors. In fact, as mentioned above, conventional wastewater treatments are commonly aimed to treat specific effluents reaching the restricted quality standards, but they often fail to remove emerging pollutants. As consequence of the failure in the proper removal of pollutants, the discharged water is among the main sources for the release of emerging pollutants

into the environment[29,30]. Therefore, it is important to ensure the quality of outcoming water in order to protect the environment and the human health.

The improvement of the quality of the treated wastewater can be achieved through the optimization of existing processes or through the combination of new treatment technologies in the tertiary treatment, such as membrane separation, advances oxidation and adsorption onto non-conventional solids[4,31,32]. The implementation of tertiary treatments with other advanced processes is proved to be effective in the reduction of the effluent toxicities and in the reaching of the appropriate quality criteria[33].

New treatment technologies, which have already been combined to conventional wastewater treatments or evaluated for the improvement of the water quality, will be presented in the following sections.

1.3.1 Membrane separation processes

Membrane separation processes, such as microfiltration (MF), ultrafiltration (UF), nanofiltration (NF), reverse osmosis (RO) and forward osmosis (FO), have been widely used in wastewater treatments to improve the removal of emerging contaminants from treated effluents. Different types of materials have been used as membranes, including polymeric and inorganic materials. Polymeric-based membranes are the most used, due to the high processability and low cost. Among the membrane-based technologies, MF and UF are low-pressure separation processes, which are usually employed to treat wastewater effluents in the secondary treatment process, in which the separation performance is often improved by combining them with several pre-treatments, such as ozonation, biological activated carbon or coagulation, resulting in higher removal of dyes, organic substances and microorganisms [34,35]. These two membranes are able to completely remove the suspended solids, thanks to the physical barrier provided by their porous sizes (ranges from 0.1 - 1 μm and 0.01 - 0.04 μm in MF and UF, respectively)[29]. Contrarily, NF has been investigated as a tertiary treatment process to remove pharmaceutical residues from secondary effluents, reaching removal efficiency values strongly dependent from the physicochemical properties of the investigated

pollutants[36]. The rejection of organic compounds by NF and RO membranes can occur for three different events: size exclusion, adsorption or electrostatic repulsion, through the formation of the Donnan potential on the membrane surface in the latter case. In the NF membranes, the pore size range is from 1 to 10 nm, higher than the one of RO membranes (pore size < 1 nm)[37]. Although the pressure-driven NF and RO processes are effective for the removal of many organic contaminants, they require high-energy consumption and produce waste stream with high content of organic and inorganic matter, whose disposal is challenging[29,36]. Moreover, the surface of the membranes is subjected to fouling deterring the filtration performance, therefore it is important to develop membranes in which the fouling is minimized. The FO membrane operates under an osmotic driving force, without requiring a pressure difference and it is a suitable alternative to RO for the rejection of organic compounds (Figure 1.2a). The osmotic pressure gradient drives water from the diluted feed solution to the concentrated draw solution through a semipermeable membrane, which rejects salts and organic contaminants in the feed solution. Since the osmotic pressure is the driving force in this separation process, unlike the hydraulic pressure in NF and RO, the water transfer is bi-directional, showing a forward diffusion of water from feed solution coupled with the reverse draw diffusion (Figure 1.2b)[38].

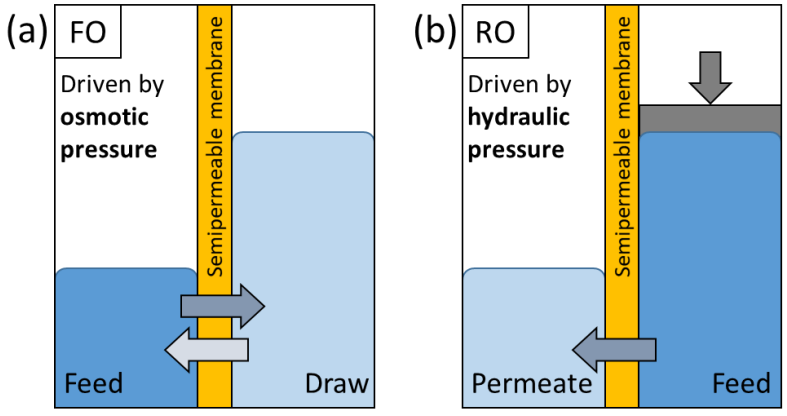

Figure 1.2. Schematic diagram of (a) FO and (b) RO membranes.

FO has been successfully employed in wastewater treatment, in which the treated effluent is used as feed solution[39]. Draw solution provides the osmotic pressure, driving

therefore the FO separation. An appropriate draw solution should minimize reverse diffusion and be compatible with the post-treatment steps[40]. FO membranes have revealed high retention values, reaching above 99% rejection in case of heavy metal ions, such as Cd, Cr, Hg and Pb, due to the combination of heavy metal transport across the membrane, their hydration radii and the instauration of the Donnan potential[41]. In case of organic compounds, FO membranes have reached higher rejection values for large hydrophobic molecules and for ionic compound, due to the instauration of hydrophobic and electrostatic interactions[41]. The use of membrane separation processes based on FO is therefore considered a promising solution for the improvement of the quality of water in wastewater treatment, thanks to the lower energy demand, to the lower susceptibility to membrane fouling and to the high water recovery[42].

In general, compared to other water treatments such as adsorption processes, membrane separation processes show acceptable performance, despite their poor efficiency in treating particular contaminants, like heavy metals, mostly in case of high concentration[43]. Moreover, membrane separation processes, with the exception of particular cases, are not selective and often require the combination with other physicochemical treatments, since its easy subjection to fouling[4,43].

1.3.2. Adsorption processes

Adsorption processes have been recognized as a feasible technology for water purification, compared to other physical or chemical techniques. In fact, techniques such as coagulation, flocculation, ozonation etc. can cause the formation of hazardous by-products, resulting thus in secondary pollution, but also require high energy consumption and high cost to work properly[33]. Adsorption is a physicochemical method widely used for the wastewater treatment, due to its cost-effectiveness, easy operation and simplicity of design. Usually, adsorption processes are employed to remove dissolved organic compounds, which remain in the treated effluent after the secondary or tertiary treatment. The adsorption of one or more compounds from the fluid phase to the solid phase occurs with the balancing of the interaction forces between the adsorbate, the adsorbent surface

and the fluid. The affinity between the adsorbate and the adsorbent is the main interaction force controlling the adsorption process. Based on the type of the established interaction, the adsorption process can be classified as a physical or chemical adsorption (physisorption and chemisorption, respectively). In a physisorption, the interaction occurs without electron exchange by the instauration of hydrogen bonds, electrostatic and van der Waals forces. Through this interaction, a multilayer adsorption can occur on the surface of the adsorbent, in which the adsorption is characterized by low binding energies, ranging from 5 to 40 kJ/mol. In this case, the adsorbed substance can easily desorb under specific conditions. Chemisorption involves the transfer, exchange or sharing of electrons between adsorbate and adsorbent, due to the formation of ionic and covalent bonds with binding energy in the order of 40 – 800 kJ/mol. The adsorption is therefore irreversible, with the formation of a monolayer of adsorbate on the adsorbent surface. Usually, in a real-world situation, the classification between physical or chemical adsorption is not so strict and each case has to be considered separately.

In wastewater treatment, adsorption processes can be combined to other tertiary treatments, both discontinuously in batch reactors, or continuously in fixed-bed reactors. The continuous adsorption systems are suitable for water treatment in large-scale applications using packed-bed columns, although the contact time between the effluent and the adsorbent is lower than the one in batch reactors. Furthermore, some parameters should be considered before scaling up the continuous systems to ensure the maximum performance, such as the bed adsorption capacity, the mass transfer processes and the saturation times. However, the removal efficiency of continuous systems is usually below the one achieved for batch reactors[44].

Ideal adsorbents should have a high surface area and pore volume, with good mechanical, chemical and thermal stability. Furthermore, they should present high adsorption capacity and rapid adsorption kinetics, ensuring restrained costs of the overall adsorption process. Since the adsorbent performance gradually decreases due to the progressive accumulation of the adsorbate on its surface, the regeneration of exhausted adsorbents represents a fundamental aspect to be considered for choosing the adsorption

process in wastewater treatments. In fact, the regeneration potential establishes the economic feasibility of the employment of the adsorbent in the wastewater treatment.

Activated carbon (AC) is the most common adsorbent used to treat wastewater, due to its high specific surface area and good adsorption capacity towards different contaminants. AC is derived from various organic precursor, such as bituminous coal, lignite, peat, wood and coconut shell, through physical or chemical activation[45]. To treat the effluents, AC is mainly used in the form of granules in fixed-bed columns or as powder in slurry form, showing good adsorption capacity for most of the refractory organic substances, even at low concentrations and/or in the presence of competitor compounds for the same adsorption sites[46–48]. The high cost of commercial AC and the difficult regeneration limit however its use, encouraging the research of alternative precursor sources, by means of renewable and cheaper byproducts or residues from industrial and agricultural activities[46,49]. The production of low-cost AC, starting from residues of processing industries, contributes to a sustainable waste management, resulting in a profitable circular economy[49].

As an alternative of the AC adsorbents, a large number of low-cost adsorbents have been developed and investigated for the removal of different compounds, such as heavy metal ions, nutrients, dyes, pesticides and pharmaceuticals, from water and wastewater[50,51]. Specifically, lignocellulosic materials from agricultural waste, such as agricultural peel-based biosorbents, have been proposed as feasible adsorbents for real applications[52]. Agricultural waste peels are formed in great amounts during the industrial processing of fruits and vegetables and, together with their particular chemical composition, make them an inexpensive, abundant and eco-friendly resource able to effectively remove diverse types of compounds from water without requiring sophisticated pre-treatments[52]. This ability is explained by the several polar functional groups of their main components, such as lignin and cellulose, which are able to efficiently interact with various organic and inorganic pollutants[52–55].However, these low-cost adsorbents have been evaluated mostly in the powder form, and for experiments at lab-scale, in which only few studies reported the results on the treatment of real wastewater

effluents. Although the results show a remarkable affinity towards a wide range of contaminants, further studies are required to assess their applicability in full-scale wastewater treatments as an alternative to AC.

1.3.3. Advanced oxidation processes

Advanced oxidation processes (AOPs) are promising and environmentally friendly technologies based on the *in-situ* production of highly reactive radical species capable of oxidizing organic compounds in aquatic media. AOPs are of particular interest in wastewater treatment because these processes provide a sustainable and effective option for the removal of recalcitrant organic pollutants, which persist in the treated effluents after the employment of conventional treatments[56,57]. Differently from the previously discussed treatments, the AOPs can be effectively employed as destructive methods for the removal of toxic compounds forming less complex and harmful intermediates. The generation of highly reactive radical species, such as hydroxyl (•OH), superoxide ($•O_2^-$), hydroperoxyl ($HO_2•$) and sulfate ($SO_4^{-•}$) radicals, is achieved through a wide range of different methods, which are in part represented in Figure 1.3.

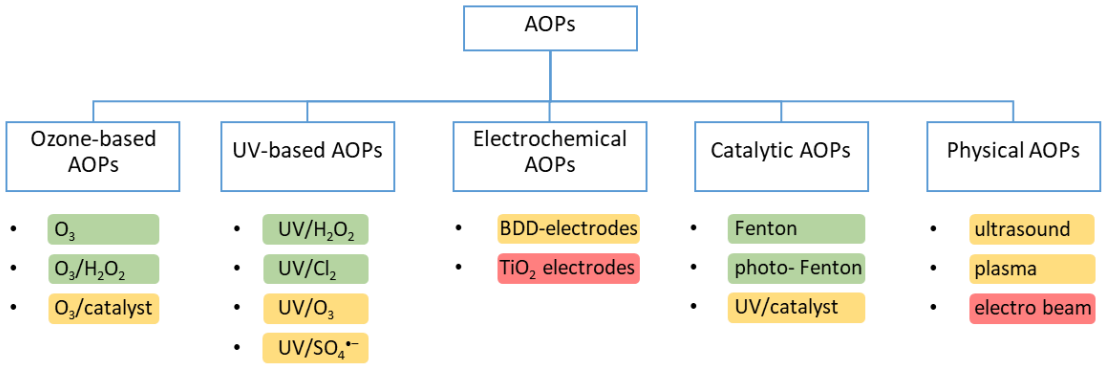

Figure 1.3. Classification of the different methods in AOPs. Processes established at full scale (green), investigated at pilot- and lab-scale (orange) and only at lab-scale (red).

Some of the processes consist of a combination of different technologies and, for this reason, it is difficult to strictly categorize the AOPs in separate methods. As shown in Figure 1.3, the effectiveness of several AOP applications at full-scale in real wastewater treatment plants has been already demonstrated, resulting in the improvement on the

removal of a wide range of organic compound[56]. Among the ozone-based AOPs, it can be also included the ozonation, due to the generation of •OH in water under certain conditions. Ozonation and peroxonation (O_3/ H_2O_2) have been implemented in full-scale wastewater treatment, usually in combination with other techniques, in order to overcome process-specific limitations[58]. Ozone is commonly used as a selective strong oxidant (oxidation potential of 2.08 V vs. SCE) and as a disinfectant in water treatment. In a pilot-scale, O_3/ H_2O_2 has been combined with UV/ H_2O_2 and granular biofiltration processes for the abatement of contaminants of emerging concern. The combination of these three processes, in which O_3/ H_2O_2 is followed by biofiltration and then UV/ H_2O_2, allows to reach removal efficiencies comparable of those observed for the membrane-based train composed by UF and RO membranes[58]. The presence of the other oxidant (H_2O_2) strongly improves the generation of •OH, resulting in a significant enhancement of the abatement of contaminants[59].

The removal of several antibiotics has been improved by the implementation of UV-based AOPs (UV/H_2O_2 and UV/ SO_4^{-}• processes) via conventional short-wavelength ultraviolet (UV-C) disinfection reactor already installed, as complementary processes in the tertiary treatment. The generation of •OH and SO_4^{-}• under UV light induces a more effective degradation of the antibiotics than the one observed with only the UV-C treatment during the disinfection step[60]. Other AOPs implemented as tertiary treatments are catalytic-based methods such as Fenton and photo-Fenton processes. Fenton oxidation process is based on the formation of highly oxidative •OH that can quickly and non-selectively degrade most organic pollutants. The formation of •OH is observed upon the decomposition of hydrogen peroxide catalyzed by iron (II) under strong acid. The Fe^{2+} is oxidized to Fe^{3+} (eq. 1), which is subsequently reduced to Fe^{2+} with excess addition of H_2O_2 (eq. 2).

$$Fe^{2+} + H_2O_2 + H^+ \rightarrow Fe^{3+} + H_2O + {}^{\bullet}OH \quad (1)$$

$$Fe^{3+} + H_2O_2 \rightarrow Fe^{2+} + {}^{\bullet}O_2H + H^+ \quad (2)$$

In the photo-Fenton process, the combination of UV or visible light to the conventional oxidation process ensures an improvement of the degradation of the

pollutants, resulting also in a lower production of the iron sludge which is formed by the precipitation of the Fe^{3+} ions as ferric hydroxide oxide at pH above 3[61]. The Fenton oxidation process is already used in industrial full scale applications[56] and in pilot wastewater treatment plants[62]. The use of photo-active catalysts and the basic principles for the removal of organic pollutants from water by heterogeneous photocatalysis is discussed in the following chapter.

Physical AOPs, such as ultrasound, plasma (liquid-phase electrical discharge) and electronic beam irradiation, have been investigated for different wastewater treatments. In these processes, the abatement of contaminants is induced by the instauration of highly energetic events. However, the physical AOPs are energy- and capital-intensive, hindering their implementation in wastewater treatments[56].

1.3.3.1. Heterogeneous photocatalysis

Heterogeneous photocatalytic oxidation is one of the most promising AOPs for oxidizing organic pollutants into more biodegradable and less harmful compounds[63]. The process can be described as the acceleration of a photoreaction in the presence of a catalyst by adsorption of the reactants on its surface, without itself being consumed. The use of metal oxides as photocatalysts has aroused great interest thanks to their significant features, such as the desired band gap, abundancy in nature, biocompatibility and good stability in a variety of conditions.

The light-driven reactions at semiconductor surfaces have been extensively studied since 1960s, using well-defined monocrystalline materials. The potential of heterogeneous photocatalysis was further recognized by Fujishima and Honda in 1972, when they demonstrated the photo-assisted electrochemical water splitting to H_2 and O_2 on n-type semiconductor titanium dioxide (TiO_2), encouraging strong improvements in the research especially in relation to energetic and environmental applications[64]. In fact, heterogeneous photocatalysis is one of the most investigated AOPs for the removal of contaminants of emerging concern from water, showing good process scalability, and it

can operate both in continuous or in a batch depending on the target compound (as also shown in Figure 1.3)[29,65].

Among the metal oxides, TiO_2 semiconductor is extensively used as photocatalyst, due to its low cost, high chemical stability and biocompatibility. Most importantly, TiO_2-assisted photocatalytic oxidation is demonstrated to be effective in the degradation of a wide range of organic pollutants under mild conditions[65].

The definition of a semiconductor is easily obtained considering the available energies of the electrons in the material. In crystalline solids composed by N atoms, by decreasing the interatomic spacing, the coupling between adjacent atoms with discrete electronic energy levels leads to the overlapping of the atomic wave functions, resulting in the formation of continuous energy bands of discrete but closely spaced energy levels. The most external energy band completely full of electrons is defined as valence band (VB), while the upper vacant band is called conduction band (CB). The forbidden gap between VB and CB is called energy band gap (Eg). The Eg is the minimum energy required for the excitation of an electron from its bound state (VB) to a free state (CB). The electronic properties of solids depend on the differences in energy bands position and the distribution of electrons in each band, distinguishing between conductors, semiconductors and insulators, as shown in the simplified energy diagram in Figure 1.4. In fact, the distribution of the electrons in the energy bands determines the electrical conductivity in the solid. Bands that are partially filled have higher energy levels still available for the electrons to move upon application of an electric field and their movement leads to the electrical conduction.

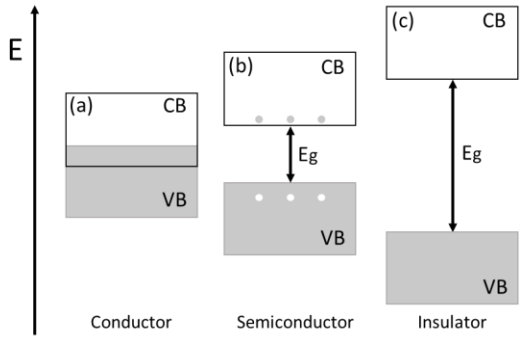

Figure 1.4. Energy band diagrams for (a) conductor, (b) semiconductor and (c) insulator.

In a conductor, the VB can be either partially or completely filled; in case of half-filled VB, as for metal that have only one valence electron per atom like copper and silver, the electrons can move in the available energy levels at slightly higher energies, while for full VB, the high electrical conductivity is the consequence of the overlapping between the VB and the CB (Figure 1.4a). Typical conductors are, in fact, metals, in which the outer electrons of the atoms are loosely bound and can move through the solid. In an insulator, the VB is filled and separated from the CB by a large Eg, precluding, at least for ordinary temperatures, the electrons from reaching the CB, and therefore no electrical conductivity occurs (Figure 1.4c). Representative examples of insulators are glass and paper. In semiconductors, such as TiO_2, the VB is close enough to the CB, with a relatively low Eg, and therefore electrons can reach the CB given some external energy, with the formation of holes in the VB (Figure 1.4b). In the absence of energy supply, the distribution of electrons and holes is ruled by the Fermi distribution, which takes into account the tendency of electrons and holes to recombine.

The photocatalytic properties of the semiconductors are influenced by several factors, such as the energy band gap, the mobility and mean lifetime of the photo-excited carriers, the absorption coefficient of the material and the nature of the liquid- or gas-solid interface.

In the overall cyclic process of the heterogeneous photocatalysis, it is possible to establish five independent steps:

1. mass transfer of the reactant to the catalyst surface
2. adsorption of the reactant onto the catalyst surface
3. photocatalytic reaction in the adsorbed phase
4. desorption of the products from the catalyst surface
5. mass transfer of the products from the interface region to the bulk fluid.

When a reactant is near to the photoactivated catalyst, it can preferentially concentrate, or be adsorbed, on its surface. Depending on the established relationship between the adsorbed compound and the catalyst surface, it is possible to distinguish between two principal adsorption mechanisms, based on physical and chemical

interactions. In the physical adsorption, the event quickly reaches the equilibrium via van der Waals or weak hydrogen bonds and it is reversible, allowing easy regeneration of the catalyst. The chemical adsorption involves the formation of coordination bonds via Lewis acid-base interactions or dissociative adsorption via Brønsted acid-base interaction, requiring more energy to regenerate the catalyst.

In general, after the adsorption of the reactants on the surface catalyst, the photocatalytic reaction occurs upon irradiation with a proper electromagnetic radiation. The interaction of the surface charge carriers with the adsorbed reactants can promote surface chemical processes that can be described by two catalytic mechanisms, Langmuir-Hinshelwood (LH) model and Eley-Rideal (ER) model, as shown in Figure 1.5. The reactant adsorption is an exothermic equilibrium, which is favored at low temperature and high pressure, differently from the molecule desorption and regeneration of the catalyst, which are favored at higher temperature and lower pressure.

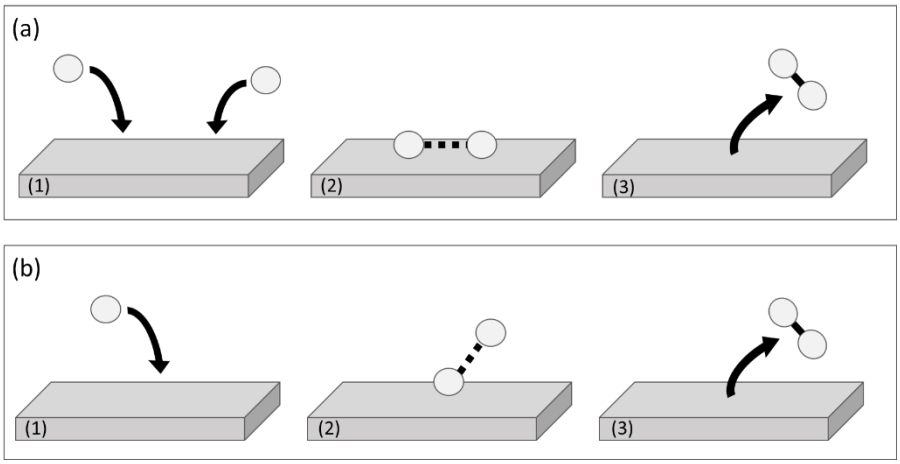

Figure 1.5. (a) LH and (b) ER mechanisms in a gas-solid reaction, involving the formation of molecular hydrogen at the catalyst surface.

In the LH model (Figure 1.5a), the catalytic reaction occurs on the surface of the catalyst. Specifically, in the case of gas-solid reaction, such as the formation of hydrogen, two atoms are first adsorbed onto the catalyst surface, where they diffuse until they are close to interact, then the formed molecule desorbs from the surface. Differently from the LH model, in the ER mechanism (Figure 1.5b), the reaction occurs between an adsorbed atom and another atom in the gas phase. The photocatalytic degradation of organic

pollutants on the semiconductor surface is usually described, with minor deviations, by the LH model, which is widely applied to liquid-solid reactions[66,67]. After the reaction in the adsorbed phase, the formed compound is then desorbed from the catalyst surface.

To describe in detail the photocatalytic reaction, it is useful to define the main phenomena that occur at the interface of an illuminated TiO_2 particle dispersed in polluted water. The photoexcitation of a semiconductor is a quite complicated process, in which the absorption of photons is strictly related to the nature of the active site on the crystalline semiconductor. The general mechanism of the photocatalytic oxidation process for the degradation of organic pollutants on a metal-oxide based semiconductor is described in Figure 1.6.

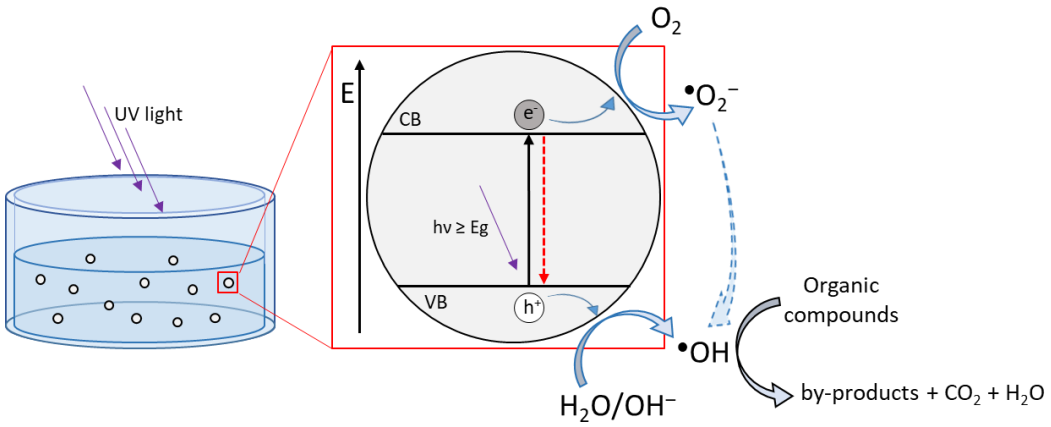

Figure 1.6. General mechanism of the photocatalytic process on TiO_2 particle dispersed in polluted water.

When the aqueous suspension of the semiconductor powders is irradiated by light, the absorption of photons, whose energy is equal or higher than the catalyst energy band gap, results in the formation of electron-hole pairs, with the dissociation of photo-electrons in the conduction band and photo-holes in the valence band. The photo-generated electron-hole pairs migrate to the surface or interface of the semiconductor, where various redox reactions occur with the adsorbed compound, resulting in the formation of reactive oxygen species (ROSs). The generation of ROSs at the H_2O-TiO_2 interface can be described according to the following scheme[68]:

$$TiO_2 + h\nu \rightarrow TiO_2 (e^-_{(CB)} + h^+_{VB})$$

$$OH^- + h^+ \rightarrow {}^\bullet OH$$

$O_2 + e^- \rightarrow {}^\bullet O_2^-$

${}^\bullet O_2^- + H^+ \rightarrow {}^\bullet O_2H$

$2{}^\bullet O_2H \rightarrow O_2 + H_2O_2$

$H_2O_2 + {}^\bullet O_2^- \rightarrow OH^- + {}^\bullet OH + O_2$

Typically, for the wide band gap TiO_2 photocatalyst under UV light, the photo-excited electrons are trapped by dissolved O_2 in water, producing ${}^\bullet O_2^-$, while the photo-generated holes react with H_2O/OH^- to generate ${}^\bullet OH$. The formed ROSs are highly active oxidants, which can oxidize the organic pollutants promoting their degradation. However, most of the electron-hole pairs may recombine before reaching the catalyst surface (red dotted arrow in Figure 1.6), decreasing the quantum efficiency of the photocatalytic process. Usually, the electron-hole recombination in a catalyst can occur due to the presence of energy states within the band gap in which electrons can easily pair-up with holes, or due to the short lifetime of the photo-generated electron hole pairs. For this reason, different strategies have been proposed to prevent the charge recombination, improving the photocatalytic oxidation of aqueous pollutants.

1.4. Nanotechnologies and nanomaterials for water remediation

The improvement of conventional wastewater treatments is required to address the increasing demand for clean water. The significant difference in the local composition of wastewater streams makes extremely important the individual optimization of the treatment processes and plants. Further research is required for the minimization of the impact on the environment and, consequently, on the human health concern caused by an inappropriate water management. This may be achieved by the exploration of new sustainable, safe and cost effective methods as alternative to conventional processes that are often considered chemically, energetically and operationally intensive [69].

The advance in nanotechnology offers promising solutions to address the water management challenges[28], as it offers the possibility to use new advanced engineered nanomaterials for wastewater treatment. This results in processes with enhanced performance, and with a consequent reduction of energy and cost requirements compared to the conventional wastewater treatment materials. Furthermore, the enhancement of the performance of engineered nanomaterials results in a higher effectiveness of the water treatments, reducing consequently the consumption of chemicals and of the cost and energy requirements associated to conventional treatments[70].

The control of the size, morphology and chemical structure of the engineered nanomaterials ensures the preparation of novel multifunctional systems with the desired optical, adsorptive, catalytic, electrical and antimicrobial properties. These multifunctional nanomaterials enable the concurrent combination of several treatment processes, resulting in the removal of a wider range of contaminants with different physio-chemical properties, which would instead require the use of different separate processes. In addition, depended on the application, they can be also designed to selectively remove specific pollutants[71]. Thanks to the implementation of engineered nanomaterials to the next-generation of membrane-separation, advanced oxidation and adsorption processes, it is possible to design adaptive and highly efficient wastewater treatments which can overcome the limitation of the traditional processes[71].

A wide number of engineered nanomaterials has already been proved to be effective in the enhancement or replacement of conventional wastewater treatments in a laboratory or pilot scale, facing however hurdles in the scale-up phase. Since the nanomaterials-based advanced processes show a relation between the volume of treated water and their efficiency and energy consumption, the treatment of small fraction of water ensures thus reduced operational costs. Therefore, the right key for the real use of nanomaterials-based processes in large scale applications[72] is through the innovative redesign of the treatment processes, by means of the decentralization of the large-scale treatment plants. The establishment of an interdependent hierarchical network of separate infrastructures allows the adaptation of the treatment processes through nanotechnology-

enabled water treatments to efficiently address specific effluents[71,72]. Decentralized nanotechnology-based processes will ensure a more reliable and affordable access to clean water, due to the versatility of a modular treatment approach for the abatement of specific contaminants, enhancing the overall ability to treat different water streams[28,32]. However, the redesign of the water infrastructures, through the upgrading with hybrid centralized/decentralized systems, requires a deep investigation of many factors, including financial and political aspects, which could hinder the implementation of these systems[32]. Despite this, decentralized systems have been already demonstrated to play an important role in different urban areas[73,74], confirming this solution as the appropriate route for the implementation of the nanotechnologies to the wastewater treatments.

1.5. Motivation of the thesis

The application of nanotechnology in water remediation is a promising strategy for the highly efficient removal of organic compounds from water. The advancement in nanotechnologies positively affect the emerging wastewater treatments, such as the photocatalytic oxidation processes, which can improve the quality of the effluents if used in combination with the tertiary treatments. Among the emerging wastewater treatments, heterogeneous photocatalysis can be considered a destructive process able to potentially mineralize organic contaminants, especially persistent organic substances, which are not completely removed from the effluents by conventional wastewater treatments. Photocatalytic degradation of organic pollutants can therefore be used to improve their abatement or their conversion in less toxic and more biodegradable organic compounds.

The use of nano-photocatalysts allows to achieve impressive photoactivity, thanks to their large surface area, abundant surface states and relatively simple modification. However, the impact on the aqueous environment of accidentally discharged nano-sized materials strongly limits their usability in real-world applications. The harmful effects of nanomaterials on aquatic organisms (*e.g.* algae, crustaceans and fishes) has been fully

demonstrated and their toxicity has been connected to the concentration, exposure time and reactivity of the nanomaterials in water bodies[75]. Another limitation of the use of free nanomaterials is the requirements of energy and time-consuming steps for their recovery from the treated water, which usually do not result in their complete removal. Therefore, the potential risks on the ecosystems and on the human health, together with the difficulties in separation and effective collection of the nanomaterials, have led to the development of composites for the immobilization of nanomaterials.

The immobilization of the photo-active nanomaterials on a porous support allows the fabrication of functional solid composites, preventing their loss in the environment. The formation of an interconnected porous matrix ensures a high surface area material, in which organic pollutants from the permeate water can interact with a high number of active sites. This aspect allows to reach a good compromise in terms of the reduced exposed surface area of the embedded nanomaterials with the achieved benefit of no complex recovery steps. Polymers have been recently proposed as supports for nanomaterials due to their low weight, flexibility and easy conversion in different morphologies[76–81]. In fact, the chemical resistance, mechanical strength and relatively simple processability of some polymers make them a convenient choice as porous substrates in the development of composites for water treatment applications.

Besides the wide variety of synthetic polymers, the use of biopolymers has many advantages for the preparation of functional composites. Biopolymers are macromolecules formed from living organisms[82], which are usually isolated and extracted from renewable feedstock sources or from waste products by several chemical processing techniques. The natural abundance of this class of biomaterials and their well-defined chemical composition allow the formation of low-cost composites that are usually biodegradable and non-toxic[83]. The use of biopolymers as polymeric supports allows to prepare materials characterized by nano and macroscale features, thanks to their direct assembly in insoluble ordered structures.

In addition to the composites prepared with inorganic materials[84,85] for water treatment applications, biopolymers can also be combined with natural by-products, such

as agricultural crops, in order to form a fully biocomposite adsorbent. In this case, the incorporation of agro-food by-products, as low-cost active filler, to form a sustainable composite allows their valorization reducing the costs associated to water treatments and the volume of waste derived from food processing. Conversely from heterogeneous photocatalysis, the use of biocomposite adsorbents does not ensure the mineralization of organic compounds, but they can nevertheless be easily used in case of high content of organic pollutants to concentrate them.

1.6. Thesis Outline

This thesis is focused on the investigation of different techniques for the preparation of porous composite materials aimed at the removal of organic compounds from water. First, the used fabrication techniques to obtain the porous matrix are presented in Chapter 2, considering their advantages and disadvantages on the formation of the porous structure. Then two strategies to incorporate the active material in the composite are proposed, specifically the incorporation of pre-formed nanomaterials and their direct synthesis inside the polymeric matrix, highlighting their convenience when developing a composite.

After a general introduction on the fabrication procedures, the following part of the thesis describes the different developed porous composite materials and their use to remove model organic compounds by adsorption process and by photocatalytic degradation. Chapter 3 addresses the first composite material, which is a highly porous adsorbent prepared through the immobilization of an agro-waste powder in a bio-polymeric matrix for the efficient removal of methylene blue dye from water. The effect of the agro-waste incorporation on the gelation process of the biopolymer and the formation of the final porous structure is discussed. Then the adsorption efficiency of the embedded low-cost adsorbent is compared to that of the free powder. The proposed biocomposite can be considered as an alternative to powder-like or synthetic solid sorbents in wastewater treatment.

The second material discussed in Chapter 4 is an electrospun composite mat for the heterogeneous photocatalytic degradation of organic pollutants in water, in which the photoactive nanomaterial is directly formed inside the polymeric matrix, obtaining a solid porous system. Besides the innovative *in-situ* synthetic approach to incorporate the nanomaterial in the polymer, the fixed metal oxide is further modified with noble metals through different approaches and the effect on its photocatalytic performance under UV light is studied.

Chapter 5 is based on a different photoactive metal oxide and its incorporation in a porous composite through both the proposed synthetic strategies. The enhancement of its photocatalytic performance is investigated by means of different approaches, to improve the light harvesting of the solar spectrum. In the first part of the chapter, the metal oxide is directly formed in a polymeric electrospun mat and its modification with a noble metal allows the activation of the photocatalytic degradation of the organic compound under visible light, improving thus the visible light harvesting. In the second part of the chapter, the metal oxide is separately synthesized and then incorporated in a porous composite. The effect on the photocatalytic activity will be evaluated by doping to modulate the point defects in the metal oxide. The preliminary results on the incorporation of the metal oxide in the porous composite are discussed, evaluating the possible future directions. In addition, the size control study of the metal oxide is reported in Appendix 2. The adaptation of colloidal synthesis ensures the preparation of batches with different sizes of the metal oxide, which will be used as a support for an atomically dispersed catalyst, in order to study the role of the size of the support during the photocatalytic CO oxidation.

Beyond the preparation of porous composite materials for the removal of aqueous contaminants, the preliminary results of the development of a sensitive polymeric coating as an active layer of an optical sensor are also presented in Appendix 3. The study of the stability of the proposed polymeric film and its interaction with mercury ions in water are reported, confirming its potential use as a sensitive coating deposited on fiber Bragg

grating for the detection of mercury, which is the most widespread aqueous pollutant in the European water bodies.

Chapter 2

Fabrication methods

The advantages of the implementation of nanotechnologies and nanomaterials in water remediation have been highlighted in the previous chapter. However, the use of active nano- or micro-particles is often hindered by difficulties in post-processing steps to recover them from the treated water. Therefore, a way to overcome these difficulties is to incorporate the active components into porous polymeric matrices to form polymer-based nanocomposites.

The development of new materials with incorporated nano- or micro-sized active particles requires an effective immobilization of the fillers on high surface area materials. Ideal polymeric supports for wastewater treatment should have high specific surface area, porosity, surface functional groups and they should exhibit chemical inertness towards a wide variety of harsh conditions. Conversely to inorganic supports, the use of polymers ensures several advantages, such as the relatively easy modification of the physiochemical properties of the material and the relatively lower production cost[86]. Polymeric supports, based on synthetic polymers or biopolymers, can exhibit attractive peculiarities in terms of morphology, flexibility and mechanical properties, which make them a valid alternative to classic inorganic supports for environmental applications[87].

This chapter introduces the theoretical concepts of the approaches mainly used to prepare the polymeric-based porous matrices. Methods on the complex incorporation of the active components in the polymeric matrices are then presented, focusing on two main approaches. Specifically, the incorporation approaches concern the direct dispersion of pre-synthetized nanoparticles (NPs) in the polymeric solutions before the formation of the porous nanocomposites (presented as *ex-situ* strategy) and the direct functionalization of the surfaces of already formed polymeric porous materials through *in-situ* synthesis of NPs.

2.1. Gel drying

Depending on the type of the polymer, solid porous matrices can be prepared starting from gels, by means of different drying techniques to remove the solvent from the gel pores. A polymer gel consists in wet soft solid-like material, in which the liquid phase fills the interstitial spaces of the elastic cross-linked solid[88]. Since gels are prone to deform or crack during drying, one of the main difficulties in the drying process is to preserve the original nano- and micro-porous structure. Different approaches can be used to dry the gels, such as the evaporative drying, the freeze-drying and the supercritical drying[89]. In case of the simple evaporative drying, the liquid is removed from within a solid porous material by its evaporation (at ambient pressure or under vacuum). However, the surface tension and the capillary stress induced by the removal of the solvent can cause the disruption of the porous network which often collapses due to the material shrinking. For this reason, the evaporative drying process is not widely used, unless in specific conditions, where the porous structure is considered a secondary feature with respect to the formation of a dried solid material.

2.1.1. Freeze-drying technique

Although freeze-drying is mainly used in the pharmaceutical field to dry diluted solutions, it has been recently used also for the removal of the solvent in NPs and in solid materials, thanks to its advantages with respect to other conventional drying techniques. In fact, the freeze-drying technique works at low temperature, usually below 20 °C and, therefore it can be used to dry materials composed by thermolabile compounds. Furthermore, it ensures the preservation of the physiochemical characteristics of the components. The freeze-drying process deals with the removal of a solvent, mostly water, from the frozen gel by the sublimation and by the desorption of sorbed solvent under vacuum, producing high quality dried products. The process involves three subsequent steps and the first freezing phase is the most critical, affecting the overall process. The gel is cooled down, in atmospheric pressure, to a temperature below the eutectic point of the

solvent under an optimal freezing rate. The rate of freezing determines the crystalline size and, therefore, the features of the final porous structure, such as the shape of the pores, the pore size distribution and the pore connectivity[90]. Slow freezing rate induces the formation of larger crystalline structures, which leads to a fast sublimation of the frozen solvent out of the dried material. On the other hand, fast freezing rate results in the formation of small crystals, decreasing the destabilizing mechanical stresses on the porous structure[91]. After the freezing step, the sublimation of the frozen solvent is performed during the primary, or main, drying step. The conversion of the frozen solvent directly into vapor is obtained by transferring heat to the material under vacuum to speed up the process. The vapors are collected on a condenser and at the end of this phase, almost all the solvent is removed. In the last step of the drying process, the secondary drying involves the removal of the bound solvent that has not been sublimated. In this step, which is usually faster than the main drying step, the temperature is raised at higher value while the pressure is set lower than those of the primary drying.

The use of this drying technique results in the formation of a foam-like dried material with relatively high porosity and low density. One of the main disadvantages of this technique is the difficult control of the freezing rate, which may cause the formation of larger crystals of solvent or their melting during the drying steps, thereby affecting the final porous structure[92]. Furthermore, the freeze-drying process can be also used to remove organic solvents from gels. However, particular safety considerations and special systems are needed to handle volatile and potentially harmful solvents and to reach the lower temperatures required for their freezing and condensation.

2.1.2. Supercritical fluid-assisted drying technique

The supercritical fluid-assisted drying technique is an alternative process to remove organic solvent preserving the original porous structure without effects of surface tension and capillary stress. Moreover, there is no effect of the mechanical stress caused by the solvent freezing such as in the freeze-drying technique.

Supercritical fluids are a unique class of substances that above certain conditions of temperature and pressure have properties between those of a gas and a liquid. As shown in Figure 2.1, it is possible to define a supercritical fluid as a single phase that occurs when a fluid is held above its critical temperature and pressure. Above the critical point, the fluid shows a density and solubility similar to those of the liquids, while its compressibility is comparable to that of the gases.

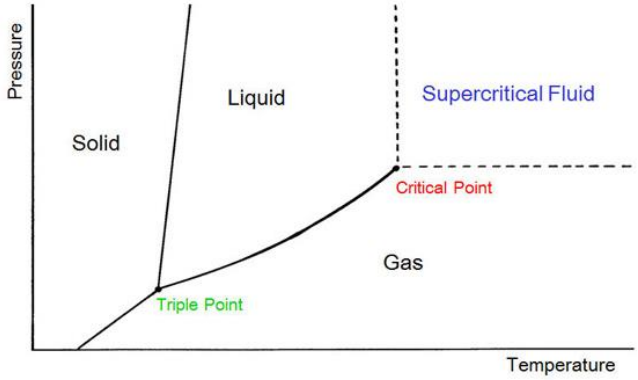

Figure 2.1. Phase diagram for CO_2.

Most organic solvents have a relatively high critical temperature (T_c) of 200 – 600 °C and critical pressure (P_c) of 50 – 100 atm. In Table 2.1, the T_c and P_c values of some of the most diffused organic solvent are compared with the ones of the carbon dioxide (CO_2). The lower critical parameters for CO_2 make its critical point easily accessible. Therefore, among the supercritical fluids, CO_2 is the most used because not only it is cheap, chemically inert, non-toxic and non-flammable, but also because it can be processed at mild conditions without forming harmful residues[93].

Table 2.1. Critical points of various solvents[94].

Solvent	T_c (°C)	P_c (atm)
Acetone	235.1	46.385
Carbon dioxide	31.13	72.786
Ethanol	241	60.567
Hexane	234.6	29.854
Isopropanol	235.3	47.017
Methanol	239.5	79.783
Toluene	318.8	40.563

The supercritical CO_2 ($scCO_2$) has been used in industrial drying procedures, to dry mostly organic or inorganic gels, which are prepared using sol-gel techniques[95]. In fact, the $scCO_2$ is miscible with numerous organic solvents and it can easily be recovered after the drying process, making this supercritical fluid a good choice as a drying medium[95].

In the $scCO_2$ drying of a gel, the liquid solvent, which is usually a mixture of water and organic solvent, is first substituted by a pure organic solvent characterized by a good miscibility with $scCO_2$. The soaking of the gel in the pure solvent is important to remove the residues of water from the pores. After that, the gel is placed in a pressure vessel with liquid CO_2 to displace the organic solvent. When the organic solvent has been completely replaced, the liquid CO_2 is heated above its critical point, which causes its conversion in gas. At this point, the $scCO_2$ can be removed from the pores of the material by means of an isothermal depressurization of the fluid. The use of $scCO_2$ drying has been demonstrated effective in the removal of different organic solvents from biopolymer-based gels, obtaining interconnected porous structures in NPs and in solid aerogels[96,97].

2.2. Electrospinning

Electrospinning is a common technique used to produce micro- and nano-fibrous structures by means of an electrohydrodynamic process. In this process, the uniaxial stretching or elongation of a viscoelastic jet is formed from a polymer solution under the application of a sufficiently high voltage, ensuring the rapid solvent loss and the formation of solid fibers. A basic setup for electrospinning consists of a high voltage power supply, a metallic needle spinneret and a grounded conductive collector electrode, as shown in Figure 2.2a.

The polymer solution is placed in a syringe, which is connected to the needle spinneret and pushed by a system able to provide a stable and suitable feed rate. During the electrospinning process, the high voltage source induces an electric field between the positively charged metallic needle and the grounded collector. Under the effect of the

electric field, the charged polymer solution forms a pendant droplet which deforms in a conical projection at the edge of the needle, called Taylor's cone (Figure 2.2b).

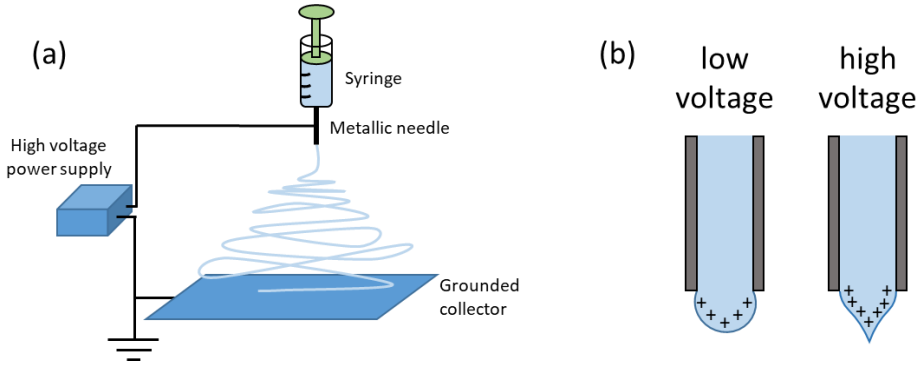

Figure 2.2. (a) Schematic diagram of a conventional electrospinning setup and (b) illustration of the formation of the Taylor's cone.

The formation of the Taylor's cone is induced by the electrostatic repulsion among the surface charges of the same sign. The electric stresses concentrated on the tip of the Taylor's cone leads to the ejection of the fluid jet. The jet initially extends in a stable straight line and then, it enters an unstable bending stage, with vigorous whipping motions for the bending instabilities. When the jet travels towards the grounded collector, the polymer solution is simultaneously subjected to the rapid solvent evaporation, emphasized by the high surface area of the narrow fluid jet, causing the decrease of the jet diameter[98]. Therefore, the jet begins to thin and solidify in fibers before they randomly arrange on the collector forming an interconnected porous structure with a wide pore size distribution. Controlling the instabilities that affect the establishment of the fluid jet ensures the successful fibers formation, preventing the jet break up which causes the transition from the electrospinning to the electrospray process. In the electrospray process, the jet breaks into droplets resulting in the formation of polymer beads instead of continuous fibers. Nevertheless, the easy operation of the electrospinning process, numerous parameters have to be considered in order to prepare electrospun fibers with desired morphology and dimension. These parameters are divided in three broad categories, consisting in the properties of the polymer solution, the processing parameters and the environmental conditions.

The solution properties include volatility, dielectric constant, conductivity and surface tension. The concentration of the polymer solution is also an important factor for the successful fibers formation. In fact, low polymer concentration induces the electrospray process instead of the electrospinning, while higher concentrations of polymer leads to the formation of beads or helix-shaped micro-ribbons on the continuous fibers [99,100].The volatility of the solvent is important to guarantee the formation of a continuous fluid jet, in which, the solvent evaporation rate would allow the solidification of the fibers on the grounded collector. In addition, the combination of a highly volatile solvent with a high boiling point solvent is an effective approach to prepare porous micro- or nano-fibers, in which the pore formation arises from the induced phase separation caused by the rapid solvent evaporation[101,102]. The modification of the surface tension by using additives or solvent mixtures can assist in the formation of smooth fibers. The addition of salts, for example, can also increase the conductivity of the polymer solution, enabling the jet formation[103]. Furthermore, the enhancement of the intermolecular interaction thanks to the increase of the polymer concentration can prevent the break of the jet. Higher viscosity of the polymer solution as a consequence of high polymer concentration, leads to the increase of the fibers diameter[103,104].

The processing parameters are associated to the experimental setup. It is possible to vary the applied voltage, the feed rate of the polymer solution and the distance between the needle spinneret and the grounded collector. In the Taylor's cone, the Coulombic repulsive force will stretch the viscoelastic polymer solution and, if the applied voltage is excessively high, the jet may accelerate faster, forming a smaller and less stable cone. The formation of the fluid jet is also hindered if the feed rate is not enough to maintain a continuous supply of the polymer solution. The control of both the feed rate and the voltage is therefore important to ensure the jet formation. The distance between the needle and the collector affects the flight time of the fluid jet and the strength of the electric field. The distance should be adequate to guarantee the evaporation of the solvent before the fibers are collected, in order to avoid the merging of the fibers or the formation of physical junctions[105].

The environmental conditions, such as the humidity and temperature, can strongly affect the morphology of the electrospun fibers. Inappropriate humidity and temperature during electrospinning may cause phase separation phenomena during the solvent evaporation phase. The fluid jet consists of polymer rich and polymer lean phases which solidify differently. The concentrated phase solidifies shortly forming the polymeric matrix, while the drying of the lean phase results in the porous structure[101,106]. An increase of the relative humidity during the electrospinning process shows also effects on the orientation of the fibers during the deposition on the grounded collector[106].

Electrospinning process is a promising technique to prepare porous materials characterized by a high surface area. The control of the several factors ensures the formation of electrospun fibers with desired features depending on the type of application. In fact, electrospun-based materials have been widely applied in many application, such as medical[102,107], industrial[108] and electronics[109,110] applications. The incorporation of active components in the fibrous matrices opens up the route for the development of functional porous nanocomposites of high surface area.

2.3. Incorporation of active nanomaterials

The use of free NPs in industrial applications has several drawbacks, such as, the necessity of time-consuming procedures to separate and recover the powder, which often causes its partial loss[111], and the potential human health and environmental risk caused by their exposure[112,113]. These aspects can be overcome by the immobilization of the nanomaterials on suitable solid supports[111,114,115]. With this aim, polymeric supports have been recently introduced because of their low-weight, flexibility and their easy conversion in different morphologies, making them an interesting choice[76–81].

The choice of the polymeric support is also an important aspect, because the polymeric matrix defines the final physio-chemical characteristics of the composites; for example, the polymer support can act as a filter or can promote the adsorption of

particular compounds thanks to the presence of specific functional groups[116,117]. Furthermore, an ideal polymeric support should have large surface area, advantageous adhesion with the nanomaterial and good chemical and mechanical stability[111].

The incorporation of NPs in a polymeric matrix is the most critical parameter to control in order to have homogeneous dispersion and therefore to ensure their functionality in the composite[118,119]. The agglomeration of NPs in the solid polymeric matrix reduces their interfacial surface area causing a decrease of the NPs activity. Furthermore, the incorporation of NPs inside the polymeric matrix affects the mechanical, rheological, optical and thermal properties of the polymer in the composite[120]. In fact, the presence of NPs clusters leads to the formation of defects in the nanocomposite, resulting in a worsening of its mechanical properties. For the preparation of organic-inorganic nanocomposites, different approaches have been investigated, involving the synthesis of the NPs directly within the porous matrix (*in-situ* synthetic strategy) [121–123] and the incorporation of pre-formed NPs (*ex-situ* synthetic strategy). The latter can be obtained through different deposition techniques (*e.g.* layer by layer[124], physical vapor[111] and chemical vapor deposition[125,126]) or through the formation of NP-polymer blends[123,127].

2.3.1. Ex-situ synthetic strategy

The incorporation of preformed active NPs in polymer matrices allows to have a better control of the size, shape and composition of the particles. Thanks to the development in the synthesis of colloidal nanocrystals (NCs), high quality nanomaterials can be achieved on large scales with good reproducibility. The possibility to synthetize different functional inorganic nanomaterials, such as quantum dots, plasmonic or metal oxide NPs, results in the preparation of composites with desired functions for practical use.

In order to prevent undesirable NPs agglomeration, the surface of the NPs is generally treated by physical or chemical methods to improve the compatibility between NPs and polymer and to reduce the interactions among the NPs. The physical treatment

involves the use of low molecular weight surfactants or high molecular weight polymers to cover the NPs surface through the instauration of hydrogen bonding, van der Waals or electrostatic forces[128]. The physical treatment with high molecular weight polymers instead of surfactants is more effective due to their stronger adsorption on the NPs surface and the higher control over the inter-particle interactions. On the other hand, the lower diffusion of these polymers among the clusters of NPs due to the higher molecular weight than that of the surfactants may reduce the effectiveness of their physical stabilization[129]. In the chemical treatment, the NPs surface is usually modified by a grafting with ligands that are miscible with the polymeric solution. In this way, the NPs are stabilized during the formation of the blend with the polymer, resulting in a stable dispersion. Typically, the grafted compounds are polymer chains, which act as molecular spacers to control the particle separation distances, hence the particle dispersion[130]. When the molecules are grafted as in the chemical treatment, their desorption from the surface of the NPs is remarkably lower than that of the physical treatment.

2.3.1.1. Colloidal synthesis of NCs

Colloidal synthesis is a surfactant-assisted fabrication approach of nanocrystalline materials that ensures a high control of their morphology, size distribution and chemical composition. In a typical colloidal synthesis, a metal salt precursor is added to a mixture of a surfactant and a high boiling point organic solvent in a three neck round bottom flask and the overall process occurs under an inert atmosphere (Figure 2.3a). This method is defined as bottom-up approach, in which the monomers (atomic, ionic or molecular units) are assembled through various reactions to form nanostructures, differently from the top-down approach, in which nanomaterials are synthetized by breaking down bulk solids by means of physical and lithographic methods[131]. The surfactants usually employed are alkylthiols, amines, carboxylic acid etc[132]. Among the surfactants, oleylamine (Oam) is a versatile reagent commonly used in the synthesis of various NPs. It is a long-chain primary alkylamine that can act as a surfactant, solvent and reducing agent at elevated

temperatures. Its wide use can be justified by the several economical and practical advantages. In fact, Oam is in liquid state at room temperature, making it easy to be removed via centrifugation from the reaction mixture after the ending of the reaction[133].

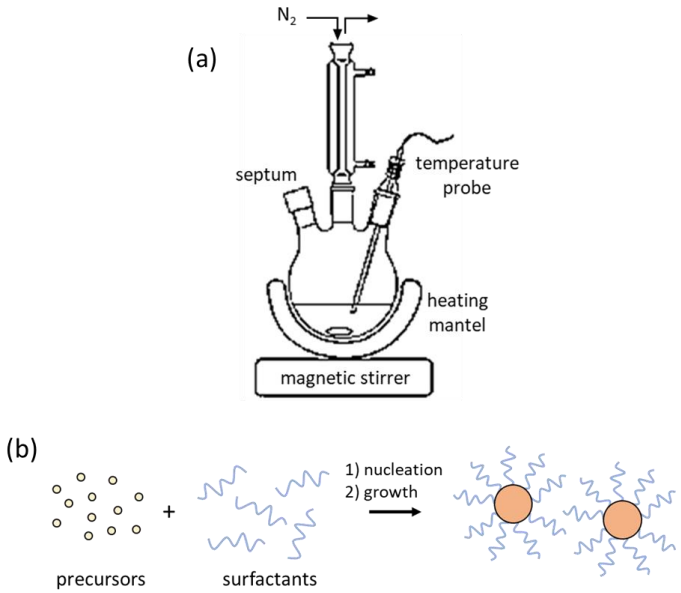

Figure 2.3. (a) Schematic setup used for a colloidal synthesis and (b) synthesis of NPs.

The three components (metal salt precursor, surfactant, and the high-boiling-point organic solvent) are heated up to induce the thermal decomposition of the metal precursor, forming highly reactive species called monomers that lead to the nucleation and support the growth of the NPs (Figure 2.3b). In the heat-up colloidal synthesis, the precursor begins to react with the surfactants as the temperature increases. Conversely, in the hot-injection synthetic approach, the reactive precursor is injected into the reaction mixture when the latter is at high temperature, and therefore the concentration of monomers necessary for the reaction to occur is reached almost immediately. This results in a homogeneous nucleation event, in contrary to the heat-up synthesis, where the formation of the monomers is thermodynamically driven, and a fine control of the heating rate and, therefore, of the precursor reactivity is required[134].

In general, the colloidal synthesis can be described as the sequence of three stages, as shown in Figure 2.4. In the first stage, the metal salt precursors gradually decompose to initiate the buildup of the reactive monomers. When the concentration of the free

monomers reaches a critical concentration (critical supersaturation), the nucleation stage starts, in which the monomers are rapidly consumed to form the NC seeds or nuclei. After the concentration of the monomers drops below the critical supersaturation, the reaction enters the growth stage. During this stage, the growth of NCs in influenced by the diffusion of the monomers to the surface of the particles and by their incorporation in the crystal bulk[135]. The adsorption/desorption dynamics of the surfactants on the surface of the formed clusters prevent their aggregation during the growth step, assisting the growth process. Moreover, the surfactants can be adsorbed onto some specific facets of the growing clusters, reducing their surface energy which results in the control of their growth rate for the tuning of the final shape of the NPs[131]. The precise control over the physical and chemical properties of the nano-sized objects that can be achieved by colloidal synthesis is promising for the development of homogeneous components in functional composites, with well-known photocatalytic behavior.

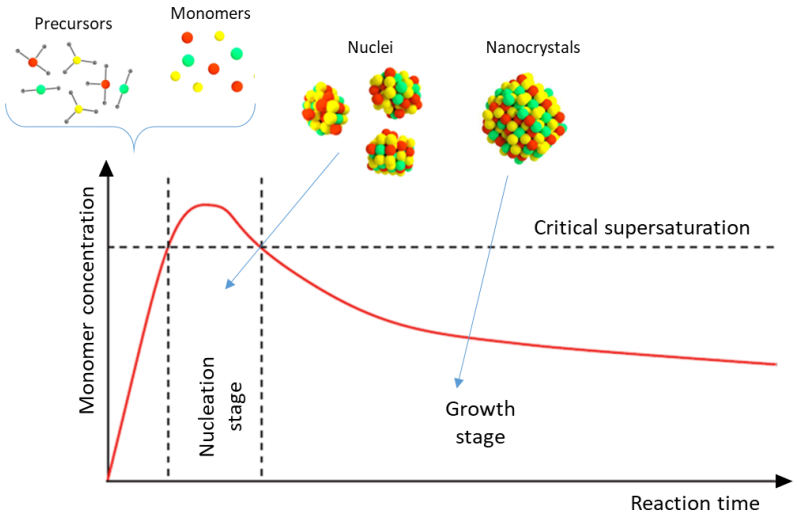

Figure 2.4. La Mer diagram describing the three stages involved in a colloidal synthesis.

2.3.2. In-situ synthetic strategy

Recently, the preparation of nanocomposites by a direct in-situ synthesis of active nanostructures inside a polymeric matrix has attracted great interest in the development of functional materials. Thanks to this relatively simple approach, the agglomeration of the active inorganic NPs inside the nanocomposite can be avoided, ensuring the good

performance of the final material. In this approach, the NPs synthesis can occur before the formation of the solid polymeric matrix. In this case, the precursors are mixed with the monomers and the synthesis can be induced during the polymerization by means of different methods (e.g. sol-gel chemistry[136], hydrothermal synthesis[137], photo-reduction[138]). Furthermore, the simultaneous preparation of the NPs with the polymeric matrix can reduce synthesis time and costs, avoiding to resort to priming synthetic steps.

Another approach is the in-situ NPs synthesis directly in the solid polymeric matrix[121]. The precursor of the active nanomaterial is previously loaded in the polymeric matrix and the NPs synthesis can be carried out by a solid-state reaction which can be chemically[139–141], thermally[122,142,143] or photo-induced[121,144], causing the nucleation and the growth of NPs with a good spatial distribution in the polymeric matrix. Thermally-induced solid-state reactions in a polymeric matrix usually involve temperatures where the polymer is thermodynamically stable and long reaction time due to their special reaction mechanism[122,143]. The synthesis is then quenched exposing the composite to ambient conditions. The important aspects that have to be considered for the selection of the right precursor-polymeric system include a good solubility of the metal salt in the polymeric solution, a working temperature range for the salt decomposition which does not affect the polymeric matrix and the chemical compatibility between the metal salt and the polymer, avoiding thus secondary unwanted reactions. Most of the solid-state reactions of inorganic compounds involve the formation and release of gaseous by-products upon the decomposition of the metal precursor. The generally accepted theory of solid-state reaction describes the precursor decomposition as the sequence of two steps. The first step involves the formation of the nuclei and the second step is their growth[145]. The decomposition of the metal salt can be studied in order to define information about the activation energy, the kinetics and the types of the structural transformation in the solid matrix[146]. The understanding of these aspects is useful to define the optimal conditions under which the solid-state reaction occurs minimizing the influence of the mass-transfer in the overall synthesis. The slow diffusion of the reactants

is usually the main limiting step in the reaction rate[146]. Moreover, the growth of the nuclei in the polymeric matrix is affected by the polymeric matrix, which causes a physical constraint[122,143]. After the NPs formation by in-situ synthesis, the presence of unreacted precursors may affect the properties of the final nanocomposite. Nevertheless, this is a minor disadvantage if considering the good solubility in water of most of the NPs precursors, which are generally metal salts, allowing their easy removal by washing in water.

2.4. Challenges for the incorporation of active nanomaterials in composites for water treatments

The choice of the incorporation strategy has to be carefully considered when preparing the nanocomposite for non-conventional wastewater treatments. Water treatments, like adsorption and heterogeneous photocatalysis, are affected by the mass transfer phenomena, therefore they require maximized surface area of both the polymeric support and the active nanomaterials. Thanks to the fabrication methods proposed in the previous section, it is possible to prepare polymeric matrices, such as highly porous foams and polymeric fibrous mats, characterized by a high specific surface area. Although the surface area of the porous nanocomposites is lower compared to that of the suspended powders, resulting thus in a slight reduction in performance, the significant advantages concerning the usability in practical applications make the porous solid materials much more prominent for realistic water remediation applications. For optimal performance, the active nanomaterials should be homogeneously distributed on the porous polymeric matrix, mostly exposed on the polymer surface. This is an important aspect to ensure a high density of active sites easily accessible to the surface processes involved in the removal of the aqueous pollutants. Although the ex-situ synthetic strategy, in which the active nanomaterials are previously formed and then incorporated in a polymeric matrix, guarantee the great control over the morphology, size, chemical composition and,

therefore, over the physical properties of the NPs, their immobilization on a solid matrix surface may be difficult. Physical treatments, by means of the addition of surfactants or higher molecular weight compounds to stabilize the NPs dispersion in the polymeric solution, shows weak adsorption of the compounds on the NPs surface. The lower concentration of the compounds on the surface of the NPs may result in the possible formation of NP clusters or in an ineffective NPs incorporation in the polymeric matrix.

A higher immobilization efficiency of pre-formed NPs in the polymeric matrix can be achieved by a chemical treatment, in which the NPs are covalently bonded to the polymer. However, the covalent bonding between the NP surface and the ligand can directly influence the optical, electrical, magnetic and catalytic properties of the NPs, showing an evident impact on its performance in the water treatment process. For example, the introduction of mid-gap electronic states due to the ligand binding increases the rate of non-radiative relaxations, reducing the photocatalytic performance[147].

The in-situ synthetic strategy allows the direct embedding of the NPs inside the polymeric matrix, due to the decomposition of the metallic precursors which are previously loaded in the solid matrix. The main disadvantage of this approach is the lower control of the size distribution, and shape of the formed NPs compared to the colloidal ones. Nevertheless, the possibility to avoid a multi-step procedure, such as the complicated chemical synthesis in terms of time, chemicals and energy consumption, makes the in-situ NPs synthesis a promising approach for the formation of cost-effective functional nanocomposites. Furthermore, the NPs formed by the in-situ synthesis usually appear well distributed in the polymeric matrix, without the formation of agglomerates. Thanks to this synthetic strategy, the NPs are formed both in the bulk and on the surface of the composite, on which the NPs are not covered by any polymeric layer as in the case of direct mixing. The direct contact between the active sites on the surface of the nanomaterials and the aqueous compounds leads to effective water treatment.

Chapter 3

Porous bio-composite for the removal of organic pollutants by adsorption process

3.1. Introduction

Most of the commercial materials utilized so far for adsorption processes in water treatment present several limitations such as low sorption capacity, high-cost and high level of required maintenance to regenerate the sorbent[53]. For this reason, the research activities are now focused on the development of cost-effective smart materials characterized by high performance, in terms of high affinity, selectivity, and adsorption capacity for specific aqueous pollutants.

As anticipated in Chapter 1.3.2, the utilization of agricultural waste as low-cost adsorbents has recently aroused great interest for water remediation applications. One of the most abundant agro-waste in the food industry is the orange peel (OP), which represents almost a quarter of the whole fruit mass after the juice extraction processing[148,149]. The hydroxyl and carboxylic groups of main components of OP (*e.g.* cellulose, pectin, hemi-cellulose, lignin, chlorophyll pigments and other low molecular weight hydrocarbons[150]) can bond the water contaminants, specifically the heavy metal ions (*e.g.*, Pb^{2+}, Ni^{2+}, Cu^{2+}), dyes (*e.g.*, reactive blue 19, methylene blue, direct red 79), pesticides *etc*.[52,53], through different binding mechanisms, such as ions exchange, complexation and electrostatic interactions. For this reason, OP powder is a promising low-cost adsorbent for water remediation applications. To further enhance the OP adsorption efficiency specific treatments have been proposed, such as carbonization, alkali saponification and acid oxidation[52]. Nevertheless, wide use of OP powder in

large-scale water treatment could be considerably difficult, due to the time-consuming and complicated processes required for the recovery of the powder after the remediation process. Therefore, a strategy to improve the handling of OP in large-scale water treatment is ensured by fixing the powder in a solid porous system[151], in which the aqueous pollutants of the permeated water can selectively interact and be concentrated on the exposed OP active components. After the remediation process, the solid composite can be easily removed from the water, simplifying thus the post treatment for the collection of dispersed powders.

Several agricultural waste materials are already used as low-cost fillers in different polymers to prepare functional composites[152–156], although their incorporation in porous composites for wastewater treatment is still in the first steps of development. In a recent work, a food/agro-waste powder has been combined with a synthetic polymer forming a macroscopic porous composite for the removal of heavy metal ions from water. However, the polymer was here used to confer solely structural integrity to the porous structure, without showing a significant effect in the adsorption process[151]. To further improve the performance of the solid porous material to adsorb water pollutants, OP particles are incorporated in an active polymeric matrix, forming a solid material. In particular, the proposed polymer can specifically interact with the water contaminants, resulting in solid OP based bio-composites with significantly high adsorption performance.

The active polymeric matrix is the protein extracted from *Bombyx mori* silk cocoons, silk fibroin (SF), which is receiving great attention in the water remediation field due to its active components able to interact with various water pollutants, together with its remarkable mechanical properties, environmental stability and easy processability in various material structures[84,157]. SF has been proved to efficiently interact with various dyes (such as direct orange, disperse blue and methylene blue)[158] or heavy metal ion (such as Cu^{2+})[159]. Its performance can be further enhanced by forming ultrathin filtration membranes[160] or by its combination with various polymers[161][162] and organic or inorganic fillers[163][84]. In fact, SF can be processed in various structural

arrangements characterized by high surface area, such as fibers[163] and foams[164], making it an interesting choice for the preparation of porous bio-composite adsorbents. The solubility in water of SF-based materials is controlled by means of different physiochemical treatments depending on the variation of pH, temperature, organic solvent, *etc.*[165], which act on the crystalline content forming thermodynamically stable β-sheet regions that serve as physical cross-links in the material structure. Furthermore, SF biopolymer could potentially be extracted by the leftover of the silk fiber manufacturing processes[158], representing an example of a circular economy if combined with OP agro waste. In this case, the agricultural waste is efficiently valorized developing an advanced system for the treatment of contaminated water, specifically for the removal of methylene blue (MB), a cationic thiazine dye.

The presented silk fibroin-orange peel powder (SFOP) composite foams can be considered an efficient alternative to the powder-like and synthetic solid sorbents due to its manageability, good removal capacity, cost effectiveness and its reduced environmental impact. Thanks to the immense variety of agro-waste powders available, with the present approach, various possibilities are opened up for the development of a great number of porous biocomposite foams with advanced properties.

3.2. Experimental methods

3.2.1. Materials

Bombyx mori silk cocoons were supplied by Cantiere della Provvidenza SPA Scs Onlus Italy. Sodium carbonate (Na_2CO_3), lithium bromide (LiBr), methanol, ethanol and methylene blue (MB) were purchased from Sigma-Aldrich. All chemicals were used without any further purification. Orange peel waste was collected from the canteen of the research institute.

3.2.2. Bio-sorbent preparation

Orange waste peels were washed twice with deionized water and then with Milli-Q® water in order to remove contaminants from the surface. Subsequently, the washed peels were dried in a convection oven for 24 h at 60 °C. The dried orange peels were then grounded with a domestic mixing grinder and sieved to particle size less than 50 μm. The final average particles size of the OP particles was 16.4 ± 9.5 μm, evaluated through SEM image analysis by using ImageJ software to measure the diameters of more than 300 particles.

3.2.3. Silk fibroin extraction protocol

Firstly, the protein was extracted from silk cocoons by using a conventional method [166]. Briefly, silk cocoons were boiled in a 0.02 M solution of Na_2CO_3 to remove the sericin from the silk and then rinsed with distilled water to remove the salt residue. The dried SF was dissolved in 9.3 M solution of LiBr at 60 °C for 4 h and the obtained protein solution was dialyzed against Milli-Q® water using a dialysis membrane (Spectra/Por 1, Standard RC Tubing, Maximum Weight Cut-Off 6-8 kD) changing six times the water within 48 h. The solution was then centrifuged twice at 9000 rpm at 4 °C for 20 min to remove impurities and then it was stored at 4 °C to slow down the fibroin gelation process. The SF aqueous solution with 6 %$_{w/v}$ of protein was employed to prepare SF foams and SFOP composite foams.

3.2.4. Foams preparation

The SF and the silk fibroin-orange peel powder (SFOP) alcogels were prepared by adding 200 μL of methanol to 1 mL of 6 %$_{w/v}$ SF aqueous solution or to 1 mL of the OP-SF aqueous suspension, in which was added around 50%$_{w/w}$ of OP powder with respect to the SF content, respectively. The addition of the organic solvent induced the fibroin gelation and the mixtures was placed in an ultrasonic bath for 3 h to favor a homogeneous dispersion of the OP particles in the SF matrix. Then, the prepared alcogels were immersed in ethanol for two days in order to exchange the methanol. The alcogels were subsequently cut in five samples with similar dimensions (about 10 mg each) and kept in

EtOH until drying. The foaming process was performed by the $scCO_2$ drying with a K850WM large chamber supercritical point dryer (Quorum Technologies).

Specifically, the chamber temperature was first lowered to 10 °C, then the alcogels were loaded and flushed three times with liquid CO_2 at 50 bar, which was maintained in the chamber for 15 minutes for each cycle to completely substitute the ethanol inside the porous samples. After that, the chamber was filled with liquid CO_2, making sure that the samples were completely covered, and the temperature was increased to 35 °C to allow the increase of the pressure until 80 bar, over the critical point, inducing the transition of CO_2 from liquid to supercritical gas. The samples were maintained in the chamber for 15 minutes once the critical point was reached before the isothermal depressurization of the surpercritical fluid with a decompression of 3 $bar \cdot min^{-1}$.

3.2.5. Characterization

The morphological characterization of the foams was performed with a JEOL JSM-7500F high-resolution scanning electron microscope (HR-SEM) equipped with a cold field emission gun, applying an accelerating voltage of 5 kV. The samples were coated with a thin layer (2-4 nm) of gold/palladium by a sputter coater (Cressington 208HR), in order to avoid the occlusion of the porous structure and to confer electrical conductivity. Both surface and cross section images were acquired to evaluate the possible morphological differences of the porous structure across the foam. Energy-dispersive X-ray spectroscopy (EDS) was carried through a JEOL JSM-7500F HR-SEM to evaluate the OP dispersion in the SFOP foam.

The specific surface area and the pore size distribution of the mesopores and macropores of the foams were characterized using the nitrogen physisorption technique and mercury intrusion porosimetry. Nitrogen physisorption measurements were carried out at 77 K using a gas sorption analyzer, model Autosorb-iQ (Quantachrome Instruments). The samples were initially degassed for 3 h at 60 °C under vacuum conditions to remove weakly adsorbed species. The specific surface areas were calculated by using the multipoint Brunauer-Emmett-Teller (BET) model, considering 11 equally spaced points in the p/p_0 range from 0.05 to 0.3. The pore size distribution was determined from the

desorption isotherms (range $0.35 < p/p_0 < 1$) by means the Barrett-Joyner-Halenda (BJH) method, taking into account 32 points.

Mercury intrusion porosimetry (MIP) was performed by using Pascal 140 Evo and Pascal 240 Evo mercury porosimeters (Thermo Fisher Scientific). The pressure of mercury intrusion was set at 0.0136 MPa and was continuously increasing up to 200 MPa, under a rate of 6 - 14 $MPa \cdot min^{-1}$. The contact angle of mercury with the samples and the surface tension of pure mercury were assumed to be 140° and 0.48 $N \cdot m^{-1}$ respectively, while the Washburn equation is used to calculate the pore size from the applied pressure, assuming that the pores are of cylindrical shape. The measurements of the real density of the foams were performed by Pycnomatic ATC (Thermo Fisher Scientific). This measure is based on the helium displacement; in fact, due to its small radius, helium is able to permeate also in the narrow pores of the sample ensuring the determination of the real volume occupied by the solid. The real density was then calculated by the ratio of the dried sample mass and its volume.

Fourier transform infrared attenuated total reflectance (FTIR-ATR) measurements were performed in order to investigate the possible chemical interactions and the effect of the presence of OP on the SF crystallinity. FTIR-ATR spectra were recorded using Vertex 80 Bruker Fourier transform infrared spectrometer coupled with a diamond/ZnSe crystal, in the range from 4000 to 600 cm^{-1} with a resolution of 4 cm^{-1} and collecting 64 scans for each spectrum. For the investigation of the crystallinity of the SF polymer matrix, the deconvolution of the FTIR spectra in the amide I region (1700 – 1600 cm^{-1}) were achieved by using PeakFit 4.11 software. The OP spectral contribution was subtracted from the FTIR spectrum of the SFOP foam after the previous normalization with respect to the stretching of the C-O-C bond of the polysaccharides (1100 cm^{-1}) of the baseline corrected spectra. The deconvolution process was carried out considering 11 fixed fitting peaks, which were held constant for each sample. The wavenumber peak positions were selected according to previous studies[165,167].The Gaussian shape analysis was set up with an amplitude threshold of 3%. The deconvolution analysis of the FTIR data was performed in three different samples in order to determine the average secondary structure content.

The FTIR-ATR spectra of the OP filler were also acquired before and after the MB adsorption experiments to evaluate the effect of the dye adsorption on the OP powder.
The X-ray diffraction (XRD) was performed by a PANalytical Empyrean X-ray diffractometer with Cu K_α radiation operating at 45 kV and 40 mA to evaluate the crystallinity of the protein in the prepared foam. The diffractograms were recorded in reflection mode, with a step time of 500 s and step size 0.1°, for 2θ range from 10° to 35°.
In order to further understand the interaction between the dye and the adsorbent material, UV-vis spectra of the samples were acquired after the adsorption experiments, measuring the optical density by using a Varian Cary 6000i UV-Vis-NIR spectrophotometer. The foams, OP and solid MB were grounded and blended with NaCl to obtain discs (11 mm diameter and 0.5 mm thickness) by pressing (CrushIR, PIKE Technologies) with a load of 8 tons, while pure NaCl discs were used for the background correction.

3.2.6. Water uptake experiments

The maximum water uptake capacity and the weight loss of the SF and the SFOP foams were evaluated by performing water dipping experiments. The foams were weighed and placed in a glass vial with 10 mL of Milli-Q® water and kept under constant slow stirring for 24 hours at room temperature in order to reach the swelling equilibrium. The swollen samples were then drained on filter paper to remove the water excess and weighed; the water uptake capacity values ($\Delta m_s\%$) were calculated by Equation 3.1,

$$\Delta m_s\% = \frac{(m_s - m_i)}{m_i} \cdot 100 \qquad \text{(Equation 3.1)}$$

where m_s is the mass of the swollen foam and m_i is the initial mass. The swollen samples were then dried, and their weights were used to calculate the weight loss ($\Delta m\%$) by Equation 3.2, in which m_i is the initial mass and m_d is the mass of the dried sample.

$$\Delta m\% = \frac{(m_i - m_d)}{m_i} \cdot 100 \qquad \text{(Equation 3.2)}$$

The $\Delta m_s\%$ and $\Delta m\%$ were calculated as average of the values obtained by repeating the water dipping-drying experiments on the same samples for three cycles.

3.2.7. Adsorption experiments

The capacity of the foams to remove pollutants was evaluated through adsorption experiments of MB, as model molecule. The adsorption experiments were performed by dipping around 10 mg of adsorbent material in 10 mL of MB aqueous solutions with a known concentration. The MB solutions were kept under continuous stirring at room temperature and aliquots were collected at specific time intervals, ranging from few minutes to 24 hours. The dye percentage removal was monitored through UV-Vis spectroscopy, measuring the absorbance value at the MB maximum absorption wavelength (664 nm). To avoid the absorbance saturation for the experiments with high dye concentration, the collected aliquots were further diluted with a known amount of water before the analysis. The absorbance values were correlated to the dye concentration by means of a linear regression equation ($R^2 > 0.9983$) of the MB calibration curve. In particular, the calibration curve was obtained by plotting the absorbance value at 664 nm of different aqueous solutions containing MB of known concentrations (ranging from 0.2 to 4 $mg \cdot L^{-1}$). The adsorption capacity (Q_t) of the adsorbent material was calculated by Equation 3.3

$$Q_t = \frac{(C_i - C_t)}{m} \cdot V \qquad \text{(Equation 3.3)}$$

where C_i and C_t are the initial concentration and the concentration at the time t of the MB aqueous solution ($mg \cdot L^{-1}$), V is the volume (L) of the MB solution and m is the mass (g) of the adsorbent material. The adsorption capacity at the equilibrium (Q_e) was calculated by Equation 3.3, substituting the C_t with the concentration of the MB aqueous solution ($mg \cdot L^{-1}$) after 24 h of interaction with the adsorbent (C_e). The experimental data were analyzed to define the kinetics of MB adsorption, by applying the pseudo-first order (Equation 3.4) and the pseudo-second order (Equation 3.5) kinetic models.

$$Q_t = Q_e(1 - e^{-k_1 t}) \qquad \text{(Equation 3.4)}$$

$$Q_t = \frac{k_2 Q_e^2 t}{1 + k_2 Q_e^2 t} \qquad \text{(Equation 3.5)}$$

In these models, Q_t ($mg \cdot g^{-1}$) is the adsorption capacity in time (t), Q_e ($mg \cdot g^{-1}$) is the adsorption capacity at the equilibrium and k_1 (min^{-1}) and k_2 ($g \cdot mg^{-1} min^{-1}$) are the first-order and the second-order reaction rate equilibrium constants respectively.

In order to explore possible interaction mechanisms between the dye and the adsorbents, the adsorption data were fitted with the Langmuir and the Freundlich isotherm models, in their non-linear forms, as reported in the Equation 3.6 and 3.7.

$$Q_e = \frac{Q_{max} K_L C_e}{1 + K_L C_e} \qquad \text{(Equation 3.6)}$$

$$Q_e = K_F C_e^{1/n} \qquad \text{(Equation 3.7)}$$

$$R_L = \frac{1}{1 + K_L C_0} \qquad \text{(Equation 3.8)}$$

C_e ($mg \cdot L^{-1}$) is the equilibrium concentration of MB in solution, while and Q_e ($mg \cdot g^{-1}$) and Q_{max} ($mg \cdot g^{-1}$) are the adsorption capacity (equilibrium amount of MB adsorbed per gram of adsorbent) and the maximum adsorption capacity. K_L and K_F are the constants of the Langmuir and the Freundlich models, respectively. The parameters obtained from the Langmuir model were used to calculate the equilibrium parameter (R_L) by using the Equation 3.8.

3.3. Results and discussion

3.3.1. Gelation process

The biopolymer SF is first extracted from the *Bombyx mori* silkworm cocoons, in which represents around 70-85% of the initial cocoon weight[166]. The structure of the *B. mori* silk is schematized in Figure 3.1, in which the fibroin forms the core as two round or trilobal filaments, embedded in a sheath formed by sericin. The latter is the second prevailing protein in the silk, which forms a glue-like hydrophilic layer around SF contributing to the formation of the cocoons. It consists of a group of soluble globular proteins with molecular weights ranging from 10 to 310 kDa and it is characterized by

rubber-elastic properties. During the SF extraction, the sericin component is removed and the remaining solid SF is dissolved obtaining an aqueous solution of pure SF.

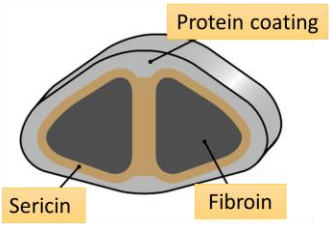

Figure 3.1. Raw silk fiber composition, with two fibroin filaments embedded in a sericin sheath and covered by a protein coating.

The particular composition of SF makes it susceptible to the action of external stimuli, resulting in the formation of different conformational structures. Specifically, SF consists of a heavy chain ($M_w \approx 390$ kDa) and a light chain ($M_w \approx 25$ kDa), linked together by disulfide bonds; and by another fraction ($M_w \approx 27$ kDa) which is associated to the previous ones by non-covalent bonds[168]. In fact, the composition of the dominant heavy chain shows alternating hydrophobic blocks and small hydrophilic segments, which confers to SF a natural block-polymer design. The protein can self-assemble from a less-ordered water soluble form (silk I), composed by random coils and intermediate structures such as β-turns or β-bends, into a ordered semi-crystalline structures (silk II), mainly formed by β-sheet dispersed into an amorphous matrix[164,168]. The silk II conformation is the water insoluble form of the protein, in which the β-sheet crystallites act as physical cross-linkers, conferring mechanical enhancement to the silk fibroin gels[164,169,170]. Apart from these two conformations, the native silk molecules can form another secondary conformation, called silk III, which is assembled with a helical structure at air-liquid interfaces[164].

As shown in Figure 3.2, after the SF extraction from the silk cocoons, the OP particles are mixed with the SF aqueous solution. The silk fibroin-orange peel powder (SFOP) alcogel is therefore prepared with the addition of methanol, which induces the sol-gel transition of the biopolymer. The organic solvent causes the desolvation of the SF molecules starting, thus, the non-solvent induced phase separation. The resulting protein gelation process arises from the instauration of inter- and intramolecular interactions

between the SF molecules, involving hydrophobic interactions and hydrogen bonds, which results in the formation of water-insoluble crystalline β-sheet structures[171]. The thermodynamic stability of the β-sheets makes the protein gelation an irreversible process[172]. The subsequent removal of the solvent from the SFOP alcogel by means of the $scCO_2$ drying allows a fast and effective solvent elimination, preserving the original gel nanostructure in the dried SFOP foam. The near zero surface tension effect caused by the supercritical CO_2 prevents, in fact, the collapsing of the structure during the drying process[173,174].

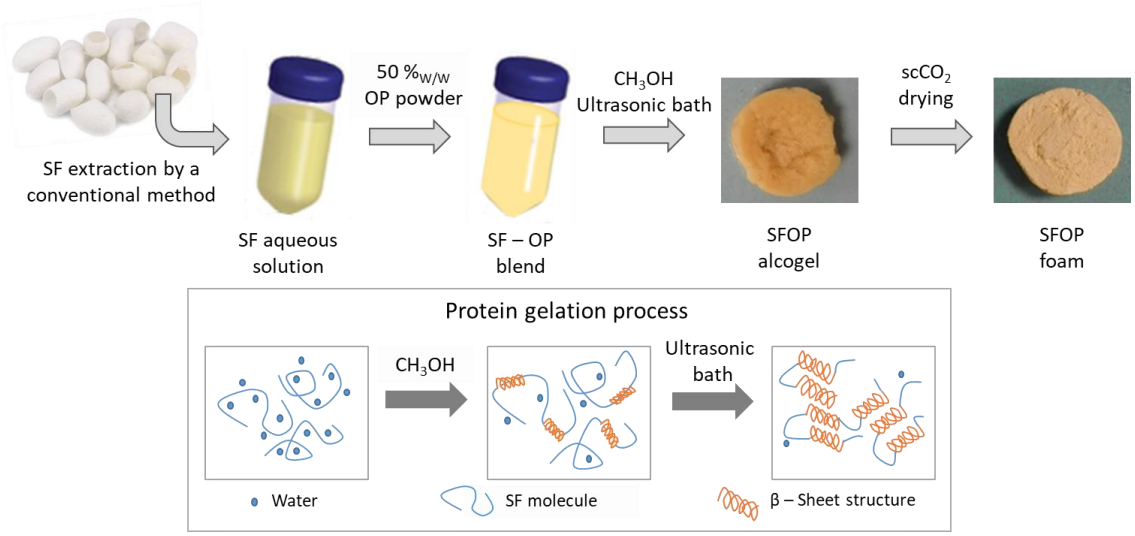

Figure 3.2. Process for the fabrication of the SFOP foam and detail of the protein gelation process.

3.3.2. Physiochemical properties of the foams

3.3.2.1. Morphology and structural characterization

The morphology and porous structure of the SF and SFOP foams are presented in Figure 3.3. The biopolymeric matrix forms a highly porous structure arranged in an interconnected network for both types of foams. In the case of the SFOP foam, the OP powder is homogeneously distributed in the SF matrix, as confirmed by the EDS mapping of calcium (Figure 3.4a), which is one of the chemical elements commonly present in this type of agricultural waste[148].

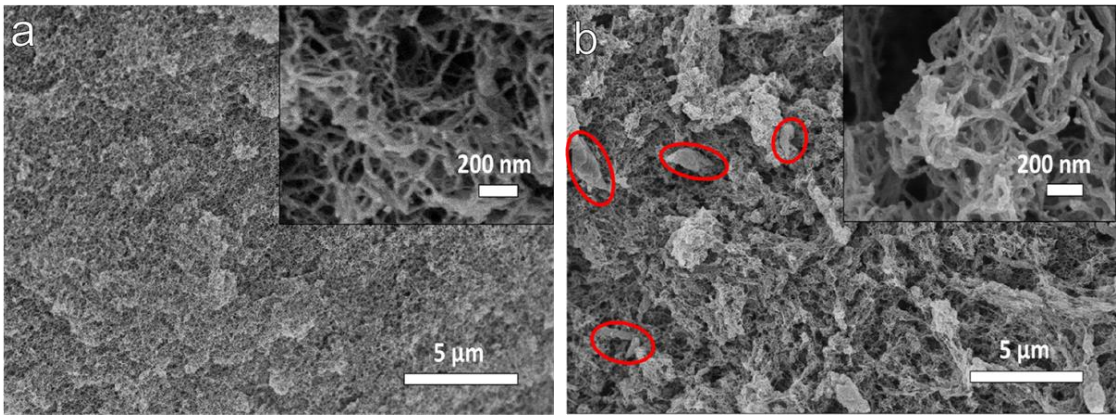

Figure 3.3. HR-SEM images of (a) SF and (b) SFOP foams after the scCO₂ drying. The OP particles are highlighted in the red ovals.

Furthermore, the observed morphology for both foams does not change from the surface to the bulk (Figure 3.4b,c), in which the bulk porous structure appears similar to that on the surface, proving the successful formation of uniform foams during the removal of the solvent by scCO2 drying technique. The bio-polymeric matrix is organized in a fibrillary network in both samples, showing a looser structure in the presence of OP powder.

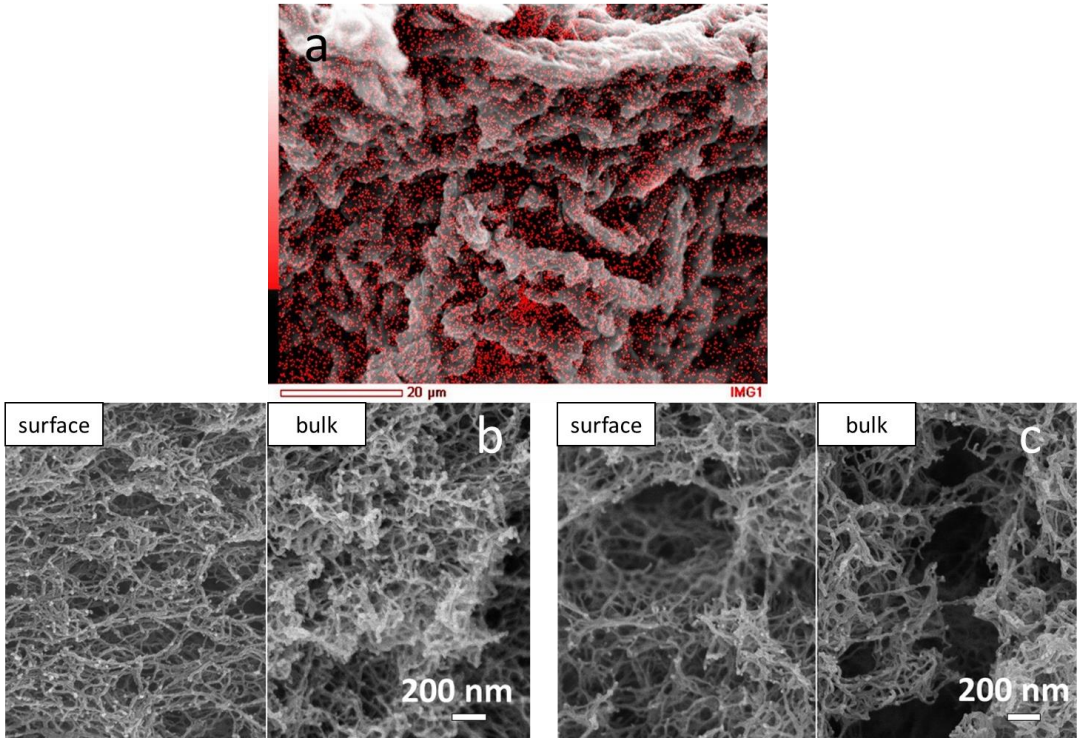

Figure 3.4. (a) EDS mapping of the calcium (red) from a HR-SEM image of SFOP foam and HR-SEM images of (b) SF foam and (c) SFOP foam.

The characterization of the porous structure of the dried samples is evaluated by combined nitrogen physisorption and mercury intrusion porosimetry measurements. The complementary information obtained by these two methods ensures a comprehensive description of the specific surface area and pore size distribution of the foams[175]. The nitrogen adsorption/desorption isotherms of the two foams (Figure 3.5a,b) can be classified, according to the classification from the international union of pure and applied chemistry (IUPAC), as Type IV isotherms, which are typical of materials characterized by meso- and macropores[175,176]. In particular, the manifestation of narrow H3 hysteresis loops (as identified by IUPAC) is characteristic of nitrogen condensation within the mesopore structures associated with restricted slit-shaped pores. The presence of pores in the macropore range is instead confirmed by the absence of the plateau in the nitrogen isotherms at higher relative pressure[175]. The incorporation of OP particles in the SF matrix leads to an increase of the BET specific surface area (S_{BET}) from 13.22 to 174.45 $m^2 \cdot g^{-1}$ and of the total pore volume (V_P), which rises from 0.128 to 1.813 $cm^3 \cdot g^{-1}$. As estimated from the adsorption branch of the isotherms by the application of the BJH model (Figure 3.5c,d) the mesopore size distribution appears broad for both foams, while the average pore diameter (D_P) is centered at around 42.12 and 44.65 nm for SF and SFOP foams respectively.

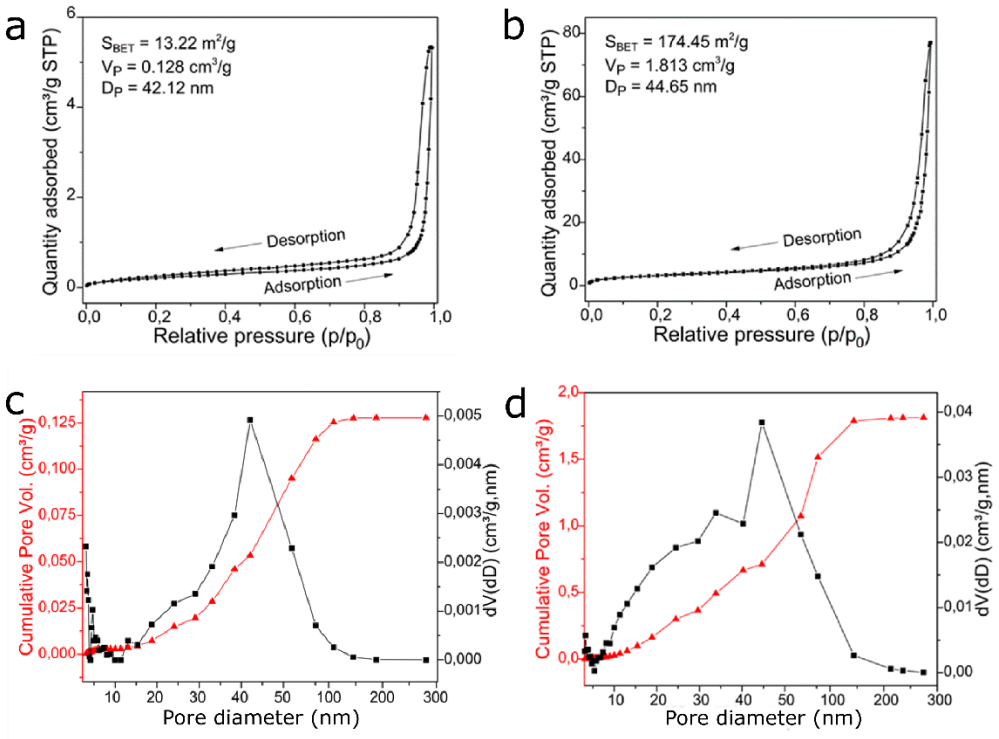

Figure 3.5. Nitrogen adsorption/desorption isotherms of (a) SF and (b) SFOP foams and BJH pore size distribution of (c) SF and (d) SFOP.

The pore size distribution of the macropores, which cannot be evaluated by the nitrogen physisorption analyses due to their size, has been defined by the MIP measurements. From the intrusion/extrusion curves (Figure 3.6a,b), it is possible to demonstrate the presence of an interconnected porous system due to a large amount of entrapped mercury in the foams after the measurements[177]. The pore size distribution of the SF and SFOP foams was calculated in a size range without effects of sample compression caused by the increase of pressure to force the mercury intrusion. In fact, the difference in the volume that is measured during the compression causes a misreading of the porosity, because the compressed pore volume is added to the total pore volume even without mercury intrusion in the sample. Besides this aspect, the applied pressure can also induce the collapsing of the porous structure during the analysis, and therefore also the closed pore volume will concur to the total porosity. To understand when the sample is subjected to the effect of compression, it is important to measure its real density. Thanks to this parameter, it is possible to calculate the real specific total pore volume (V_d), which

is shown in the mercury intrusion curves in Figure 3.6. The measured specific pore volume above this value is related to sample compression and therefore it can be excluded from the mathematical determination of the pore size. In this way, the pore structure analysis is based only on the open macropores, which are accessible to the polluted water during the adsorption experiments. In this range, the SF foam exhibits a dense porous structure, with pores showing a prevalent pore diameter less than 100 μm (Figure 3.6c). On the other hand, the SFOP exhibits a broader pore size distribution, with a pore diameter range from 300 nm to 100 μm, without an evident effect of pore structure collapse during the measurement (Figure 3.6d). The difference in the pore size distribution between the two types of foams can be attributed to the incorporation of the OP particles in the SFOP foam. In fact, the OP affects the protein gelation due to a physical interference between the protein domains during the self-assembling process, resulting in the formation of different content of β-sheet structures during the formation of the interconnected porous network in the alcogel compared to the SF.

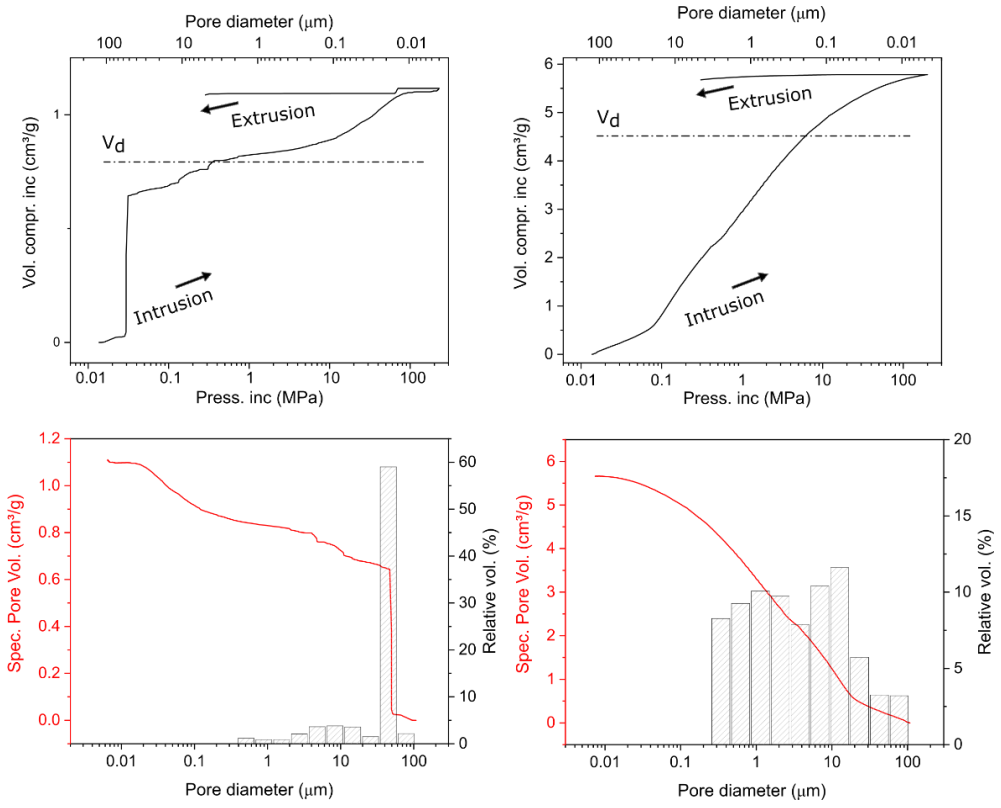

Figure 3.6. Mercury intrusion/extrusion curves of (c) SF and (d) SFOP foam and pore size distribution calculated by the mercury intrusion of (e) SF and (f) of SFOP foams.

3.3.2.2. Chemical Characterization and Water Uptake

The effect on the sol-gel transition of the SF matrix due to the incorporation of the OP particles is investigated by performing FTIR and XRD analysis, in order to evaluate the variation of crystallinity in the foams and the possible interactions between the components.

The FTIR spectra of the SFOP and SF foams exhibit similar vibrational bands at the same wavenumbers, indicating that no chemical interactions occur between the protein and the organic filler (Figure 3.7a). In both cases, the broad band at 3283 cm^{-1} is associated to the N-H stretching of the amide A, while the broad signal at 3037 cm^{-1} is due to the stretching vibration of the intramolecular hydrogen bonded N-H group of the amide B. The absorption band centered at 1621 cm^{-1} mainly arises from the C=O stretching vibration of the amide I and other minor contributions such as the out-of-phase C-N stretching, CCN deformation and N-H bending. The signal at 1514 cm^{-1} arises from the amide II band, which is attributed to the out-of-phase combination of the N-H in-plane bending and the C-N stretching. The peak at 1231 cm^{-1} is the amide III band that originates from the in-phase combination of the N-H bending and the C-N stretching vibration[178].

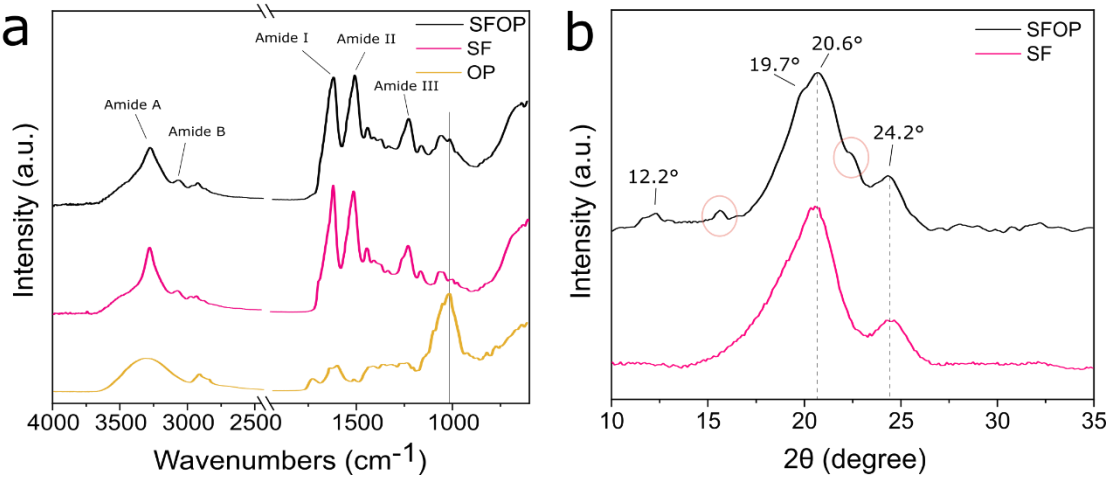

Figure 3.7. (a) FTIR spectra of the foams and of the OP powder and (b) XRD patterns of SFOP and SF foams.

In the FTIR spectrum of the SFOP foam, the identification of the OP absorption peaks is challenging because most of them occur at similar wavenumbers as the ones of the SF (Table 3.1 summarizes the vibrational assignments of OP). The only clear spectral

contribution of the filler can be observed at 1010 cm^{-1} (highlighted by a continuous line in Figure 3.7a), where lies the strong broad absorption band attributed to the C-O-C stretching of the polysaccharides, part of the OP components[179].

Table 3.1. Vibrational assignments of the amide I region of the SF matrix and of the OP powder.

SF (amide I vibrations)		**OP particles**	
Wavenumber (cm^{-1})	Secondary Structure assignment	Wavenumber (cm^{-1})	Assignment
1620	Intermolecular β-sheet (strong)	3320	O-H stretching
1633	Intramolecular β-sheet (strong)	2925-2856	C-H asym. And sym. stretching
1645	Random coils / extended chains	1736	C=O stretching
1651	Random coils	1645-1608	C=C stretch. (conjugate alkene)
1659	α-helix	1521	C=C ring stretching (lignin)
1668-1682	Turns	1418-1362	C-H bending
1698	Intermolecular β-sheet (weak)	1096-1048-1010	C-O-C stretch. (polysaccharides)

FTIR analysis is also used to quantify the amount of secondary structures in the SF matrix to determine how the OP filler affects the crystallinity of the SF. Specifically, the quantification is based on the analysis of the broad amide I region, which is often used to study the composition of secondary structures of the SF protein[165,180], due to its sensitivity to the strength of hydrogen bonds involved in the protein self-arrangements[180]. Since the amide I band has a characteristic broadness, the quantification of the different contributions of the secondary structures is obtained by applying the spectral deconvolution to this peak[181] (Figure 3.8). In Table 3.1, the vibrational assignments of the SF secondary structure contributions in the amide I are listed. As shown they are composed of β-sheets, random coils, α-helices, turns and side chains. For both foams, β-sheet secondary structures are prevalent, as expected due to the methanol treatment necessary for the gelation of the protein solution[171,182]. However, the presence of the organic filler in the SFOP foam causes a statistical increase of the contribution of both random coils and turn structures (from 23% and 22% to 28% and 26%, respectively), which are compensated by a decrease in β-sheets contribution (from 41% to 34%), whereas the content of α-helices and side chains does not significantly change. XRD diffraction patterns of the SF and the SFOP foams exhibit a prevalent highly ordered structure (Figure 3.7b). In both foams, the most intense peak at 20.6° is typical of the silk

II conformation, characterized by highly ordered crystalline intra-hydrogen-bonded β-sheet structures, and corresponds to a crystalline spacing of 4.3 Å[170]. The peak at 24.2° is one of the main diffraction peaks attributed to the silk I form, from less ordered crystalline β-sheet structures with a crystalline spacing of 3.7 Å[170,183]. The diffraction profile of the SFOP foam shows some additional weak peaks characteristic of the silk I conformation at diffraction angles of 12.2° and 19.7° (crystalline spacing of 7.4 and 4.5 Å)[183], which are also associated to the less ordered β-strand structures[170]. This can be attributed to the presence of the OP filler, which influences the self-assembly into β-sheet crystallites during the protein gelation, causing an increase of the less ordered content. Furthermore, it is possible to observe two additional diffraction peaks at 15.7° ad 22.6° attributable to the crystalline forms of the cellulose, which is one of the main components of the OP powder[184].

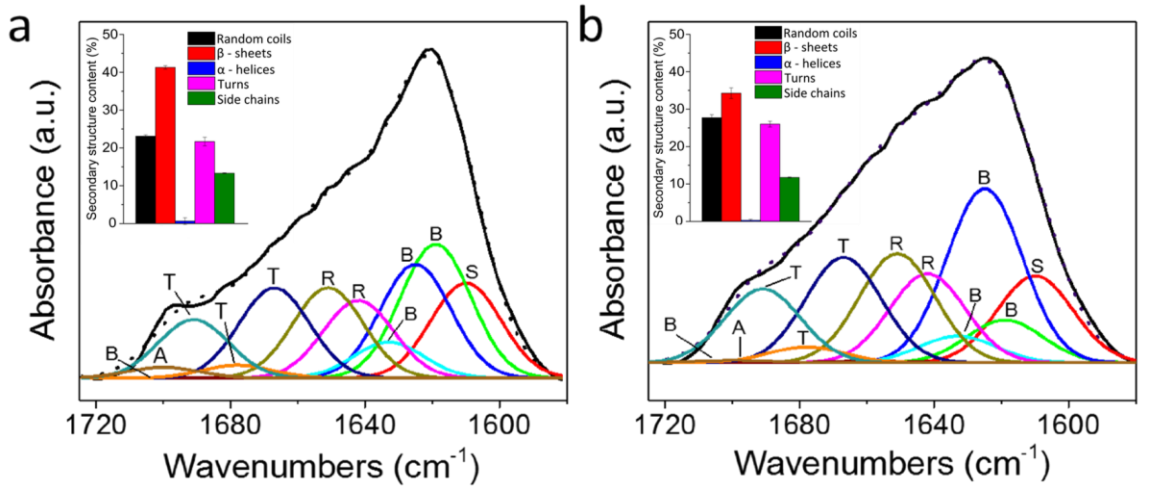

Figure 3.8. Deconvoluted FTIR spectra of the amide I region for (a) SF and (b) SFOP foams. The black curve represents the original FTIR spectrum while the dotted one is the spectral fit. The colored curves are the 11 secondary structure contributions and they are marked as random coils (R), β-sheets (B), α-helices (A), turns (T) and side chains (S). Sum of the percentage content of the secondary structure contributions to the amide I band are shown as insets.

Therefore, as previously observed in the XRD patterns, the crystallinity in the biocomposite material seems to be affected by the presence of OP, which causes a decrease in the highly ordered crystalline content. Although the content of less ordered secondary structures, typical of the silk I conformation, increases when the OP is incorporated in the

SF matrix, the overall structural stability of the foam is not compromised, as can be observed from the water dipping experiments.

The weight loss (Δm%) and the water uptake (Δm_s%) values measured from the water dipping experiments are useful parameters for the development of materials suitable for adsorption processes. After three water uptake cycles, the mean Δm% calculated is very low for both types of foams, 1.0 ± 0.4% and 5.0 ± 2.6% for SF and SFOP respectively, confirming their good structural stability. The higher Δm% value, for the composite foam, can be mainly attributed to the OP not perfectly embedded in the SF matrix, which is released in the water upon the foam swelling during the first water uptake cycle. Furthermore, the incorporation of OP in the foam leads to a significant increment of the mean Δm_s%, from 61.0 ± 2.6% to 78.0 ± 0.6% as calculated for three successive water uptake cycles. The water diffusion is therefore facilitated in the SFOP porous structure, due to the incorporation of the OP filler, which results in a more hydrophilic environment. This is attributed to the hydrophilic components of the OP filler and the lower crystallinity of the SFOP foam. In fact, the decrease of hydrophobic β-sheet content induces a higher exposition of the more hydrophilic aminoacidic domains expressed in the N- and C-termini and the spacer regions[183,185].

3.3.3. Adsorption performance

3.3.3.1. Definition of the optimal experimental conditions

The adsorption performance of the prepared biocomposite foam is studied towards the removal of MB, which is a blue cationic thiazine dye widely used in textile, paper and plastic industries. Since the composition of certain industrial wastewater can greatly vary based on the processing manufactory, the presence of dyes in their composition has been reported to range from low to extremely high concentration values[186]. The good water solubility of synthetic dyes together with the, frequently, ineffective wastewater treatments results in their persistence at low concentrations in water resources[51]. The MB is often used as a model molecule for the evaluation of the

adsorption performance of developed materials and therefore of the water treatment efficacy. The ability of the biocomposite foam to adsorb MB was studied under the effect of different pH values of the dye aqueous solution and of the contact time between the dye and the adsorbent. Figure 3.9a shows the dependence of the MB adsorption capacity on different initial pH values in the case of the SFOP foam and its components, SF foam and OP particles. As expected, in the case of solely OP powder, the increase of the pH from 2 to 8 causes a significant enhancement of the MB adsorption capacity, attributed to the electrostatic attraction between the OP negative charged groups[187] and the cationic dye. Conversely, concerning the SF foam, the MB adsorption capacity slightly increases with the increase of the pH, while after pH 7, the dye adsorption capacity does not significantly change. This is also the case for the SFOP foam, although the effect is here more evident. Compared to the SF foam behavior, the more intense increase in the adsorption capacity of the SFOP at higher pH values can be attributed to the combination of the SF with the OP powder. Specifically, the SFOP foam establishes mainly hydrophobic interactions between the SF bio-polymeric crystalline β-sheet structures and the MB hydrophobic aromatic group. The further increase of the MB adsorption in SFOP foam for pH higher than 5 can be attributed to the contribution of the electrostatic interactions to the hydrophobic ones in the overall adsorption process. At pH values above 5, the protein is also able to establish electrostatic interactions with the positively charged dye, due to its net negative charge (isoelectric point of 4.03)[171,188]. Considering the marginal improvement of the MB adsorption capacity for basic pH, the following adsorption experiments were conducted at neutral pH.

Figure 3.9b compares the normalized MB adsorption capacity (Q_t) of the SFOP composite foam with the one of the SF foam and the OP powder at different contact times with the dye aqueous solution (C_i = 5 mg·L^{-1}). The suspension of OP particles exhibits a fast MB adsorption rate thanks to the availability and accessibility of the active adsorption sites on the adsorbent surface. The equilibrium is reached after 15 min, time that does not significantly change if other initial dye concentrations are tested.

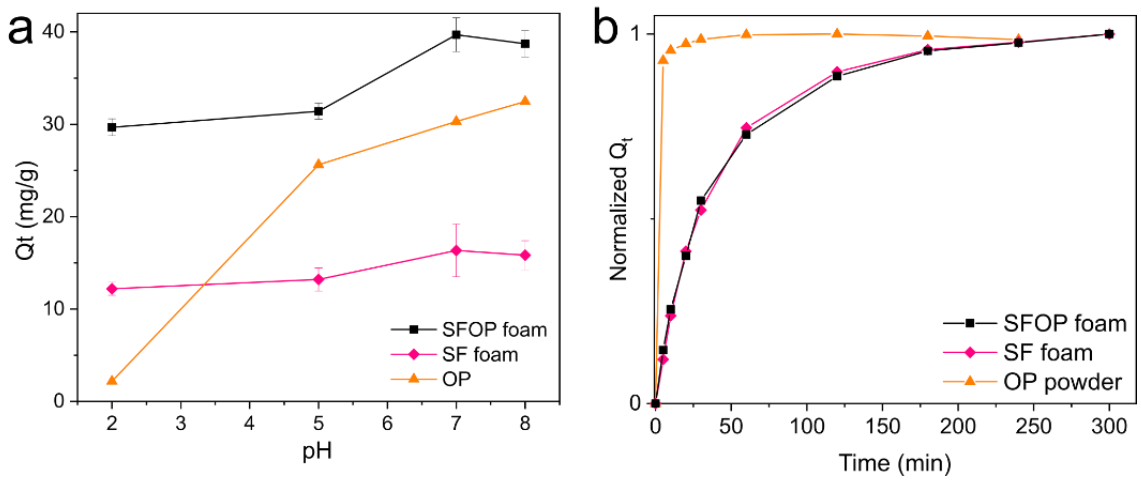

Figure 3.9. Effect of (a) the pH on the MB adsorption capacity (C_i = 50 mg·L^{-1}) after 24 hours of contact between the dye and the adsorbents and of (b) the contact time on the normalized adsorption capacity for MB (C_i = 5 mg·L^{-1}).

In the case of foams, the MB adsorption process is slower, due to the time needed for the MB aqueous solution to diffuse into the solid porous material. For both types of foams, the Q_t rises with the increase of the contact time and the equilibrium conditions are almost reached after 5 h. In order to assure that the samples reach the real equilibrium conditions, the contact time was set at 24 h in the following adsorption experiments. Although the bare OP powder shows faster dye absorption compared to the foams, it has to be taken into account that OP requires extra steps to be recovered after the adsorption process. On the other hand, the utilization of a stable solid material provides a practical alternative to avoid time-consuming separation steps.

3.3.3.2. Definition of the maximum adsorption capacity

The adsorption isotherms for both foams and the OP filler are shown in Figure 3.10, which summarizes the effect of different initial MB concentrations on the adsorption capacity at the equilibrium condition (Q_e). As demonstrated in all cases, the increase of the initial MB concentration causes the Q_e increase until, at a specific MB concentration in each case, a plateau is reached. This indicates that above this MB concentration no further improvement on the Q_t is observed, and this value is defined as the maximum adsorption capacity (Q_{max}). In fact, higher initial MB concentrations lead to an increase of the MB dye

mass transfer in the adsorbents and, therefore, a higher adsorption capacity can be reached due to the enhanced possibility of interaction between the MB molecules and the adsorbent active sites[189–191]. The Q_{max} is succeeded when all the active sites of the adsorbents are occupied and consequently the material cannot adsorb further pollutant molecules.

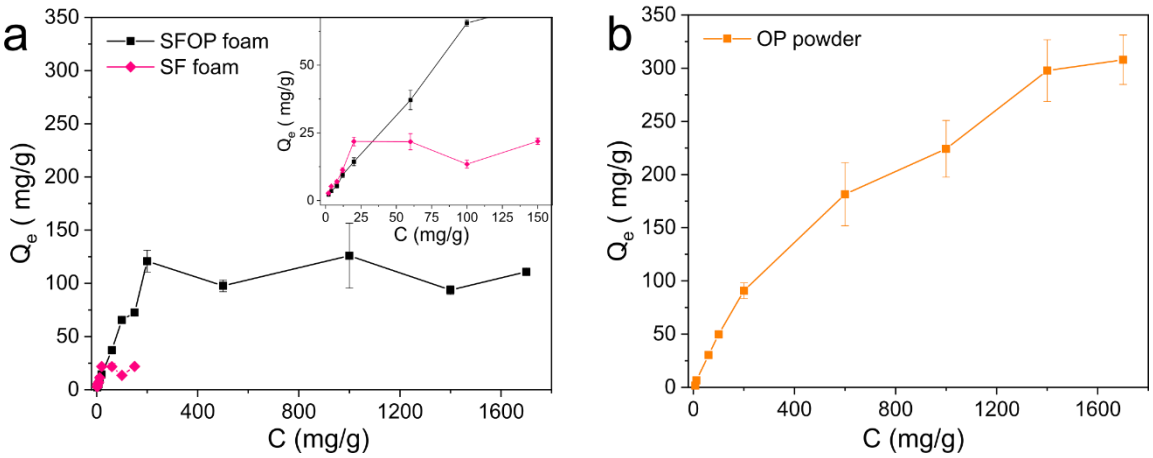

Figure 3.10. Effect of the initial MB concentration on the Q_e after a contact time of 24 h for (a) the SFOP and the SF foams and for (b) the OP in powder form.

As shown in Figure 3.10a, the Q_e of the SFOP foam is significantly higher compared to the SF foam indicating that the incorporation of the OP filler induces an improvement in its adsorption performance. In particular, for the SFOP foam, a Q_{max} of 113.8 ± 12.5 mg·g^{-1} is reached for dye concentrations higher than 200 mg·L^{-1}. Contrarily, the Q_e of the SF foam increases as the initial MB concentration rises from 2 to 20 mg·L^{-1}, and then the plateau is reached with a Q_{max} of 21.8 ± 1.2 mg·g^{-1}.

The incorporation of the organic filler offers to the SFOP foam a higher number of available active sites, which are saturated at higher MB concentrations. In fact, in the case of the OP powder (Figure 3.10b) the Q_{max} reached is 297.7 ± 29 mg·g^{-1}, at MB concentrations higher than 1400 mg·L^{-1}. This is in the same range with values reported in previous works on the MB sorption by OP waste powder, in which the reported theoretical maximum MB adsorption capacities are 218 and 246 mg·g^{-1} at neutral pH[53,187]. The different values reported for the same sorbent could be attributed to the different particle sizes and thus to the different surface areas of the OP powders used. In particular, the powder utilized

in this work has a much higher surface area due to the significantly lower particle size (average particle size of 16.4 ± 9.5 μm) compared to the one used in both studies referred above (powder size ranging from 1.2 to 2 mm and less than 0.5 mm, respectively).

In this work, the Q_{max} values of the OP powder when incorporated in the solid SFOP foam and of bare are rather comparable (219.8 ± 10.2 $mg \cdot g^{-1}$ for OP in SF and 297.7 ± 29 $mg \cdot g^{-1}$ for the bare OP, if considering that the OP amount is 50 $\%_{w/w}$ of the composite foam), demonstrating that the OP activity is well preserved in the polymer matrix. The slightly lower Q_{max} for the solid material can be attributed to a lower amount of active sites of the embedded OP that are accessible to MB. Nonetheless, the obtained value is comparable with those reported in other studies based on the adsorption of MB on unconventional low-cost adsorbents obtained from agricultural by-products, without further chemical modification, such as grass waste, pomelo peel,[192] garlic straw,[193] maize silk,[194] etc.

3.3.4. Adsorption mechanism

3.3.4.1. Kinetics studies

To understand the adsorption mechanism of the MB molecules on the SFOP biocomposite foam, the experimental data were investigated by evaluating the adsorption kinetics. Regarding the kinetics studies, the parameters calculated from the data fitting with the pseudo-first and pseudo-second order kinetic models are shown in Table 3.2. The accuracies of the pseudo-first and pseudo-second fits are deduced by considering the better consistency of the equilibrium adsorption capacity (Qe) and by the higher correlation coefficient (R^2) achieved[55,194].

It is possible to observe that, in the case of the SFOP, at a low initial MB concentration (5 $mg \cdot L^{-1}$) the pseudo-first order kinetics model fits better the adsorption data compared to the case where the initial dye concentration is higher (50 $mg \cdot L^{-1}$). In the latter case, the obtained data are well fitted by the pseudo-second order model (Figure 3.11).

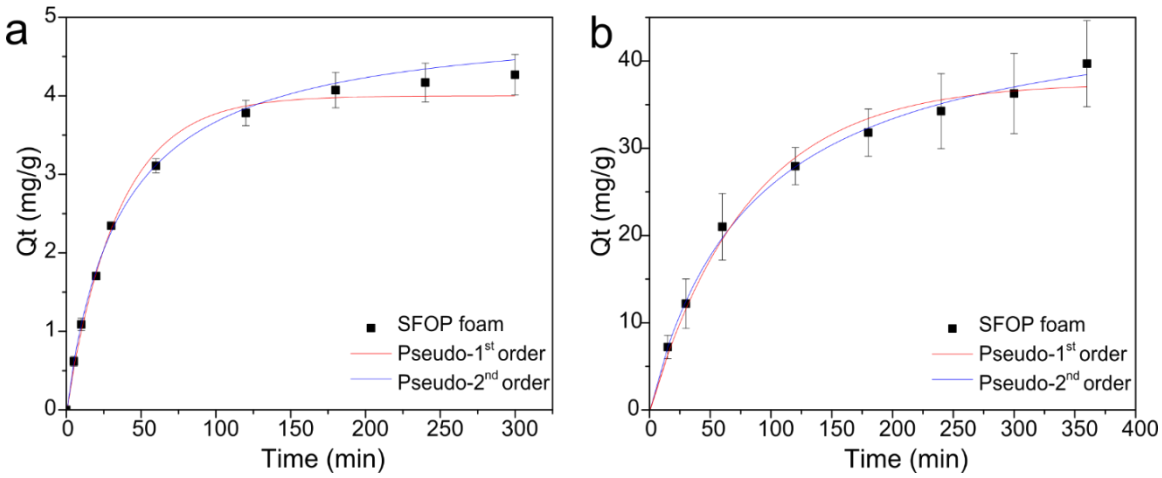

Figure 3.11. The non-linear fitting curves of the MB adsorption on the SFOP foam by pseudo-first and pseudo-second order models for an initial MB concentration of (a) 5 mg·L^{-1} and (b) 50 mg·L^{-1}.

Specifically, at low initial MB concentrations, the value of the calculated adsorption capacity at the equilibrium condition ($Q_{e(calc)}$) obtained by applying the pseudo-first order model better reflects the experimental ones ($Q_{e(exp)}$) and, moreover, the R^2 value is higher than the ones calculated from the pseudo-second order model (0.9894 and 0.9864 respectively). Conversely, for higher initial dye concentrations, the $Q_{e(calc)}$ value obtained from the pseudo-second order equation is closer to that of $Q_{e(exp)}$ than the one of the pseudo-first order fitting, and the R^2 shows the higher value (0.9980 instead of 0.9812 for the pseudo-first order fit). Considering the SF foam, for all the initial MB concentrations tested, the adsorption performance is better described by the pseudo-first order model. Conversely, in the case of the bare OP powder, the adsorption performance is better described by the pseudo-second order model. Therefore, considering these observations, the dominant adsorption process of MB on the SFOP foam at low dye initial concentrations, is governed by the presence of the biopolymer and seems to be diffusion-controlled, which is well explained by a pseudo-first order rate law. On the other hand, at higher dye concentrations, the presence of the OP organic filler induces an MB adsorption which seems to be controlled by the adsorption reaction between the dye and the adsorbent[55,195,196].

Table 3.2. Results obtained from the non-linear fitting of the experimental adsorption data by using the pseudo-first and pseudo-second order models.

			Pseudo-first-order kinetic model			Pseudo-second-order kinetic model		
Samples	**C_0 (mg·L^{-1})**	**$Q_{e(exp)}$ (mg·g^{-1})**	**$Q_{e(calc)}$ (mg·g^{-1})**	**k_1 (min^{-1})**	**R^2**	**$Q_{e(calc)}$ (mg·g^{-1})**	**K_2 (g·mg^{-1}·min^{-1})**	**R^2**
SFOP foam	5	4.54	4.99	0.029	0.9894	5.99	0.0055	0.9864
	50	39.70	37.51	0.012	0.9812	47.43	0.00025	0.9980
SF foam	5	4.37	4.22	0.027	0.9979	5.05	0.0052	0.9968
	50	16.34	16.19	0.014	0.9879	18	0.001	0.9820
OP	5	1.58	1.56	0.54	0.4273	1.58	1.63	0.9184
	50	30.31	29.03	0.14	0.5495	29.89	0.013	0.8403

3.3.4.2. Adsorption isotherms

The Langmuir and Freundlich isotherm models are applied to fit the equilibrium adsorption data in order to explore the interactions between the dye and the adsorbents and to estimate the maximum theoretical adsorption capacity ($Q_{max\ (theor)}$)[53,55,196]. The parameters derived from the fitting of the data using the non-linear forms of the isotherm models are shown in Table 3.3.

Table 3.3. Parameters calculated from the fitting of the equilibrium data by using the non-linear form of the Langmuir and Freundlich adsorption isotherms.

		Langmuir isotherm			Freundlich isotherm		
Samples	**$Q_{max\ (exp)}$ (mg·g^{-1})**	**$Q_{max\ (theor)}$ (mg·g^{-1})**	**K_L (L·mg^{-1})**	**R^2**	**n**	**K_F (L·g^{-1})**	**R^2**
SFOP foam	113.8	111.2	0.034	0.9683	3.785	17.306	0.8817
SF foam	21.81	22.61	0.7675	0.8546	5.212	9.791	0.6659
OP	302.8	383.6	0.003	0.9944	2.053	9.494	0.9866

In all the cases, the Langmuir model fits better the experimental data compared to the Freundlich model (Figure 3.12), as can be also observed from the higher R^2 values. This indicates that the MB adsorption process occurs onto a homogeneous surface, where

all the active sites have a similar affinity with the dye. In such case, the MB is distributed forming a monolayer on the homogeneous surface, rather than the formation of several monolayers on an inhomogeneous surface in which the active sites show different affinity towards the dye[53,197], which would be better described by the Freundlich isotherm model. The theoretical maximum adsorption capacity ($Q_{max\ (theor)}$) values obtained by the Langmuir isotherm fitting are quite similar to the experimental values ($Q_{max\ (exp)}$) confirming the validity of the model.

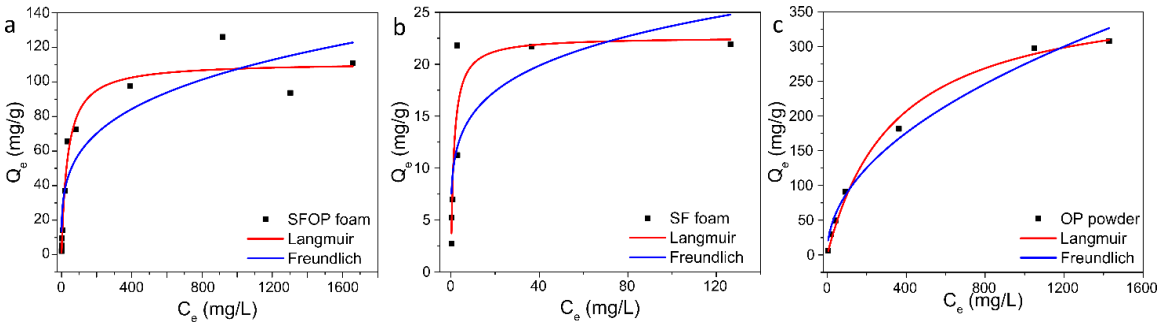

Figure 3.12. The non-linear fitting curves of MB adsorption on (a) the SFOP foam, (b) the SF foam and (c) the OP by Langmuir and Freundlich isotherm models (295.15 ± 1 K). The fittings are performed by using the Origin software.

The dimensionless constant (R_L) calculated from the parameter obtained with the Langmuir isotherm is an equilibrium parameter called separation factor, which can be used to define whether a process is favorable[151,198]. For all the adsorbents, the R_L values are $0 < R_L < 1$, confirming that the MB adsorption on the adsorbent materials is favorable (0.014, 0.009 and 0.144 for SFOP foam, SF foam and OP powder, respectively).

3.3.4.3. Spectroscopic studies

To confirm the adsorption of the dye molecules on the adsorbent surface as a mono- or multilayer, the UV-vis spectra of the adsorbent samples are acquired. In the liquid state, the MB molecules are prevalently in the form of monomers, in which the main absorption band, centered at around 664 nm, corresponds to n-π* transitions, characterized by a shoulder at 610 nm that arises from the vibrational ground states to the excited states 0-1 transition. After the MB adsorption takes place, the absorption spectra

of the adsorbent materials are recorded as described in the experimental section (chapter 3.2.5). As shown in Figure 3.13a (pink curve), when the MB adsorption occurs on the SF foam, a broad band attributable to the formation of MB trimers and higher aggregates appears at around 590 nm, while the typical band of the MB monomers is evident at around 670 nm[199]. Comparing the contributions of the signals on the final SF foam spectrum, it is possible to conclude that the majority of the adsorbed MB molecules are forming aggregates on the foam surface, while the MB monomer content is suppressed, indicating that the MB-MB molecular interactions are more favorable compared to the MB-surface interactions[199,200]. Similar behavior can be also observed in the case of MB molecules adsorbed on the surface of OP bare powder (orange curve in Figure 3.13a.). Specifically, the dye absorption band is centered around 607 nm, due to the prevalence of MB dimers[200], while the characteristic MB monomer band is shifted at 675 nm. The higher relative intensity of the MB monomer band with respect to the SF foam one, suggests that OP powder surface possibly promotes interaction with the dye in monomer form finer than the one established with the surface of the SF foam, thanks to its particular chemical composition. Alternatively, when the adsorption process takes place on the SFOP foam, the dye molecules are adsorbed on the foam surface mainly in the form of monomers as evident from the absorption bands at 620 and 685 nm (Figure 3.13a, black curve)[199], confirming the more favorable MB-surface interaction in this case. In addition, the red shift of the prevalent monomer absorption compared to the SF foam (685 nm for SFOP instead of 670 nm for the SF) indicates that the environment is more polar, resulting in a more favorable interaction between the dye and the SFOP foam[200].

The interaction established between the dye and the bare OP powder was further investigated by recording the FTIR spectrum of the filler before and after the MB adsorption experiment (Figure 3.13b). The MB adsorption on the OP surface causes a shift of the broad band attributed to the hydrogen-bonded OH groups from 3297 to 3316 cm^{-1}. Moreover, the bands at 1736 and 1010 cm^{-1}, which are associated with the C=O and C-O stretching vibrations, are shifted to higher wavenumbers, at 1744 and 1017 cm^{-1}, respectively. The increase of the signal intensity at 1594 cm^{-1} is caused by the C=C

stretching of the MB aromatic ring vibrations. The observed shifts towards higher wavenumbers of the main vibrational modes can be attributed to the weakening of the hydrogen bond interactions in the OP due to the presence of MB on its surface.

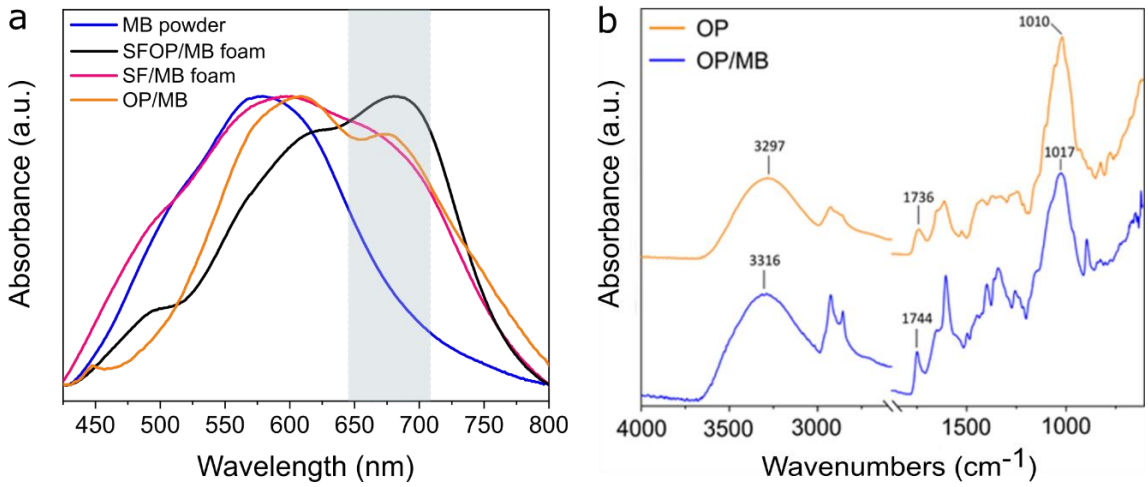

Figure 3.13. (a) Absorption spectra of SFOP and SF foams and of OP powder after the MB adsorption. The highlighted spectral range indicates the region of the MB monomer absorption band. (b) FTIR spectra of OP before and after the MB adsorption.

To sum up, the incorporation of the OP filler in the SFOP foam significantly affects the MB adsorption performance, by remarkably increasing the Q_{max} due to the combination of the higher polluted water uptake and the more favorable MB-surface interactions. The bio-composite adsorbent can be partially regenerated in acidic solution at pH 2, where the MB molecules adsorbed via electrostatic interactions on the exposed OP component can be desorbed[187]. Although the desorption process still needs to be explored in detail, the main advantage of the prepared bio-composite is the simple combination of two waste products, which results in a highly porous adsorbent that can be easily handled and disposed of after the MB remediation process.

3.4. Concluding remarks

In conclusion, a fully bio-based natural porous composite is prepared by a simple approach resulting in the successful incorporation of OP agro-waste particles in a polymeric matrix. The presence of OP affects the physio-chemical properties of the SF matrix, by influencing the final foam morphology and crystallinity, as well as by promoting a more polar environment. The stable and highly porous biocomposite foam present an MB maximum adsorption capacity which is significantly higher than the one reached with the pure SF foam. The MB adsorption on the SFOP foam is facilitated by both electrostatic and hydrophobic interactions and it occurs by the formation of a monolayer onto the adsorbent surface, as suggested by applying the Langmuir isotherm model. The kinetics of the adsorption process is described by a pseudo-second order kinetics model and the MB molecules are prevalently adsorbed in their monomer form. The immobilization of the powder in the porous matrix can outweigh the marginally lower adsorption capacity compared to the one obtained with the same amount of OP because of the derived improvements, such as the handling of a solid adsorbent without further expensive and time-consuming processes for the recovering of the particles. With the present work, the utilization of OP waste as a component of a highly porous bio-composite foam opens up the possibility to valorize the functionalities of this agro-waste without compromising its usability, resulting in a promising material for water remediation processes.

Chapter 4

ZnO based porous composite materials for heterogeneous photocatalysis

4.1. Introduction

The growing demand for clean water urges the improvement of the commonly used treatments for the wastewater management[27]. In case of emerging and recalcitrant pollutants, advanced oxidation processes (AOPs) are employed to ideally destroy organic pollutants from the contaminated water, thanks to the *in-situ* production of strong oxidant species, induced by solar, chemical or other forms of energy[31,56,63,201].

As already discussed in Chapter 1, heterogeneous photocatalytic oxidation is one of the most promising AOPs for oxidizing organic pollutants into more biodegradable and less harmful compounds[63]. Typically, wide band gap, nano or micro-scale sized semiconductors, are used as photocatalysts able to absorb incident photons causing the subsequent formation of a conduction-band electron and a valence-band hole. The photo-excited carriers can generate hydroxyl radicals and other reactive oxygen species (ROS), which react with the organic molecules in the contaminated water causing their degradation, through an eco-compatible process since the oxidation occurs in mild conditions [5]. The semiconductor particles are usually dispersed in the contaminated water to ensure a high exposed surface area in contact with the pollutants and therefore, a high volumetric generation rate of ROS. However, the main limitation in their use for water remediation applications is the demand of energy and time consuming additional steps for their recovery from the treated water. To avoid these post-treatment steps, the photo-catalyst powders can be immobilized on suitable solid supports [9,10]. To this aim,

polymeric supports have been recently introduced due to their low-weight, flexibility and their easy conversion in different morphologies [11–16]. In particular, fibrous polymeric mats are porous materials characterized by superior mechanical properties[86] and by high surface to volume ratio, which allows higher contact surface with the polluted water. Furthermore, their preparation process through the electrospinning technique is relatively simple and easily scaled up [9,17]. The electrospun mats could be also used to prepare multifunctional membranes, in which the photocatalytic activity of the fixed catalysts is combined with the filtration process.

The incorporation of the active filler inside the fibrous mats can easily occur by the *in-situ* conversion of the catalyst precursor salt loaded in the electrospun fibers, resulting in the synthesis of NPs directly inside the porous polymeric matrix. Compared to traditional mixing processes, the *in-situ* synthetic strategy offers the advantageous formation of NPs homogeneously distributed not only in the whole volume of the fiber, but also exposed on its surface. Furthermore, limitations such as the complex rheology of polymer/NPs solutions which can limit the electrospinning process and, thus, the formation of fibrous nanocomposites, can be avoided[78,122].

Among the diverse types of NPs developed so far following this approach[78,122,202], zinc oxide (ZnO) based nanocomposite mats are a promising system for the water remediation through the photocatalytic approach. In fact, ZnO is of great interest not only because it is environmental friendly, non-toxic, low-cost and abundant, but also because of its optoelectronic properties[114,203–206]. In particular, the n-type ZnO is a direct wide band gap semiconductor (E_g = 3.37 eV), characterized by a high exciton binding energy (60 meV) which allows efficient excitonic emission even at room temperature[207]. However, due to the high photo-generated electron-hole pair recombination, the photocatalytic performance and, therefore, the utilization of the ZnO in wastewater purification can be limited. For this reason, the enhancement of the separated electron-hole lifetime is one of the factors on which the efforts are focused in order to improve the ZnO photocatalytic performance[208–210]. This aspect can be achieved through various methods, such as the modification of the morphology of the

ZnO nanostructures[204,211], the incorporation of metallic[212,213] and non-metallic dopants[214] in their crystalline structure, and the preparation of hybridized structures with other materials[203,204,215,216].

Concerning the last method, the combination of ZnO NPs with noble metal NPs has been recently considered an effective route to enhance the local density of states at the metal-semiconductor interface, prolonging thus the electron-hole separation lifetime[203,215]. Specifically, the use of Au NPs to modify the ZnO surface has improved the photocatalytic performance of the semiconductor due to the surface plasmonic resonance effect and to the establishment of the Schottky junctions. The combination with Au NPs improves therefore the utilization of the solar spectrum and simplifies the charge carrier separation, resulting in the increasing the ROS generation [217,218].

Considering the above, PMMA/ZnO composite mats are developed following the *in situ* synthesis approach and the effect of the modification of the photo-active ZnO with noble metal NPs is studied, evaluating their photocatalytic performance on the removal of organic pollutants from water. Specifically, ZnO NPs are synthetized by a thermally induced solid state reaction directly in the electrospun polymeric fibers, obtaining an easily handled flexible solid porous material. The addition of Au NPs on the PMMA/ZnO composite mats is performed by using two fabrication routes. In the first case, the gold precursor is directly added to the polymer/zinc precursor salt solution before the electrospinning process and the Au NPs are then synthetized directly in the polymeric fibers, together with the ZnO NPs formation. In the second case, the Au/ ZnO hybrid structures are formed by a dip-coating process of the PMMA/ZnO composite mats in the gold precursor solution and the subsequent thermal treatment of the samples results in the direct formation of Au NPs in the surface of the fibers and, therefore, on the exposed ZnO NPs. By comparing the performance of both types of composite mats, the one with the best performance was chosen for a further study on the photocatalytic performance upon UV light irradiation for the degradation of MB and of the emerging pollutant bisphenol A (BPA). In particular, among the two approaches for the addition of Au NPs, only the dip-coating process allows the formation of exposed Au/ZnO hybrid structures,

characterized by a high active metal-semiconductor interfacial area. For this specific PMMA/ZnO-Au nanocomposite mat, the amount, size and localization of the formed Au NPs for different gold precursor concentrations have been correlated to their photocatalytic performance.

The reported straightforward fabrication method ensures the formation of light-weight and flexible polymeric fiber mats of high surface area with high level of immobilized active catalysts for photocatalytic applications. This valuable alternative to the existing systems for the incorporation of active nanomaterials represents an innovative route for the fabrication of multifunctional membranes for advanced water treatments, without requiring costly and time consuming post treatment processes as in the case of the separation of suspended powders from the treated water.

4.2. Experimental methods

4.2.1. Materials

Poly(methyl methacrylate) (PMMA, average Mw ~ 350 kDa), zinc acetate dihydrate ($Zn(CH_3CO_2)_2 \cdot 2H_2O$ 99,999%), N,N- Dimethylformamide (DMF, ≥99.8%), chloroauric acid trihydrate ($HAuCl_4 \cdot 3H_2O$, 99.999%), methylene blue (MB), bysphenol A (BPA, ≥99%), acetone (≥99.5%), ethanol (EtOH, ≥99.8%), sodium hydroxide (NaOH, ≥98%, anhydrous), hydrochloridric acid (HCl, 37%) and nitric acid (HNO_3, 70%), were purchased by Sigma Aldrich. All chemicals were used without any further purification.

4.2.2. Preparation of PMMA/ZnO composite mats

The nanocomposite fibers were prepared following a preparation procedure described elsewhere[122]. In brief, 1.5 g of PMMA were added in 10 mL of DMF and left under stirring at 50 °C until the complete dissolution of the polymer. Then, 1.1 g (c.a. 40 %wt) of $Zn(CH_3CO_2)_2$ were added to the polymer solution and stirred at 40 °C, until a clear solution is obtained. The electrospun fibers were prepared by means of electrospinning in a vertical setup, obtaining the PMMA/$Zn(CH_3CO_2)_2$ composite mats.

The prepared solution was placed in a 10 mL syringe with a 22G needle and the flow rate was set to 600 $\mu L \cdot h^{-1}$. The voltage applied to the syringe needle was 23 kV and the grounded collector was kept at a distance of 16 cm from the needle. To remove the eventual residual solvent, the electrospun fibers were dried for 8 h under dynamic vacuum. The *in-situ* growth of the ZnO NPs on the electrospun mats was then achieved by placing the electrospun composite mats in a convection oven for 48 h at 110 °C, inducing the thermal decomposition of the incorporated zinc salt. The obtained PMMA/ZnO composite mats were then washed in 10 mL of a H2O/EtOH mixture (8:2 v/v) for 24 h and dried at 60 °C for 4 h. As defined by ICP-OES, the total zinc loss during this washing step is around 1.17 ± 0.16%wt of the total zinc. This can be attributed either to the loss of ZnO NPs not perfectly fixed on the surface of the fibers, or, also, to the water-soluble zinc acetate, which was not fully converted during the synthesis.

4.2.3. Preparation of PMMA/ZnO-Au composite mats by *in-situ* reduction

The nanocomposite fibers were prepared dissolving 1.5 g of PMMA in 10 mL of DMF, then 1.1 g (c.a. 40 %wt) of $Zn(CH_3CO_2)_2$ and 0.0066 g (c.a. 1 %wt of Au NPs with respect to ZnO NPs) of $HAuCl_4 \cdot 3H_2O$ were added to the polymer solution and stirred at 40 °C, until a clear solution is obtained. The electrospun fibers were prepared by the same procedure described above and the *in-situ* reduction of Au NPs was achieved during the thermal decomposition of the incorporated precursors, simultaneously to the formation of the ZnO NPs. The sample was identified as PMMA/ZnO-Au_In.

4.2.4. Preparation of PMMA/ZnO-Au composite mats by dip-coating process

Three PMMA/ZnO composite mats (40 mg each), prepared as described in section 4.2.2, were dipped in 20 mL of a H_2O/EtOH mixture (8:2 v/v) of $HAuCl_4 \cdot 3H_2O$ for 24 h in dark under gentle stirring. The gold precursor solution was previously neutralized to pH 6.5 by using an aqueous solution of NaOH 0.1 M. Different initial concentration of the aqueous based $HAuCl_4$ $3H_2O$ solution was tested (1.5 mM, 3 mM and 4.6 mM) to explore

the effect of the different amount of Au to the photocatalytic performance of the PMMA/ZnO-Au mats. The composite mats were then collected and washed three times with water. The reduction of the gold ions was obtained by the subsequent thermal treatment of the samples at 60 °C for 4 h, obtaining three PMMA/ZnO-Au_Ex mats named PMMA/ZnO-Au1, PMMA/ZnO-Au3 and PMMA/ZnO-Au6, respectively. Each sample was then divided in four similar pieces of 10 mg each for further analysis.

4.2.5. Characterization

The fibers morphology was investigated by a scanning electron microscope (SEM, JEOL JSM 6490LA) and a high-resolution scanning electron microscope (HR-SEM, JEOL JSM 7500FA), which is equipped with a cold field emission gun applying an accelerating voltage of 15 kV. The specimens were previously coated with 10 nm thick carbon layer by a carbon coater (Emitech K950X, Quorum Technologies Ltd). The morphology of the ZnO and Au NPs in the composite mats were investigated by a transmission electron microscope (TEM, Jeol JEM 1400 Plus) operating at an acceleration voltage of 120 kV. To do so, the polymeric fibers were dissolved in acetone and the suspension was sonicated and centrifuged in order to separate the NPs from the polymer. Then, 30 μL of the suspension were deposited on a copper grid (CF300-Cu-UL) for further investigation. High angle annular dark-field scanning TEM (HAADF-STEM) images and energy dispersive X-ray spectroscopy (EDS) maps were acquired with a high-resolution FEI Tecnai G2 F20 equipped with a Schottky field emission gun (FEG). The average size and the size distribution of the fibers and NPs were explored using the Fiji/ImageJ software.

The X-ray diffraction (XRD) analysis was performed on a PANalytical Empyrean X-ray diffractometer with 1.8kW CuKα ceramic X-ray tube (λ = 1.5418 Å), PIXcel3D area detector (2×2 mm^2) and operating at 45 kV and 40 mA. The diffractograms were recorded in parallel-beam geometry and symmetric reflection mode, for 2θ range from 25° to 80°, with a step time of 383.67 sec and step size 0.026°. The average crystallite size was calculated by using the Debye-Scherrer equation (as descripted in section 4.2.6). The zinc and the gold content in the composite mats was obtained by ICP-OES analysis (iCAP 6300, Thermo) of the digested solid samples. Specifically, 2.5 mL of aqua regia (HCl/HNO_3, 3:1)

were added to 2.5 mg of the composite fibers and the solid degradation reaction was performed by using a microwave digestion system (MARS Xpress, CEM) at 180 °C for 15 min. The samples were then diluted with milliQ water up to 50 mL and filtered through polytetrafluoroethylene (PTFE) syringe filters (diameter 15 mm, pore size 0.45 μm, Sartorius).

The optical properties of the nanocomposite fibers were evaluated by diffuse-reflectance measurements in the range between 200 – 800 nm, using a Varian Cary 6000i (Agilent) UV-visible-NIR spectrophotometer equipped with integrating sphere. The energy bandgap of ZnO and ZnO/Au NPs was then extrapolated by applying the Kubelka-Munk method to the reflectance results (see section 4.2.7). The Raman spectra of the composite mats were acquired by a Raman LabRam HR800 (Horiba Jobin-Yvon) spectrometer equipped with a built-in microscope with objectives 10X (NA 0.25) and 50X (NA 0.75), using the 632.8 nm He-Ne laser excitation. The experimental setup consists of a grating 600 lines·mm^{-1} with a spectral resolution of approximately 1 cm^{-1}.

4.2.6. Crystallite size approximation by Debye-Scherrer equation

The crystallite size was estimated by using the Debye-Scherrer equation (Equation 4.1),

$$D_{hkl} = \frac{K\lambda}{\beta cos\theta_{hkl}} \qquad \text{(Equation 4.1)}$$

where D_{hkl} is the crystallite size (nm), K is a dimensionless factor referred to the crystallite shape, λ is the wavelength of the target (0.15406 nm for Cu), β is the Full-Width-Half-Maximum (FWHM) of the diffraction peak (rad) and θ_{hkl} is the diffraction peak angle. The presented crystallite sizes is the mean value obtained by the D_{hkl} values calculated from the three main diffraction peaks of the ZnO wurtzite phase at 31.8°, 34.3° and 36.1°.

4.2.7. Band gap energy extrapolation by Kubelka-Munk method

Band gap energy (E_g) was deduced from the diffuse reflectance spectra through the Kubelka-Munk (KM) function (Equation 4.2),

$$F(R_\infty) = \frac{(1-R_\infty)^2}{2R_\infty} = \frac{K}{S} \qquad \text{(Equation 4.2)}$$

where F(R∞) is the KM function, R∞ is the absolute reflectance of the sample obtained by the ratio between the diffuse reflectance of the sample and the diffuse reflectance of the

standard (MgO), K and S are the absorption and scattering coefficient respectively. Considering that Eg can be approximated from K as a function of the photon energy (hν) as shown in Equation 4.3,

$$K \propto \frac{(h\nu - E_g)^n}{h\nu} \qquad \text{(Equation 4.3)}$$

in which n is related to the type of optical transition, it is possible to determine E_g by plotting $(F(R_\infty)\cdot h\nu)^{1/n}$ as a function of hν and extrapolating the value from a linear regression of the straight part at $F(R_\infty) = 0$. In our case, the n value is defined to be ½, which is the value for a direct allowed transition, since it is well known that ZnO is a direct band gap semiconductor. The specific allowed or forbidden transition is experimentally determined from the best linear fit.

4.2.8. Photocatalytic performance of PMMA/ZnO-Au composite mats

The photocatalytic performance of the developed materials was evaluated by immersing 10 mg of the mats in quartz cuvettes filled with 3 mL of MB or BPA aqueous solutions (0.0125 mM and 0.044 mM respectively). To evaluate the adsorption of the organic molecules on the developed mats, experiments in dark conditions were performed overnight. For the photocatalytic experiments, the solutions containing the samples were placed at a distance of 10 cm under a UVA lamp emitting at a wavelength range from 315 nm to 400 nm (937 μW/cm^2 at 365 nm, 10 cm from source) connected to a climatic chamber (ICH 110 L, Memmert). The UVA irradiance (μW/cm^2) of the UV light source was measured by using a combined photo-radiometric probe (LP 471 P-A, Delta Ohm) at the fixed experimental distances between the source and the samples. Before starting the UV irradiation, the mats were maintained in the dark for 60 min. The decrease of the organic molecule concentrations was monitored by recording the UV-vis absorption spectra at specific time intervals. The test was also performed for a reference sample, namely a quartz cuvette filled with the MB or BPA solution, in order to estimate the self-degradation of the pollutants under the UV light irradiation.

The photocatalytic degradation efficiency (DE%) was obtained from the Equation 4.4, while the first order rate constant (k) was calculated by fitting the experimental data with the pseudo-first order model expressed in Equation 4.5

$$DE\% = \left(1 - \frac{C}{C_0}\right) \cdot 100 \qquad \text{Equation 4.4}$$

$$\ln\left(\frac{C_0}{C}\right) = kt \qquad \text{Equation 4.5}$$

in which C0 is the initial concentration of the pollutant and C is the concentration after a specific irradiation time (t). The organic molecule concentrations were determined by using two calibration curves with linear regression (R2 values of 0.9983 and 0.9998 for MB and BPA, respectively). For the MB, the calibration curve was obtained by monitoring the absorbance of the MB at the wavelength of maximum absorbance (λmax = 664 nm) with concentrations ranging from 0.00087 to 0.0125 mM. For the BPA calibration curve, the aqueous solution concentrations ranged from 0.0031 to 0.05 mM, and the absorbance variation was monitored at 276 nm.

Before and after the photocatalytic degradation of the organic molecules, the Total Organic Carbon (TOC) of the solutions was analyzed by a membraPure uniTOC lab analyzer. The total amount of organic bound carbon in the aqueous samples is measured by mean of a UV/reagent-promoted oxidation into carbon dioxide (CO_2) which is then quantified by a non-dispersive infrared detector. After the photocatalytic degradation experiment, the MB and BPA aqueous solutions were collected from the quartz cuvettes and diluted with MilliQ water, in order to reach 15 mL in each case. To remove any possible solid residue, the aqueous solutions were centrifuged and then filtered using a polytetrafluoroethylene (PTFE) syringe filters (diameter 15 mm, pore size 0.20 μm, Sartorius). The reagent used is an acidic aqueous solution of sodium persulfate (10%$_{W/V}$) and phosphoric acid (3%$_{V/V}$). The inorganic carbon content is firstly removed and measured by the internal acidification step. The TOC value is used to evaluate the mineralization of the MB and of the BPA, and therefore, the efficiency of the photocatalytic degradation.

The stability of the composite mats was evaluated by repeating the photocatalytic experiments on the same samples over three cycles. The composite mats were washed before starting the subsequent cycle by dipping in clean water for 1 h under UV light irradiation (same conditions as previously described) in order to remove the possible adsorbed pollutants. In addition, to evaluate the loss of ZnO and Au NPs from the composite mats, the ICP-OES analysis (iCAP 6300, Thermo) was performed on the liquids after the photocatalytic degradation process. The samples (125 μL) were previously treated with 2.5 mL of aqua regia, and then they were diluted up to 25 mL with milliQ water and filtered through PTFE syringe filters (diameter 15 mm, pore size 0.45 μm, Sartorius).

4.3. Results and discussion

4.3.1. Morphology of the electrospun composite mats

4.3.1.1. Effect of zinc salt loading on the polymeric fiber formation

The electrospinning process ensures the preparation of mats with large specific surface area and high porosity, which is originated from the random entanglement of fibers with diameters in the range from tens of nanometers up to few micrometers. Despite the addition of high content of the metal oxide precursor salt in the PMMA solution, it has been possible to prepare PMMA/$Zn(CH_3CO_2)_2$ electrospun fibers with continuous defect-free polymeric fibers characterized by smooth surface. Compared to the PMMA fibers (Figure 4.1a,b), the PMMA/$Zn(CH_3CO_2)_2$ fibers exhibit a higher mean diameter with a broader size distribution, while their morphology remains rather similar, in accordance with a previous work[122] (Figure 4.1b,c). In particular, even if the electrospinning operating parameters are preserved, the mean diameter of the polymeric fibers increases from 1.5 ± 0.3 to 6.2 ± 3.7 μm (for PMMA and PMMA/$Zn(CH_3CO_2)_2$ respectively). The increase in the average diameter is caused by the higher viscosity of the solution (from

1.57 ± 0.05 Pa·s to 4.10 ± 0.15 Pa·s, for PMMA and PMMA/$Zn(CH_3CO_2)_2$ solutions respectively) due to the presence of the precursor salt[122].

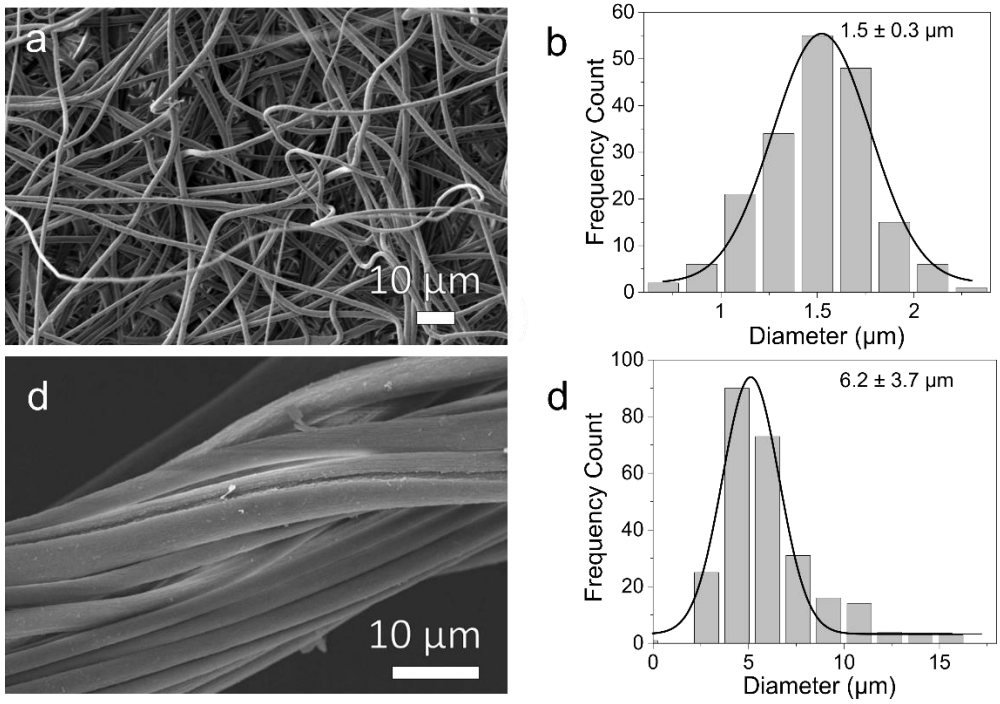

Figure 4.1. SEM images and size distribution analysis of the diameter of the fibers of the (a,b) PMMA and (c,d) PMMA/$Zn(CH_3CO_2)_2$ fibrous mats.

4.3.1.2. Effect of zinc salt thermal decomposition on the formation of ZnO NPs

After the thermal treatment of the PMMA/$Zn(CH_3CO_2)_2$ fibrous mats, ZnO NPs are directly formed in the polymeric matrix upon the appropriate thermal treatment. The *in-situ* formed ZnO NPs appear well distributed on the surface of the fibers but also in their bulk, as shown in Figure 4.2a. The thermal treatment is therefore effective for the synthesis of the active nanomaterials inside the porous polymeric matrix, without affecting the fibers morphology. The content of ZnO NPs obtained after the zinc salt conversion is about 11.7 ± 0.9%$_{w/w}$ with respect to the composite, as calculated by the ICP-OES analysis. Furthermore, the thermal treatment does not affect the overall size distribution of the polymeric fibers, which remains unchanged (Figure 4.2b).

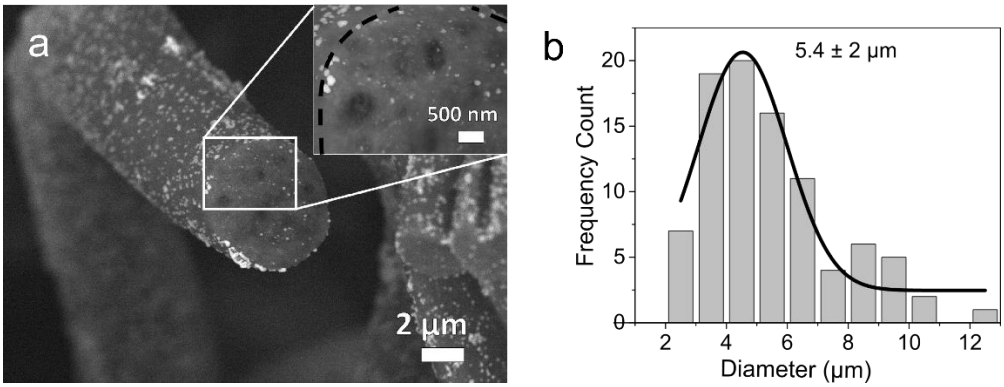

Figure 4.2. (a) HRSEM image of PMMA/ZnO with the cross-section detail. (b) Diameter size distribution of the PMMA/ZnO composite mat.

The thermally induced solid state reaction leads to the formation of two different sets of ZnO NPs depending on the growth area. As shown in Figure 4.3a, the ZnO NPs that grow mainly on the surface of the polymeric fibers (in accordance with the Figure 4.2a) exhibit a spherical branched structure with an average diameter of 135 ± 38 nm. The selected area electron diffraction (SAED) pattern, shown as inset in the Figure 4.3a, confirms the attribution of the NPs to ZnO of hexagonal wurtzite phase. The second type of particles formed during the thermal decomposition of the loaded precursor are shown in Figure 4.3b. These smaller and irregular ZnO NPs, with average diameters ranging from 12 nm to 50 nm, are mainly formed in the internal part of the polymeric matrix, which restrains their growth[122].

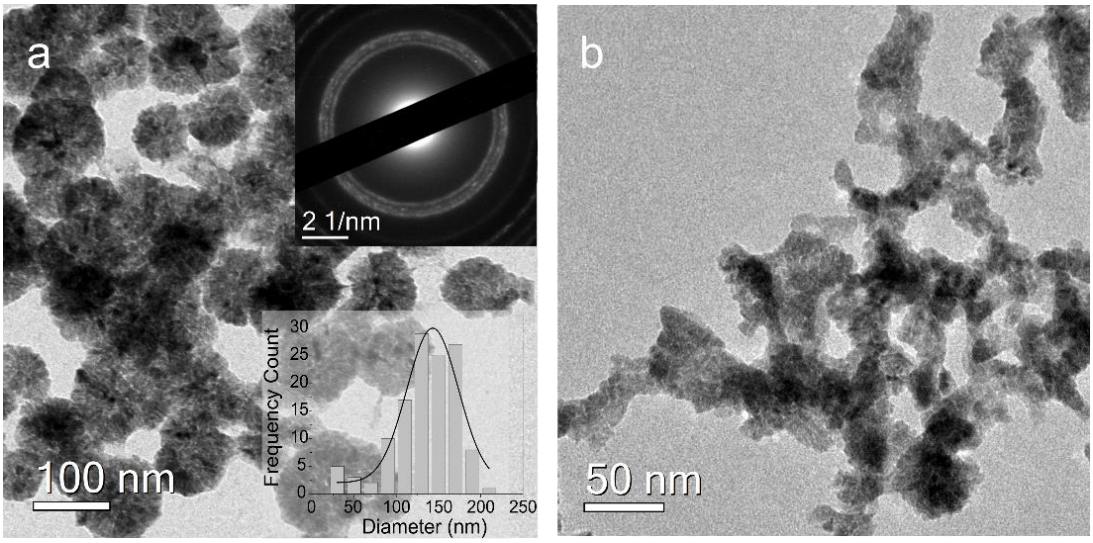

Figure 4.3 TEM images of the ZnO NPs grown (a) on the surface and (b) in the bulk of the fibers. The two insets of the first image show the SAED pattern and the diameter size distribution of the NPs.

4.3.2. Strategies to improve photocatalytic activity of the fixed ZnO NPs

The enhancement of the photoreactivity of ZnO is investigated by combining the semiconductor NPs with noble metals, in order to induce the formation of Schottky junctions or to promote the absorption of visible light by means of the localized surface plasmon resonances (LSPRs) typical of noble metal NPs. Different strategies to combine the ZnO NPs with two noble metals (gold and silver) have been explored. The preliminary results obtained using Ag NPs to form heterostructures with ZnO NPs are discussed in Appendix 1, while in this chapter the discussion is focused on the use of Au NPs to modify the *in-situ* formed ZnO, since this system was proved to be the most promising.

The two synthetic strategies to obtain the ZnO/Au NPs hybrid structures on the polymeric fibers are described in Figure 4.4. The PMMA/ZnO-Au_In composite fibrous mats are prepared by a simultaneously *in-situ* synthesis of both ZnO and Au NPs, induced by the thermal decomposition of the loaded precursors in the polymeric fibers. Conversely, the PMMA/ZnO-Au_Ex composite fibrous mats are formed in a two-steps process, with the *in-situ* formation of ZnO NPs in the PMMA electrospun fibers and the subsequent *ex-situ* formation of Au NPs, upon the reduction of the Au adsorbed ions on the surface of the formed ZnO after a dip-coating process. In the latter case, the PMMA/ZnO composite mats are dipped in the gold precursor aqueous solutions of different initial concentrations. The neutralization of the acidic gold precursor solution, performed to avoid the solubilization of the amphoter ZnO NPs, determines the presence of $[AuCl_2(OH)_2]^-$ species which are favorably adsorbed on the positively charged surface of the ZnO NPs. The successive thermal treatment leads to the formation of Au NPs mainly on the surface of the ZnO NPs.

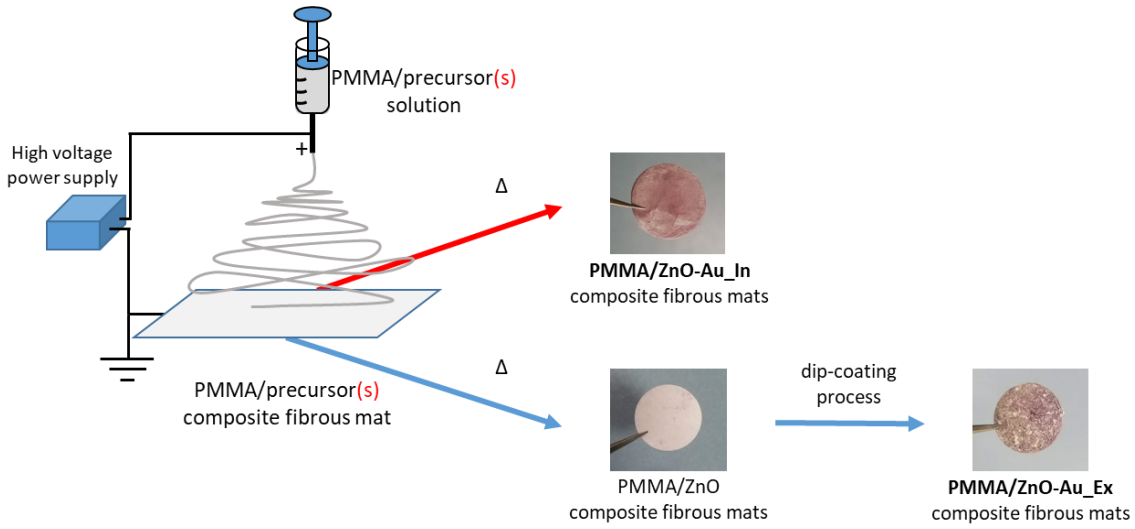

Figure 4.4. Scheme of the synthetic strategies to form ZnO/Au NPs hybrid structures on the PMMA/ZnO composite mats.

4.3.2.1. Comparison of morphology and Au NPs distribution for in-situ and ex-situ modification of polymeric composite mats

Figure 4.5 shows the PMMA/ZnO-Au composite mats prepared following the *in-situ* and the *ex-situ* strategy. Both samples, PMMA/ZnO-Au_In and PMMA/ZnO-Au_Ex, show similar morphology, in which the average diameter of the continuous fibers is unaffected by the formation processes followed. On the surface of the polymeric fibers, which is homogeneously decorated by spherical branched ZnO NPs, it is possible to observe also the presence of smaller Au NPs for both cases. As can be seen in the insets of Figure 4.5, in the PMMA/ZnO-Au_In, where the Au NPs are formed simultaneously with the ZnO NPs, the Au appears distributed also on the surface of the polymeric fibers, in contrast to the Au NPs formed after the ZnO NPs growth (PMMA/ZnO-Au_Ex) which appear mainly on the surface of the metal oxide as a consequence of the favorable adsorption process.

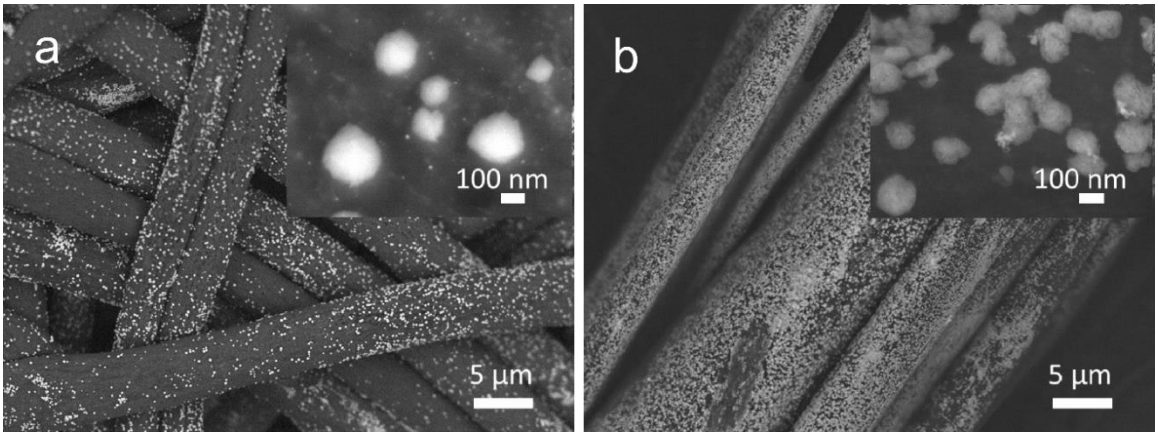

Figure 4.5. HRSEM images of the (a) PMMA/ZnO-Au_In and (b) PMMA/ZnO-Au_Ex composite fibrous mats prepared with a final Au content of around 1% wt. with respect to the composite.

Details of the formed ZnO-Au heterostructures for both cases, are reported in Figure 4.6 which compares the TEM images of the in-situ formed ZnO NPs with the ZnO NPs modified with the noble metal, collected after the removal of the polymeric matrix (details of the experimental procedure in section 4.2.5). The *in-situ* and the *ex-situ* Au NPs modification does not considerably affect the morphology and the size of the ZnO NPs, with the exception of the noticeable superficial decoration with Au NPs for the ZnO-Au_Ex heterostructures (Figure 4.6 c).

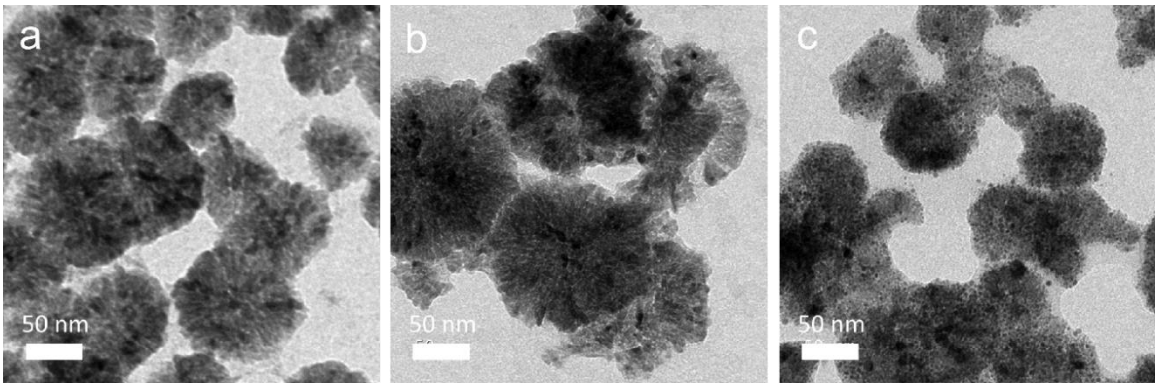

Figure 4.6. TEM images of the (a) ZnO NPs formed by thermal decomposition of the loaded zinc salt in the polymeric fibers and of the ZnO-Au heterostructures formed by (b) the in-situ and (c) ex-situ synthetic strategies in which the content of Au NPs is around 1 %wt. with respect to the composite.

The distribution of the Au NPs is further investigated by acquiring the TEM images in dark field mode (Figure 4.7), which ensures a better contrast between Au and ZnO NPs. In fact, the images are formed by the electrons that have been scattered by the

specimens, therefore areas with Au NPs appear brighter than those with ZnO NPs, due to the more intense scattering of the electrons caused by the heavier atoms that constitute the particles. Compared to the ZnO (Figure 4.7a), the addition of Au NPs is highlighted by the presence of brighter spots in the Figure 4.7b,c. When the ZnO-Au heterostructure is formed with the in-situ strategy, beside the formation of Au NPs on the polymeric fiber surface and on the exposed ZnO NPs (Figure 4.5a and Figure 4.6b), it is possible to observe also the formation of core-shell NPs, consisting in a thick shell of ZnO grown on a core of Au NP (Figure 4.7b).

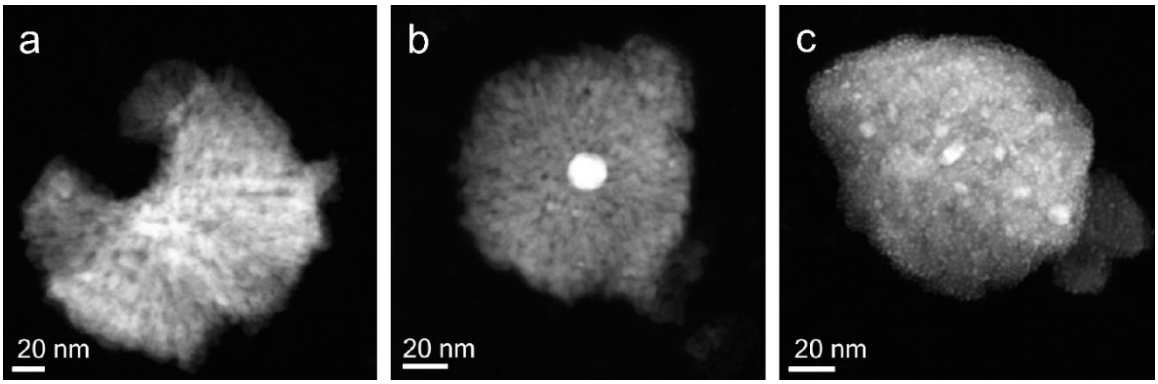

Figure 4.7. Dark field TEM images of (a) ZnO NPs and of (b) ZnO-Au_In and (c) ZnO-Au_Ex heterostructures formed on the PMMA fibers.

The formed Au NPs by in-situ synthesis show an average diameter of 18.46 ± 5.54 nm, while the ex-situ synthesis ensures the formation of Au NPs with average diameter of c.a. 8 ± 3nm. The distribution of the Au NPs is further confirmed by acquiring the EDS maps of the ZnO-Au_In and of the ZnO-Au_Ex (Figure 4. 8). The EDS mapping shows the spatial distribution of the elements in the samples, in which it is possible to distinguish Au as the core in the ZnO-Au_In hybrid structure, while Au is distributed on the ZnO surface in the ZnO-Au_Ex.

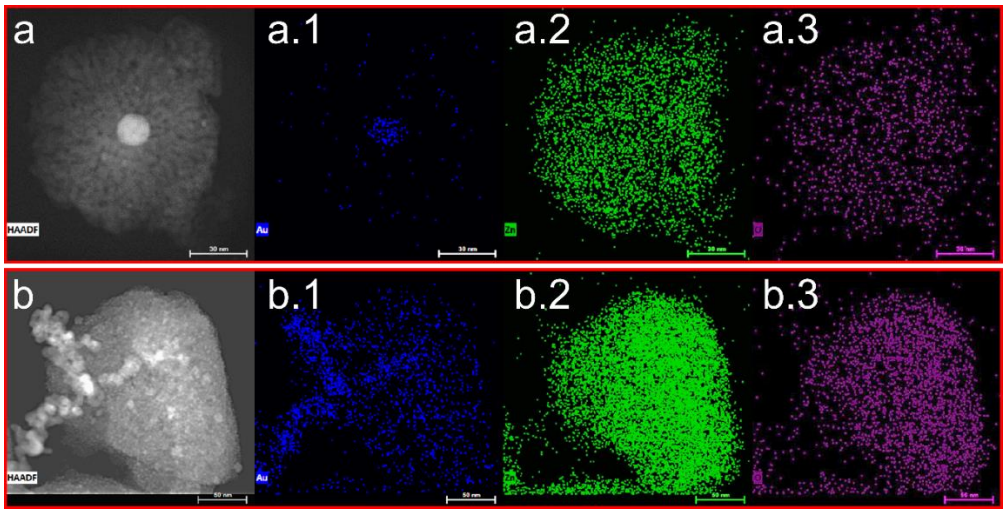

Figure 4.8. Dark field TEM images of (a) ZnO-Au_In (scale bar 30 nm) and (b) ZnO-Au_Ex (scale bar 50 nm) heterostructures and EDS maps of (1) Au, (2) Zn and (3) O.

The formation of a core-shell structure is probably induced by the presence of Au NPs in the PMMA/precursors solution during the fabrication of the fibers, which behave as nucleation centers for the overgrowth of thick ZnO shells. In fact, the formation of Au NPs has been reported in presence of the solvent used for the electrospinning process (DMF), which can also act as a reducing agent[219]. As can be seen in Figure 4.7c, the gold ions adsorption on the exposed preformed ZnO NPs during the *ex-situ* synthetic strategy, results in the growth of tiny Au NPs which appear well distributed on the surface of the photocatalyst.

4.3.2.2. Comparison of the photocatalytic performance of the PMMA/ZnO-Au composite mats prepared trough *in-situ* and *ex-situ* synthetic strategies

In order to evaluate the effect of the two proposed synthetic strategies for the modification of the ZnO NPs, a preliminary photocatalytic degradation experiment under UV light irradiation was performed by using the MB dye. As shown in Figure 4.9a, there is a negligible adsorption of the organic pollutant on the fibrous composites, evaluated after dipping the composite mats in the dye solutions under dark conditions.

The photocatalytic performance of the PMMA/ZnO mat is compared to those observed for the two composite mats with the different types of ZnO-Au heterostructures (Figure

4.9b). Although the Au content is around 1%wt. with respect to the composite for both the PMMA/ZnO_Au mats, it is possible to observe different photocatalytic performance under the same experimental conditions; while the dye self-degradation under UV light is negligible.

The PMMA/ZnO-Au_Ex shows in fact the higher photocatalytic efficiency for the removal of MB, while the photocatalytic efficiency of the PMMA/ZnO-Au_In appears to be lower compared to those of the PMMA/ZnO-Au_Ex and PMMA/ZnO. This decrease in the degradation efficiency can be attributed to the type of Au-ZnO heterostructures formed during the *in-situ* formation of Au NPs simultaneously with the growth of ZnO NPs, which leads to a lower active interface between the exposed ZnO and the Au NPs.

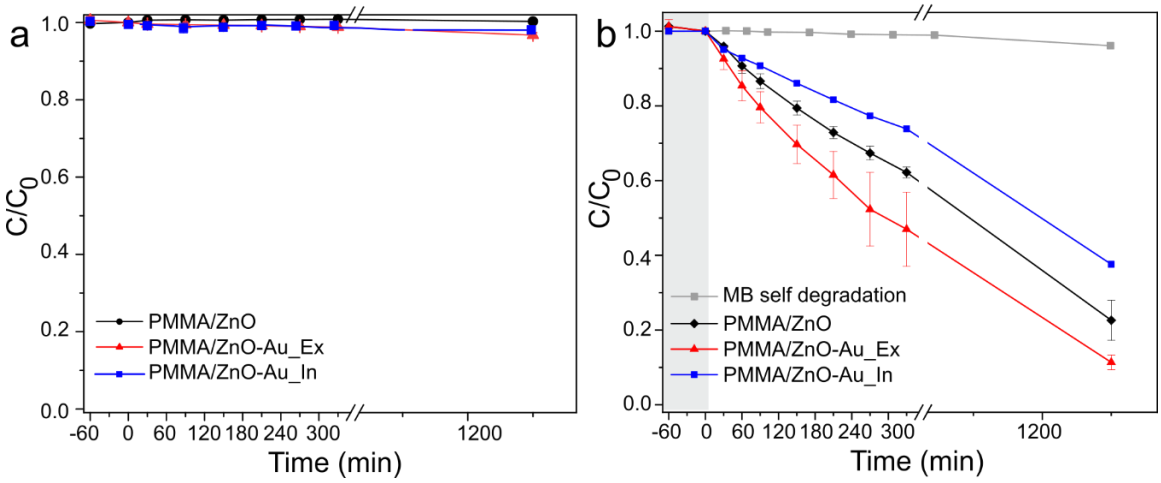

Figure 4.9. (a) Evolution of the normalized concentration of MB solutions in presence of the composite mats with Au 1%wt. with respect to the composite in dark. (b) Photocatalytic degradation curves of MB in presence of the composite mats under UV light. Before the UV irradiation, the solutions were kept in dark for 60 min in the presence of the composite mats.

Since the poor control over the growth of ZnO-Au heterostructures with the *in-situ* approach leads to low metal-semiconductor interfaces, the following sections will be focused on the development of different Au NPs coverage on the PMMA/ZnO mats by *ex-situ* modification. The research for the optimal content of Au NPs will be performed in order to enhance the photocatalytic performance of the fixed ZnO.

4.3.3. Investigation of different Au NPs content in the *ex-situ* modification of the PMMA/ZnO composite mats

4.3.3.1. Morphology and structural characterization

To further explore the photocatalytic activity of the PMMA/ZnO-Au_Ex composite mats, the PMMA/ZnO mats are dipped in three gold precursor solutions with different initial concentrations (photos of the prepared PMMA/ZnO_Au_Ex are displayed in Figure 4.10, compared to PMMA/ZnO).

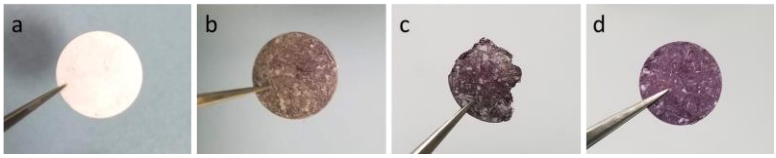

Figure 4. 10. Photos of the (a) PMMA/ZnO as prepared after thermally induced solid state reaction and of the PMMA/ZnO-Au_Ex prepared by dip-coating and subsequent thermal treatment of the composite mats, forming (b) PMMA/ZnO-Au1, (c) PMMA/ZnO-Au3 and (d) PMMA/ZnO-Au6.

Figure 4.11 shows the morphology of the three different PMMA/ZnO-Au_Ex nanocomposite mats. In all cases, the formed Au NPs are well distributed on the surface of the composite mats. As already observed, Au NPs appear mainly attached on the surface of the ZnO NPs, also in the cases of the composite mats prepared with the highest gold content, as confirmed by the surface details in the corresponding insets of the Figure 4.11. It is possible to observe a difference in the gold coverage of the mats. Higher initial concentration of gold species leads to an increase of the coverage of the composite fibers by Au NPs which, for the highest concentration (PMMA/ZnO-Au6), tend to form nanowires and aggregates on the surface of the composite mats, as can be seen in Figure 4.12. The amount of Au NPs formed on the composite mats is approximately 1%, 3% and 6% wt. of Au with respect to the composite, for the PMMA/ZnO-Au1, PMMA/ZnO-Au3, and PMMA/ZnO-Au6 respectively, as defined from the ICP-OES analysis.

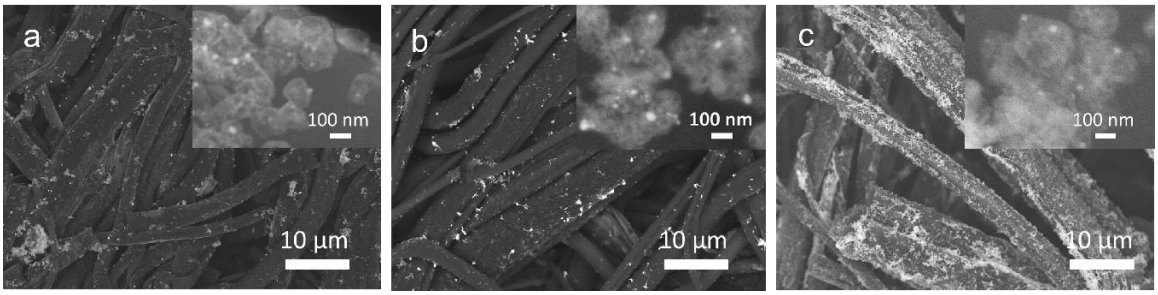

Figure 4. 11. HRSEM images of the (a) PMMA/ZnO-Au1, (b) PMMA/ZnO-Au3 and (c) PMMA/ZnO-Au6 composite mats. Insets report the surface detail for the PMMA/ZnO with the different content of Au NPs.

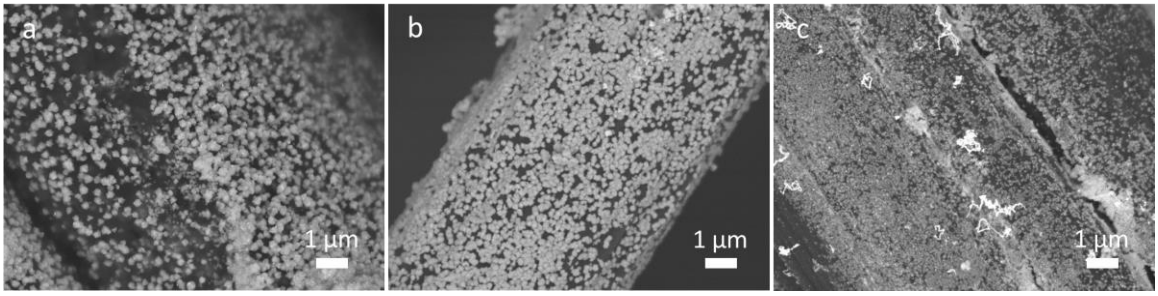

Figure 4. 12. HRSEM images of the (a) PMMA/ZnO-Au1, (b) PMMA/ZnO-Au3 and (c) PMMA/ZnO-Au6 composite mats with details of Au nanowires for higher Au content.

In all the composite mats, the formed Au NPs have an average diameter of c.a. 8 ± 3 nm, thirteen times smaller than the ZnO branched NPs, proving that the size of Au NPs is not significantly affected by the initial concentration of the gold precursor solution. The lower mean diameter of the Au NPs compared to the ZnO allows a high superficial contact between the two types of NPs and, therefore, an efficient charge separation.

The structure and the crystallite size of the ZnO NPs before and after the modification with Au NPs have been explored by XRD analysis (Figure 4.13). In all the composite mats, the ZnO NPs exhibit the characteristic diffraction peaks of the hexagonal wurtzite phase. In presence of Au NPs, a new diffraction peak appears at 38°, which is assigned to the (111) crystal plane of the cubic Au phase (dotted line in Figure 4.13). For the PMMA/ZnO-Au6 composite mat, it is also possible to observe an additional diffraction peak at 44° (highlighted with an arrow in Figure 4.13) related to the Au (002) lattice plane due to the higher amount of Au NPs on the surface compared to the other composite mats. The presence of Au does not cause shifts of the position of the ZnO

diffraction peaks, therefore the crystal structure of the ZnO NPs is not affected by the post-synthetic growth of the Au NPs. Furthermore, no extra phase or other peaks are observed, confirming the absence of crystalline impurities inside the samples. The average crystallite size of the ZnO NPs is approximated to 9 nm, as estimated by using the Debye-Scherrer equation (details in section 4.2.6).

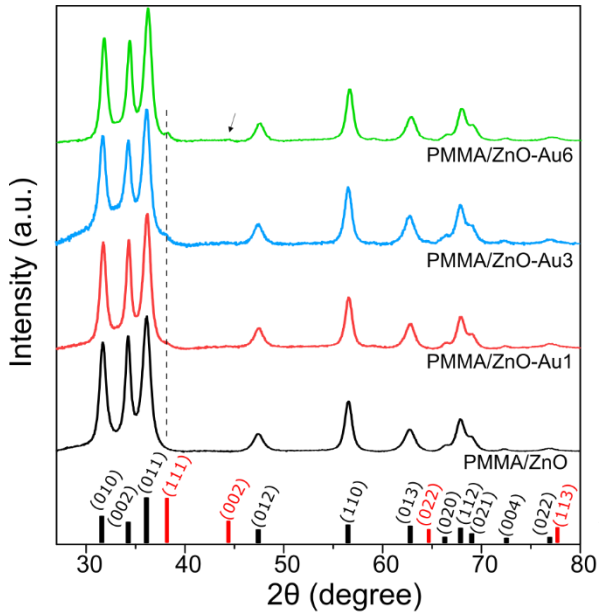

Figure 4.13. XRD patterns of the PMMA/ZnO composite mats before and after the modification with Au NPs by ex-situ approach. Stick reference pattern of ZnO (black) and of Au (red) are shown along x-axis.

4.3.3.2. Optical characterizations

The metal-semiconductor interface in the Au/ZnO NPs hybrid structure has been investigated through diffuse reflectance and Raman spectroscopy. The diffuse reflectance spectra of the different composite mats are shown in Figure 4.14a. In all cases, it is possible to observe the characteristic absorption of the ZnO NPs in the UV region originated by the direct band gap transitions[208]. The presence of the Au NPs leads to the addition of another absorption band with a maximum at 550 nm, attributed to the surface plasmon resonance of the Au NPs. The E_g of the ZnO is estimated by applying the Kubelka-Munk (KM) method to the data obtained by the reflectance spectra, as shown in Figure 4.14b (details of the KM equation in section 4.2.7). The calculated E_g values demonstrate that the

presence of the Au NPs does not cause any modification to the E_g of the ZnO present in the composite mats. In particular, the E_g is 3.25 ± 0.01 eV for the PMMA/ZnO, and 3.23 ± 0.02 eV, 3.23 ± 0.04 eV and 3.25 ± 0.01 eV for the PMMA/ZnO-Au1, PMMA/ZnO-Au3 and PMMA/ZnO-Au6 respectively.

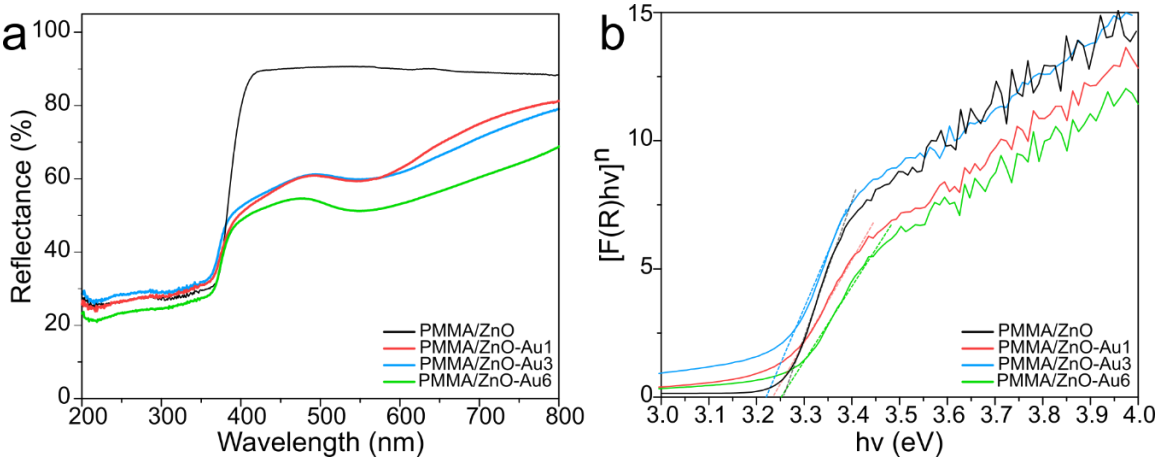

Figure 4.14.(a) Diffusive reflectance spectra and (b) Kubelka-Munk plots of the composite mats with different Au NPs contents. The Eg value is extrapolated from a linear regression of the KM plot.

The formation of the Au/ZnO NP heterostructures is confirmed by the Raman spectroscopy. Typically, the optical phonon modes predicted by the group theory for the hexagonal wurtzite ZnO structures are the polar Raman and infrared active modes A_1, E_1, the non-polar Raman active $2E_2$, and the silent $2B_1$ modes. The A_1 and E_1 modes are split in the transverse optical (TO) and longitudinal optical (LO) modes with different frequencies due to the manifestation of the macroscopic electric field of the LO phonons. The two E_2 are splitted in the high and low frequency modes (E_2^{high} and E_2^{low}) which are associated with the oxygen atoms and the zinc sublattice, respectively[220,221]. In the Raman spectrum of the PMMA/ZnO composite mat (Figure 4.15), all the peaks observed are attributed to the PMMA[222], whose assignments are listed in Table 4.1, while the Raman active modes of the wurtzite ZnO are not evident possibly due to the presence of the polymer matrix and to the used experimental conditions[223].

Table 4.1. Assignment of the Raman modes of the PMMA[222].

Raman shift (cm^{-1})	Assignment
482	C-C skeletal deformation of CC_4
559	O-C=O deformation
603	O-C=O deformation
735	O-C=O deformation coupled with CH_2 rocking
812	symmetric CC_4 stretching
838	C=O deformation coupled with CH_2 rocking
968	main chain C-C stretching
987	main chain C-C stretching
1059	CH_2 wagging
1122	C-O stretching coupled with CH_2 rocking
1158	C-O stretching coupled with CH_2 rocking
1185	C-C degenerate stretching of CC_4
1240	C-C degenerate stretching of CC_4
1391	CH_3 symmetric bending
1451	CH_2 deformation
1484	CH_3 asymmetric bending

It is possible to observe the characteristic modes of the ZnO only after the plasmonic enhancement provided by the contact with the Au NPs in the ZnO/Au hybrid systems. In fact, in the Raman spectrum of PMMA/ZnO-Au_Ex (Figure 4.15), additional peaks appear at 450 cm^{-1} and 560 cm^{-1}, which are respectively assigned to the E_2^{high} and A_1(LO) modes of the ZnO, proving the non-resonant surface enhanced Raman scattering of the ZnO optical modes in the proximity of Au NPs[220,224,225].

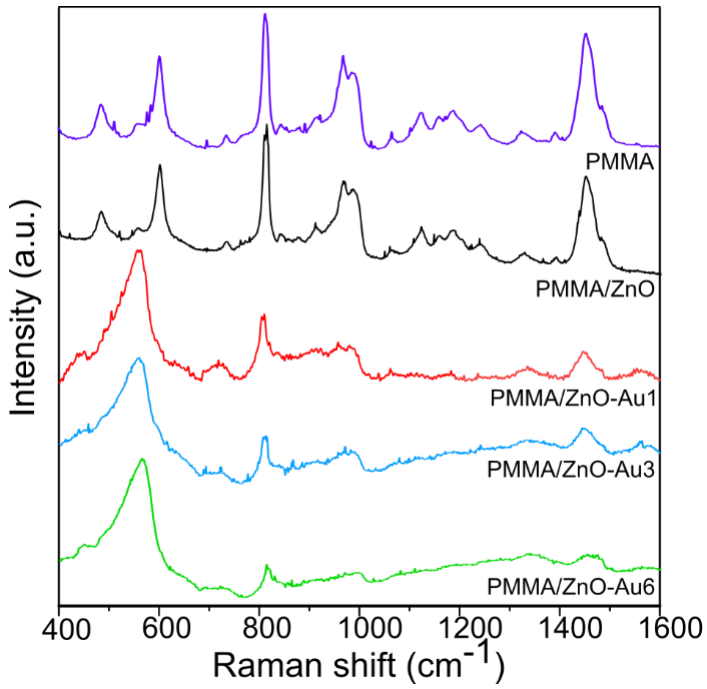

Figure 4. 15. Raman spectra of the polymeric fibers and of the PMMA/ZnO before and after the superficial modification with Au NPs by ex-situ synthetic approach.

4.3.4. Photocatalytic performance

The effect of different amounts of Au NPs on the photocatalytic degradation performance of the composite mats is then investigated using MB and BPA aqueous solutions. The MB is a cationic dye which can be found in wastewater deriving mainly from textile, paper and plastic industries. It is commonly adopted as a model pollutant for testing the photocatalytic performance of various materials under UV light irradiation. The BPA is a recalcitrant aqueous pollutant, classified as endocrine disruptor, which is widely present in water due to its broad application in plastic industry[25].

In order to evaluate the adsorption of the organic pollutants on the fibrous composites, the mats were dipped in the organic pollutant solutions in dark conditions. As shown in Figure 4.16, there is a negligible MB adsorption on the fibers. The concentration of BPA slightly decreases over time in the presence of the PMMA/ZnO and of the PMMA/ZnO-Au with 1% and 3% of Au contents. On the contrary, the PMMA/ZnO-Au6 shows a higher adsorption capacity compared to the other composites, adsorbing c.a.

39% of the initial BPA, due to the instauration of dispersive bonding interactions between the aromatic rings of the BPA and the gold surface, which is in a relatively high amount on the composite fibers[226,227].

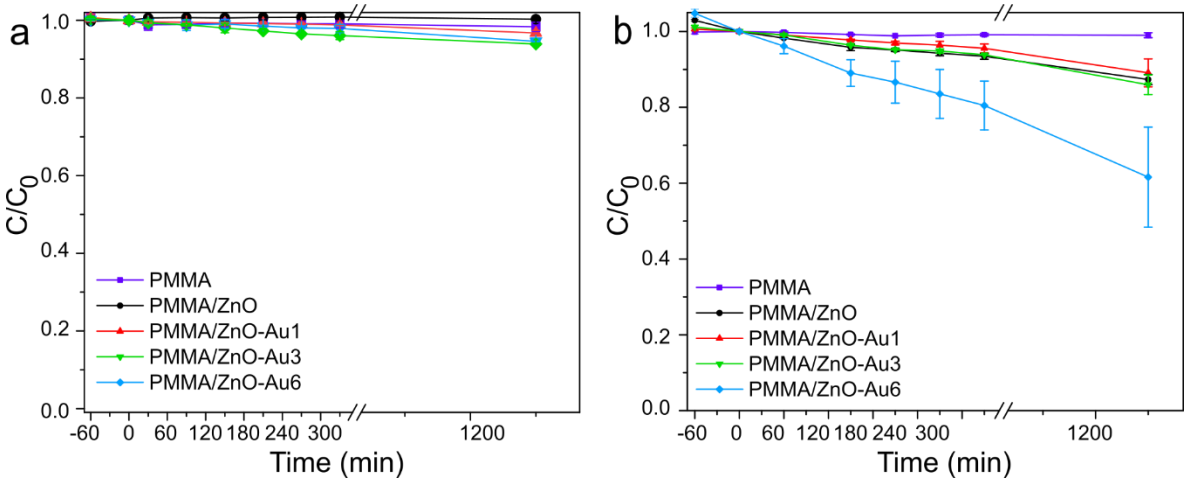

Figure 4.16.Evolution of the normalized concentration of (a) MB and (b) BPA solutions in presence of the developed composite mats in dark.

Under UV irradiation, the concentration of both organic pollutants decreases in time only in the presence of the nanocomposite fibrous mats. In fact, their self-degradation is negligible, while for the pure PMMA fibrous mat there is not significant change in the concentration of the pollutants, confirming the absence of photocatalytic activity. When the composite mats are dipped in the solutions, it is possible to observe a more efficient photocatalytic degradation of the organic pollutants in the presence of the Au/ZnO hybrid structures. Furthermore, the photocatalytic degradation curves of the pollutants follow a pseudo-first order kinetic for all the developed materials.

In particular, as shown in Figure 4.17a, the PMMA/ZnO mat is able to decolorize 77% of the initial MB solution while in the presence of the PMMA/ZnO-Au1, the efficiency reaches 88% after 20 hours of irradiation. By increasing the content of Au, the MB photocatalytic degradation tends to slightly decrease reaching 80% for the PMMA/ZnO-Au3, while for the PMMA/ZnO-Au6, it is lower compared to the one observed for the PMMA/ZnO. The enhanced performance of the PMMA/ZnO-Au1 composite is also reflected on the degradation rate constant (k_1) extrapolated for the first 5 hours of irradiation (Figure 4.17b). In fact, the photocatalytic degradation of MB with the

PMMA/ZnO-Au1 reaches the maximum value of k_1 $2.33 \cdot 10^{-3}$ min^{-1}, significantly higher than the one obtained using the PMMA/ZnO, $1.44 \cdot 10^{-3}$ min^{-1}, and the other composite mats, as shown in Table 4.2.

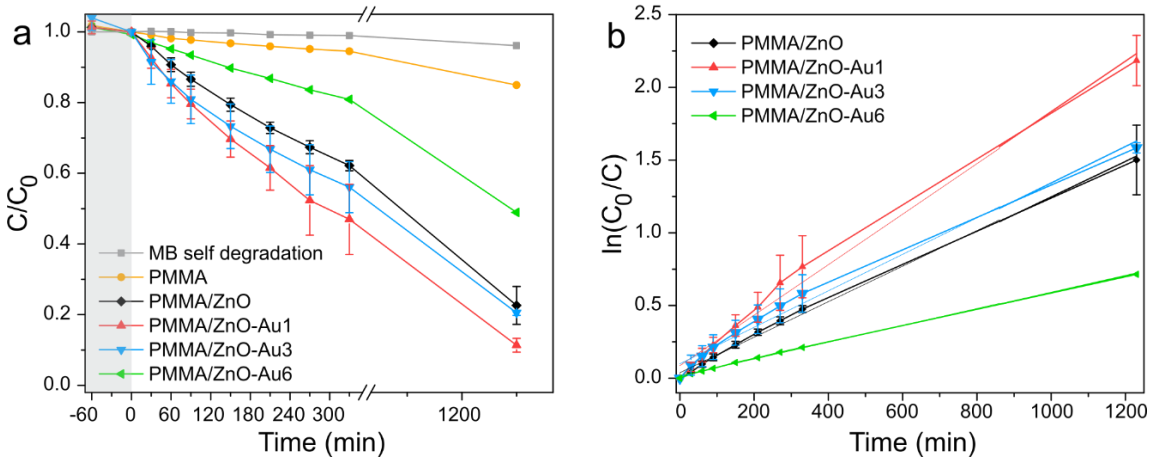

Figure 4.17. (a) Photocatalytic degradation curves of MB in presence of the composite mats under UV light. Before the UV irradiation, the solutions were kept in dark for 60 min in the presence of the composite mats. The self-degradation of MB under UV is also presented. (b) Pseudo-first-order reaction kinetics for MB applied on the experimental data obtained in the first 5 hours of reaction.

A similar behavior is also observed for the photocatalytic degradation of BPA. As shown in Figure 4.18a, the PMMA/ZnO-Au1 induces a decrease of around 63.5% of the initial BPA concentration after 20 h of UV irradiation, remarkably higher compared to the BPA reduction achieved with the PMMA/ZnO mat (DE% of 34%). For higher amounts of Au NPs, the photocatalytic degradation efficiency is around 61% and 41%, for the PMMA/ZnO-Au3 and PMMA/ZnO-Au6 respectively. The k_1 values calculated by applying the first order kinetics model on the experimental data are in accordance with the photodegradation efficiency results. The PMMA/ZnO-Au1 displays the faster reaction rate ($1.12 \cdot 10^{-3}$ min^{-1}) compared to the PMMA/ZnO-Au3 and PMMA/ZnO-Au6 ($0.96 \cdot 10^{-3}$ and $0.82 \cdot 10^{-3}$ min^{-1} respectively) and to the PMMA/ZnO (k_1 $0.69 \cdot 10^{-3}$ min^{-1}). The k_1 values and the respective R^2 values calculated by applying the pseudo-first order model for both MB and BPA are listed in Table 4.2.

Table 4.2. Photo-degradation rate constants and linear regression coefficients obtained from the linear fitting of the experimental data by using the pseudo-first order model.

	MB		BPA	
Samples	**10^{-3} k_1 (min^{-1})**	**R^2**	**10^{-3} k_1 (min^{-1})**	**R^2**
PMMA/ZnO	1.44	0.9979	0.69	0.9820
PMMA/ZnO-Au1	2.33	0.9982	1.12	0.9895
PMMA/ZnO-Au3	1.71	0.9887	0.96	0.9923
PMMA/ZnO-Au6	0.63	0.9958	0.82	0.9478

Despite the results obtained for the MB, the PMMA/ZnO-Au6 composite mat displays a more effective reduction of the initial BPA concentration compared to the one of the PMMA/ZnO mat. However, this is not attributed to the photocatalytic degradation but to the high adsorption of the BPA on the surface of the Au NPs, as demonstrated with the adsorption experiment (Figure 4.16b).

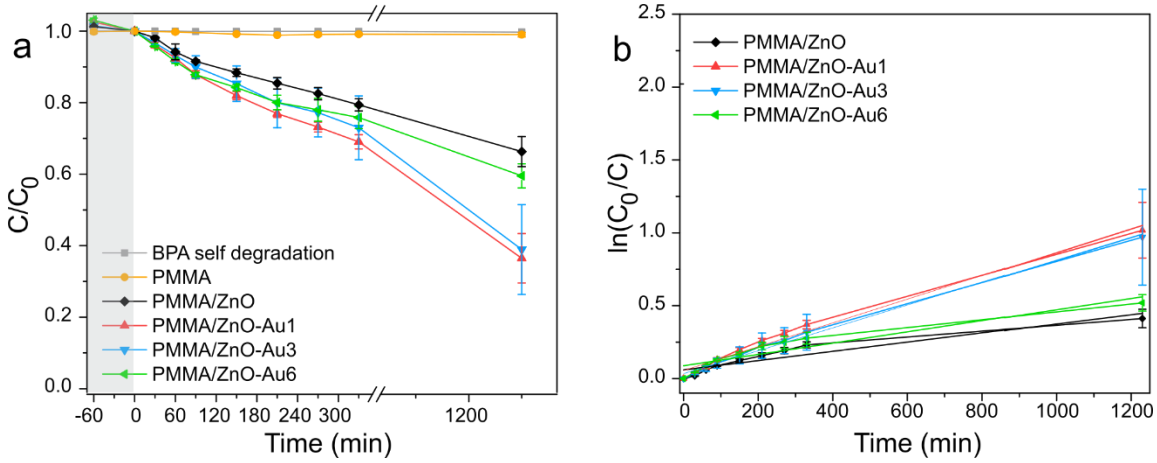

Figure 4. 18. (a) Photocatalytic degradation curves of BPA in presence of the composite mats under UV light. Before the UV irradiation, the solutions were kept in dark for 60 min in the presence of the composite mats. The self-degradation of BPA under UV is also presented. (b) Pseudo-first-order reaction kinetics for BPA applied on the experimental data obtained in the first 5 hours of reaction.

For both the pollutants studied, the enhanced photocatalytic activity using the PMMA/ZnO-Au1 hybrid structures indicates that the specific ZnO-Au combination is favorable for the formation of the Schottky barrier at the metal-semiconductor interface, which enhances the charge carrier separation and therefore the ROS formation[203,228]. In fact, as observed in the SEM analysis, when the content of Au is low, the NPs are better distributed on the fibers without forming large aggregates, as in the case of higher amount

of Au (PMMA/ZnO-Au6). The presence of Au aggregates on the ZnO NPs catalyst causes a decrease of their active surface exposed towards the organic pollutants and also a less effective light penetration due to a screening effect[204,210,229]. This result is also confirmed by previous studies; as a matter of fact, there is an optimal concentration of metallic NPs for the surface modification of the metal oxide semiconductors, beyond which the photocatalytic performance declines[228,230].

In order to evaluate the conversion of the organic pollutants into CO_2 and, therefore, the efficiency of the developed materials to mineralize the organic pollutants upon photocatalytic degradation, the mineralization of MB and BPA has been investigated by TOC studies of the solutions before and after the irradiation experiments. Based on the obtained results (Table 4.3), it can be assured that 60% of MB is mineralized in the presence of the PMMA/ZnO-Au1 mat upon UV irradiation, higher compared to 45.5% obtained using the PMMA/ZnO.

Table 4.3. Degradation and mineralization values obtained from the photocatalytic degradation of the MB and BPA aqueous solution in presence of the mats after 20 h under UV light irradiation.

	MB		**BPA**	
Samples	%degradation	%mineralization	%degradation	%mineralization
PMMA/ZnO	77	45.5	34	-
PMMA/ZnO-Au1	88	60	63.5	15

In the case of BPA, the PMMA/ZnO-Au1 is able to mineralize 15% of the photodegraded molecules (63.5%), while no changes in the TOC have been detected after using PMMA/ZnO. The lower mineralization of BPA compared to the one obtained for the MB can be ascribed to the recalcitrant nature of this organic pollutant. The effective removal of the BPA molecules is greatly challenging due to their complex aromatic structure, which, together with their low biodegradability, makes BPA one of the principal pollutants detected in the effluents of the wastewater treatment plants[231].

4.3.4.1. Reusability and comparison of the electrospun composite mats with other ZnO-based composites

Since the PMMA/ZnO-Au1 mats show the best performance in terms of photocatalytic degradation of both MB and BPA organic pollutants, their stability is investigated by performing three consecutive irradiation cycles. The loss of Zn and Au from the composite mats is negligible after the first irradiation cycle, since about 0.022 ± 0.001%wt. of Zn with respect to the total Zn amount in the composites was detected in the liquids, while it has not been possible to determine the content of Au due to the low concentration. The overall photocatalytic performance of the PMMA/ZnO-Au1 is maintained unvaried for two consecutive cycles in terms of degradation efficiency of the MB (Figure 4.19a), while, in the third cycle, the performance slightly decreases to 72.5%.

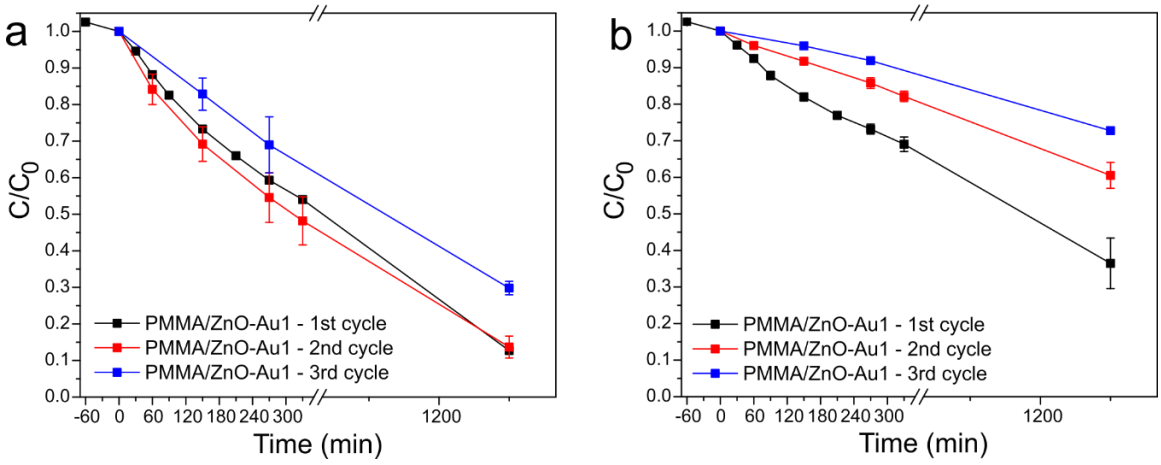

Figure 4.19. Photocatalytic degradation activity after three cycles using the same PMMA/ZnO-Au1 composite mats of (a) MB and (b) BPA under UV light.

This is also the case of the PMMA/ZnO sample (Figure 4.20) indicating the fact that this reduction in the performance can be possibly attributed to a low photo-corrosion effect of the ZnO[232]. In the case of BPA, the photocatalytic performance of the PMMA/ZnO-Au1 shows a more evident decrease after the second cycle compared to the one observed for the MB, lowering further in the third cycle (Figure 4.19b). Despite this reduction, the degradation efficiency of the third cycle is higher than the one reached for the PMMA/ZnO mat, in which only 10% of the BPA is photodegraded (Figure 4.20b). This

aspect confirms the improvement of the catalytic activity of the mat due to the presence of 1% of Au NPs also in the removal of a recalcitrant aqueous pollutant.

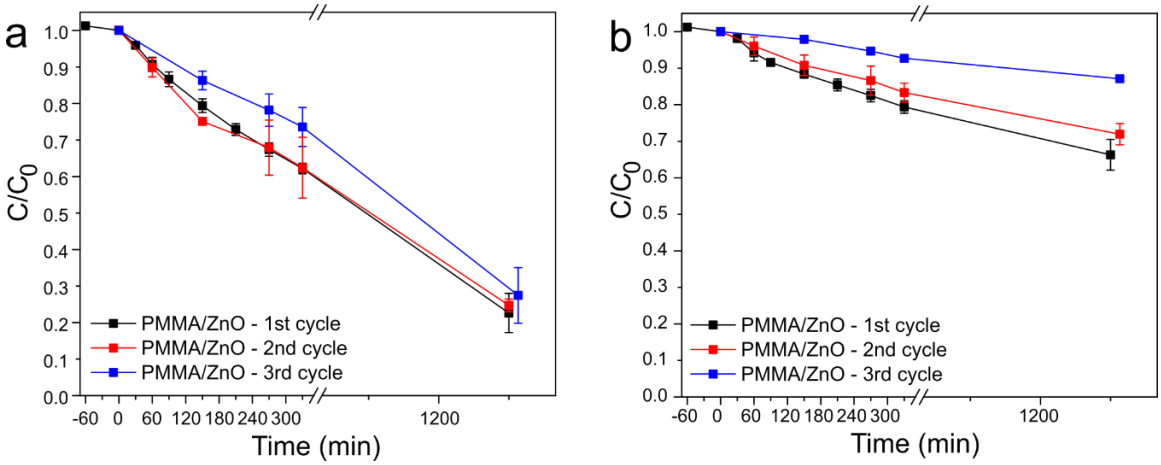

Figure 4. 20. Photocatalytic degradation activity after three cycles using the same PMMA/ZnO composite mats of (a) MB and (b) BPA under UV light irradiation.

The photocatalytic degradation performance under UV light irradiation of the PMMA/ZnO-Au1 is comparable to those obtained using other recently developed ZnO based polymeric fibrous composites. In particular, the presented PMMA/ZnO-Au1 is able to degrade 0.48 mg of MB per Au/ZnO gram and irradiation hour (0.48 mg/g·h), which is similar to the dye degradation achieved by the ZnO based nanostructured on polyethersulfone fibers developed by Ognibene *et al.*[114] (0.59 mg/g·h, calculated upon normalization with the mass of the photoactive material and the irradiation time). Although the photocatalytic degradation process is faster in the second case, possibly due to a higher content of exposed photoactive material and different irradiation conditions, the efficiency of this ZnO based composite decreases of about 10% if reused for a second cycle, contrary to what observed in the herein presented work[114]. Considering the BPA, the photocatalytic degradation obtained by the PMMA/ZnO-Au1 is 0.9 mg/g·h, which is comparable to the value (1.12 mg/g·h) observed for the Ce-doped ZnO supported on poly(styrene-co-maleic anhydride) nanofiber mats[233]. Most important, the degradation rate constant calculated in this work is remarkably higher than the one reported ($1.12 \cdot 10^{-3}$ min^{-1} and $2 \cdot 10^{-4}$ min^{-1} respectively), indicating a faster removal of the BPA[233].

4.1. Concluding remarks

The *in-situ* formation of ZnO NPs in a polymeric matrix allows the formation of spherical branched NPs in the bulk and exposed on the surface of randomly distributed polymeric fibers. The enhancement of the photocatalytic activity of the PMMA/ZnO composite mats is here investigated through the formation of nanostructures between the semiconductor and Au NPs by means of a straightforward fabrication approach. The hybrid Au/ZnO nanostructures are fixed on a polymeric support through a thermally induced solid-state synthesis directly on the surface of electrospun polymeric fibers, obtaining an easily handled porous material. Two modification strategies have been investigated, specifically through the simultaneous formation of Au NPs during the growth of ZnO NPs, or with the deposition of Au NPs on the in-situ formed ZnO NPs. The latter strategy ensures a higher Au-ZnO interfacial active surface. For these samples, in fact, the Au NPs appear homogeneously distributed on the surface of the ZnO NPs, allowing an effective metal-semiconductor interface, fundamental for the improvement of the photocatalytic performance of the ZnO semiconductor. In fact, the presence of the Au NPs on the PMMA/ZnO composite mats enhances the photocatalytic degradation of both the organic pollutants studied, MB and BPA. Although the BPA degradation is less effective than the one obtained for the MB, due to the intrinsic nature of the BPA molecules, the presence of Au induces the significant photodegradation performance compared to other studies. Therefore, the proposed use of PMMA/ZnO-Au composite mats can be considered as a valid approach for the improvement of the photocatalytic performance of supported catalysts for water remediation applications, without the need of post treatment steps for their removal from the treated water which may restrict their wide applicability as well as causing secondary pollution.

Chapter 5

CeO_2 based porous composite materials for heterogeneous photocatalysis

5.1. Introduction

Heterogeneous photocatalytic processes have been widely employed for the degradation of various aqueous pollutants[234–236], showing promising results as combined advanced treatments to enhance the effectiveness of conventional tertiary treatments in wastewater remediation process. One of the main advantages of these types of AOPs is the requirement of ambient conditions to occur, in terms of temperature and pressure. Recently, the development of materials for solar light-driven photocatalysis has gathered significant interest, due to the potential reduction of energy consumption and cost by using solar radiation as a clean and unlimited source of energy[212,237]. Since visible light, with wavelengths in the range from 400 to 700 nm, accounts for 43% of the solar radiation, while the incoming UV light represents only 5% of it, the harvesting of the solar spectrum can be improved through the development of materials with visible-light response.

Cerium oxide (CeO_2) is increasingly used as an alternative to more conventional TiO_2-based photocatalysts for the degradation of organic pollutants in water[78,238,239] and it is attracting growing interest as a photocatalyst for solar light applications[239]. Cerium is the most abundant rare earth element and its abundance on the Earth's crust is comparable with that of the more used zinc and copper[240]. Furthermore, the low price of CeO_2[239,241], together with its unique properties, such as the electronic and optical structures due to the presence of 4f electrons and the convenient physical and chemical

properties, such as the easy formation of oxygen defects and the reversible Ce^{4+}/Ce^{3+} conversion, make it interesting for photocatalytic applications[242]. The potential application of CeO_2-based materials in the field of wastewater treatments derives from the absence of toxicity, the chemical inertness and the strong oxidizing capability of the metal oxide[242].

The good photocatalytic performance of CeO_2 can be attributed to the favorable capacity to adsorb organic molecules on the surface and to the high electron transfer from the adsorbed molecule to oxygen species, thanks to the electron configuration of the metal oxide[239]. Depending on the size and morphology of the particles, CeO_2 shows a wide bandgap (3.0 - 3.4 eV) and, as a consequence, the photocatalytic activity under visible light irradiation may be restricted. In order to improve the photocatalytic performance of CeO_2 also in the visible range, some of the investigated approaches consist in tuning the morphology[243], in its combination with plasmonic metals[244,245] and in the inclusion of dopants[246,247].

CeO_2 is here incorporated in the porous polymeric matrix by means of the two synthetic strategies discussed in Chapter 2.3 and it is differently modified in order to harvest as much of the solar spectrum as possible. In the first part of this Chapter, the *in-situ* synthesis of the active nanomaterials directly in the polymeric matrix will be presented, similar to the work described in Chapter 4. The photocatalytic performance of the prepared CeO_2-based nanocomposite fibers with different CeO_2/Au nanostructures is investigated resulting in improved photocatalytic degradation of the MB dye activated under visible light[78]. Regarding the second synthetic strategy proposed in Chapter 2.3, the preliminary results of the incorporation of pre-formed CeO_2 NCs into the porous polymeric matrix are then reported. The improvement of the photocatalytic activity of CeO_2 is investigated by changing the oxygen vacancy concentrations by doping with different metal ions.

5.2. Incorporation of CeO_2 by *in-situ* synthetic strategy

5.2.1. Experimental methods

5.2.1.1. Materials

Poly(vinylidene fluoride-co-hexafluoropropylene) (PVDF-HFP, average MW ~ 455 kDa), ammonium cerium(IV) nitrate ($(NH_4)_2Ce(NO_3)_6$, 99.99%), chloroauric acid ($HAuCl_4$, 99.999%), methylene blue (MB), N,N-dimethylformamide (DMF, ChromasolPlus), acetone (≥99.5%, GC grade), ethanol (EtOH, GC grade), sodium hydroxide solution (NaOHaq, Titrisol), toluene (Chromasolv Plus), hydro- chloridric acid (HCl, 37%), and nitric acid (HNO_3, 70%) were purchased by Sigma-Aldrich. All chemicals were used as received without any further purification.

5.2.1.2. Preparation of PVDF-HFP/CeO_2/Au nanocomposite fibers

Details of the fibers preparation can be found in reference[78]. Briefly, PVDF-HFP fibers with in-situ formation of CeO_2 NPs were prepared by dissolving 2.24 g of $(NH_4)_2Ce(NO_3)_6$ in 18.5 mL of DMF/acetone (volume ratio 6/4) under stirring at room temperature. After the complete dissolution of the cerium salt, 4 g of PVDF-HFP pellets were added to the solution, which was left stirring at 70 °C to speed up the polymer dissolution. The preparation of PVDF-HFP/CeO_2/Au_in nanocomposite was achieved by adding 0.012 g of $HAuCl_4$ to the PVDF-HFP/$(NH_4)_2Ce(NO_3)_6$ solution. The solutions were electrospun by using electrospinning with a vertical setup (applied voltage of 27 kV, flow rate of 0.8 mL h^{-1} and collector distance of 25 cm). The dried electrospun fibers were placed in an oven (Air Concept, Firlambo) at 150 °C for 48 h in air to thermally induce the in situ synthesis of the CeO_2 in the PVDF-HFP/CeO_2 and of the Au NPs in the PVDF-HFP/CeO_2/Au_in nanocomposite. In addition, PVDF-HFP/CeO2/Au_ex nanocomposite fibers were prepared by *ex-situ* synthesizing Au NPs on previously prepared PVDF-HFP/CeO_2 fibers, placing the fibers in a sealed round-bottom flask in the presence of a

solution of 20 mL of EtOH and a given amount (0.012 g) of $HAuCl_4$ basified with few drops of NaOHaq (0.01 M) to adjust to pH 9; the system was stirred and heated at 50 °C for 24 h. The growth of Au NPs was achieved with a thermal post treatment (at 60 °C for 4 hours).

5.2.1.3. Characterization

The fibers morphology was investigated by a high-resolution scanning electron microscope (HR-SEM, JEOL JSM 7500FA) equipped with a cold field emission gun, applying an accelerating voltage of 10 kV (chamber pressure of 9.6 × 10−5 Pa). The specimens were previously coated with 10 nm thick carbon layer by a carbon coater (Emitech K950X, Quorum Technologies Ltd.). The size and morphology of the synthesized NPs were investigated by a transmission electron microscope (TEM, JEOL JEM-1011) equipped with a tungsten thermionic electron source, operating at 100 kV. High angle annular dark-field scanning TEM (HAADF-STEM) images were acquired at 200 kV with a high- resolution FEI Tecnai F20T TEM equipped with a Schottky field emission gun (FEG).

5.2.1.4. Photocatalytic performance of PVDF-HFP/CeO_2/Au nanocomposite fibers

The photocatalytic performance of the nanocomposite fibers was evaluated by performing photodegradation experiments using an aqueous solution of MB (6.5×10^{-3} mM), as model molecule. The experiments were carried out under a visible light irradiation, employing a light source composed by a seven LEDs array (SR-01-WC310 5650K, Luxeon Star) powered at constant voltage of 18 V. The employed light source presents two emission ranges: 410−470 nm and 500−750 nm (emission spectrum in Figure 5.5a). Approximately 5 mg of each sample were placed in a quartz cuvette filled with 3 mL of MB aqueous solution. Before starting the irradiation, the samples were kept in the MB solution in the dark for 1 h to reach the adsorption/desorption equilibrium of the dye on the surface of the sample. The cuvettes were then placed in fixed position at a distance

of 20 cm under the LEDs array. The MB degradation was monitored by recording the UV−vis absorbance spectra at specific time points, up to 330 min, using a Varian Cary 6000i UV−vis−NIR spectrophotometer and Milli-Q water as reference. For each experiment three samples were tested, and a quartz cuvette was filled with the MB solution as a control sample to estimate the self-degradation of the dye under the irradiation. The first-order rate constant (k_1) is calculated by fitting the MB photodegradation tests with the pseudo-first-order kinetic model (Equation 4.2 in Chapter 4.2.4). The MB concentrations were determined through a linear regression of the calibration curve, extracted as described in Chapter 4.2.4. Moreover, experiments in dark conditions were performed to investigate the possible MB adsorption on the neat PVDF fibers.

5.2.2. Results and discussion

5.2.2.1. Morphology of the CeO_2 based porous polymeric nanocomposite

The *in-situ* synthesis of CeO_2 NPs in the polymeric fibers is ensured by combining the electrospinning technique with the solid-state reaction to synthesize the CeO_2 NPs directly in the fiber bulk and, most important, also on the surface of the fibers (PVDF/CeO_2). The fibers average diameter changes when the cerium salt is added to the PVDF-HFP solution, increasing from 0.47 ± 0.26 μm for the solely PVDF fibers to around 1.07 ± 05 μm for the PVDF/cerium precursor fibers, due to the increase of the viscosity of the solution, which affects the electrospinning process[78]. After the thermally induced formation of the CeO_2 NPs, it is possible to observe a slightly further increase of the diameter to 1.56 ± 0.90 μm, which is not affected by the modification with Au NPs.

The thermal decomposition of the cerium precursor salt loaded in the polymeric matrix induces the *in-situ* growth of the CeO_2 NPs that appear homogeneously distributed on the surface of the polymeric fibers[78], as shown in Figure 5.1a. It is possible to observe also the formation of small agglomeration of CeO_2 NPs on the randomly distributed polymeric fibers. The *in-situ* formed CeO_2 NPs show a branched morphology with an

average diameter of 39 ± 15 nm without observing significant differences in all the prepared nanocomposite fibers (Figure 5.1b).

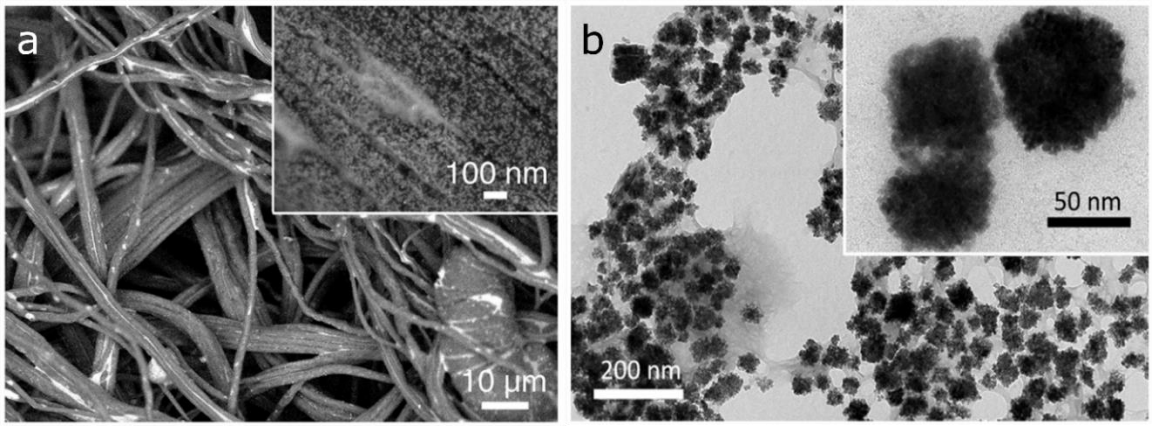

Figure 5.1. (a) HRSEM image of the PVDF/CeO_2 composite fibers. (b) TEM image of the in-situ synthetized CeO2 NPs (details of the morphology in the inset). Adapted from reference[78].

Figure 5.2 shows the photos and the morphologies of the PVDF/CeO_2 nanocomposite fibers after the modification with Au NPs through the previously described methods, resulting in the formation of two types of Au/CeO_2 nanostructures.

In the PVDF/CeO_2/Au_in fibers, it is possible to discern the presence of Au NPs on the fiber surfaces (inset of Figure 5.2a), where the simultaneous *in situ* synthesis of both CeO_2 and Au NPs induces their formation in separated domains with comparable dimensions (Figure 5.3a). Specifically, Au NPs exhibit a pentagonal shape, which is a typical gold morphology when Au NPs have sizes ranging from 33 nm to 101 nm[78]. In the PVDF/CeO_2/Au_ex fibers, the Au NPs are formed on the already existing CeO_2 NPs by the nanocomposite fibers dipping in a gold precursor solution and the subsequent thermal treatment, which leads to a very small Au NPs (12 ± 6 nm) nucleate on the exposed metal oxide (inset of Figure 5.2b and Figure 5.3b).

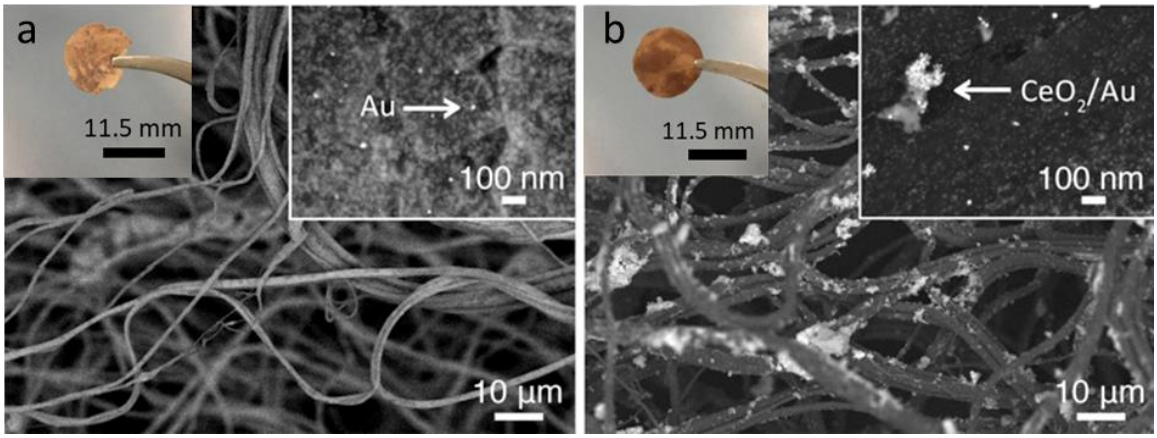

Figure 5.2. HRSEM images of (a) PVDF/CeO_2/Au_in and (b) PVDF/CeO_2/Au_ex. Insets show the photos of the samples and details of the surface of the fibers in higher magnification images. Adapted from reference[78].

The Au/CeO_2 nanostructures formed within the PVDF/CeO_2/Au_in fibers show smaller interfacial connections, mainly limited at the domain boundaries, between the noble metal and the metal oxide, due to the growth in separate domains, as well as their similar sizes. In the case of PVDF/CeO_2/Au_ex fibers, the nucleation and growth of Au NPs on pre-formed CeO_2 leads to a high interfacial area between the two fillers, strengthened also by the difference in the size of the Au with respect to the CeO_2.

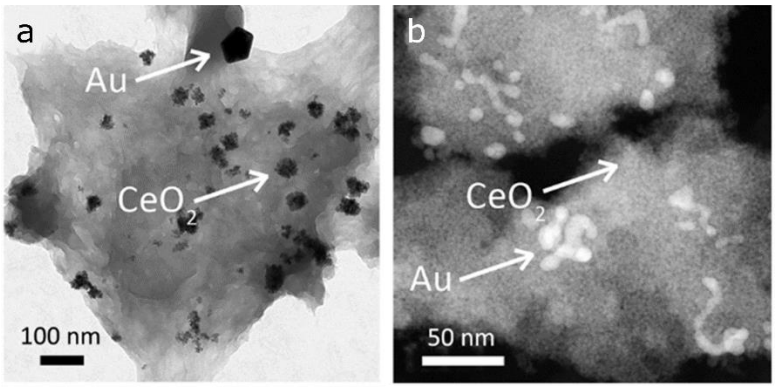

Figure 5. 3. (a) TEM image of the in-situ formed CeO_2 and Au NPs from the sample PVDF/CeO_2/Au_in. (c) Dark-field TEM image of CeO_2 aggregates with ex situ synthesized Au NPs on their surface, from the sample PVDF/CeO_2/Au_ex. Adapted from reference[78].

Further structural and chemical characterizations of the *in-situ* CeO_2 based porous polymeric nanocomposite are described in reference[78].

5.2.2.2. Photocatalytic performance

The photocatalytic performance of the prepared nanocomposite fibers is investigated towards the degradation of MB under visible light since the combination of metal NPs with the CeO_2 not only enhances the photocatalytic efficiency, but it is also expected to cause a narrowing on the bandgap of the metal oxide. The morphological details of the CeO_2 nanostructures, such as the shape, size and interface between the particles have a significant impact on their photo-activities. As shown in Figure 5.4, the photocatalytic degradation curve of the PVDF/CeO_2 nanocomposite fibers under visible light irradiation is completely overlapped with the one obtained for neat PVDF fibers, indicating that the CeO_2 does not exhibit any significant photocatalytic activity under such conditions.

The higher reduction of the MB concentration for the PVDF fibers compared to that observed for the dye self-degradation is due to the adsorption of the MB on the polymeric fibers. In Figure 5.5b it is reported the adsorption experiment of the dye under dark conditions, observing adsorption of around 5% of the initial MB, which is comparable to the MB reduction reported for the PVDF fibers under visible light.

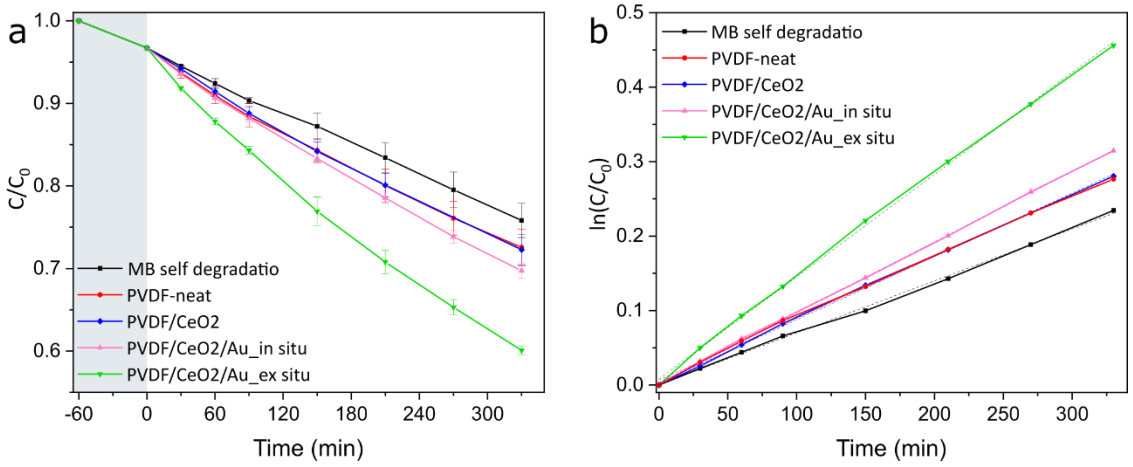

Figure 5.4. (a) Photocatalytic degradation curves of MB in presence of the nanocomposite fibers under visible light. Before the irradiation, the solutions were kept in dark for 60 min in the presence of the nanocomposite fibers. The self-degradation of MB is also presented. (b) Pseudo-first-order reaction kinetics for MB applied on the experimental data obtained in the first 5 hours of reaction.

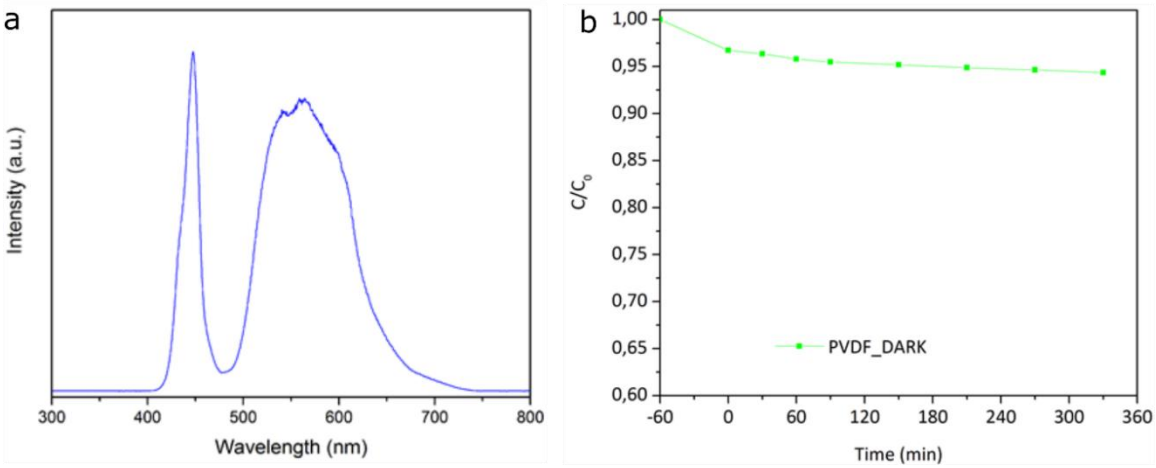

Figure 5.5. (a) Emission spectrum of the seven LEDs array (SR-01-WC310 5650K, Luxeon Star) employed as irradiation source for the photocatalytic test. (b) Methylene blue absorption experiment carried out in dark conditions on neat PVDF fibrous membranes.

When CeO_2 is combined with the Au NPs, an improvement of the photocatalytic activity is observed. In particular, after 330 min of visible light irradiation, the initial concentration of MB decreases of 30% for the PVDF/CeO_2/Au_in sample and of 40% for the PVDF/CeO_2/Au_ex (Figure 5.4a).

The photocatalytic degradation of MB follows pseudo-first order kinetics (Figure 5.4b) for all samples, and the photodegradation rate constant, k_1, for neat PVDF and PVDF/CeO_2 are similar ($0.8 \cdot 10^{-3}$ min^{-1}) confirming that CeO_2 NPs do not cause any photodegradation of the dye when irradiated by visible light. On the other hand, the photodegradation rate constant increases to a value of $0.9 \cdot 10^{-3}$ min^{-1} and $1.4 \cdot 10^{-3}$ min^{-1} for PVDF/CeO2/Au_in and PVDF/CeO2/Au_ex respectively. These results are explained considering the Eg values. The diffuse reflectance data of the CeO_2 based porous polymeric nanocomposite were appropriately plotted to estimate the Eg by means of the KM function. The extrapolated Eg value of CeO_2 decreases when the Au/CeO_2 nanostructures are formed, from an initial Eg of 3.26 eV in the case of PVDF/CeO_2 to 3.18 and 2.97 eV for PVDF/CeO_2/Au_in and PVDF/CeO_2/Au_ex, respectively. The narrowing of the Eg values can be ascribed to the increase of the oxygen vacancy of the metal oxide[78]. The decrease of the Eg values results in the activation of the photocatalytic degradation of the MB under visible light. Another plausible explanation of the improved photocatalytic performance of the PVDF/CeO_2/Au_ex is the type of the CeO_2/Au interface

that is formed by the *ex-situ* modification of the metal oxide. In this case, the CeO_2/Au interfacial area is higher than that observed for PVDF/CeO_2/Au_in thanks to the formation of smaller Au NPs mostly on the surface of the exposed CeO_2. If placed in intimate contact, the Schottky junction formed between Au and CeO_2 may be accountable for the improvement of the photocatalytic performance under visible light, inducing an LSPR sensitization effect.

5.3. Incorporation of CeO_2 by *ex-situ* synthetic strategy

5.3.1. Experimental methods

5.3.1.1. Materials

The synthesis processes are adapted by following a published method[248] and they are conducted by using a Schlenk line with dry glassware under nitrogen atmosphere. The used materials were cerium (III) nitrate hexahydrate ($Ce(NO_3)_3{\cdot}6H_2O$, 99.99%), gallium(III) nitrate hydrate ($Ga(NO_3)_3{\cdot}xH_2O$, 99.9%), gadolinium(III) nitrate hexahydrate ($Gd(NO_3)_3{\cdot}6H_2O$, 99.99%), 1-octadecene (ODE, 90%), N,N-dimethylformamide (DMF, 99.8%) and nitrosyl tetrafluoroborate ($NOBF_4$, 95%), cellulose acetate (CA, $M_n \approx 40$kDa), polyvinylpyrrolidone (PVP, average mol wt 10 kDa) which were purchased from Sigma Aldrich. Oleylamine (Oam, 70%) was purchased from Acros Organics. Hexanes (ACS grade), toluene (ACS grade), isopropanol (ACS grade) and ethanol (EtOH, ACS grade) were purchased from BDH.

5.3.1.2. Colloidal synthesis of CeO2, Ga:CeO_2 and Gd:CeO_2 NCs

The un-doped CeO_2 NCs were prepared by combining 2 mmol of $Ce(NO_3)_3{\cdot}6H_2O$ with 20 mmol of Oam and 5 mL of ODE in a 50 mL round bottom flask under continuous magnetic stirring. In the case of the doped CeO_2 NCs, high levels of metal dopant

precursors were added to the reaction mixture as 5% and 10% of the cerium precursor. The mixture was heated to 80 °C and maintained at this temperature for 1 h in order to homogenize the solution. The solution was then degassed at 120 °C for 1 h under a vacuum pressure below 100 mTorr. The temperature was then raised to 250 °C and the solution was aged for 2 h to react. After the reaction time was over, the dark brown mixture was cooled in air and 7.5 mL of toluene were added to the mixture when the temperature was around 80 °C. The NCs were then purified to remove the unreacted cerium salt, the surfactant and the solvent. The mixture was centrifuged at 1600 rpm for 10 min and the supernatant was divided into two centrifuge tubes, in which isopropanol was added as 5 times of the initial volume and centrifuged at 7000 rpm for 10 min. The precipitated nanocrystals were dispersed with 5 mL of hexane in each centrifuge tube, mixed with 2 times of isopropanol and centrifuged at 7000 rpm for 10 min. The pellets were then dispersed with 5 mL of hexane and subjected to size-selective precipitation (as described in Appendix 4, in section A4.3.2.4) narrowing the size distribution. The obtained final concentration of CeO_2 based NCs was around 60 $mg \cdot mL^{-1}$.

5.3.1.3. Ligand stripping procedure

To remove the ligand from the surface of the NCs, 8 mL of CeO_2 NCs dispersion in hexane (5 mg/mL) were added to 8 mL of DMF solution of 0.02 M of nitrosyl tetrafluoroborate ($NOBF_4$) at room temperature. The two-phase mixture was put in an ultrasonic bath for 30 min to promote the ligand stripping and then was gently shaken until the transfer of the NCs from hexane to DMF. The NCs were washed six times using toluene as antisolvent.

5.3.1.4. Fabrication of the CeO_2 based porous polymeric composite

The CeO_2 based porous polymeric composite was prepared via phase inversion by immersion precipitation. The homogeneous casting solution was prepared by adding the polymer solution to the CeO_2 NCs dispersion in DMF. Specifically, 0.3776 g of CA were

dissolved in 1.2 mL of DMF, while the CeO_2 NCs were separately dispersed in the PVP/DMF solutions. The latter was prepared by dissolving 0.070 g of PVP in 0.8 mL of DMF and the NCs were dispersed by ultrasonic bath for 30 min. The final amounts of CA and PVP were maintained at 16 wt.% and 3 wt.% respectively. Different weight fractions of CeO_2 NCs were added around 0.5 wt.%, 1 wt.% and 2 wt.% of CeO_2 with respect to the final content, which ensured a content of NCs of 1.5 wt.%, 3 wt.% and 6 wt.% with respect to the CA in the porous composite. The prepared solution was then cast on glass support by spin coating and immediately dipped into a distilled coagulation bath for 48 h. To exclude the loss of CeO_2 NCs during the precipitation of the polymeric matrix, the water coagulation baths have been analyzed recording the UV-vis absorption spectra.

5.3.1.5. Characterization

The morphology of the un-doped and doped CeO_2 NCs was investigated by a transmission electron microscope (TEM, JEOL 2010F) operating at 200 kV accelerating voltage. The samples were prepared by drop-casting a diluted nanocrystal solution in hexane on ultrathin carbon film type A (Ted Pella, 01822-F, 400 mesh) TEM grids. Dopant contents were quantified through ICP-OES spectrometer (iCAP 6500, Thermo). For the digestion of the samples, 2.5 mL of aqua regia were added to a small aliquot of the CeO2 NCs, then the samples were diluted up to 25 mL with milliQ water and filtered through PTFE syringe filters (diameter 15 mm, pore size 0.45 μm, Sartorius). The ICP-OES results were confirmed with XPS measurements, which were performed using a SPECS-Lab spectrometer with a non-monochromatic Mg Kα source ($h\nu$ = 1253.6 eV) operated at 15 kV with an emission current of 10 mA. Charge neutralization consisting of low-energy (ca. 7 eV) electrons was applied and energy scale calibration was performed by setting the C-C/C-H component of C1s spectrum at 285 eV. Spectra deconvolution was carried out using Casa XPS software. The optical absorption properties of CeO_2 NCs, which were deposited on quartz substrate by spin coating, were evaluated in the range between 200 – 1000 nm, using a Varian Cary 5000 (Agilent) UV-visible-NIR spectrophotometer.

5.3.1.6. Crystallite size approximation by Debye-Scherrer equation

The crystallite size was estimated by using the Debye-Scherrer equation (5.1)

$$D_{hkl} = \frac{K\lambda}{\beta cos\theta_{hkl}} \qquad \text{(Equation 5.1)}$$

where D_{hkl} is the crystallite size (nm), K is a dimensionless factor referred to the crystallite shape, λ is the wavelength of the target (0.15406 nm for Cu), β is the Full-Width-Half-Maximum (FWHM) of the diffraction peak (rad) and θ_{hkl} is the diffraction peak angle. The FWHM values were estimated by fitting the diffraction peaks (28.51°, 32.98°, 47.45°, 56.30° and 58.93°) of the CeO_2 cubic fluorite phase with a pseudo Voigt function. The presented crystallite size is the mean value obtained by the D_{hkl} values calculated from the above-mentioned diffraction peaks.

5.3.1.7. Band gap energy extrapolation by Tauc method

The bandgap energies (E_g) of un-doped and doped CeO_2 were deduced by plotting the optical absorption data with respect to energy, through the Tauc method. The colloidal suspensions of the synthetized NCs were deposited on quartz support by spin coating. Specifically, the optical absorption strength depends on the difference between the photon energy and the E_g as defined in the following relation (Equation 5.2),

$$(\alpha h\nu)^{1/n} = C(h\nu - E_g) \qquad \text{(Equation 5.2)}$$

where α is the absorption coefficient, h is Planck's constant, ν is the frequency of the photons and C is the proportionality constant. The exponent value (n) is related to the nature of the electronic transition and it assumes a value n = ½ for direct allowed transitions. The α value can be calculated from the absorption data with the following relation (Equation 5.3),

$$\alpha = (2.303\, A/t) \qquad \text{(Equation 5.3)}$$

where A is the optical absorbance and t is the thickness of the film. The t values of the CeO_2 NCs films on the quartz substrates was measured by AFM analysis on the scratched

film (AFM system XE-100, Park Scientific). The E_g value was then extrapolated from the linear portion of the Tauc plot, which is obtained by plotting $(\alpha h\nu)^2$ with respect to $h\nu$.

5.3.1.8. Photocatalytic performance of CA/CeO_2 porous composite

The photocatalytic performance of the porous composite was evaluated by immersing 10 mg of the samples in quartz cuvettes filled with 3 mL of MB aqueous solutions (0.0125 mM). To evaluate the adsorption of the organic molecules on the developed mats, experiments in dark conditions were performed overnight. For the photocatalytic experiments, the solutions containing the samples were placed at a distance of 10 cm under a UVA lamp emitting at a wavelength range from 315 nm to 400 nm (937 μW/cm2 at 365 nm, 10 cm from source) connected to a climatic chamber (ICH 110 L, Memmert). The UVA irradiance (μW/cm2) of the UV light source was measured by using a combined photo-radiometric probe (LP 471 P-A, Delta Ohm) at the fixed experimental distances between the source and the samples. Before starting the UV irradiation, the samples were maintained in the dark for 60 min. The decrease of the organic molecule concentration was monitored by recording the UV-vis absorption spectra at specific time intervals. The test was also performed for a reference sample, namely a quartz cuvette filled only with the MB solution, in order to estimate the self-degradation of the dye under the UV light irradiation. The dye adsorption experiments were performed with the same experimental conditions, keeping the quartz cuvettes under dark. The dye concentration was determined by using a calibration curve (linear regression with R2 values of 0.9983), obtained by monitoring the absorbance of the MB solutions at the wavelength of maximum absorbance (λmax = 664 nm) with concentrations ranging from 0.00087 to 0.0125 mM.

5.3.2. Results and discussion

5.3.2.1. Morphology of the synthetized CeO_2 NCs

The synthesis of CeO_2 NCs employs the thermal decomposition of the cerium precursor in the presence of Oam as ligand molecules in a high boiling point solvent under an inert atmosphere. The inclusion of Oam, an amine surfactant, enables the formation of non-aggregating and uniformly sized NCs. The decomposition of the metal precursor starts at a temperature above 200 °C, with the formation of nuclei that rapidly grow consuming the available monomers from the solution. In order to synthesize high quality NCs, the growth stage is maintained for 2 h, obtaining a narrow particle size distribution. In Figure 5.6, the un-doped CeO_2 NCs show a pseudo-spherical shape and they are uniform in size. The obtained average diameter (D_{TEM}) of the NCs is 3.91 ± 0.48 nm.

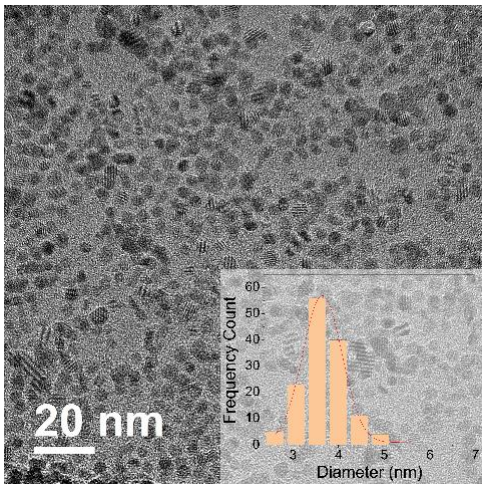

Figure 5.6. TEM image of un-doped CeO_2 NCs. Diameter size distribution is shown as an inset.

5.3.2.2. Incorporation of different contents of dopants in CeO_2 NCs

The variation of the optical properties of CeO_2 NCs has been evaluated through heterovalent doping, incorporating a high level of impurities in a different valence state than the Ce (IV) cations. The effective incorporation of dopants in the crystalline lattice is achieved balancing the reactivity of the host and dopant precursor. In this case, the used

host and dopant precursors have the same coordinating ligand. In fact, doping with a metal cation can remarkably affect the electrical and optical properties, which are dominated by the defect chemistry. The incorporation of trivalent dopants in CeO_2 induces a net negative charge, causing the formation of oxygen vacancies to maintain neutrality. In this way, it is possible to tune the concentration of the oxygen vacancies inside the system, which are formed to counterbalance the acceptor defects. Controlling the oxygen vacancy concentration is important to prepare a suitable photocatalyst because they can trap photoexcited electrons or photogenerated holes restraining the recombination of electron-hole pairs and, therefore, improving the photocatalytic performance[249]. Moreover, the presence of oxygen vacancies can also affect the Ce^{4+} to Ce^{3+} ratio, resulting in the enhanced visible-light induced photocatalytic activity when the Ce^{3+} content is increased[250].

After the incorporation of gallium and gadolinium in the CeO_2 NCs, the modification of the morphology and optical properties of the photocatalyst is studied. Figure 5.7 shows the TEM images of the doped CeO_2 NCs with a high level of dopants. It is possible to observe a pseudo-spherical shape for all the prepared doped NCs. The tested high level of dopants has a slight effect on the growth process of the NCs and their size. The D_{TEM} observed are 4.95 ± 0.88 nm, 4.60 ± 0.84 nm for the addition of 5% and 10% of Ga and 3.74 ± 0.69 nm and 4.39 ± 0.82 nm for 5% and 10% of Gd.

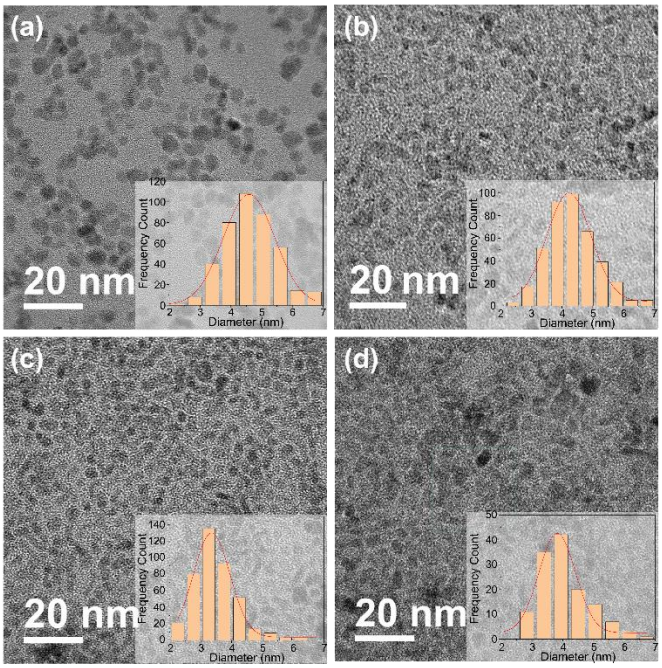

Figure 5.7. TEM images of (a) Ga:CeO_2 5%, (b) Ga:CeO_2 10%, (c) Gd:CeO_2 5% and (d) Gd:CeO_2 10%. The particle size distributions are shown as an inset.

5.3.2.3. Effects on the crystalline structure

The crystalline purity and the structural information are evaluated by XRD analysis (Figure 5.8). The XRD patterns of the un-doped and of the doped CeO_2 NCs show the characteristic diffraction peaks of the cubic fluorite structure phase of ceria, without observing any other diffraction peaks from crystalline impurities. The mean crystallite size (D_{DS}) of CeO_2 NCs, estimated by using the Debye-Scherrer equation, is 4.14 ± 0.26 nm, similar to the ones calculated for the doped CeO_2 NCs. Table 5.1 lists the lattice constant (a) and the D_{DS} values extrapolated from the XRD diffractograms. For comparison, it is also displayed the D_{TEM} estimated from the TEM images. The a value for the un-doped CeO_2 NCs is in accordance with the theoretical prediction of a = 5.4210 Å for ceria in the fluorite crystal structure.

In the diffractograms of Ga:CeO_2 the diffraction peaks appear shifted towards higher 2θ values and, increasing the dopant concentration, this shift increases of about 0.1% compared to the one observed for Ga:CeO_2-5%. The shift to higher 2θ values suggests a decrease in the a values (as shown in Table 5.1). This can be explained considering the

ionic radius of Ga^{3+} (0.62 Å), which is smaller than that of Ce^{4+} (0.97 Å) in accordance with Vegard's law prediction[251]. In fact, the substitution of Ce^{4+} ions with Ga^{3+} ions induces the shrinking of the host lattice with a gradual decrease of the lattice parameters for higher Ga doping.

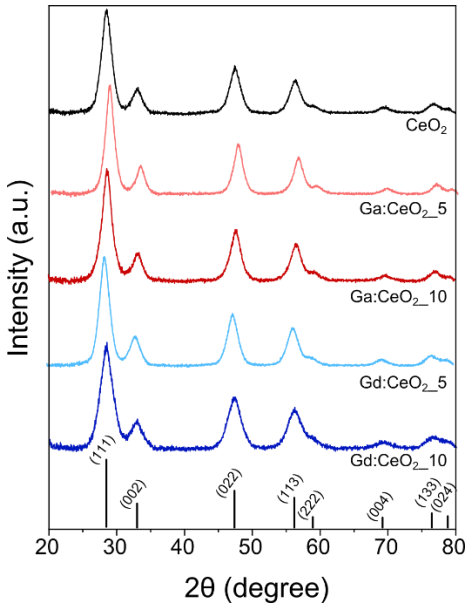

Figure 5.8. XRD patterns of un-doped and doped CeO_2 NCs. Stick reference pattern is shown along the x-axis.

Table 5.1. Lattice parameter and crystallite size of the prepared CeO_2 NCs

Samples	a (Å)	D_{DS} (nm)	D_{TEM} (nm)
CeO_2	5.4223 ± 0.006	4.14 ± 0.26	3.91 ± 0.48
Ga:CeO_2 5%	5.4010 ± 0.004	4.76 ± 0.36	4.95 ± 0.88
Ga:CeO_2 10%	5.3981 ± 0.005	4.35 ± 0.32	4.60 ± 0.84
Gd:CeO_2 5%	5.4238 ± 0.005	4.22 ± 0.2	3.74 ± 0.69
Gd:CeO_2 10%	5.4480 ± 0.013	3.46 ± 0.1	4.39 ± 0.82

In the case of the Gd doped CeO_2 NCs, only the diffractogram of Gd:CeO_2-10% shows a shift to lower 2θ values of the diffraction peaks, suggesting an increase of the lattice parameters. The ionic radius of Gd^{3+} (1.053 Å) is bigger than the one of Ce^{4+} and, therefore, its incorporation results in the expansion of the host lattice. The addition of a nominal content of Ga and Gd precursor as 5% of Ce precursor allows the incorporation of a high level of cations in the CeO_2 crystalline lattice. The quantification of the actual

amount of dopant cations is obtained by means of ICP-OES and XPS measurements. When Ga is added with a nominal content of 5%, the percentages of the incorporated cation are 21.7% and 15.15%, from ICP-OES and XPS results respectively. Increasing the Ga content to 10% with respect to Ce precursor in the reaction flask induces the incorporation of a higher amount of cations in the CeO_2 NCs, resulting in a doping percentage around 30% from both the analysis. The Gd:CeO_2-5% and Gd:CeO_2-10% NCs show a similar doping percentage of 20% from both the analysis, as a maximum amount of dopant that can be incorporated in the host lattice.

5.3.2.4. Effects on the optical properties

Figure 5.9 shows the UV-Vis spectra of the prepared CeO_2 NCs. In all the spectra, it is possible to observe a well-defined absorption of CeO_2 NCs in the ultraviolet region, with a maximum at 290 nm, which corresponds to O^{2-} to Ce^{4+} charge transfer transition [247]. The band gap energy (E_g) of CeO_2 is estimated using the Tauc model, extrapolated from the linear part of the (αhv)^1/n versus (hv), obtaining an E_g value of 3.711 ± 0.010 eV. The incorporation of high level of the dopants inside CeO_2 has a slight effect on the Eg, showing a decrease of the E_g value which is more evident for a higher content of dopant, observing a red-shift. Furthermore, the shift toward lower energies is higher for Ga:CeO_2 NCs compared to Gd:CeO_2. The extrapolated Eg are 3.700 ± 0.009 eV, 3.665 ± 0.014 eV for Ga:CeO_2 with the nominal content 5% and 10% respectively and 3.728 ± 0.007 eV, 3.697 ± 0.008 eV for Gd:CeO_2 with the nominal content 5% and 10% respectively.

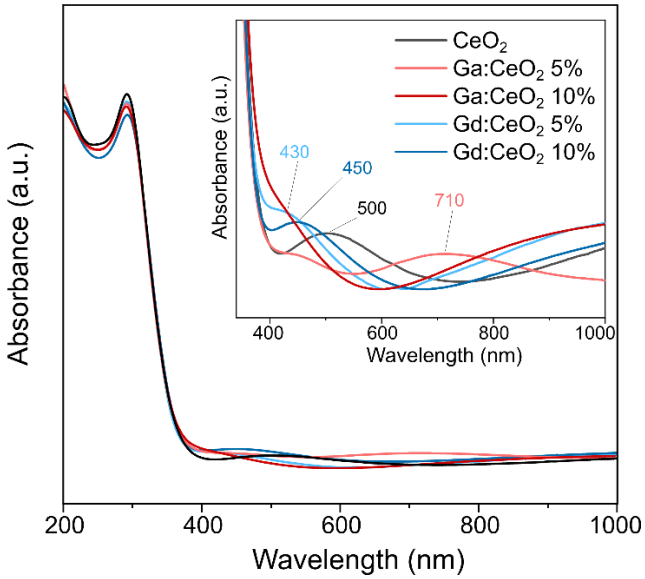

Figure 5.9. UV-Vis spectra of the un-doped and doped CeO_2 NCs deposited on quartz substrates before the ligand stripping. Inset shows details of the absorption spectra.

As can be noted in the inset of Figure 5.9, in the UV-Vis spectrum of the CeO_2 NCs there is a second absorption peak at 500 nm, which can be attributed to the absorption contribution of Ce^{3+} [243]. The presence of Ce^{3+} in the ceria NCs is further confirmed by the XPS analysis, showing a ratio of Ce^{3+}/Ce^{4+} of 0.15. When dopants are incorporated in the host lattice, the content of Ce^{3+} increases compared to the one observed in the un-doped CeO_2, observing a ratio of Ce^{3+}/Ce^{4+} of 0.48 and 0.39 for the Ga and, 0.39 and 0.40 for the Gd for an increasing nominal content. In the case of Ga, the content of Ce^{3+} appears to be slightly lower for higher content of dopant and this behavior can be due to a higher substitution of Ce^{3+} with Ga^{3+} in the host lattice, reducing the overall content of Ce^{3+} [246]. The doping with Ga and Gd affects the optical properties, showing weak absorption peaks in the visible and near-infrared regions, as shown in the inset of Figure 5.9.

5.3.2.5. Incorporation of CeO_2 NCs in a polymeric porous matrix

The pre-formed CeO_2 NCs are then incorporated in a polymeric matrix in order to obtain a porous composite. The preliminary data of the preparation of the composite by *ex-situ* approach are described in these two last sections.

One strategy adapted to prepare the composite is based on the precipitation of the polymeric phase by phase inversion by dipping the samples in a coagulation bath. Figure 5.10 shows the cross-section and the inner structure of the CA porous film and the CA/CeO_2 porous composite. Both samples exhibit an asymmetric porous structure with a thickness below 100 μm, which consists in the combination of a finger-like and a dense porous layer. The addition of 3 wt.% of CeO_2 concerning the CA affects the diffusion mass transfer of the solvents during the polymer precipitation, reducing the formation of the finger-like macrovoids (Figure 5.10 b).

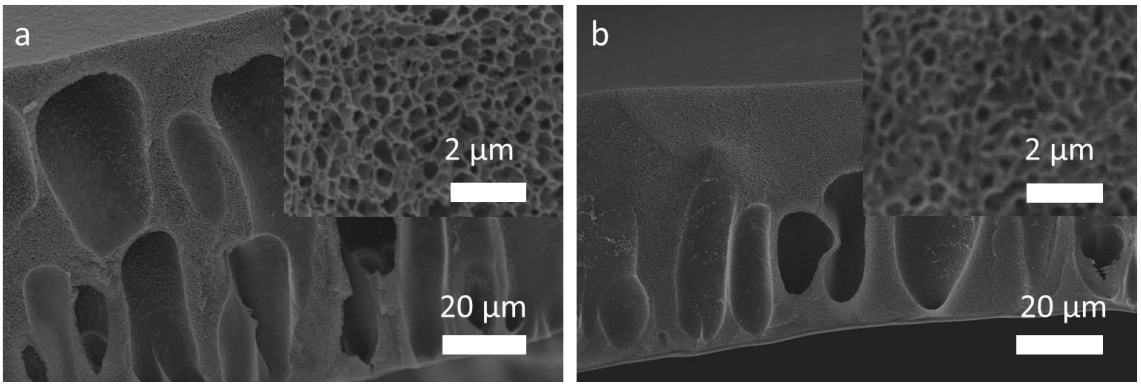

Figure 5.10. SEM images of (a) CA porous film and (b) CA/CeO_2 porous composite.

The SEM analysis does not allow to discern the presence of possible CeO_2 aggregates in the polymeric matrix, therefore further studies on the morphology of the composite are required through different imaging techniques with higher resolving power.

5.3.2.5. Preliminary results on photocatalytic performance of the porous composite

The preliminary photocatalytic degradation of the MB dye by the CA/CeO_2 porous composite is shown in Figure 5.11a. Unfortunately, the as-prepared sample does not show any photocatalytic activity under the UV irradiation. The photocatalytic degradation curve of the MB by CA/CeO_2 is overlapped to that of the MB self-degradation, while the decrease of the MB content due to the CA porous film (red curve) is due to the dye

adsorption on the polymer, as confirmed by the adsorption experiment shown in Figure 5.11b.

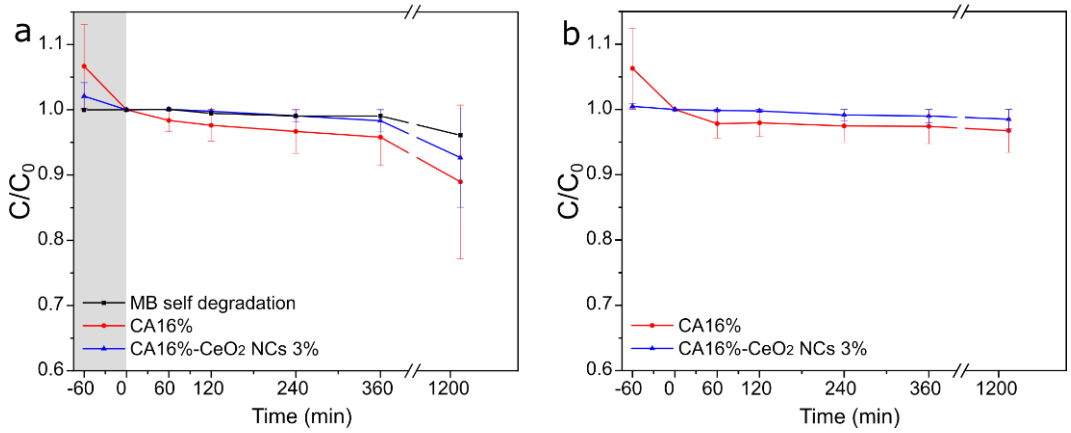

Figure 5. 11. Photocatalytic degradation curves of MB in presence of the samples under UV light. Before the UV irradiation, the solutions were kept in dark for 60 min in the presence of the samples. The self-degradation of MB is also presented. (b) MB absorption under dark conditions.

Further studies are required for the optimization of the fabrication procedure of the porous composite, studying the effect of different contents of photocatalysts and how they are distributed in the polymeric matrix. The absence of photoactivity of the investigated composite may be due to inadequate CeO_2 content or to the incorporation of the NCs only in the bulk of the polymer structure, which hinders the formation of ROSs.

5.4. Concluding remarks and future perspectives

The *in-situ* synthetic strategy to incorporate the metal oxide is based on the combination of the electrospinning technique with the *in-situ* thermally activated conversion of the cerium salt in CeO_2 NPs, which leads to its direct growth in the electrospun fibers forming the PVDF/CeO_2 composite. The *in-situ* synthesized CeO_2 NPs show a branched morphology and they appear distributed on the surface and the bulk of the fibers. The modification of the metal oxide with the noble metal induces the activation of the photocatalytic activity of the CeO_2 under visible light, thanks to the synergic effect of the metal oxide and noble metals. Specifically, the higher improvement of the

photocatalytic dye degradation is observed for the PVDF/CeO_2/Au_ex, for which 40% of the initial MB concentration is decolorized after 330 min under visible light. In this sample, the *ex-situ* growth of Au NPs on the already formed CeO_2 NPs allows the instauration of a better Au/CeO_2 contact interface resulting in a higher LSPR sensitization effect.

Besides the direct growth of the metal oxide in the polymeric matrix, the possible incorporation of *ex-situ* formed NCs is also investigated in the last section of the chapter. High quality CeO_2 NCs are prepared through colloidal synthesis to have control over their morphology and size. The doping strategy allows the incorporation of high levels of Ga^{3+} and Gd^{3+} cations in the CeO_2 lattice, inducing the formation of oxygen vacancies that can trap photoexcited electrons or photogenerated holes restraining the recombination of electron-hole pairs, resulting in an improvement of the photocatalytic performance.

A preliminary study for the preparation of a porous composite through the incorporation of the synthesized CeO_2 NCs is based on the formation of a solid porous material by a non-solvent induced phase inversion technique. However, the results obtained so far show no photocatalytic activity of the incorporated CeO_2 NCs (around 3 wt.% with respect to CA) for the removal of MB under UV light. Further research is therefore needed to optimize the *ex-situ* strategy to prepare a porous composite decorated by un-doped and doped NCs and to select the experimental set-up, *i.e.* selecting different light sources, for the photocatalytic degradation test.

Chapter 6

Conclusion

In this thesis, porous composite materials with potential applications for the removal of organic compounds from water have been prepared through the combination of different techniques. The incorporation of active micro- or nanosized materials in a porous polymeric matrix ensures the preparation of solid functional composites for which do not require the use of expensive and time-consuming post-operational steps to collect the active particles after the water treatment. The simple processability of the employed polymers allows to easily obtain low weight porous substrates in which the active filler is successfully incorporated preserving its performance.

Concerning the developed bio-based porous composite, the incorporation of OP agro-waste particles in the SF matrix has been fulfilled through the conversion of the prepared alcogel into a highly porous biocomposite upon $scCO_2$ drying. The sol-gel transition of the biopolymer induces the formation of thermodynamically stable β-sheets which act as physical crosslinks in the polymer matrix. The presence of OP affects the physiochemical properties of the SF matrix and leads to remarkable higher adsorption of the studied cationic dye than the one reached by the sole SF porous material.

The valorization of the OP waste as a component of a highly porous biocomposite opens up the possibility to convert agro-waste materials into low-cost adsorbent composites without compromising their adsorption capacity.

Besides the biocomposite adsorbent, an electrospun composite mat has been prepared by following an innovative approach for the incorporation of photoactive nanomaterials on the electrospun polymeric fibers for the heterogeneous photocatalytic degradation of organic pollutants. In this case, the removal of aqueous organic compounds occurs through a destructive process that may potentially lead to the complete mineralization of recalcitrant organic contaminants.

In the proposed composite, branched ZnO NPs are directly formed in the polymeric matrix upon thermal conversion of the zinc salt loaded onto the PMMA electrospun mat. To enhance the photocatalytic activity of the PMMA/ZnO composite mats in the removal of organic compounds, different strategies are investigated for the formation of Au/ZnO heterostructures. The higher photocatalytic degradation performance under UV light is observed for the porous composite with the heterostructure formed by the adsorption dipping process of the PMMA/ZnO composites in a gold solution, which ensures the gold ions adsorption and the subsequent Au NPs reduction on the surface of the already formed ZnO NPs. The high Au/ZnO interfacial active surface improves the photocatalytic activity of the ZnO semiconductor by means of the possible formation of Schottky junctions. Therefore, the fabrication of PMMA/ZnO composite mats can be considered as a valid approach for the immobilization of the active photocatalyst, whose photocatalytic performance can be easily improved by means of the formation of heterostructures with a noble metal.

The incorporation of a different photocatalyst in a porous polymeric matrix is then proposed by following both the in-situ and ex-situ synthetic strategies for the CeO_2 preparation in the porous composite materials. The *in-situ* synthesis followed for the fabrication of the PVDF/CeO_2 electrospun composite ensures the formation of branched CeO_2 NPs homogeneously distributed on the surface and the bulk of the polymeric fibers. The photocatalytic activity of the CeO_2 has been activated under visible light through its superficial modification with Au NPs. The higher photocatalytic degradation of the cationic dye occurs for the porous composite, in which the Au NPs grew on the formed CeO_2 NPs, assuring the instauration of a better Au/CeO_2 contact interface and therefore of a higher LSPR sensitization effect.

The incorporation of pre-synthesized CeO_2 NCs in a porous polymeric matrix is then studied by means of non-solvent induced precipitation of the polymer-based mixture, in which CeO_2 has been dispersed. The preliminary results show the formation of an asymmetric porous structure along with the thickness of the polymeric film. High quality CeO_2 NCs have been previously synthesized through colloidal synthesis and their

doping with high levels of Ga^{3+} and Gd^{3+} cations in the CeO_2 lattice induces the formation of oxygen vacancies that can trap photoexcited electrons or photogenerated holes restraining their recombination which may result in an improvement of the photocatalytic performance. Further research is needed for the optimization of the *ex-situ* incorporation of the un-doped CeO_2 NCs in the porous composite before to evaluate the effect of the doping on the photocatalytic activity of the metal oxide.

Appendix 1.

Effect of deposited Ag NPs on the photocatalytic activity of PMMA/ZnO composite mats

A1.1. Introduction

The combination of semiconductors with noble metals is a widely used approach to improve the photocatalytic performance of semiconductor photocatalysts. Since wide band gap semiconductors can absorb UV light, which consists in only about 3% of the incoming solar energy, the potential use of the heterogeneous photocatalytic process in wastewater treatments by using sunlight is restricted. The deposition of Ag NPs on the *in-situ* formed ZnO ensures instead the formation of materials with a visible-light response, allowing better use of the solar light, in which the visible light takes around 50 % of the total. The improvement in the visible absorption of the catalyst can be attributed to the surface plasmon resonance effects, in which the excitation of the localized surface plasmon resonance (LSPR) under visible light generates electrons on Ag NPs that are then injected into the CB of the ZnO to activate the formation of ROSs. The effect of combining Ag NPs with ZnO can further enhance the semiconductor photoreactivity, due to the formation of Schottky junctions. The presence of Ag NPs in intimate contact with ZnO induces a charge driving force, which inhibits the photogenerated electron-hole recombination, boosting the photocatalytic performance.

The PMMA/ZnO composite mats prepared following the *in-situ* synthetic approach for the incorporation of the active nanomaterials inside the porous polymeric matrix, as described in Chapter 4, are combined with Ag NPs to evaluate the synergistic effects on

the photocatalytic degradation of a dye under different light sources. Different thicknesses of Ag NPs are deposited on the composite mats before the thermal conversion of the metal salt precursor, by using the supersonic cluster beam deposition. The photoactivity of ZnO NPs that are formed below the Ag NP coating is studied, evaluating therefore the effect of the established metal-semiconductor interface on the removal of MB.

A1.2. Experimental methods

A1.2.1. Materials

Poly(methyl methacrylate) (PMMA, average Mw ~ 350 kDa), zinc acetate dihydrate (Zn(CH3CO2)2·2H2O 99,999%), N,N- Dimethylformamide (DMF, ≥99.8%), methylene blue (MB), acetone (≥99.5%), ethanol (EtOH, ≥99.8%), hydrochloridric acid (HCl, 37%) and nitric acid (HNO3, 70%), were purchased by Sigma Aldrich. All chemicals were used without any further purification.

A1.2.2. Preparation of the PMMA/ZnO-Ag

The nanocomposite polymeric fibers were prepared with a similar procedure as described in Chapter 4.2.1. The conversion of the PMMA/$Zn(CH_3COO)_2$ solution into electrospun fibers was achieved through electrospinning in a vertical setup. On the as PMMA/$Zn(CH_3COO)_2$ electrospun fibers were deposited silver NP layers of three different thicknesses by using the supersonic cluster beam deposition (SCBD) in collaboration with the group of Prof. Luca Gavioli, Interdisciplinary Laboratories for Advanced Materials Physics (i-LAMP) & Dipartimento di Matematica e Fisica, Università Cattolica del Sacro Cuore, Brescia.

The nanocomposite fibers with the three thicknesses of Ag NP layers were then placed in an oven at 110 °C for 48h to induce the thermal decomposition of the zinc salt in ZnO; this treatment in terms of time and temperature consents to reach a precursor conversion of

more than 90%, and, therefore, the added amount of zinc salt allows to obtain a content of around 20 wt.% of ZnO NPs in respect to the PMMA.

A1.2.3. Characterization

The morphological characterization was performed with scanning electron microscopy (SEM and HR-SEM), while the morphology and dimensions of the particles in the different samples were investigated by transmission electron microscopy (TEM). Specifically, the morphology of the fibers was investigated using mainly JEOL JSM-7500F high-resolution scanning electron microscope (HR-SEM) equipped with a cold field emission gun, applying an accelerating voltage of 5 kV. The samples were coated with a layer (10 nm) of carbon by a carbon coater (Emitech K950X, Quorum Technologies Ltd) and the average diameter size and the diameter size distribution were determined with Fiji/ImageJ software, collecting 200 fibers diameters for each image. The TEM images of the starting Ag NPs/composite fibers were acquired using JEOL JEM-1011 transmission electron microscopy (TEM) equipped with a tungsten thermionic electron source, operating at 100 kV. The polymeric fibers were dissolved in acetone and then the diluted suspension was deposited on a support grid (300 Mesh Cu Carbon only). The physiochemical characterization of the polymeric fibers was performed with X-ray Diffraction (XRD) by using a PANalytical Empyrean X-ray diffractometer with Cu K_α radiation operating at 45 kV and 40 mA. The diffractograms were recorded in reflection mode, for 2θ range from 10° to 75°, with a step time of 500 s and step size 0.1°.

The estimation of E_g of samples with different silver coating thicknesses was obtained from diffuse reflectance measurements, performed with a Varian Cary 6000i UV-Vis-NIR spectrophotometer, by applying the Kubelka-Munk (K-M) method as previously described (Chapter 4.2.7).

A1.2.4. Photocatalytic performance of PMMA/ZnO-Ag composite mats

The photocatalytic performance of the composite fibrous membranes with three different silver coating thicknesses was evaluated by putting 5 mg of the photocatalytic material in quartz cuvette filled with 3 mL of 4 ppm MB aqueous solution. Before starting the light irradiation, the fibers were maintained in the MB solution under dark conditions for 30 min, in order to reach the adsorption equilibrium of the dye on the samples. Then the MB photodegradation was monitored by recording the UV-vis absorption spectra at specific time intervals. The test was also performed for a reference sample, namely a quartz cuvette filled with solely MB solution, in order to estimate the self-degradation of the dye under the light irradiation. The photodegradation experiments were performed with two different light sources. Specifically, the experiments under UV light were performed by using a handled UV lamp (UVGL-58, Analytik Jena) equipped with a filter in longwave mode (0.5078 mW/cm^2 at 365 nm, 6 cm from source). The experiments under visible light were carried out with a super-quiet xenon lamp (LIGHTNINGCURE Spot light source L9588-04, HAMAMATSU), which emits a radiant wavelength range from 300 nm to 800 nm (4500 mW/cm^2 at 365 nm, 10 mm from source), maintaining a distance of 20 cm between the samples and the light source.

A1.3. Results and discussion

The PMMA/ZnO composite mats presented in Chapter 4 are here combined with Ag NPs in order to evaluate the effect on the photocatalytic performance of the immobilized catalyst in presence of UV-vis light. In fact, the wide Eg of ZnO requires UV light irradiation to promote the establishment of the photocatalytic reactions. The coating of three layer thicknesses of Ag NPs (1 - 5 - 10 nm) on the PMMA/Zn(CH_3COO)$_2$ electrospun mats is evaluated in order to understand for which PMMA/ZnO-Ag composite mats the interfacial electron transfer from the photo-excited Ag NPs to the ZnO NPs ensures an improved photocatalytic performance for the degradation of MB as a model molecule. The thermally induced synthesis of ZnO after the deposition of Ag NPs

guarantees an intimate contact between the semiconductor and the noble metal. Figure A1.1 shows the photos of the fibrous mats after the thermal treatment to induce the growth of ZnO in the PMMA.

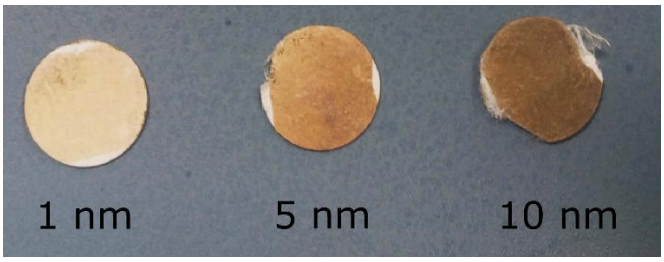

Figure A1.1. Photos of PMMA/ZnO with three thicknesses of Ag NPs

The prepared fibrous mats, before and after the thermal treatment, show a non-continuous fibrous-like structure, with inhomogeneous sizes in the order of few microns (Figure A1.2). The high content of the loaded $Zn(CH_3COO)_2$ leads to the formation of crystalline structures which protrude from the surface of the fibers, clearly evident in the insets of Figure A1.2b,c. As already described, the thermal treatment on the PMMA/precursor fibers induces the nucleation and growth of ZnO NPs without affecting the polymeric fibers. The obtained PMMA/ZnO fibrous membranes show an average diameter size of 7.05 ± 2.70 μm, in which the ZnO NPs cover uniformly the polymeric fibers. The Ag NPs coating on the PMMA/$Zn(CH_3COO)_2$ fibrous membranes is clearly visible for the samples with 5 and 10 nm of Ag coating thicknesses (Figure A1.2b,c). The EDS mapping image of the PMMA/ZnO with 10 nm of Ag NPs confirms the superficial deposition of the noble metal on the sample (Figure A1.3). The presence of an area of the fiber in which there is a minor silver distribution is probably caused by the overlapping of another fiber during the NPs deposition with the SCBD method.

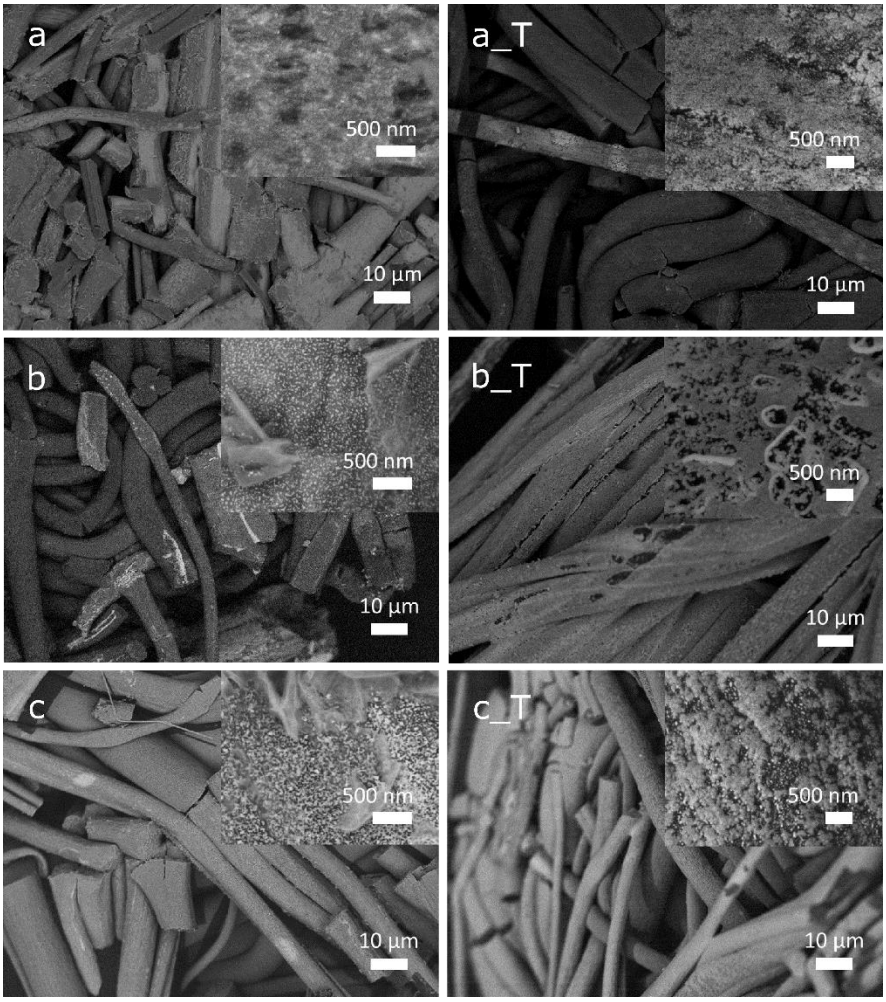

Figure A1.2. HRSEM images of the electrospun mats with the three thicknesses of Ag NPs before and after the thermal treatment. PMMA/Zn(CH₃COO)₂ and of PMMA/ZnO (labeled with _T) with a coating of (a) 1 nm, (b) 5 nm and (c) 10nm of Ag NPs.

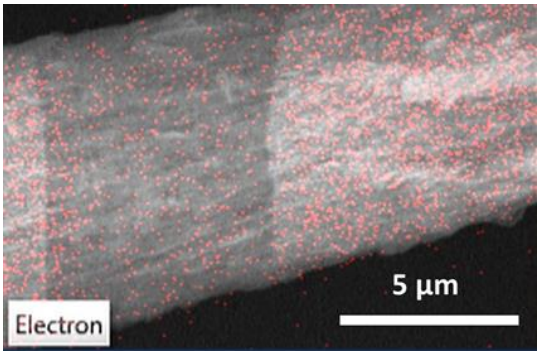

Figure A1.3. EDS mapping of Ag distribution on the PMMA/ZnO mats with 10 nm of Ag NPs coating.

The PMMA/ZnO composite mats prepared with 1 nm and 10 nm thick Ag NPs coatings are analyzed with TEM, where the formed ZnO NPs exhibit a spherical branched

structure (Figure A1.4a), as reported in Chapter 4. The presence of Ag NPs in the PMMA/ZnO fibers with a silver coating of 1 nm is difficult to confirm in the TEM images due to the low concentration of the silver. In the nanocomposite fibers with a silver coating of 10 nm it is instead possible to notice the presence of two different size distributions with spherical shape NPs and an average size of 3.60 ± 0.72 nm and 5.91 ± 0.98 nm (Figure A1.4b). The electron diffraction patterns, included in Figure A1.4b, confirms the structure identification of Ag as face centered cubic structure.

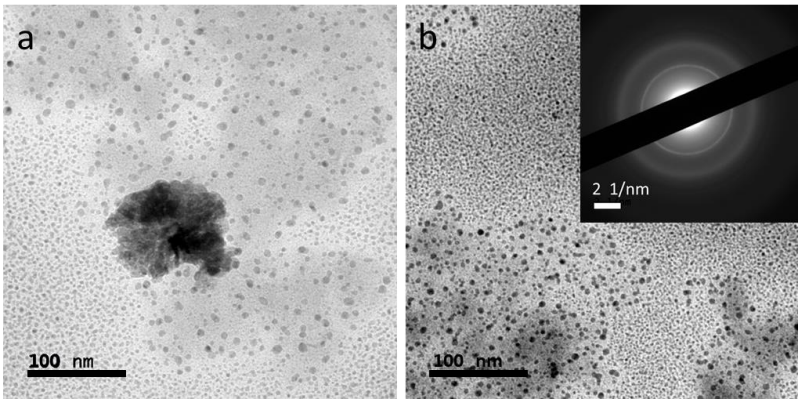

Figure A1.4. TEM images of (a) a ZnO NP and Ag NPs and (b) details of the two size populations of Ag NPs after the dissolution of the polymeric matrix in the PMMA/ZnO-10 nm Ag NPs. Inset reports the electron diffraction pattern of the Ag NPs.

The XRD patterns of the composite fibers with 10 nm of Ag NPs thickness coating before and after the thermal treatment are shown in Figure A1.5. All the diffraction peaks presented in the diffractogram of the PMMA/$Zn(CH_3COO)_2$ fibers are associated to the hexagonal crystalline structure of $Zn(CH_3COO)_2$ and, after the thermal treatment, these peaks are replaced by all the characteristic diffraction peaks attributable to the hexagonal wurtzite ZnO structure, confirming the complete decomposition of the precursor in all the composite fibers, as observed in a previous work[122]. The diffraction peak due to the presence of the Ag NPs can be observed only in the XRD pattern of the samples prepared with a coating of 10 nm. The peak at 38° corresponds to the face centered cubic structure of Ag NPs [203]. The absence of this peak in the samples with a minor thickness of silver is attributed to its low concentration that makes difficult the detection.

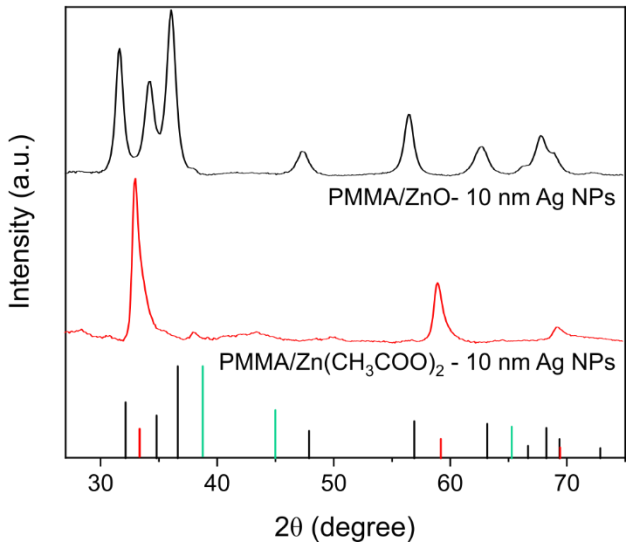

Figure A1.5. XRD patterns of the PMMA/ZnO composite mats with 10 nm of Ag NPs coating before (red line) and after (black line) the thermal treatment. Stick reference patterns of $Zn(CH_3COO)_2$ (red), ZnO (black) and Au (green) are shown along x-axis.

The estimation of the E_g has been calculated through the KM method on the UV-vis diffuse reflectance spectra of all the samples, assuming a direct band-to-band transition. The band gap values are shown in Table A1.1, in which the E_g of the ZnO formed in the polymeric matrix without silver modification is shifted from 3.281 ± 0.063 eV to slightly lower values when it grows in the presence of Ag NPs on the fibers surface.

Table A1.1. Experimental E_g values for the composite mats by using KM method, assuming a direct transition.

Samples	**Eg (eV)**
PMMA/ZnO	3.281 ± 0.063
PMMA/ZnO – 1 nm Ag NPs	3.266 ± 0.051
PMMA/ZnO – 5 nm Ag NPs	3.250 ± 0.040
PMMA/ZnO – 10 nm Ag NPs	3.254 ± 0.060

The photocatalytic performance of the composite fibrous mats with three different silver coating thicknesses is evaluated for an initial concentration of MB aqueous solution of 1.4 10^{-5} M. The composite mats are tested under UV light to evaluate the effect of the noble metal coating on the photocatalytic activity of the composites. The experimental results, shown in Figure A1.6, confirm the enhanced photocatalytic performance for the

PMMA/ZnO fibers with silver coating compares to the PMMA/ZnO fibers. Specifically, the photocatalytic performance enhances from composite fibers with Ag NPs layer of 5 nm to 10 nm, while it decreases for the composite fibers with lower silver coating. The PMMA/ZnO-Ag with 5 nm of NP coating exhibits higher photocatalytic activity compared to the other samples and it is able to reduce around 25% of the initial MB within 6 h. Furthermore, the self-degradation of the dye under UV light is negligible. It has been observed that the use of metallic NPs used for catalyst doping has an optimized concentration, beyond which the photocatalytic performance gets worse[203]. The decrease in the photocatalytic performance of the ZnO with higher thickness of Ag NPs on the surface can be attributed to a less effective light absorption due to the coating of the noble metal on the surface.

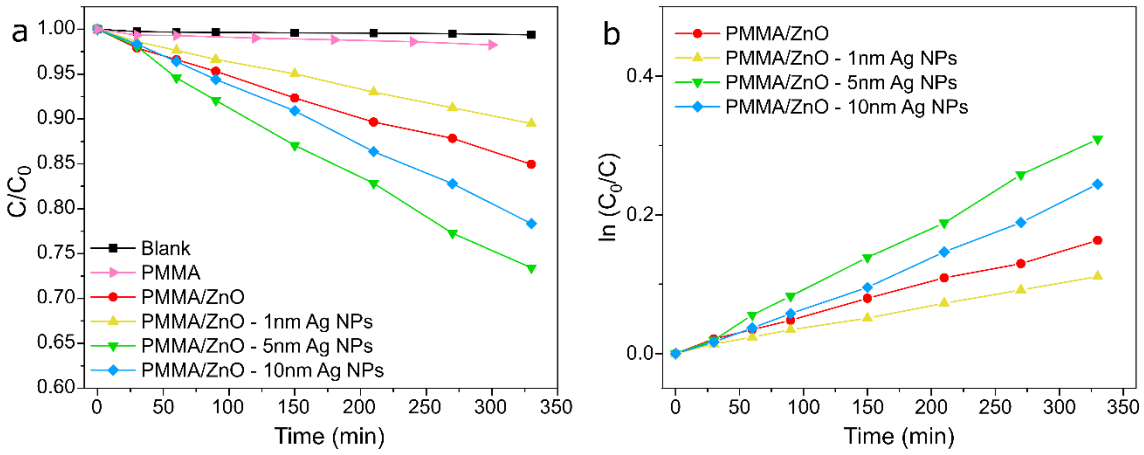

Figure A1.6. (a) Photocatalytic degradation curves of MB in the presence of the composite mats under UV light. The self-degradation of MB is also presented. (b) Pseudo-first-order reaction kinetics for MB.

The photocatalytic degradation of the dye follows a pseudo-first order kinetic reaction, $\ln(C_o/C) = k_1 t$, where k_1 is the photodegradation rate constant. The kinetics of the photocatalytic degradation of MB are shown in Figure A1.6b, while the rate constants for all the samples are listed in Table A1.2.

Table A1.2. Photo-degradation rate constants and linear regression coefficients (R^2) obtained from the linear fitting of the experimental data by using the pseudo-first order model.

	UV light	
Samples	**10^{-3} k_1 (min^{-1})**	**R^2**
MB self-degradation	-	-
PMMA	-	-
PMMA/ZnO	0.480	0.9969
PMMA/ZnO – 1 nm Ag	0.329	0.9984
PMMA/ZnO – 5 nm Ag	0.948	0.9985
PMMA/ZnO – 10 nm Ag	0.736	0.9964

The extrapolated k1 values from the slope of the linear pseudo-first equation increase from $0.480 \cdot 10^{-3}$ to $0.948 \cdot 10^{-3}$ min-1 when the ZnO NPs are *in-situ* synthesized in the composite mat with 5 nm of Ag NPs coating. This enhancement of the rate constant when the semiconductor is in contact with the noble metal is consistent with the possible formation of Schottky barrier that can trap the photo-excited electrons, promoting thus efficient photocatalysis processes.

A1.4. Conclusion

A prelaminar study of the effect of different coating thicknesses of silver NPs on the photocatalytic degradation performance of a ZnO-based mats has been reported under UV light. Photocatalytic degradation experiments performed under UV-vis light have not shown significant improvement of the removal of the dye for the absorption of the visible component by the formed ZnO-Ag hybrid system. In these experiments, the dye self-degradation under the light source has mainly contributed to the MB removal. For both the light sources, the presence of a coating of 5 nm of Ag NPs on the PMMA/ZnO composite mats results in an improvement of the photocatalytic activity and of the rate of degradation of MB. The positive effect of the deposition of Ag on the photocatalytic process can be attributed to the formation of Schottky barrier with the *in-situ* formed ZnO

NPs on a polymeric porous matrix. However, one of the problems encountered with the deposition of the Ag NPs layer on the surface of the mats by means of SCBD is the total loss of the coating during the handling of the samples and, therefore, the loss of the improved photocatalytic efficiency of the semiconductor metal oxide.

Appendix 2.

Sensitive polymeric coating on a fiber Bragg grating for the detection of mercury ions in water

A2.1. Introduction

Mercury is considered one of the most harmful water pollutants due to its high toxicity and high mobility[12]. Besides the natural sources of mercury, its presence in the environment is also caused by anthropogenic activity[11,252]. In fact, one of the main concerns caused by rapid industrialization is the increase of heavy metal content in water resources. Therefore, it is important to develop monitoring systems for fast, selective and sensitive detection of mercury ions (Hg^{2+}) in water, in order to control, for example, the effectiveness of the water remediation process. Optical fiber sensors are commonly employed for monitoring pollution parameters, thanks to their robustness, light-weight and high flexibility[253]. The use of polymeric sensitive coatings on the fibers enables the development of sensors with specific selectivity toward the desired pollutants, in which the polymer can be used as solid support of the active component or directly as the chemical transducer[254].

A2.2. Experimental methods

A2.2.1. Materials

Poly(vinyl alcohol) (PVA, Mw 146 -186 kDa, 99+% hydrolyzed), citric acid (CA, anhydrous), L-Cysteine (CYS, 97%) and Mercury(II) chloride ($HgCl_2$, ACS reagent, ≥99.5%) were purchased from Sigma Aldrich and used without further purification. The fiber Bragg grating on which the sensitive coating was deposited were provided by Dr. Stavros Pissadakis and Dr. Mary Konstantaki, of the Institute of Electronic Structure and Laser (IESL) in the Foundation for Research and Technology-Hellas (FORTH) at Crete.

A2.2.2. Preparation of PVA/CA/CYS film

250 mg of PVA were added in 5 mL of H_2O under stirring at 90 °C until its complete dissolution. After the solution was cooled to room temperature, 80 mg of CA and 100 mg of CYS were added and the clear solution was left to stir overnight. The PVA/CA/CYS aqueous solution was deposited via spin coating on a silicon wafer and quartz substrate having a surface area of 1.78 ± 0.66 cm^2 (1500 rpm, 3 min). Then the films were dried at 140 °C for 2 h in order to induce the crosslinking of the PVA chains. To deposit the PVA/CA/CYS coating directly on the core of the optical fiber in the region without cladding, the optical fiber was dipped in the PVA/CA/CYS solution with a constant speed of 0.33 cm/s for three times in order to achieve the desired layer thickness. Between each immersion, the core was maintained in the solution for 1 min and then pulled upward at the same constant speed and left to dry in air before to start the next deposition cycle. After the third dip coating step, the coating on the optical fibers was dried at 140 °C for 2 h in a convection oven. To remove any excess of no reacted polymer and chemicals, the films were washed in MilliQ water for 2 h.

A2.2.3. Characterization

Differential scanning calorimetry (DSC) was performed using a DSC 250 (TA Instruments) with a heating rate of 10 °C/min from 20 °C to 180 °C and a cooling rate of 10°C/min to 20 °C. The water stability of the films was studied monitoring the Total

Organic Carbon (TOC) of the solutions by a membraPure uniTOC lab analyzer (details of the experiment are clarified in Chapter 4.2.4). The spectroscopic ellipsometry to characterize Psi and Delta parameters was performed by using a VASE Ellipsometer (J. A. Woollam), following the methodology described elsewhere[255]. Six replicates were modeled simultaneously with a Sellmeier model for refractive index (n) and a Tauc-Lorenz model for the absorption coefficient (k). The thickness of the coating was evaluated by atomic force microscopy (AFM) system XE-100 by Park Scientificand scanning electron microscope (SEM, JEOL JSM 6490LA). For the AFM imaging, the thickness was measured by the average value of step height across a scratch edge made along with the film. The images were processed by using the free and open source software Gwyddion. The adsorption experiments were performed in 10 mL of Hg^{2+} aqueous solutions at 10 ppm of concentration and the quantitative analysis of the mercury ions is performed using an ICP-OES spectrometer (iCAP 6300, Thermo). To perform the analysis, 2.5 mL of aqua regia (HCl/HNO_3, 3:1) were added to 125 μL of each solution, then the samples were diluted with milliQ water up to 25 mL and filtered through polytetrafluoroethylene (PTFE) syringe filters (diameter 15 mm, pore size 0.45 μm, Sartorius). The percentage removal has been normalized considering the mass of the film on the support.

A2.3. Results and discussion

This appendix shows the preliminary results of the fabrication of a polymeric matrix as a selective element of an optical sensor for the monitoring of heavy metal ions in water. For the development of an eco-friendly light-sensitive coating able to detect heavy metal ions in water, different solutions have been investigated. However, only the presented material shows the advantageous features needed to prepare a coating on the fiber Bragg grating, such as a low refractive index and uniform finish. The suggested polymeric coating is prepared starting from a water-based solution, in which CYS is added as a sensitive component to mercury ions in water. PVA has been chosen as

polymeric support because it is a biodegradable and low cost material, characterized by a low refractive index (nD20, 1.4791)[256]. It shows a good chemical resistance and it can be easily used to form films with a good mechanical strength[257]. Since the PVA is a water soluble polymer, the polymeric chains can be cross-linked in order to obtain water stability, by using the conjugate compound formed between CA and CYS[258,259]. The crosslinking of the PVA is obtained through a multi-dehydration reaction under high temperature[258], as shown in the reaction scheme (Figure A2.1). CYS is added in 1:2 CA/CYS molar ratio, to have CYS with –SH thiol groups free to interact with Hg^{2+} ions upon adsorption.

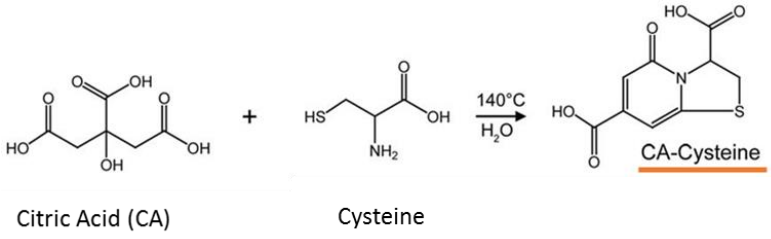

Figure A2.1. Reaction scheme for multi-dehydration reaction under high temperature. Adapted from reference[258].

To optimize the polymer cross-linking, PVA/CA/CYS films before and after the thermal treatment are analyzed by DSC. The interpretation of the results obtained from the thermal analysis measurement ensures qualitative information about the physiochemical variations that occur in the film. In the first heating cycle, it is possible to observe a large exothermic peak for the film before the thermal treatment, which is remarkable less intense in the DSC curve of the film obtained after the cross-linking by the thermal treatment (Figure A2.2). The exothermic peak is still present in the PVA/CA/CYS film after the thermal treatment, although it exhibits a smaller residual heat and an onset at higher temperature (around 100 °C), due to the partial crosslinking of the PVA chains. Since the analyzed sample was treated at 130 °C for 1 h, the temperature of the thermal treatment was increased to 140 °C for 2 h, in order to induce a higher cross-linking.

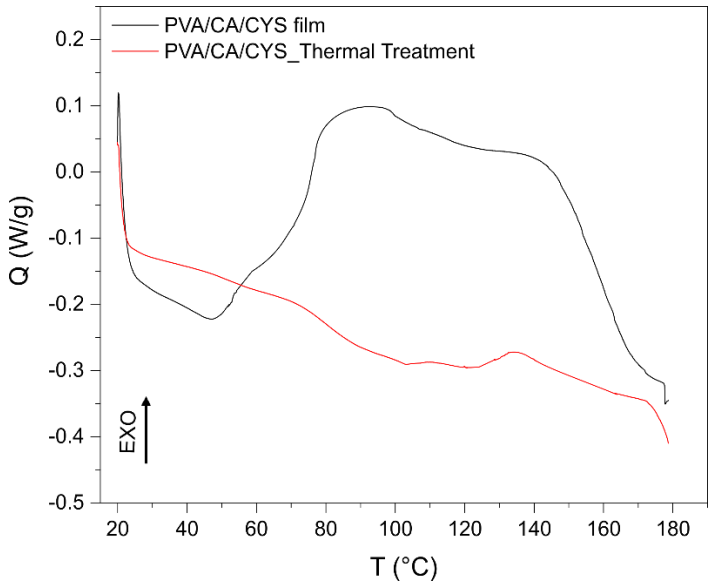

Figure A2.2. DSC data of the PVA/CA/CYS film before and after the thermal treatment.

The stability in water of the films was monitored analyzing the TOC value of the water after the washing to remove the excess of cross-linker and possible PVA not fully cross-linked. The TOC value measured using coatings obtained at a higher temperature and time of the thermal treatment, after the first washing, is 1.52 ± 0.2 ppm, remarkably lower compared to the one obtained with the non-optimized treatment (8.49 ± 1.24 ppm). After the second washing step, this value becomes negligible. In fact, during the first washing, the thickness of PVA/CA/CYS film, measured by AFM imaging, has reduced of around 20% of the initial (from 967.74 ± 47.73 nm to 763.086 ± 37.0 nm) and it is stable after the second washing (758.03 ± 48.28 nm).

The FTIR characterization confirms the multi-dehydration reaction (Figure A2.3). In fact, the FTIR spectrum of the PVA/CA/CYS film shows the main absorption peaks of PVA and new peaks due to the formation of amides and esters after the crosslinking. New absorption peaks at 1713 and 1520 cm^{-1} are assigned to the C=O and N-H stretching of the primary amide, while the peak at 1645 cm^{-1} is attributed to the tertiary amide C=O stretching. In the intense absorption at 1713 cm^{-1} there is also the contribution of the formed esters, in which the signal at lower frequencies can be ascribed to the resonance effect of the conjugation.

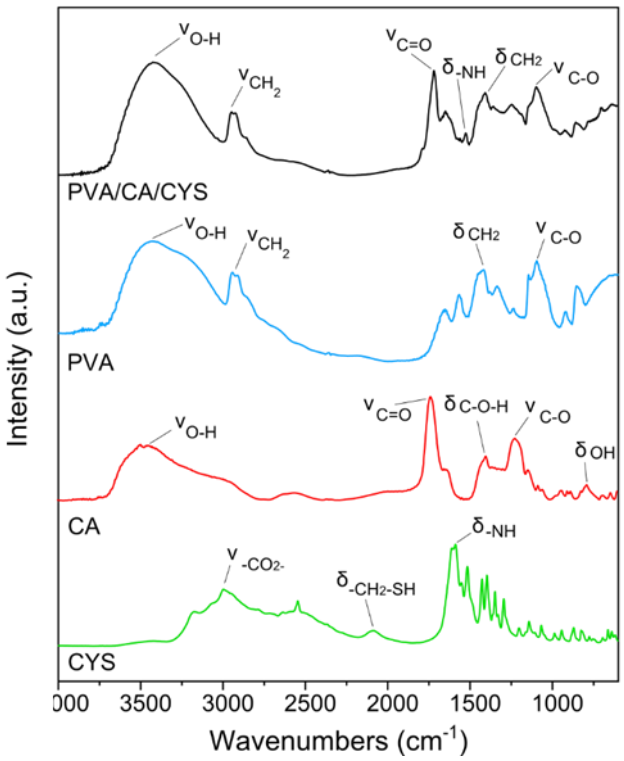

Figure A2.3. FTIR spectra of the PVA/CA/CYS film and of the individual components.

The heterocyclic compound formed by CA-CYS, which is used as cross-linker, induces a blue fluorescence emission of PVA/CA/CYS film when excited by wavelength 365 nm [259]. In the absorbance spectrum of the film (Figure A2.4a), differentially from the absorption spectrum of the pure PVA, a new absorption peak appears at 364 nm which is due to n-pi* transition of the CA-CYS compound [258], confirming the crosslinking of the PVA.

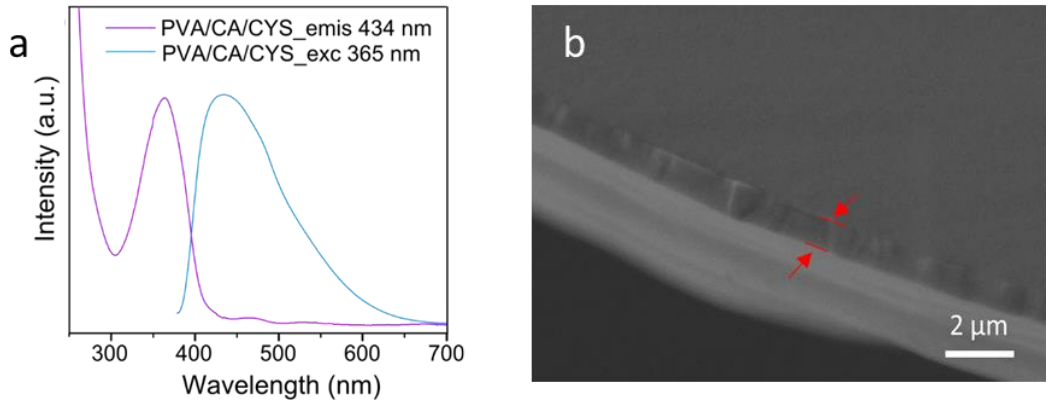

Figure A2.4. (a) Excitation and emission spectra of the PVA/CA/CYS and (b) SEM image of the coating on the optical fiber with fiber Bragg grating.

In order to evaluate the use of the composite film as a sensitive coating on optical fibers, the adsorption capacity and the variation of the n are evaluated after the adsorption of mercury ions from water. The PVA/CA/CYS films adsorb 4.40 ± 0.36 mg of Hg^{2+} per gram of sample. The optical constants (n and k) of the as prepared PVA/CA/CYS film, after the water dipping, and after the mercury adsorption are determined by ellipsometric measurements. After the first washing, n is not affected, while it is possible to observe a remarkable increase in the n value after mercury adsorption, as shown in Table A2.1. This variation in n is higher at longer wavelengths (*i.e.* IR). The change of n after the binding of Hg^{2+} on the PVA/CA/CYS film confirms the potential use of this system as a sensitive polymeric coating for the fabrication of a refractive index sensor.

Table A2.1. Refractive index of the PVA/CA/CYS film measured by ellipsometry at two different wavelengths.

Samples	n at 980 nm	n at 628 nm
PVA/CA/CYS film	$1.538 \pm 2E10^{-4}$	$1.548 \pm 2E10^{-4}$
PVA/CA/CYS film_Hg^{2+} ads	$1.541 \pm 2E10^{-4}$	$1.551 \pm 2E10^{-4}$

The optical fibers employed to fabricate the potential sensor for Hg^{2+} in water are fiber Bragg grating, in which the fiber core is photo-imprinted with a periodic pattern, inducing a permanent refractive index modulation. This modification of the core of the optical fiber leads to the reflection of the light that is propagating along the fiber only in a small range of wavelengths for which the Bragg condition is satisfied, while all the others are transmitted. The reflected wavelength, called Bragg wavelength (λ_B), is directly proportional to the effective modal refractive index (n_{eff}) by the condition $\lambda_B = 2n_{eff}\Lambda$ where Λ is the Bragg grating period. The binding of specific compounds on the deposited sensitive coating on the core of the fiber Bragg grating induces a variation of the coating refractive index resulting in a λ_B shift which is detectable even in case of low-order magnitude. This aspect makes the fiber Bragg grating a promising sensing device for monitoring low sample concentrations.

The deposition of the PVA/CA/CYS solution on the fiber Bragg grating support by dip coating process is investigated by using different constant dipping speeds without observing a significant variation in the thickness of the deposited layer. To obtain the

desired thickness on the core of the optical fiber, the substrate is immersed in the PVA/CA/CYS solution for three consecutive times, resulting in the formation of a layer of a thickness of 972.11 ± 150 nm after the thermal treatment and the washing step (Figure A2.4b).

A2.4. Concluding remarks

The PVA/CA/CYS coating results stable in water and it can adsorb 4.40 ± 0.36 mg/g of Hg^{2+} from an aqueous solution. At the same time, the refractive index of the grating increases making possible their utilization for the mercury ions detection in water. In fact, as a following step, the coated fiber Bragg gratings, will be tested as sensors for potential applications in monitoring heavy metal ions in water in collaboration with Dr. Stavros Pissadakis and Dr. Mary Konstantaki, of the Institute of Electronic Structure and Laser (IESL) in the Foundation for Research and Technology-Hellas (FORTH) at Crete, Greece.

Appendix 3

Size control of cerium oxide nanocrystals as support for Pt photocatalysts

A3.1. Introduction

High level of emissions from industry and motor transport leads to a dangerous effect on the air and water quality[260]. It is important to reach highly effective conversion of carbon monoxide (CO) to meet the regulations for its emission in air. Therefore, good Pt/CeO_2 catalysts for CO oxidation are critically needed for improving the catalytic converters in exhaust systems of cars[261]. In fact, it has been demonstrated that the photocatalytic CO oxidation on Pt can be driven and controlled through the resonant photoexcitation of the hybridized electronic states due to the strong chemisorption of CO on the supported metal surfaces[262]. The direct photoexcitation mechanism is mediated by the metal-to-adsorbate charge transfer mechanism, based on the predominant metal and molecular character of the hybridized bonding and antibonding states, respectively. The Pt-CO bonds activation with visible photons is the dominant photoexcitation mechanism by using Pt NPs smaller than 5 nm, in which the photon absorption occurs at the high fraction of surface atoms that are directly bonded to CO, differentially from larger NPs where photon absorption occurs mostly at bulk Pt sites. Under the same experimental conditions, larger Pt NPs show lower CO oxidation quantum yields compared to sub-5 nm Pt NPs, due to the spatial separation of the processes of photon absorption and metal-adsorbate bond photoexcitation[262]. Thanks to these properties, Pt based catalysts are widely used to selectively oxidize the CO contaminant in the H_2 fuel gas, improving the durability of fuel cells[263], since the proton exchange membrane fuel cell (PEMFC) performance remarkably decrease due to a poisoning effect on the anode. Recently,

PEMFC has become a real alternative to the fossil fuel energy system, due to the zero-emission and high energy conversion.

Since reducing the size of the noble metal clusters leads to an improvement of their catalytic activity for CO oxidation, it has been recently suggested the preparation of thermally stable single atom catalysts dispersed on metal oxide supports[264]. Catalyst support plays an important role in CO oxidations as it dictates the catalyst-support interactions[265]. Cerium oxide (CeO_2) is a promising support material for metal catalysts because it prevents the sintering of metal catalysts[266]. Furthermore, CeO_2 is able to stabilize Pt in the form of isolated atoms, as already observed for other metal oxide supports[267,268], by trapping single atoms through covalent bonds[266].

A3.2. Experimental methods

The synthesis steps are adapted by following published method[248] and they are conducted by using a standard Schlenk line with dry glassware under nitrogen atmosphere.

A3.2.1. Materials

Cerium (III) nitrate hexahydrate ($Ce(NO_3)_3 \cdot 6H_2O$, 99.99%), 1-octadecene (ODE, 90%), octadecylamine (ODA, 90%) and potassium hydroxide (KOH) were purchased from Sigma Aldrich. Oleylamine (Oam, 70%) was purchased from Acros Organics. Hexanes (ACS grade), toluene (ACS grade), isopropanol (ACS grade) and ethanol (EtOH, ACS grade) were purchased from BDH.

A3.2.2. Synthesis of the small sized CeO_2 NCs batch

The small sized NCs batch is obtained by combining 2 mmol of $Ce(NO_3)_3 \cdot 6H_2O$ with 20 mmol of Oam and 5 mL of ODE in a 50 mL round bottom flask under continuous

magnetic stirring. The mixture is heated to 80 °C and maintained at this temperature for 1 h in order to dissolve completely the cerium salt and homogenize the solution. The solution is then degassed at 120 °C for 1 h under a vacuum pressure below 100 mTorr. The temperature is then raised to 250 °C and the solution is aged for 2 h to react. After the reaction time is over, the dark brown mixture is cooled in air and 7.5 mL of toluene are added to the mixture when the temperature is around 80 °C. The NCs are then purified to remove the unreacted cerium salt, surfactant and solvent. The mixture is centrifuged at 1600 rpm for 10 min and the supernatant is divided in two centrifuge tubes in which isopropanol is added with 5 times of the initial volume and centrifuged at 7000 rpm for 10 min. The precipitated nanocrystals are dispersed with 5 mL of hexane in each centrifuge tube, mixed with 2 times of isopropanol and centrifuged at 7000 rpm for 10 min. The pellets are then dispersed with 5 mL of hexane, yielding a final concentration of CeO_2 NCs around 60 mg/mL.

A3.2.3. Synthesis of the medium sized CeO_2 NCs batch

The medium sized NCs batch is synthetized mixing 7.5 mmol of ODA with 7.5 mmol of Oam with 2.5 mL of ODE in a 50 mL round bottom flask under continuous magnetic stirring. The mixture is heated to 75 °C to dissolve the ODA and, when the solution is clear, 5 mmol of $Ce(NO_3)_3 \cdot 6H_2O$ are added and, the mixture is then mixed at 80 °C for 1 h to homogenize the solution allowing the decrease of the formed purple foam on the top of the solution. The solution is then degassed at 120 °C for 1 h under a vacuum pressure below 100 mTorr. After the degassing is complete, the solution is heated to 230 °C for 30 min. The dark brown mixture is then cooled in air and when the temperature reaches 80 °C, 4 mL of toluene are added to the mixture. The nanocrystals are washed with the same procedure already described previously, yielding a CeO_2 NCs final concentration of around 180 mg/mL.

A3.2.4. Synthesis of the large sized CeO_2 NCs batch

The big sized NCs batch is prepared by mixing 7.5 mmol of ODA with 7.5 mmol of Oam with 2.5 mL of ODE in a 50 mL round bottom flask under continuous magnetic stirring. The mixture is heated to 75 °C to dissolve the ODA and, when the solution is clear, 5 mmol of $Ce(NO_3)_3 \cdot 6H_2O$ are added, and the mixture is then mixed at 80 °C for 1 h to homogenize the solution allowing the decrease of the formed purple foam on the top of the solution. The solution is then degassed at 120 °C for 1 h under a vacuum pressure below 100 mTorr. After the degassing, 40 mmol of MilliQ water are injected to the reaction flask and the solution is heated to 230 °C for 30 min. The dark brown mixture is then cooled in air and when the temperature reaches 80 °C, 4 mL of toluene are added to the mixture. The nanocrystals are washed with the same procedure already described, yielding a CeO_2 NCs final concentration of around 100 mg/mL.

A3.2.5. Size-selective precipitation to improve the particle size distribution

The size distribution of the different batches is narrowed by a post-synthetic precipitation method performed on all the three types of CeO_2 NCs batches. The CeO_2 NCs dispersion is first centrifuged at 2500 rpm for 5 min to remove possible large unstable NPs. Then EtOH, a polar antisolvent, is added dropwise to the NCs dispersion resulting in the precipitation of the unstable fraction of the bigger NCs and the dispersion is centrifuging at 8000 rpm for 10 min. The supernatant is collected and two times of isopropanol are added. After centrifugation at 8000 rpm for 10 min, the pellet is dispersed in 5 mL of hexane and another cycle of size-selective precipitation is performed. The dispersion is then filtered using a 0.45 μm PTFE syringe filter.

A3.2.6. Ligand stripping procedure

The NCs are washed adding two times in volume of EtOH and centrifuged at 8000 rpm for 10 min. In the scale up version of the ligand stripping procedure, 100 mL of CeO_2

NCs in hexane (2 mg/mL) are slowly poured on 100 mL of an aqueous solution of KOH 1 M, forming a two phase mixture. The ligand exchange process, with the subsequent phase transfer of the NCs from hexane to the basic aqueous solution, occurs within 20 – 24 days. The NCs in the aqueous phase are then washed to remove the excess of ligand and KOH by using Amicon Ultra-15 centrifugal filters at 4500 rpm for 15 min for two times. The NCs are collected in 3 mL of H_2O with a final concentration of around 50 mg/mL.

A3.2.7. Characterization

The morphology of the un-doped and doped CeO_2 NCs was investigated by a transmission electron microscope (TEM, JEOL 2010F) operating at 200 kV accelerating voltage. The X-ray diffraction (XRD) analysis was performed on a PANalytical Empyrean X-ray diffractometer with 1.8kW CuKα ceramic X-ray tube (λ = 1.5418 Å), PIXcel3D area detector (2×2 mm^2) and operating at 45 kV and 40 mA. The diffractograms were recorded in parallel-beam geometry and symmetric reflection mode, for 2θ range from 20° to 80°. Thermogravimetric analysis (TGA) was carried out by Thermal Analysis System TGA 2 (Mettler-Toledo International Inc.), in an aluminum crucible, under N_2 flux with a heating rate of 10 °C/min from 25 °C to 600 °C.

A3.3. Results and discussion

The study of the role of the nanocrystal size as support for the photocatalytic CO oxidation on atomically dispersed Pt requires the preparation of three sub-10 nm CeO_2 NCs batches. The desired nanocrystal sizes are around 4 nm, 7 nm and 9 nm in order to have distinguished response variance for the photocatalysis experiments. The adaptation of a colloidal synthesis enables the preparation of three types of CeO_2 NCs, starting from the same cerium precursor, by adding co-surfactants and water. Smaller CeO_2 NCs are obtained by using a previously reported method[248], which has been successfully reproduced, producing pseudo-spherical and uniform CeO_2 nanocrystals with an average diameter of 3.91 ± 0.48 nm (Figure A3.1a). In the proposed bottom-up approach, the molecular units are assembled through the thermal decomposition of the cerium

precursor dissolved in a high boiling point and inert organic solvent. The use of an amine surfactant allows for non-aggregated nanocrystals with uniform size distribution. In this heat-up synthesis, the surfactant, Oam, is a long chain primary alkylamine which is a commonly used ligand in colloidal synthesis due to its low cost and high boiling point[133]. Oam is in liquid state at room temperature, making it easy to be removed via centrifugation from the reaction mixture[133].

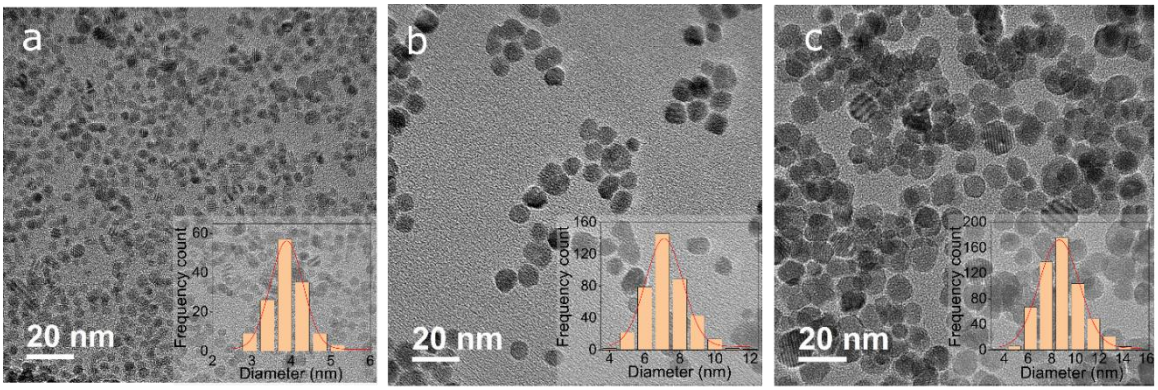

Figure A3.1. TEM images of CeO_2 NCs with average diameter of (a) 3.91 ± 0.48 nm, (b) 7.60 ± 1.27 nm and (c) 9.28 ± 1.79 nm. The diameter size distribution of the different size batch is shown as an inset.

Larger CeO_2 NCs are synthesized by adapting a synthesis method previously reported in the literature[248]. To increase nanocrystal size, the molar ratio between the precursor and the ligand has been changed from 1:10 to 1:3, considering the stabilizing effect of the ligand involved and to promote the formation of bigger nanocrystals[269]. Furthermore, ODA is used with Oam in order to change the synthesis kinetics. As already reported, the addition of water in the reaction mixture can help to increase the size of nanocrystals[270]. Synthetic adaptations including (i) increasing the reactant mixing time in order to better homogenize the system[134], (ii) adding a degassing step which was absent in the previous synthesis, and (iii) reducing the reaction time (30 min instead of 1 h). Specifically, increasing the reactant mixing time prior to raising the temperature to degas temperature helps dissolve the thick layer of foam on the top of the mixture completely. This leads to an increase in yield of CeO_2 nanocrystals (final solution goes from 40 mg/mL to 100 mg/mL given the same volume of solutions). The addition of water after degassing the reaction flask results in larger CeO_2 nanocrystals (9.28 ± 1.79 nm in

diameter), which is in good agreement with prior reports[248]. The shape of large nanocrystals remains pseudo-spherical, similar to that of the small nanocrystals (Figure A3.1). However, a wider size distribution was observed in the large-size synthesis.

To obtain medium size of CeO_2 NCs, we first tried to modify the synthesis method of 4 nm CeO_2. More specifically, we replaced Oam with a tertiary amine, trioctylamine, to reduce the reactivity of the ligand during the nucleation and therefore the synthesis kinetics[271]. The obtained nanocrystals show a pseudo-spherical shape and an average diameter of 5.31 ± 1.13 nm, however the colloidal dispersion in hexane is not stable due to the steric hindrance of trioctylamine, causing a slow aggregation and precipitation of the CeO_2 NCs. Due to the precipitation issue, the synthesis with trioctylamine ligands was not adopted to make medium size. In the development of the 9 nm synthesis, the effect of adding different amounts of water in the reaction mixture is investigated (comparing no water, 20 mmol of water, and 40 mmol of water). The medium CeO_2 NCs with an average diameter of 7.60 ± 1.27 nm are obtained by using the 9 nm synthesis with no addition of water (Figure A3.1b). The addition of 20 mmol of water enables the preparation of pseudo-spherical CeO_2 NCs with 7.74 ± 1.21 nm of average diameter. The addition of 40 mmol water results in CeO_2 NCs with an average diameter of 9.28 ± 1.79 nm (Figure A3.1c).

All the prepared samples show diffraction peaks at 2θ values of 28.46°, 33.08°, 47.38°, 56.23°, 76.53° and 78.92° (Figure A3.2b) which match to the cubic fluorite structure. No other crystalline impurities are observed. The average crystallite sizes of CeO_2 NCs, according to Debye-Scherrer formula for the stronger peak (111), are 4.25 nm, 7.34 nm and 8.69 nm for the small, medium and large CeO_2 NCs. In order to efficiently remove the ligand via KOH reaction to have a phase transfer of NCs from nonpolar to polar solvent, it is important that the amount of Oam and Oam/ODA in the colloidal dispersion in hexane is around 10%. Prior to the ligand stripping procedure, the amount of ligand adsorbed on the NCs surface is measured by TGA. The thermogravimetric profiles show two different weight losses in addition to the loss at around 100 °C which can be attributed to the loss of physically adsorbed water (Figure A3.2a). The first weight loss at around 260 °C can be attributed to the decomposition of free Oam in the dispersion, whereas the

second weight loss at 460 °C can be attributed to the decomposition of the adsorbed Oam on NCs. The weight loss of the adsorbed ligand in the range from 325 °C to 520 °C is of 12.24 wt%, 9.05 wt% and 6.37 wt% for the small, medium and large CeO_2 NCs, respectively. The excess of free Oam in the colloidal dispersion after applying the size selective precipitation to CeO_2 NCs, is removed with another cycle of purification with EtOH before to start the ligand stripping procedure.

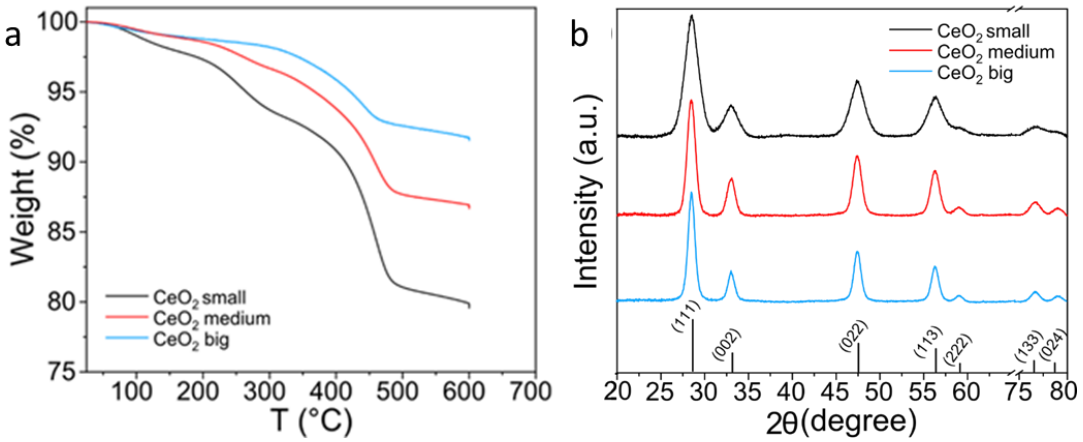

Figure A3.2. (a) TGA curves and (b) XRD patterns of the different CeO_2 NCs batch. Stick reference pattern of CeO_2 is shown along x-axis.

A3.4. Concluding remarks

Pseudo-spherical CeO_2 NCs with tunable sizes are prepared by adapting a colloidal synthesis approach. A phase transfer from hexane to water is obtained with a KOH ligand stripping. The prepared CeO_2 NCs will be used as support of atomically dispersed Pt catalyst, by the group of Prof. Phillip Christopher, (Department of Chemical Engineering in the University of California at Santa Barbara). Pt will be prepared by a wet impregnation technique[264,272], in which $[Pt(NH_3)_4]^{2+}$ complexes are deposited via strong electrostatic adsorption onto CeO_2 NCs, reducing the cluster formation. The photocatalytic experiments will be performed in Harrick High Temperature Reaction chamber, in which a quartz window is added for the catalyst bed illumination[262], in order to evaluate the size effect of the used support for the CO oxidation.

Bibliography

1. Wada, Y.; Flörke, M.; Hanasaki, N.; Eisner, S.; Fischer, G.; Tramberend, S.; Satoh, Y.; Van Vliet, M.T.H.; Yillia, P.; Ringler, C.; et al. Modeling global water use for the 21st century: The Water Futures and Solutions (WFaS) initiative and its approaches. *Geosci. Model Dev.* **2016**, *9*, 175–222.

2. Boretti, A.; Rosa, L. Reassessing the projections of the World Water Development Report. *npj Clean Water* **2019**, *2*.

3. Rakib, M.A.; Sasaki, J.; Matsuda, H.; Fukunaga, M. Severe salinity contamination in drinking water and associated human health hazards increase migration risk in the southwestern coastal part of Bangladesh. *J. Environ. Manage.* **2019**, *240*, 238–248.

4. Crini, G.; Lichtfouse, E. Advantages and disadvantages of techniques used for wastewater treatment. *Environ. Chem. Lett.* **2019**, *17*, 145–155.

5. Escher, B.I.; Aït-Aïssa, S.; Behnisch, P.A.; Brack, W.; Brion, F.; Brouwer, A.; Buchinger, S.; Crawford, S.E.; Du Pasquier, D.; Hamers, T.; et al. Effect-based trigger values for in vitro and in vivo bioassays performed on surface water extracts supporting the environmental quality standards (EQS) of the European Water Framework Directive. *Sci. Total Environ.* **2018**, *628–629*, 748–765.

6. Faust, M.; Backhaus, T.; Altenburger, R.; Dulio, V.; van Gils, J.; Ginebreda, A.; Kortenkamp, A.; Munthe, J.; Posthuma, L.; Slobodnik, J.; et al. Prioritisation of water pollutants: the EU Project SOLUTIONS proposes a methodological framework for the integration of mixture risk assessments into prioritisation procedures under the European Water Framework Directive. *Environ. Sci. Eur.* **2019**, *31*.

7. Nazarpour, A.; Watts, M.J.; Madhani, A.; Elahi, S. Source, Spatial Distribution and Pollution Assessment of Pb, Zn, Cu, and Pb, Isotopes in urban soils of Ahvaz City, a semi-arid metropolis in southwest Iran. *Sci. Rep.* **2019**, *9*, 1–11.

8. Salvo, A.; La Torre, G.L.; Mangano, V.; Casale, K.E.; Bartolomeo, G.; Santini, A.; Granata, T.; Dugo, G. Toxic inorganic pollutants in foods from agricultural producing areas of Southern Italy: Level and risk assessment. *Ecotoxicol. Environ. Saf.* **2018**, *148*, 114–124.

9. Väänänen, K.; Leppänen, M.T.; Chen, X.P.; Akkanen, J. Metal bioavailability in ecological risk assessment of freshwater ecosystems: From science to environmental management. *Ecotoxicol. Environ. Saf.* **2018**, *147*, 430–446.

10. Kim, H.S.; Kim, Y.J.; Seo, Y.R. An Overview of Carcinogenic Heavy Metal:

Molecular Toxicity Mechanism and Prevention. *J. Cancer Prev.* **2015**, *20*, 232–240.

11. Rua-Ibarz, A.; Bolea-Fernandez, E.; Maage, A.; Frantzen, S.; Sanden, M.; Vanhaecke, F. Tracing Mercury Pollution along the Norwegian Coast via Elemental, Speciation, and Isotopic Analysis of Liver and Muscle Tissue of Deep-Water Marine Fish (Brosme brosme). *Environ. Sci. Technol.* **2019**, *53*, 1776–1785.

12. Zhu, S.; Zhang, Z.; Žagar, D. Mercury transport and fate models in aquatic systems: A review and synthesis. *Sci. Total Environ.* **2018**, *639*, 538–549.

13. Chen, C.Y.; Driscoll, C.T.; Eagles-Smith, C.A.; Eckley, C.S.; Gay, D.A.; Hsu-Kim, H.; Keane, S.E.; Kirk, J.L.; Mason, R.P.; Obrist, D.; et al. A Critical Time for Mercury Science to Inform Global Policy. *Environ. Sci. Technol.* **2018**, *52*, 9556–9561.

14. Srogi, K. Monitoring of environmental exposure to polycyclic aromatic hydrocarbons: A review. *Environ. Chem. Lett.* **2007**, *5*, 169–195.

15. Abdel-Shafy, H.I.; Mansour, M.S.M. A review on polycyclic aromatic hydrocarbons: Source, environmental impact, effect on human health and remediation. *Egypt. J. Pet.* **2016**, *25*, 107–123.

16. Klöting, N.; Hesselbarth, N.; Gericke, M.; Kunath, A.; Biemann, R.; Chakaroun, R.; Kosacka, J.; Kovacs, P.; Kern, M.; Stumvoll, M.; et al. Di-(2-ethylhexyl)-phthalate (DEHP) causes impaired adipocyte function and alters serum metabolites. *PLoS One* **2015**, *10*, 1–19.

17. Gardner, M.; Jones, V.; Comber, S.; Scrimshaw, M.D.; Coello-Garcia, T.; Cartmell, E.; Lester, J.; Ellor, B. Performance of UK wastewater treatment works with respect to trace contaminants. *Sci. Total Environ.* **2013**, *456–457*, 359–369.

18. Trajanov, A.; Kuzmanovski, V.; Real, B.; Perreau, J.M.; Džeroski, S.; Debeljak, M. Modeling the risk of water pollution by pesticides from imbalanced data. *Environ. Sci. Pollut. Res.* **2018**, *25*, 18781–18792.

19. Rizzati, V.; Briand, O.; Guillou, H.; Gamet-Payrastre, L. Effects of pesticide mixtures in human and animal models: An update of the recent literature. *Chem. Biol. Interact.* **2016**, *254*, 231–246.

20. Vizcaíno, P.; Pistocchi, A. A GIS model-based assessment of the environmental distribution of γ-hexachlorocyclohexane in European soils and waters. *Environ. Pollut.* **2010**, *158*, 3017–3027.

21. Merlin, G.; Vuillod, M.; Lissolo, T.; Clement, B. Fate and bioaccumulation of isoproturon in outdoor aquatic microcosms. *Environ. Toxicol. Chem.* **2002**, *21*, 1236–1242.

22. Cristale, J.; García Vázquez, A.; Barata, C.; Lacorte, S. Priority and emerging flame retardants in rivers: Occurrence in water and sediment, Daphnia magna toxicity and risk assessment. *Environ. Int.* **2013**, *59*, 232–243.

23. Rule, K.L.; Comber, S.D.W.; Ross, D.; Thornton, A.; Makropoulos, C.K.; Rautiu, R. Sources of priority substances entering an urban wastewater catchment-trace organic chemicals. *Chemosphere* **2006**, *63*, 581–591.

24. Schulze, S.; Zahn, D.; Montes, R.; Rodil, R.; Quintana, J.B.; Knepper, T.P.; Reemtsma, T.; Berger, U. Occurrence of emerging persistent and mobile organic contaminants in European water samples. *Water Res.* **2019**, 80–90.

25. Barrios-Estrada, C.; de Jesús Rostro-Alanis, M.; Muñoz-Gutiérrez, B.D.; Iqbal, H.M.N.; Kannan, S.; Parra-Saldívar, R. Emergent contaminants: Endocrine disruptors and their laccase-assisted degradation – A review. *Sci. Total Environ.* **2018**, *612*, 1516–1531.

26. Evans, A.E.; Mateo-Sagasta, J.; Qadir, M.; Boelee, E.; Ippolito, A. Agricultural water pollution: key knowledge gaps and research needs. *Curr. Opin. Environ. Sustain.* **2019**, *36*, 20–27.

27. Hernández-Chover, V.; Bellver-Domingo, Á.; Hernández-Sancho, F. Efficiency of wastewater treatment facilities: The influence of scale economies. *J. Environ. Manage.* **2018**, *228*, 77–84.

28. Jassby, D.; Cath, T.Y.; Buisson, H. The role of nanotechnology in industrial water treatment. *Nat. Nanotechnol.* **2018**, *13*, 670–672.

29. Rizzo, L.; Malato, S.; Antakyali, D.; Beretsou, V.G.; Đolić, M.B.; Gernjak, W.; Heath, E.; Ivancev-Tumbas, I.; Karaolia, P.; Lado Ribeiro, A.R.; et al. Consolidated vs new advanced treatment methods for the removal of contaminants of emerging concern from urban wastewater. *Sci. Total Environ.* **2019**, *655*, 986–1008.

30. Matamoros, V.; Rodríguez, Y.; Albaigés, J. A comparative assessment of intensive and extensive wastewater treatment technologies for removing emerging contaminants in small communities. *Water Res.* **2016**, *88*, 777–785.

31. Amor, C.; Marchão, L.; Lucas, M.S.; Peres, J.A. Application of advanced oxidation processes for the treatment of recalcitrant agro-industrial wastewater: A review. *Water (Switzerland)* **2019**, *11*, 205.

32. Zodrow, K.R.; Li, Q.; Buono, R.M.; Chen, W.; Daigger, G.; Duenas-Osorio, L.; Elimelech, M.; Huang, X.; Jiang, G.; Kim, J.; et al. Advanced Materials, Technologies, and Complex Systems Analyses: Emerging Opportunities to Enhance Urban Water Security. *Environ. Sci. Technol.* **2017**, *51*, 10274–10281.

33. Vo, J.; Stapf, M.; Miehe, U.; Wagner, M. Systematic Review of Toxicity Removal

by Advanced Wastewater Treatment Technologies via Ozonation and Activated Carbon. *Environ. Sci. Technol.* **2019**, *53*, 7215–7233.

34. Ibn Abdul Hamid, K.; Sanciolo, P.; Gray, S.; Duke, M.; Muthukumaran, S. Comparison of the effects of ozone, biological activated carbon (BAC) filtration and combined ozone-BAC pre-treatments on the microfiltration of secondary effluent. *Sep. Purif. Technol.* **2019**, *215*, 308–316.

35. Lee, S.; Ihara, M.; Yamashita, N.; Tanaka, H. Improvement of virus removal by pilot-scale coagulation-ultrafiltration process for wastewater reclamation: Effect of optimization of pH in secondary effluent. *Water Res.* **2017**, *114*, 23–30.

36. Garcia-Ivars, J.; Martella, L.; Massella, M.; Carbonell-Alcaina, C.; Alcaina-Miranda, M.I.; Iborra-Clar, M.I. Nanofiltration as tertiary treatment method for removing trace pharmaceutically active compounds in wastewater from wastewater treatment plants. *Water Res.* **2017**, *125*, 360–373.

37. Roy, Y.; Warsinger, D.M.; Lienhard, J.H. Effect of temperature on ion transport in nanofiltration membranes: Diffusion, convection and electromigration. *Desalination* **2017**, *420*, 241–257.

38. Li, D.; Yan, Y.; Wang, H. Recent advances in polymer and polymer composite membranes for reverse and forward osmosis processes. *Prog. Polym. Sci.* **2016**, *61*, 104–155.

39. Korenak, J.; Basu, S.; Balakrishnan, M.; Hélix-Nielsen, C.; Petrinic, I. Forward osmosis in wastewater treatment processes. *Acta Chim. Slov.* **2017**, *64*, 83–94.

40. Achilli, A.; Cath, T.Y.; Childress, A.E. Selection of inorganic-based draw solutions for forward osmosis applications. *J. Memb. Sci.* **2010**, *364*, 233–241.

41. Kim, S.; Chu, K.H.; Al-Hamadani, Y.A.J.; Park, C.M.; Jang, M.; Kim, D.H.; Yu, M.; Heo, J.; Yoon, Y. Removal of contaminants of emerging concern by membranes in water and wastewater: A review. *Chem. Eng. J.* **2018**, *335*, 896–914.

42. Lotfi, F.; Chekli, L.; Phuntsho, S.; Hong, S.; Choi, J.Y.; Shon, H.K. Understanding the possible underlying mechanisms for low fouling tendency of the forward osmosis and pressure assisted osmosis processes. *Desalination* **2017**, *421*, 89–98.

43. Rajasulochana, P.; Preethy, V. Comparison on efficiency of various techniques in treatment of waste and sewage water – A comprehensive review. *Resour. Technol.* **2016**, *2*, 175–184.

44. Dichiara, A.B.; Weinstein, S.J.; Rogers, R.E. On the Choice of Batch or Fixed Bed Adsorption Processes for Wastewater Treatment. *Ind. Eng. Chem. Res.* **2015**, *54*, 8579–8586.

45. Ahmedna, M.; Marshall, W.E.; Rao, R.M. Production of granular activated carbons from select agricultural by-products and evaluation of their physical, chemical and adsorption properties. *Bioresour. Technol.* **2000**, *71*, 113–123.

46. Ahmad, A.A.; Hameed, B.H. Fixed-bed adsorption of reactive azo dye onto granular activated carbon prepared from waste. *J. Hazard. Mater.* **2010**, *175*, 298–303.

47. Santhy, K.; Selvapathy, P. Removal of reactive dyes from wastewater by adsorption on coir pith activated carbon. *Bioresour. Technol.* **2006**, *97*, 1329–1336.

48. Dittmar, S.; Zietzschmann, F.; Mai, M.; Worch, E.; Jekel, M.; Ruhl, A.S. Simulating Effluent Organic Matter Competition in Micropollutant Adsorption onto Activated Carbon Using a Surrogate Competitor. *Environ. Sci. Technol.* **2018**, *52*, 7859–7866.

49. Centeno, T.A. Apple Waste: A Sustainable Source of Carbon Materials and Valuable Compounds. *ACS Sustain. Chem. Eng.* **2019**, *7*, 17335–17343.

50. De Gisi, S.; Lofrano, G.; Grassi, M.; Notarnicola, M. Characteristics and adsorption capacities of low-cost sorbents for wastewater treatment: A review. *Sustain. Mater. Technol.* **2016**, *9*, 10–40.

51. Crini, G. Non-conventional low-cost adsorbents for dye removal: A review. *Bioresour. Technol.* **2006**, *97*, 1061–1085.

52. Bhatnagar, A.; Sillanpää, M.; Witek-Krowiak, A. Agricultural waste peels as versatile biomass for water purification - A review. *Chem. Eng. J.* **2015**, *270*, 244–271.

53. Anastopoulos, I.; Kyzas, G.Z. Agricultural peels for dye adsorption: A review of recent literature. *J. Mol. Liq.* **2014**, *200*, 381–389.

54. Mallampati, R.; Xuanjun, L.; Adin, A.; Valiyaveettil, S. Fruit peels as efficient renewable adsorbents for removal of dissolved heavy metals and dyes from water. *ACS Sustain. Chem. Eng.* **2015**, *3*, 1117–1124.

55. Kostić, M.; Đorđević, M.; Mitrović, J.; Velinov, N.; Bojić, D.; Antonijević, M.; Bojić, A. Removal of cationic pollutants from water by xanthated corn cob: optimization, kinetics, thermodynamics, and prediction of purification process. *Environ. Sci. Pollut. Res.* **2017**, *24*, 17790–17804.

56. Miklos, D.B.; Remy, C.; Jekel, M.; Linden, K.G.; Drewes, J.E.; Hübner, U. Evaluation of advanced oxidation processes for water and wastewater treatment – A critical review. *Water Res.* **2018**, *139*, 118–131.

57. Ribeiro, A.R.; Nunes, O.C.; Pereira, M.F.R.; Silva, A.M.T. An overview on the

advanced oxidation processes applied for the treatment of water pollutants defined in the recently launched Directive 2013/39/EU. *Environ. Int.* **2015**, *75*, 33–51.

58. Piras, F.; Santoro, O.; Pastore, T.; Pio, I.; De Dominicis, E.; Gritti, E.; Caricato, R.; Lionetto, M.G.; Mele, G.; Santoro, D. Controlling micropollutants in tertiary municipal wastewater by O3/H2O2, granular biofiltration and UV254/H2O2 for potable reuse applications. *Chemosphere* **2020**, *239*, 124635.

59. Bourgin, M.; Borowska, E.; Helbing, J.; Hollender, J.; Kaiser, H.P.; Kienle, C.; McArdell, C.S.; Simon, E.; von Gunten, U. Effect of operational and water quality parameters on conventional ozonation and the advanced oxidation process O3/H2O2: Kinetics of micropollutant abatement, transformation product and bromate formation in a surface water. *Water Res.* **2017**, *122*, 234–245.

60. Rodríguez-Chueca, J.; Varella della Giustina, S.; Rocha, J.; Fernandes, T.; Pablos, C.; Encinas, Á.; Barceló, D.; Rodríguez-Mozaz, S.; Manaia, C.M.; Marugán, J. Assessment of full-scale tertiary wastewater treatment by UV-C based-AOPs: Removal or persistence of antibiotics and antibiotic resistance genes? *Sci. Total Environ.* **2019**, *652*, 1051–1061.

61. Zhang, M. hui; Dong, H.; Zhao, L.; Wang, D. xi; Meng, D. A review on Fenton process for organic wastewater treatment based on optimization perspective. *Sci. Total Environ.* **2019**, *670*, 110–121.

62. Paździor, K.; Bilińska, L.; Ledakowicz, S. A review of the existing and emerging technologies in the combination of AOPs and biological processes in industrial textile wastewater treatment. *Chem. Eng. J.* **2019**, *376*, 120597.

63. Fiorenza, R.; Bellardita, M.; D'Urso, L.; Compagnini, G.; Palmisano, L.; Scirè, S. Au/TiO2-CeO2 Catalysts for Photocatalytic Water Splitting and VOCs Oxidation Reactions. *Catalysts* **2016**, *6*, 121.

64. Fujishima, A.; Kenichi, H. Electrochemical Photolysis of Water at a Semiconductor Electrode. *Nature* **1972**, *238*, 37–38.

65. Athanasekou, C.P.P.; Likodimos, V.; Falaras, P. Recent developments of TiO2 photocatalysis involving advanced oxidation and reduction reactions in water. *J. Environ. Chem. Eng.* **2018**, *6*, 7386–7394.

66. Abdullah, A.M.; O'Shea, K.E. TiO 2 photocatalytic degradation of the flame retardant tris (2-chloroethyl) phosphate (TCEP) in aqueous solution: A detailed kinetic and mechanistic study. *J. Photochem. Photobiol. A Chem.* **2019**, *377*, 130–137.

67. Atitar, M.F.; Bouziani, A.; Dillert, R.; El Azzouzi, M.; Bahnemann, D.W. Photocatalytic degradation of the herbicide imazapyr: Do the initial degradation rates correlate with the adsorption kinetics and isotherms? *Catal. Sci. Technol.* **2018**, *8*, 985–995.

68. Augugliaro, V.; Loddo, V.; Pagliaro, M.; Palmisano, G.; Palmisano, L. *Clean by Light Irradiation Practical Applications of Supported TiO2*; 2010; ISBN 9781847558701.

69. Shannon, M.A.; Bohn, P.W.; Elimelech, M.; Georgiadis, J.G.; Marĩas, B.J.; Mayes, A.M. Science and technology for water purification in the coming decades. *Nature* **2008**, *452*, 301–310.

70. Adeleye, A.S.; Conway, J.R.; Garner, K.; Huang, Y.; Su, Y.; Keller, A.A. Engineered nanomaterials for water treatment and remediation: Costs, benefits, and applicability. *Chem. Eng. J.* **2016**, *286*, 640–662.

71. Alvarez, P.J.J.; Chan, C.K.; Elimelech, M.; Halas, N.J.; Villagrán, D. Emerging opportunities for nanotechnology to enhance water security. *Nat. Nanotechnol.* **2018**, *13*, 634–641.

72. Mauter, M.S.; Zucker, I.; Perreault, F.; Werber, J.R.; Kim, J.; Elimelech, M. The role of nanotechnology in tackling global water challenges. *Nat. Sustain.* **2018**, *1*, 166–175.

73. Bouziotas, D.; Duuren, D. Van; Alphen, H. Van; Frijns, J.; Nikolopoulos, D.; Makropoulos, C. Towards Circular Water Neighborhoods : Simulation-Based Decision Support for Integrated. *Water* **2019**, *11*.

74. Eggimann, S.; Truffer, B.; Feldmann, U.; Maurer, M. Screening European market potentials for small modular wastewater treatment systems – an inroad to sustainability transitions in urban water management ? *Land use policy* **2018**, *78*, 711–725.

75. Gehrke, I.; Geiser, A.; Somborn-Schulz, A. Innovations in nanotechnology for water treatment. *Nanotechnol. Sci. Appl.* **2015**, *8*, 1–17.

76. Neghi, N.; Kumar, M.; Burkhalov, D. Synthesis and application of stable, reusable TiO 2 polymeric composites for photocatalytic removal of metronidazole: Removal kinetics and density functional analysis. *Chem. Eng. J.* **2019**, *359*, 963–975.

77. Podasca, V.E.; Buruiana, T.; Buruiana, E.C. Photocatalytic degradation of Rhodamine B dye by polymeric films containing ZnO, Ag nanoparticles and polypyrrole. *J. Photochem. Photobiol. A Chem.* **2019**, *371*, 188–195.

78. Morselli, D.; Campagnolo, L.; Prato, M.; Papadopoulou, E.L.; Scarpellini, A.; Athanassiou, A.; Fragouli, D. Ceria/Gold Nanoparticles in Situ Synthesized on Polymeric Membranes with Enhanced Photocatalytic and Radical Scavenging Activity . *ACS Appl. Nano Mater.* **2018**, *1*, 5601–5611.

79. Colmenares, J.C.; Kuna, E. Photoactive Hybrid Catalysts Based on Natural and Synthetic Polymers : A Comparative Overview. *Molecules* **2017**, *22*.

80. Di Mauro, A.; Cantarella, M.; Nicotra, G.; Pellegrino, G.; Gulino, A.; Brundo, M.V.; Privitera, V.; Impellizzeri, G.; Mauro, A. Di; Cantarella, M.; et al. Novel synthesis of ZnO/PMMA nanocomposites for photocatalytic applications. *Sci. Rep.* **2017**, *7*, 1–12.

81. Hegedűs, P.; Szabó-Bárdos, E.; Horváth, O.; Szabó, P.; Horváth, K. Investigation of a TiO2 photocatalyst immobilized with poly(vinyl alcohol). *Catal. Today* **2017**, *284*, 179–186.

82. McNaught, A.D.; Wilkinson, A. *Compendium of Chemical Terminology, 2nd ed. (the "Gold Book")*; Blackwell Scientific Publications, Oxford, 1997; ISBN 0-9678550-9-8.

83. Schnepp, Z. Biopolymers as a flexible resource for nanochemistry. *Angew. Chemie - Int. Ed.* **2013**, *52*, 1096–1108.

84. Magrì, D.; Caputo, G.; Perotto, G.; Scarpellini, A.; Colusso, E.; Drago, F.; Martucci, A.; Athanassiou, A.; Fragouli, D. Titanate Fibroin Nanocomposites: A Novel Approach for the Removal of Heavy-Metal Ions from water. *ACS Appl. Mater. Interfaces* **2017**, acsami.7b15440.

85. Ling, S.; Kaplan, D.L.; Buehler, M.J. Nanofibrils in nature and materials engineering. *Nat. Rev. Mater.* **2018**, *3*, 1–15.

86. Poupart, R.; Grande, D.; Carbonnier, B.; Le Droumaguet, B. Porous polymers and metallic nanoparticles: A hybrid wedding as a robust method toward efficient supported catalytic systems. *Prog. Polym. Sci.* **2019**, *96*, 21–42.

87. Zhao, X.; Lv, L.; Pan, B.; Zhang, W.; Zhang, S.; Zhang, Q. Polymer-supported nanocomposites for environmental application: A review. *Chem. Eng. J.* **2011**, *170*, 381–394.

88. Osada, Y.; Gong, J.P. Soft and wet materials: Polymer gels. *Adv. Mater.* **1998**, *10*, 827–837.

89. Vareda, J.P.; Lamy-Mendes, A.; Durães, L. A reconsideration on the definition of the term aerogel based on current drying trends. *Microporous Mesoporous Mater.* **2018**, *258*, 211–216.

90. Boss, E.A.; Filho, R.M.; Vasco De Toledo, E.C. Freeze drying process: Real time model and optimization. *Chem. Eng. Process. Process Intensif.* **2004**, *43*, 1475–1485.

91. Abdelwahed, W.; Degobert, G.; Stainmesse, S.; Fessi, H. Freeze-drying of nanoparticles: Formulation, process and storage considerations. *Adv. Drug Deliv. Rev.* **2006**, *58*, 1688–1713.

92. Venkatraman, P.; Rader, C.; Bohmann, N.; Foster, E.J. Structure-property-

processing relationship of ethanol solvent exchanged PEEK. *Polymer (Guildf).* **2019**, *169*, 154–159.

93. Zhang, X.; Heinonen, S.; Levänen, E. Applications of supercritical carbon dioxide in materials processing and synthesis. *RSC Adv.* **2014**, *4*, 61137–61152.

94. Lide, D.R.; Baysinger, G.; Berger, L.I.; Kehiaian, H. V; Roth, D.L.; Zwillinger, D.; Goldberg, R.N.; Haynes, W.M. *CRC Handbook of Chemistry and Physics, 89th Edition (Internet Version 2009)*; 89th ed.; CRC Press/Taylor and Francis, Boca Raton, FL, 2009;

95. Benali, M.; Boumghar, Y. Supercritical Fluid-Assisted Drying. In *Handbook of Industrial Drying Edition: 4th*; Mujumdar, A.S., Ed.; CRC Press, 2014; pp. 1261–1269.

96. Caro-León, F.J.; Argüelles-Monal, W.; Carvajal-Millán, E.; López-Franco, Y.L.; Goycoolea-Valencia, F.M.; San Román del Barrio, J.; Lizardi-Mendoza, J. Production and characterization of supercritical CO2 dried chitosan nanoparticles as novel carrier device. *Carbohydr. Polym.* **2018**, *198*, 556–562.

97. Takeshita, S.; Sadeghpour, A.; Malfait, W.J.; Konishi, A.; Otake, K.; Yoda, S. Formation of Nanofibrous Structure in Biopolymer Aerogel during Supercritical CO 2 Processing: The Case of Chitosan Aerogel. *Biomacromolecules* **2019**, *20*, 2051–2057.

98. Xue, J.; Wu, T.; Dai, Y.; Xia, Y. Electrospinning and electrospun nanofibers: Methods, materials, and applications. *Chem. Rev.* **2019**, *119*, 5298–5415.

99. Eda, G.; Shivkumar, S. Bead-to-Fiber Transition in Electrospun Polystyrene. *J. Appl. Polym. Sci.* **2007**, *106*, 475–487.

100. Koombhongse, S.; Liu, W.; Reneker, D.H. Flat Polymer Ribbons and Other Shapes by Electrospinning. **2001**, *39*, 2598–2606.

101. Megelski, S.; Stephens, J.S.; Bruce Chase, D.; Rabolt, J.F. Micro- and nanostructured surface morphology on electrospun polymer fibers. *Macromolecules* **2002**, *35*, 8456–8466.

102. Jiang, L.; Wang, L.; Wang, N.; Gong, S.; Wang, L.; Li, Q.; Shen, C.; Turng, L.S. Fabrication of polycaprolactone electrospun fibers with different hierarchical structures mimicking collagen fibrils for tissue engineering scaffolds. *Appl. Surf. Sci.* **2018**, *427*, 311–325.

103. Ewaldz, E.; Brettmann, B. Molecular Interactions in Electrospinning: From Polymer Mixtures to Supramolecular Assemblies. *ACS Appl. Polym. Mater.* **2019**, *1*, 298–308.

104. Thompson, C.J.; Chase, G.G.; Yarin, A.L.; Reneker, D.H. Effects of parameters on

nanofiber diameter determined from electrospinning model. *Polymer (Guildf).* **2007**, *48*, 6913–6922.

105. Wang, C.; Wang, J.; Zeng, L.; Qiao, Z.; Liu, X.; Liu, H.; Zhang, J.; Ding, J. Fabrication of electrospun polymer nanofibers with diverse morphologies. *Molecules* **2019**, *24*, 834.

106. Putti, M.; Simonet, M.; Solberg, R.; Peters, G.W.M. Electrospinning poly(ε-caprolactone) under controlled environmental conditions: Influence on fiber morphology and orientation. *Polymer (Guildf).* **2015**, *63*, 189–195.

107. Rajzer, I.; Menaszek, E.; Castano, O. Electrospun polymer scaffolds modified with drugs for tissue engineering. *Mater. Sci. Eng. C* **2017**, *77*, 493–499.

108. Mirjalili, M.; Zohoori, S. Review for application of electrospinning and electrospun nanofibers technology in textile industry. *J. Nanostructure Chem.* **2016**, *6*, 207–213.

109. Zhang, D.L.; Zha, J.W.; Li, W.K.; Li, C.Q.; Wang, S.J.; Wen, Y.; Dang, Z.M. Enhanced thermal conductivity and mechanical property through boron nitride hot string in polyvinylidene fluoride fibers by electrospinning. *Compos. Sci. Technol.* **2018**, *156*, 1–7.

110. Fuh, Y.K.; Wang, B.S. Near field sequentially electrospun three-dimensional piezoelectric fibers arrays for self-powered sensors of human gesture recognition. *Nano Energy* **2016**, *30*, 677–683.

111. Komeily-Nia, Z.; Montazer, M.; Heidarian, P.; Nasri-Nasrabadi, B. Smart photoactive soft materials for environmental cleaning and energy production through incorporation of nanophotocatalyst on polymers and textiles. *Polym. Adv. Technol.* **2019**, *30*, 235–253.

112. Colvin, V.L. The potential environmental impact of engineered nanomaterials. *Nat. Biotechnol.* **2003**, *21*, 1166–1170.

113. Stark, W.J.; Stoessel, P.R.; Wohlleben, W.; Hafner, A. Industrial applications of nanoparticles. *Chem. Soc. Rev.* **2015**, *44*, 5793–5805.

114. Ognibene, G.; Cristaldi, D.A.; Fiorenza, R.; Blanco, I.; Cicala, G.; Scirè, S.; Fragalà, M.E. Photoactivity of hierarchically nanostructured ZnO-PES fibre mats for water treatments. *RSC Adv.* **2016**, *6*, 42778–42785.

115. Maučec, D.; Šuligoj, A.; Ristić, A.; Dražić, G.; Pintar, A.; Tušar, N.N. Titania versus zinc oxide nanoparticles on mesoporous silica supports as photocatalysts for removal of dyes from wastewater at neutral pH. *Catal. Today* **2018**, *310*, 32–41.

116. Wang, Y.; Wang, X.; Guan, J.; Yang, L.; Ren, Y.; Nasir, N.; Wu, H.; Chen, Z.; Jiang, Z. 110th Anniversary: Mixed Matrix Membranes with Fillers of Intrinsic

Nanopores for Gas Separation. *Ind. Eng. Chem. Res.* **2019**, *58*, 7706–7724.

117. Lofrano, G.; Carotenuto, M.; Libralato, G.; Domingos, R.F.; Markus, A.; Dini, L.; Gautam, R.K.; Baldantoni, D.; Rossi, M.; Sharma, S.K.; et al. Polymer functionalized nanocomposites for metals removal from water and wastewater: An overview. *Water Res.* **2016**, *92*, 22–37.

118. Fu, S.; Sun, Z.; Huang, P.; Li, Y.; Hu, N. Some basic aspects of polymer nanocomposites: A critical review. *Nano Mater. Sci.* **2019**, *1*, 2–30.

119. Pastoriza-Santos, I.; Kinnear, C.; Pérez-Juste, J.; Mulvaney, P.; Liz-Marzán, L.M. Plasmonic polymer nanocomposites. *Nat. Rev. Mater.* **2018**, *3*, 375–391.

120. Burgos-mármol, J.J.; Patti, A. Unveiling the impact of nanoparticle size dispersity on the behavior of polymer nanocomposites. *Polymer (Guildf).* **2017**, *113*, 92–104.

121. Morselli, D.; Scarpellini, A.; Athanassiou, A.; Fragouli, D. Single step in situ formation of porous zinc oxide/PMMA nanocomposites by pulsed laser irradiation: Kinetic aspects and mechanisms. *RSC Adv.* **2016**, *6*, 11412–11418.

122. Morselli, D.; Valentini, P.; Perotto, G.; Scarpellini, A.; Pompa, P.P.; Athanassiou, A.; Fragouli, D. Thermally-induced in situ growth of ZnO nanoparticles in polymeric fibrous membranes. *Compos. Sci. Technol.* **2017**, *149*, 11–19.

123. Thoniyot, P.; Tan, M.J.; Karim, A.A.; Young, D.J.; Loh, X.J. Nanoparticle–Hydrogel Composites: Concept, Design, and Applications of These Promising, Multi-Functional Materials. *Adv. Sci.* **2015**, *2*, 1–13.

124. Adhikari, S.; Selvaraj, S.; Kim, D.H. Progress in Powder Coating Technology Using Atomic Layer Deposition. *Adv. Mater. Interfaces* **2018**, *5*, 1–20.

125. Crick, C.R.; Bear, J.C.; Kafizas, A.; Parkin, I.P. Superhydrophobic photocatalytic surfaces through direct incorporation of titania nanoparticles into a polymer matrix by aerosol assisted chemical vapor deposition. *Adv. Mater.* **2012**, *24*, 3505–3508.

126. De Filpo, G.; Pantuso, E.; Armentano, K.; Formoso, P.; Di Profio, G.; Poerio, T.; Fontananova, E.; Meringolo, C.; Mashin, A.I.; Nicoletta, F.P. Chemical vapor deposition of photocatalyst nanoparticles on PVDF membranes for advanced oxidation processes. *Membranes (Basel).* **2018**, *8*, 35.

127. Bedar, A.; Lenka, R.K.; Goswami, N.; Kumar, V.; Debnath, A.K.; Sen, D.; Kumar, S.; Ghodke, S.; Tewari, P.K.; Bindal, R.C.; et al. Polysulfone–Ceria Mixed-Matrix Membrane with Enhanced Radiation Resistance Behavior. *ACS Appl. Polym. Mater.* **2019**, *1*, 1854–1865.

128. Corredor, L.M.; Husein, M.M.; Maini, B.B. A review of polymer nanohybrids for oil recovery. *Adv. Colloid Interface Sci.* **2019**, *272*, 102018.

129. Rong, M.Z.; Zhang, M.Q.; Ruan, W.H. Surface modification of nanoscale fillers for improving properties of polymer nanocomposites : a review. *Mater. Sci. Technol.* **2006**, *22*, 787–796.

130. Jiao, Y.; Tibbits, A.; Gillman, A.; Hsiao, M.S.; Buskohl, P.; Drummy, L.F.; Vaia, R.A. Deformation Behavior of Polystyrene-Grafted Nanoparticle Assemblies with Low Grafting Density. *Macromolecules* **2018**, *51*, 7257–7265.

131. Wu, Z.; Yang, S.; Wu, W. Shape control of inorganic nanoparticles from solution. *Nanoscale* **2016**, *8*, 1237–1259.

132. Gadiyar, C.; Loiudice, A.; Buonsanti, R. Colloidal nanocrystals for photoelectrochemical and photocatalytic water splitting. *J. Phys. D. Appl. Phys.* **2017**, *50*.

133. Mourdikoudis, S.; Liz-Marzán, L.M. Oleylamine in nanoparticle synthesis. *Chem. Mater.* **2013**, *25*, 1465–1476.

134. Van Embden, J.; Chesman, A.S.R.; Jasieniak, J.J. The heat-up synthesis of colloidal nanocrystals. *Chem. Mater.* **2015**, *27*, 2246–2285.

135. Kudera, S.; Manna, L. Bottom-Up Synthesis of Nanosized Objects. In *COLLOIDAL FOUNDATIONS OF NANOSCIENCE*; Berti, D., Palazzo, G., Eds.; Elsevier, 2014; pp. 47–80 ISBN 9780444595416.

136. Vallé, K.; Belleville, P.; Pereira, F.; Sanchez, C. Hierarchically structured transparent hybrid membranes by in situ growth of mesostructured organosilica in host polymer. *Nat. Mater.* **2006**, *5*, 107–111.

137. Liu, G.; Chen, Z.; Jiang, X.; Feng, D.Q.; Zhao, J.; Fan, D.; Wang, W. In-situ hydrothermal synthesis of molecularly imprinted polymers coated carbon dots for fluorescent detection of bisphenol A. *Sensors Actuators, B Chem.* **2016**, *228*, 302–307.

138. Cook, W.D.; Nghiem, Q.D.; Chen, Q.; Chen, F.; Sangermano, M. Simultaneous photoinduced silver nanoparticles formation and cationic polymerization of divinyl ethers. *Macromolecules* **2011**, *44*, 4065–4071.

139. Porel, S.; Singh, S.; Harsha, S.S.; Rao, D.N.; Radhakrishnan, T.P. Nanoparticle-embedded polymer: In situ synthesis, free-standing films with highly monodisperse silver nanoparticles and optical limiting. *Chem. Mater.* **2005**, *17*, 9–12.

140. Porel, S.; Hebalkar, N.; Sreedhar, B.; Radhakrishnan, T.P. Palladium nanowire from precursor nanowire: Crystal-to-crystal transformation via in situ reduction by polymer matrix. *Adv. Funct. Mater.* **2007**, *17*, 2550–2556.

141. Hong, Y.; Li, D.; Zheng, J.; Zou, G. In situ growth of ZnO nanocrystals from solid

electrospun nanofiber matrixes. *Langmuir* **2006**, *22*, 7331–7334.

142. Feng, J.; Athanassiou, A.; Bonaccorso, F.; Fragouli, D. Enhanced electrical conductivity of poly(Methyl methacrylate) filled with graphene and in situ synthesized gold nanoparticles. *Nano Futur.* **2018**, *2*, 0–8.

143. Zhang, J.; Maurer, F.H.J.; Yang, M. In situ formation of TiO2 in electrospun poly(methyl methacrylate) nanohybrids. *J. Phys. Chem. C* **2011**, *115*, 10431–10441.

144. Pikulin, A.; Smirnov, A.A.; Bityurin, N. A model for local generation of nanoparticles in photoinduced nanocomposites by the focused laser light. *Appl. Surf. Sci.* **2019**, *475*, 1010–1020.

145. Galwey, A.K. Solid state reaction kinetics, mechanisms and catalysis: a retrospective rational review. *React. Kinet. Mech. Catal.* **2015**, *114*, 1–29.

146. Gotor, F.J.; José; Criado, M.; Malek, J.; Koga, N. Kinetic analysis of solid-state reactions: The universality of master plots for analyzing isothermal and nonisothermal experiments. *J. Phys. Chem. A* **2000**, *104*, 10777–10782.

147. Boles, M.A.; Ling, D.; Hyeon, T.; Talapin, D. V. Erratum: The surface science of nanocrystals (Nature Materials (2016) 15 (141-153)). *Nat. Mater.* **2016**, *15*, 364.

148. Marín, F.R.; Soler-Rivas, C.; Benavente-García, O.; Castillo, J.; Pérez-Alvarez, J.A. By-products from different citrus processes as a source of customized functional fibres. *Food Chem.* **2007**, *100*, 736–741.

149. Widmer, W.; Zhou, W.; Grohmann, K. Pretreatment effects on orange processing waste for making ethanol by simultaneous saccharification and fermentation. *Bioresour. Technol.* **2010**, *101*, 5242–5249.

150. Embaby, A.M.; Masoud, A.A.; Marey, H.S.; Shaban, N.Z.; Ghonaim, T.M. Raw agro-industrial orange peel waste as a low cost effective inducer for alkaline polygalacturonase production from Bacillus licheniformis SHG10. *Springerplus* **2014**, *3*, 1–13.

151. Chavan, A.A.; Pinto, J.; Liakos, I.; Bayer, I.S.; Lauciello, S.; Athanassiou, A.; Fragouli, D. Spent Coffee Bioelastomeric Composite Foams for the Removal of Pb2+ and Hg2+ from Water. *ACS Sustain. Chem. Eng.* **2016**, *4*, 5495–5502.

152. Tran, T.N.; Athanassiou, A.; Basit, A.; Bayer, I.S. Starch-based bio-elastomers functionalized with red beetroot natural antioxidant. *Food Chem.* **2017**, *216*, 324–333.

153. Tran, T.N.; Bayer, I.S.; Heredia-Guerrero, J.A.; Frugone, M.; Lagomarsino, M.; Maggio, F.; Athanassiou, A. Cocoa Shell Waste Biofilaments for 3D Printing Applications. *Macromol. Mater. Eng.* **2017**, *302*.

154. Agunsoye, J.O.; Aigbodion, V.S. Bagasse filled recycled polyethylene bio-composites: Morphological and mechanical properties study. *Results Phys.* **2013**, *3*, 187–194.

155. La Mantia, F.P.; Morreale, M.; Mohd Ishak, Z.A. Processing and mechanical properties of organic filler-polypropylene composites. *J. Appl. Polym. Sci.* **2005**, *96*, 1906–1913.

156. Aigbodion, V.S.; Atuanya, C.U.; Igogori, E.A.; Ihom, P. Development of high-density polyethylene /orange peels particulate bio-composite. *Gazi Univ. J. Sci.* **2013**, *26*, 107–117.

157. Song, P.; Zhang, D.Y.; Yao, X.H.; Feng, F.; Wu, G.H. Preparation of a regenerated silk fibroin film and its adsorbability to azo dyes. *Int. J. Biol. Macromol.* **2017**, *102*, 1066–1072.

158. Xiao, S.; Wang, Z.; Ma, H.; Yang, H.; Xu, W. Effective removal of dyes from aqueous solution using ultrafine silk fibroin powder. *Adv. Powder Technol.* **2014**, *25*, 574–581.

159. Ki, C.S.; Gang, E.H.; Um, I.C.; Park, Y.H. Nanofibrous membrane of wool keratose/silk fibroin blend for heavy metal ion adsorption. *J. Memb. Sci.* **2007**, *302*, 20–26.

160. Ling, S.; Jin, K.; Kaplan, D.L.; Buehler, M.J. Ultrathin free-standing bombyx mori silk nanofibril membranes. *Nano Lett.* **2016**, *16*, 3795–3800.

161. Salama, A.; Shoueir, K.R.; Aljohani, H.A. Preparation of sustainable nanocomposite as new adsorbent for dyes removal. *Fibers Polym.* **2017**, *18*, 1825–1830.

162. Yalcin, E.; Gedikli, S.; Çabuk, A.; Karahaliloɨlu, Z.; Demirbilek, M.; Bayram, C.; Şam, M.; Saɨlam, N.; Denkbaş, E.B. Silk fibroin/nylon-6 blend nanofilter matrix for copper removal from aqueous solution. *Clean Technol. Environ. Policy* **2015**, *17*, 921–934.

163. Genovese, M.E.; Caputo, G.; Nanni, G.; Setti, C.; Bustreo, M.; Perotto, G.; Athanassiou, A.; Fragouli, D. Light Responsive Silk Nanofibers: An Optochemical Platform for Environmental Applications. *ACS Appl. Mater. Interfaces* **2017**, *9*, 40707–40715.

164. Vepari, C.; Kaplan, D.L. Silk as a biomaterial. *Prog. Polym. Sci.* **2007**, *32*, 991–1007.

165. Hu, X.; Kaplan, D.; Cebe, P. Determining Beta - Sheet Crystallinity in Fibrous Proteins by Thermal Analysis and Infrared Spectroscopy. *Macromolecules* **2006**, *39*, 6161–6170.

166. Rockwood, D.N.; Preda, R.C.; Yücel, T.; Wang, X.; Lovett, M.L.; Kaplan, D.L. Materials fabrication from Bombyx mori silk fibroin. *Nat. Protoc.* **2011**, *6*, 1612–1631.

167. Lawrence, B.D.; Omenetto, F.; Chui, K.; Kaplan, D.L. Processing methods to control silk fibroin film biomaterial features. *J. Mater. Sci.* **2008**, *43*, 6967–6985.

168. Motta, A.; Floren, M.; Migliaresi, C. Silk: A Unique Family of Biopolymers. In *Biomaterials from Nature for Advanced Devices and Therapies, First Edition*; Neves, N.M., Reis, R.L., Eds.; John Wiley & Sons, Inc., Hoboken, New Jersey, 2016; pp. 127–141 ISBN 9781119126218.

169. Lu, Q.; Zhang, B.; Li, M.; Zuo, B.; Kaplan, D.L.; Huang, Y.; Zhu, H. Degradation mechanism and control of silk fibroin. *Biomacromolecules* **2011**, *12*, 1080–1086.

170. Lu, S.; Li, J.; Zhang, S.; Yin, Z.; Xing, T.; Kaplan, D.L. The influence of the hydrophilic–lipophilic environment on the structure of silk fibroin protein. *J. Mater. Chem. B* **2015**, *3*, 2599–2606.

171. Kasoju, N.; Hawkins, N.; Pop-Georgievski, O.; Kubies, D.; Vollrath, F. Silk fibroin gelation via non-solvent induced phase separation. *Biomater. Sci.* **2016**, *4*, 460–473.

172. Matsumoto, A.; Chen, J.; Collette, A.L.; Kim, U.J.; Altman, G.H.; Cebe, P.; Kaplan, D.L. Mechanisms of silk fibroin sol-gel transitions. *J. Phys. Chem. B* **2006**, *110*, 21630–21638.

173. Baldino, L.; Cardea, S.; Reverchon, E. Loaded silk fibroin aerogel production by supercritical gel drying process for nanomedicine applications. *Chem. Eng. Trans.* **2016**, *49*, 343–348.

174. Della Porta, G.; Del Gaudio, P.; De Cicco, F.; Aquino, R.P.; Reverchon, E. Supercritical drying of alginate beads for the development of aerogel biomaterials: Optimization of process parameters and exchange solvents. *Ind. Eng. Chem. Res.* **2013**, *52*, 12003–12009.

175. Kuila, U.; Prasad, M. Specific surface area and pore-size distribution in clays and shales. *Geophys. Prospect.* **2013**, *61*, 341–362.

176. Sing, K.S.W.; EVERETT, D.; HAUL, H.R.A.W.; MOSCOU, L.; PIEROTTI, R.A.; ROUQUEROL, J.; SIEMIENIEWSKA, T. Reporting physisorption data for gas/solid systems with special reference to the determination of surface area and porosity (Recommendations 1984). *Pure Appl. Chem.* **1985**, *57*, 603–619.

177. Kaufmann, J.; Loser, R.; Leemann, A. Analysis of cement-bonded materials by multi-cycle mercury intrusion and nitrogen sorption. *J. Colloid Interface Sci.* **2009**, *336*, 730–737.

178. Barth, A. Infrared spectroscopy of proteins. *Biochim. Biophys. Acta* **2007**, *1767*, 1073–1101.

179. Munagapati, V.S.; Kim, D.S. Adsorption of anionic azo dye Congo Red from aqueous solution by Cationic Modified Orange Peel Powder. *J. Mol. Liq.* **2016**, *220*, 540–548.

180. Floren, M.L.; Spilimbergo, S.; Motta, A.; Migliaresi, C. Carbon dioxide induced silk protein gelation for biomedical applications. *Biomacromolecules* **2012**, *13*, 2060–2072.

181. Wilson, D.; Valluzzi, R.; Kaplan, D. Conformational Transitions in Model Silk Peptides. *Biophys. J.* **2000**, *78*, 2690–2701.

182. L. Wray, X. Hu, J. Gallego, I. Georgakoudi, F. Omenetto, D. Schmidt, D.K. et al. Effect of processing on silk-based biomaterials: Reproducibility and biocompatibility†. *J. Biomed. Mater. Res. Part B Appl. Biomater.* **2011**, *99(B)*, 89–101.

183. Jin, H.J.; Park, J.; Karageorgiou, V.; Kim, U.J.; Valluzzi, R.; Cebe, P.; Kaplan, D.L. Water-stable silk films with reduced β-sheet content. *Adv. Funct. Mater.* **2005**, *15*, 1241–1247.

184. Barreto, A.C.H.; Costa, M.M.; Sombra, A.S.B.; Rosa, D.S.; Nascimento, R.F.; Mazzetto, S.E.; Fechine, P.B.A. Chemically Modified Banana Fiber: Structure, Dielectrical Properties and Biodegradability. *J. Polym. Environ.* **2010**, *18*, 523–531.

185. Dubey, P.; Murab, S.; Karmakar, S.; Chowdhury, P.K.; Ghosh, S. Modulation of Self-Assembly Process of Fibroin: An Insight for Regulating the Conformation of Silk Biomaterials. *Biomacromolecules* **2015**, *16*, 3936–3944.

186. Yaseen, D.A.; Scholz, M. *Textile dye wastewater characteristics and constituents of synthetic effluents: a critical review*; Springer Berlin Heidelberg, 2019; Vol. 16; ISBN 0123456789.

187. Cui, L.; Liu, C.; Wu, G. Performance and mechanism of methylene blue biosorption on orange peel. *Environ. Technol.* **2008**, *29*, 1021–1030.

188. Wang, X.; Hu, X.; Daley, A.; Rabotyagova, O.; Cebe, P.; Kaplan, L. Nanolayer Biomaterial Coatings of Silk Fibroin for Controlled Release. *J. Control Release* **2007**, *121*, 190–199.

189. Banerjee, S.; Chattopadhyaya, M.C. Adsorption characteristics for the removal of a toxic dye, tartrazine from aqueous solutions by a low cost agricultural by-product. *Arab. J. Chem.* **2017**, *10*, S1629–S1638.

190. Low, L.W.; Teng, T.T.; Morad, N.; Azahari, B. Studies on the Adsorption of

Methylene Blue Dye from Aqueous Solution onto Low-Cost Tartaric Acid Treated Bagasse. *APCBEE Procedia* **2012**, *1*, 103–109.

191. Yagub, M.T.; Sen, T.K.; Afroze, S.; Ang, H.M. Dye and its removal from aqueous solution by adsorption: A review. *Adv. Colloid Interface Sci.* **2014**, *209*, 172–184.

192. Mohammed, M. a; Shitu, A.; Ibrahim, A. Removal of Methylene Blue Using Low Cost Adsorbent : A Review. *Res. J. Chem. Sci.* **2014**, *4*, 91–102.

193. Kallel, F.; Chaari, F.; Bouaziz, F.; Bettaieb, F.; Ghorbel, R.; Chaabouni, S.E. Sorption and desorption characteristics for the removal of a toxic dye, methylene blue from aqueous solution by a low cost agricultural by-product. *J. Mol. Liq.* **2016**, *219*, 279–288.

194. Miraboutalebi, S.M.; Nikouzad, S.K.; Peydayesh, M.; Allahgholi, N.; Vafajoo, L.; McKay, G. Methylene blue adsorption via maize silk powder: Kinetic, equilibrium, thermodynamic studies and residual error analysis. *Process Saf. Environ. Prot.* **2017**, *106*, 191–202.

195. Simonin, J.P. On the comparison of pseudo-first order and pseudo-second order rate laws in the modeling of adsorption kinetics. *Chem. Eng. J.* **2016**, *300*, 254–263.

196. Kostić, M.; Radović, M.; Velinov, N.; Najdanović, S.; Bojić, D.; Hurt, A.; Bojić, A. Synthesis of mesoporous triple-metal nanosorbent from layered double hydroxide as an efficient new sorbent for removal of dye from water and wastewater. *Ecotoxicol. Environ. Saf.* **2018**, *159*, 332–341.

197. Gomes, R.F.; de Azevedo, A.C.N.; Pereira, A.G.B.; Muniz, E.C.; Fajardo, A.R.; Rodrigues, F.H.A. Fast dye removal from water by starch-based nanocomposites. *J. Colloid Interface Sci.* **2015**, *454*, 200–209.

198. A.O, D. Langmuir, Freundlich, Temkin and Dubinin–Radushkevich Isotherms Studies of Equilibrium Sorption of Zn 2+ Unto Phosphoric Acid Modified Rice Husk. *IOSR J. Appl. Chem.* **2012**, *3*, 38–45.

199. Ouellet-Plamondon, C.; Aranda, P.; Favier, A.; Habert, G.; van Damme, H.; Ruiz-Hitzky, E. The Maya blue nanostructured material concept applied to colouring geopolymers. *RSC Adv.* **2015**, *5*, 98834–98841.

200. Cenens, J.; Schoonheydt, R.A. Visible Spectroscopy of Methylene Blue on Hectorite, Laponite B, and Barasym in Aqueous Suspension. *Clays Clay Miner.* **1988**, *36*, 214–224.

201. Philippe, K.K.; Timmers, R.; Van Grieken, R.; Marugan, J. Photocatalytic Disinfection and Removal of Emerging Pollutants from Effluents of Biological Wastewater Treatments, Using a Newly Developed Large-Scale Solar Simulator. *Ind. Eng. Chem. Res.* **2016**, *55*, 2952–2958.

202. Demir, M.M.; Gulgun, M.A.; Menceloglu, Y.Z.; Erman, B.; Abramchuk, S.S.; Makhaeva, E.E.; Khokhlov, A.R.; Matveeva, V.G.; Sulman, M.G. Palladium Nanoparticles by Electrospinning from Poly(acrylonitrile-co-acrylic acid)-PdCl2 Solutions. Relations between Preparation Conditions, Particle Size, and Catalytic Activity. *Macromolecules* **2004**, *37*, 1787–1792.

203. Andrade, G.R.S.; Nascimento, C.C.; Lima, Z.M.; Teixeira-Neto, E.; Costa, L.P.; Gimenez, I.F. Star-shaped ZnO/Ag hybrid nanostructures for enhanced photocatalysis and antibacterial activity. *Appl. Surf. Sci.* **2017**, *399*, 573–582.

204. Thanh Hoai Ta, Q.; Park, S.; Noh, J.S.; Thanh, Q.; Ta, H.; Park, S.; Noh, J.S.; Thanh Hoai Ta, Q.; Park, S.; Noh, J.S.; et al. Ag nanowire/ZnO nanobush hybrid structures for improved photocatalytic activity. *J. Colloid Interface Sci.* **2017**, *505*, 437–444.

205. He, X.; Yang, D.P.; Zhang, X.; Liu, M.; Kang, Z.; Lin, C.; Jia, N.; Luque, R. Waste eggshell membrane-templated CuO-ZnO nanocomposites with enhanced adsorption, catalysis and antibacterial properties for water purification. *Chem. Eng. J.* **2019**, *369*, 621–633.

206. Ussia, M.; Di Mauro, A.; Mecca, T.; Cunsolo, F.; Nicotra, G.; Spinella, C.; Cerruti, P.; Impellizzeri, G.; Privitera, V.; Carroccio, S.C. ZnO-pHEMA Nanocomposites: An Ecofriendly and Reusable Material for Water Remediation. *ACS Appl. Mater. Interfaces* **2018**, *10*, 40100–40110.

207. Su, Y.Q.; Zhu, Y.; Yong, D.; Chen, M.; Su, L.; Chen, A.; Wu, Y.; Pan, B.; Tang, Z. Enhanced Exciton Binding Energy of ZnO by Long-Distance Perturbation of Doped Be Atoms. *J. Phys. Chem. Lett.* **2016**, *7*, 1484–1489.

208. Guidelli, E.J.; Baffa, O.; Clarke, D.R. Enhanced UV Emission from Silver/ZnO and Gold/ZnO Core-Shell Nanoparticles: Photoluminescence, Radioluminescence, and Optically Stimulated Luminescence. *Sci. Rep.* **2015**, *5*, 1–11.

209. Li, P.; Wei, Z.; Wu, T.; Peng, Q.; Li, Y. Au-ZnO hybrid nanopyramids and their photocatalytic properties. *J. Am. Chem. Soc.* **2011**, *133*, 5660–5663.

210. He, W.; Kim, H.-K.; Wamer, W.G.; Melka, D.; Callahan, J.H.; Yin, J.-J. Photogenerated charge carriers and reactive oxygen species in ZnO/Au hybrid nanostructures with enhanced photocatalytic and antibacterial activity. *J. Am. Chem. Soc.* **2014**, *136*, 750–7.

211. Rabanal, M.E. Solvothermal synthesis of Ag / ZnO and Pt / ZnO nanocomposites and comparison of their photocatalytic behaviors on dyes degradation. **2016**, *27*, 983–993.

212. Gupta, J.; Mohapatra, J.; Bahadur, D. Visible light driven mesoporous Ag-embedded ZnO nanocomposites: reactive oxygen species enhanced photocatalysis, bacterial inhibition and photodynamic therapy. *Dalt. Trans.* **2017**, *46*, 685–696.

213. Putri, N.A.; Fauzia, V.; Iwan, S.; Roza, L.; Umar, A.A.; Budi, S. Mn-doping-induced photocatalytic activity enhancement of ZnO nanorods prepared on glass substrates. *Appl. Surf. Sci.* **2018**, *439*, 285–297.

214. Kong, J.-Z.; Zhai, H.-F.; Zhang, W.; Wang, S.-S.; Zhao, X.-R.; Li, M.; Li, H.; Li, A.-D.; Wu, D. Visible Light-Driven Photocatalytic Performance of N-Doped ZnO / g-C 3 N 4 Nanocomposites. *Nanoscale Res. Lett.* **2017**.

215. Waiskopf, N.; Ben-Shahar, Y.; Banin, U. Photocatalytic Hybrid Semiconductor–Metal Nanoparticles; from Synergistic Properties to Emerging Applications. *Adv. Mater.* **2018**, *30*, 1–10.

216. Picciolini, S.; Castagnetti, N.; Vanna, R.; Mehn, D.; Bedoni, M.; Gramatica, F.; Villani, M.; Calestani, D.; Pavesi, M.; Lazzarini, L.; et al. Branched gold nanoparticles on ZnO 3D architecture as biomedical SERS sensors. *RSC Adv.* **2015**, *5*, 93644–93651.

217. Zhang, W.; Wang, W.; Shi, H.; Liang, Y.; Fu, J.; Zhu, M. Surface plasmon-driven photoelectrochemical water splitting of aligned ZnO nanorod arrays decorated with loading-controllable Au nanoparticles. *Sol. Energy Mater. Sol. Cells* **2018**, *180*, 25–33.

218. Cheng, Y.; Jiao, W.; Li, Q.; Zhang, Y.; Li, S.; Li, D.; Che, R. Two Hybrid Au-ZnO Aggregates with Different Hierarchical Structures : a Comparable Study in Photocatalysis. *J. Colloid Interface Sci.* **2017**, *509*, 58–67.

219. Pastorizo-Santos, I.; Liz-Marzán, L.M. N,N-dimethylformamide as a reaction medium for metal nanoparticle synthesis. *Adv. Funct. Mater.* **2009**, *19*, 679–688.

220. Muravitskaya, A.; Rumyantseva, A.; Kostcheev, S.; Dzhagan, V.; Stroyuk, O.; Adam, P.-M. Enhanced Raman scattering of ZnO nanocrystals in the vicinity of gold and silver nanostructured surfaces. *Opt. Express* **2016**, *24*, A168–A173.

221. Xie, W.; Li, Y.; Sun, W.; Huang, J.; Xie, H.; Zhao, X. Surface modification of ZnO with Ag improves its photocatalytic efficiency and photostability. *J. Photochem. Photobiol. A Chem.* **2010**, *216*, 149–155.

222. Akira, M.; Yanzhi, R.; Kimihiro, M.; Hiroshi, I.; Yukio, M.; Isao, N.; Yukihiro, O. Two-dimensional Fourier-transform Raman and near-infrared correlation spectroscopy studies of poly(methyl methacrylate) blends: 1. Immiscible blends of poly(methyl methacrylate) and atactic polystyrene. *Vib. Spectrosc.* **2000**, *24*, 171–180.

223. Rumyantseva, A.; Kostcheev, S.; Adam, P.M.; Gaponenko, S. V.; Vaschenko, S. V.; Kulakovich, O.S.; Ramanenka, A.A.; Guzatov, D. V.; Korbutyak, D.; Dzhagan, V.; et al. Nonresonant surface-enhanced raman scattering of ZnO quantum dots with Au and Ag nanoparticles. *ACS Nano* **2013**, *7*, 3420–3426.

224. Antony, A.; Poornesh, P.; Kityk, I. V.; Ozga, K.; Jedryka, J.; Philip, R.; Sanjeev, G.; Petwal, V.C.; Verma, V.P.; Dwivedi, J. Methodical engineering of defects in Mn X Zn 1-X O(x = 0.03, and 0.05) nanostructures by electron beam for nonlinear optical applications: A new insight. *Ceram. Int.* **2019**, *45*, 8988–8999.

225. Milekhin, A.G.; Sveshnikova, L.L.; Duda, T.A.; Yeryukov, N.A.; Rodyakina, E.E.; Gutakovskii, A.K.; Batsanov, S.A.; Latyshev, A. V.; Zahn, D.R.T. Surface-enhanced Raman spectroscopy of semiconductor nanostructures. *Phys. E Low-Dimensional Syst. Nanostructures* **2016**, *75*, 210–222.

226. Bilic, A.; Reimers, J.R.; Hush, N.S.; Hoft, R.C.; Ford, M.J.; Biosciences, M.; Bilić, A.; Reimers, J.R.; Hush, N.S.; Hoft, R.C.; et al. Adsorption of Benzene on Copper, Silver, and Gold Surfaces. *Adsorpt. J. Int. Adsorpt. Soc.* **2006**, *2*, 1093–1105.

227. Ide, Y.; Matsuoka, M.; Ogawa, M. Efficient visible-light-induced photocatalytic activity on gold-nanoparticle-supported layered titanate. *J. Am. Chem. Soc.* **2010**, *132*, 16762–16764.

228. Kong, L.; Jiang, Z.; Lai, H.H.; Xiao, T.; Edwards, P.P. Progress in Natural Science : Materials International Does noble metal modi fi cation improve the photocatalytic activity of BiOCl ? *Prog. Nat. Sci. Mater. Int.* **2013**, *23*, 286–293.

229. Liu, H.; Hu, Y.; Zhang, Z.; Liu, X.; Jia, H.; Xu, B. Synthesis of spherical Ag/ZnO heterostructural composites with excellent photocatalytic activity under visible light and UV irradiation. *Appl. Surf. Sci.* **2015**, *355*, 644–652.

230. Gomes, F.; Lopes, A.; Bednarczyk, K.; Gmurek, M.; Stelmachowski, M.; Id, A.Z.; Quinta-ferreira, M.E.; Costa, R.; Quinta-ferreira, R.M.; Martins, R.C. Effect of Noble Metals (Ag , Pd , Pt) Loading over the Efficiency of TiO 2 during Photocatalytic Ozonation on the Toxicity of Parabens †. *ChemEngineering* **2018**, *2*, 1–14.

231. Erjavec, B.; Hudoklin, P.; Perc, K.; Tišler, T.; Dolenc, M.S.; Pintar, A. Glass fiber-supported TiO2 photocatalyst: Efficient mineralization and removal of toxicity/estrogenicity of bisphenol A and its analogs. *Appl. Catal. B Environ.* **2016**, *183*, 149–158.

232. Lee, K.M.; Lai, C.W.; Ngai, K.S.; Juan, J.C. Recent developments of zinc oxide based photocatalyst in water treatment technology: A review. *Water Res.* **2016**, *88*, 428–448.

233. Sarro, M.; Gule, N.P.; Laurenti, E.; Gamberini, R.; Paganini, M.C.; Mallon, P.E.; Calza, P. ZnO-based materials and enzymes hybrid systems as highly efficient catalysts for recalcitrant pollutants abatement. *Chem. Eng. J.* **2018**, *334*, 2530–2538.

234. Campagnolo, L.; Lauciello, S.; Athanassiou, A.; Fragouli, D. Au/ZnO hybrid nanostructures on electrospun polymeric mats for improved photocatalytic

degradation of organic pollutants. *Water* **2019**, *11*, 1–15.

235. Petronella, F.; Truppi, A.; Ingrosso, C.; Placido, T.; Striccoli, M.; Curri, M.L.; Agostiano, A.; Comparelli, R. Nanocomposite materials for photocatalytic degradation of pollutants. *Catal. Today* **2017**, *281*, 85–100.

236. Kaplan, R.; Erjavec, B.; Dražić, G.; Grdadolnik, J.; Pintar, A. Simple synthesis of anatase/rutile/brookite TiO2 nanocomposite with superior mineralization potential for photocatalytic degradation of water pollutants. *Appl. Catal. B Environ.* **2016**, *181*, 465–474.

237. Wang, C.Y.; Zhang, X.; Song, X.N.; Wang, W.K.; Yu, H.Q. Novel Bi 12 O 15 Cl 6 Photocatalyst for the Degradation of Bisphenol A under Visible-Light Irradiation. *ACS Appl. Mater. Interfaces* **2016**, *8*, 5320–5326.

238. Bellardita, M.; Fiorenza, R.; Palmisano, L.; Scirè, S. *Photocatalytic and photothermocatalytic applications of cerium oxide-based materials*; Elsevier Inc., 2020; ISBN 9780128156612.

239. Montini, T.; Melchionna, M.; Monai, M.; Fornasiero, P. Fundamentals and Catalytic Applications of CeO2-Based Materials. *Chem. Rev.* **2016**, *116*, 5987–6041.

240. Charalampides, G.; Vatalis, K.I.; Apostoplos, B.; Ploutarch-Nikolas, B. Rare Earth Elements: Industrial Applications and Economic Dependency of Europe. *Procedia Econ. Financ.* **2015**, *24*, 126–135.

241. Loddo, V.; Yurdakal, S.; Parrino, F. Economical aspects, toxicity, and environmental fate of cerium oxide. In *Cerium Oxide (CeO_2): Synthesis, Properties and Applications*; Elsevier Inc., 2020; pp. 359–373 ISBN 9780128156612.

242. Xie, S.; Wang, Z.; Cheng, F.; Zhang, P.; Mai, W.; Tong, Y. Ceria and ceria-based nanostructured materials for photoenergy applications. *Nano Energy* **2017**, *34*, 313–337.

243. Yuán, S.; Xu, B.; Zhang, Q.; Liu, S.; Xie, J.; Zhang, M.; Ohno, T. Development of the Visible-Light Response of CeO2−x with a high Ce3+ Content and Its Photocatalytic Properties. *ChemCatChem* **2018**, *10*, 1267–1271.

244. Wu, L.; Fang, S.; Ge, L.; Han, C.; Qiu, P.; Xin, Y. Facile synthesis of Ag@CeO<inf>2</inf> core-shell plasmonic photocatalysts with enhanced visible-light photocatalytic performance. *J. Hazard. Mater.* **2015**, *300*, 93–103.

245. Agrawal, A.; Cho, S.H.; Zandi, O.; Ghosh, S.; Johns, R.W.; Milliron, D.J. Localized Surface Plasmon Resonance in Semiconductor Nanocrystals. *Chem. Rev.* **2018**, *118*, 3121–3207.

246. Mohanty, B.C.; Lee, J.W.; Yeon, D.H.; Jo, Y.H.; Kim, J.H.; Cho, Y.S. Dopant induced variations in microstructure and optical properties of CeO2 nanoparticles. *Mater. Res. Bull.* **2011**, *46*, 875–883.

247. Vinothkumar, G.; Rengaraj, S.; Arunkumar, P.; Cha, S.W.; Suresh Babu, K. Ionic Radii and Concentration Dependency of RE 3+ (Eu 3+ , Nd 3+ , Pr 3+ , and La 3+)-Doped Cerium Oxide Nanoparticles for Enhanced Multienzyme-Mimetic and Hydroxyl Radical Scavenging Activity. *J. Phys. Chem. C* **2019**, *123*, 541–553.

248. Runnerstrom, E.L.; Ong, G.K.; Gregori, G.; Maier, J.; Milliron, D.J. Colloidal Nanocrystal Films Reveal the Mechanism for Intermediate Temperature Proton Conductivity in Porous Ceramics. *J. Phys. Chem. C* **2018**, *122*, 13624–13635.

249. Xu, B.; Zhang, Q.; Yuan, S.; Zhang, M.; Ohno, T. Synthesis and photocatalytic performance of yttrium-doped CeO 2 with a porous broom-like hierarchical structure. *Appl. Catal. B Environ.* **2016**, *183*, 361–370.

250. Khan, M.E.; Khan, M.M.; Cho, M.H. Ce3+-ion, Surface Oxygen Vacancy, and Visible Light-induced Photocatalytic Dye Degradation and Photocapacitive Performance of CeO2-Graphene Nanostructures. *Sci. Rep.* **2017**, *7*, 1–17.

251. Ashcroft, N.W.; Denton, A.R.; Ashcroft, N.W. Vegard Rule. *Phys. Rev. A* **1991**, *43*, 3161–3164.

252. Ouyang, W.; Wang, Y.; Lin, C.; He, M.; Hao, F.; Liu, H.; Zhu, W. Heavy metal loss from agricultural watershed to aquatic system: A scientometrics review. *Sci. Total Environ.* **2018**, *637–638*, 208–220.

253. Joe, H.E.; Yun, H.; Jo, S.H.; Jun, M.B.G.; Min, B.K. A review on optical fiber sensors for environmental monitoring. *Int. J. Precis. Eng. Manuf. - Green Technol.* **2018**, *5*, 173–191.

254. Rivero, P.J.; Goicoechea, J.; Arregui, F.J. Optical fiber sensors based on polymeric sensitive coatings. *Polymers (Basel).* **2018**, *10*, 1–26.

255. Perotto, G.; Zhang, Y.; Naskar, D.; Patel, N.; Kaplan, D.L.; Kundu, S.C.; Omenetto, F.G. The optical properties of regenerated silk fibroin films obtained from different sources. *Appl. Phys. Lett.* **2017**, *111*.

256. Schnepf, M.J.; Mayer, M.; Kuttner, C.; Tebbe, M.; Wolf, D.; Dulle, M.; Altantzis, T.; Formanek, P.; Förster, S.; Bals, S.; et al. Nanorattles with tailored electric field enhancement. *Nanoscale* **2017**, *9*, 9376–9385.

257. Yu, H.; Chong, Z.Z.; Tor, S.B.; Liu, E.; Loh, N.H. Low temperature and deformation-free bonding of PMMA microfluidic devices with stable hydrophilicity via oxygen plasma treatment and PVA coating. *RSC Adv.* **2015**, *5*, 8377–8388.

258. Chen, H.; Yan, X.; Feng, Q.; Zhao, P.; Xu, X.; Ng, D.H.L.; Bian, L. Citric Acid/Cysteine-Modified Cellulose-Based Materials: Green Preparation and Their Applications in Anticounterfeiting, Chemical Sensing, and UV Shielding. *ACS Sustain. Chem. Eng.* **2017**, *5*, 11387–11394.

259. Kim, J.P.; Xie, Z.; Creer, M.; Liu, Z.; Yang, J. Citrate-based fluorescent materials for low-cost chloride sensing in the diagnosis of cystic fibrosis. *Chem. Sci.* **2016**, *8*, 550–558.

260. Hatanaka, M.; Takahashi, N.; Tanabe, T.; Nagai, Y.; Dohmae, K.; Aoki, Y.; Yoshida, T.; Shinjoh, H. Ideal Pt loading for a Pt/CeO2-based catalyst stabilized by a Pt-O-Ce bond. *Appl. Catal. B Environ.* **2010**, *99*, 336–342.

261. Cai, H.; Guo, F.; Zhang, X.; Wang, X.; Hu, L.; Zhao, X.; Xiao, P. Fabrication of a Novel Catalyst Reactor with Improved Strength and Catalytic Performance Used for Automotive Exhaust Treatment. *Ind. Eng. Chem. Res.* **2019**, *58*, 4024–4031.

262. Kale, M.J.; Avanesian, T.; Xin, H.; Yan, J.; Christopher, P. Controlling catalytic selectivity on metal nanoparticles by direct photoexcitation of adsorbate-metal bonds. *Nano Lett.* **2014**, *14*, 5405–5412.

263. Lou, Y.; Liu, J. A highly active Pt-Fe/γ-Al2O3 catalyst for preferential oxidation of CO in excess of H2 with a wide operation temperature window. *Chem. Commun.* **2017**, *53*, 9020–9023.

264. Derita, L.; Dai, S.; Lopez-zepeda, K.; Pham, N.; Graham, G.W.; Pan, X.; Christopher, P. Catalyst Architecture for Stable Single Atom Dispersion Enables Site- Speci fi c Spectroscopic and Reactivity Measurements of CO Adsorbed to Pt Atoms , Oxidized Pt Clusters , and Metallic Pt Clusters on TiO 2. **2017**.

265. DeRita, L.; Resasco, J.; Dai, S.; Boubnov, A.; Thang, H.V.; Hoffman, A.S.; Ro, I.; Graham, G.W.; Bare, S.R.; Pacchioni, G.; et al. Structural evolution of atomically dispersed Pt catalysts dictates reactivity. *Nat. Mater.* **2019**, *18*, 746–751.

266. Jones, J.; Xiong, H.; DeLaRiva, A.T.; Peterson, E.J.; Pham, H.; Challa, S.R.; Qi, G.; Oh, S.; Wiebenga, M.H.; Hernández, X.I.P.; et al. Thermally stable single-atom platinum-on-ceria catalysts via atom trapping. *Science (80-.).* **2016**, *353*, 150–154.

267. Kale, M.J.; Christopher, P. Utilizing Quantitative in Situ FTIR Spectroscopy to Identify Well-Coordinated Pt Atoms as the Active Site for CO Oxidation on Al2O3-Supported Pt Catalysts. *ACS Catal.* **2016**, *6*, 5599–5609.

268. Li, X.; Yang, X.; Huang, Y.; Zhang, T.; Liu, B. Supported Noble-Metal Single Atoms for Heterogeneous Catalysis. *Adv. Mater.* **2019**, *1902031*, 1–19.

269. Diodati, S.; Dolcet, P.; Casarin, M.; Gross, S. Pursuing the Crystallization of Mono- and Polymetallic Nanosized Crystalline Inorganic Compounds by Low-

Temperature Wet-Chemistry and Colloidal Routes. *Chem. Rev.* **2015**, *115*, 11449–11502.

270. Lee, S.S.; Zhu, H.; Contreras, E.Q.; Prakash, A.; Puppala, H.L.; Colvin, V.L. High temperature decomposition of cerium precursors to form ceria nanocrystal libraries for biological applications. *Chem. Mater.* **2012**, *24*, 424–432.

271. Foos, E.E.; Wilkinson, J.; Mäkinen, A.J.; Watkins, N.J.; Kafafi, Z.H.; Long, J.P. Synthesis and surface composition study of CdSe nanoclusters prepared using solvent systems containing primary, secondary, and tertiary amines. *Chem. Mater.* **2006**, *18*, 2886–2894.

272. Thang, H.V.; Pacchioni, G.; DeRita, L.; Christopher, P. Nature of stable single atom Pt catalysts dispersed on anatase TiO2. *J. Catal.* **2018**, *367*, 104–114.